# STRUCTURE-FUNCTION RELATIONSHIPS IN BACTERIAL REGULATORY PROTEINS AND AN ENZYME INVOLVED IN ANTIBIOTIC BIOSYNTHESIS

by

Lanlan Han

A Dissertation Submitted in

Partial Fulfillment of the

Requirements for the Degree of

Doctor of Philosophy

in Chemistry

at

The University of Wisconsin-Milwaukee

December 2017

ABSTRACT

STRUCTURE-FUNCTION RELATIONSHIPS IN BACTERIAL REGULATORY PROTEINS AND AN ENZYME INVOLVED IN ANTIBIOTIC BIOSYNTHESIS

by

Lanlan Han

The University of Wisconsin-Milwaukee, 2017
Under the Supervision of Professor Nicholas R. Silvaggi

The first part of my thesis is focused on a new family of two-component response regulator proteins: Aspartate-Less Regulators (ALR). They lack the catalytic aspartate residue required for the phosphorylation mechanism of typical two component response regulators. We are using biophysical tools to characterize two proteins with redox-sensitive ALR domains: repressor of iron transport regulator (RitR) from *Streptococcus pneumonia* R6 and diguanylate cyclase Q15Z91 from *Pseudoalteromonas atalantica*. The structure of inactive $RitR_{C128S}$ monomer showed that the ALR domain and the DNA-binding domain are linked by an α-helix that runs the length of the entire protein, with C128 near the C-terminal end. Bioinformatic analysis of all streptococcal RitR homologs showed that Cys128 is strictly conserved, suggesting that RitR may be a novel redox sensor. Hydrogen peroxide was used to oxidize the cysteine thiol group to determine the structure of the oxidized, dimeric form of RitR. Oxidation of C128 to the disulfide caused a conformational change that caused the DBD to release from the ALR domain. Surprisingly, the freed DBD was observed bound to the ALR domain of the other, disulfide-linked molecule of RitR, recapitulating almost exactly the structure of the inactive, monomeric protein. An extended dimeric conformation was found in the $RitR_{L86A/V93A}$ variant. It binds to the target DNA according to gel filtration and differential scanning fluorimetry. The crystal structure of the

$RitR_{L86A/V93A}$ ALR domain showed an unprecedented conformational change for a response regulator protein, where helix α4 is disordered and the two protomers swap their α5 helices to form the dimer. Combined with the C128D mutant in vivo studies, it seems that oxidation of C128 is part of the activation mechanism, but there must be an additional factor that leads to dimerization of the ALR domains. The second ALR protein Q15Z91 has R61 replacing the phosphorylatable aspartate residue in the ALR domain. According to the structure of Q15Z91 with GTP and c-di-GMP, purified Q15Z91 is an activated but product-inhibited dimer. C142 is conserved in the same position as C128 in RitR, and substitution demonstrated that C142 residue is also a redox sensor that involved in Q15Z91 activity regulation.

The second part is a mechanistic enzymology project aimed at understanding the structure and mechanism of the novel pyridoxal-5'-phosphate (PLP)-dependent L-arginine hydroxylase/deaminase, MppP, from *Streptomyces wadayamensis* (SwMppP). SwMppP is predicted to be a type I/II aminotransferase based on primary sequence identity. However, NMR and ESI-MS results showed that SwMppP is not an aminotransferase, but rather a hydroxylase. The enzyme catalyzes the oxygen-dependent hydroxylation of L-arginine, forming 4-hydroxy-2-ketoarginine and the abortive side-product 2-ketoargine in a ratio of 1.7:1. This is exciting because SwMppP is the first PLP-dependent enzyme to react with oxygen in any context other than oxidative decarboxylation. The discovery of this new activity is especially surprising given that the tertiary structure of SwMppP is very similar to that of the prototypical aminotransferase, the *E. coli* aspartate aminotransferase (PDB entry 1ARS; RMSD of aligned Cα atoms is 3.7 Å). The major differences between the two enzymes are the disordered N terminus of SwMppP, and changes of a limited number of

amino acids near the PLP cofactor. The N-terminal helix transitions from a disordered, random-coil state to a helical conformation covering the active site only if/when the substrate is bound. Specific roles of the un-conserved residues in the active site are being studied by mutagenesis. So far, most of the SwMppP mutants have lost the hydroxylase activity and only produce abortive side product 2-ketoarginine. Our mechanistic studies have revealed that formation of the fully oxidized (hydroxylated) product requires 2 equivalents of dioxygen, while formation of 2-ketoarginine requires only one equivalent of dioxygen. Interestingly, the hydroxyl group of 4-hydroxy-2-ketoarginine comes from $H_2O$, not dioxygen. Mutagenesis, structural and kinetic studies were used to understand how the residues in the active site stabilize the quinonoid form of the L-arginine-PLP complex to promote the reaction with dioxygen. Our structural and kinetic characterization of the wild-type and variant forms of SwMppP have allowed us to propose a model where the oxygen incorporated in the hydroxy-arginine product is derived from water rather than from dioxygen. In addition, SwMppP exhibits very high substrate specificity. Either change on the substrate length or guanidine group would result in no binding affinity or little activity.

© Copyright by Lanlan Han, 2017
All Rights Reserved

# TABLE OF CONTENTS

ABSTRACT ..... ii

**LIST OF FIGURES** ..... x

**LIST OF TABLES** ..... xvii

**ACKNOWLEDGMENTS** ..... xxiv

**Chapter 1 Introduction to Bacterial Signal Transduction**

**1.1 Histindine Kinase** ..... 3

**1.2 Response regulators (RRs)** ..... 7

**1.2.1 Activation mechanism of phosphorylation dependent RRs** ..... 7

**1.2.2 Conserved residues in phosphorylation-dependent RRs** ..... 13

**1.2.3 Atypical, phosphorylation-independent RRs containing the conserved Asp residue** 16

**1.2.4 Aspartate-Less Regulators (ALR)** ..... 18

1.2.4.1 Repressor of iron transport regulator (RitR) ..... 19

1.2.4.2 Diguanylate cyclase Q15Z91 ..... 26

**1.3 References** ..... 34

**Chapter 2 The Atypical Response Regulator Protein Repressor of Iron Transport Regulator (RitR) Exhibits an Alternative Mechanism of Activation**

**2.1 Background** ..... 41

**2.2 Methods** ..... 41

**2.2.1 Cloning, expression, and purification of wild-type and mutant RitR** ..... 41

**2.2.2 Preparation of purification of the oxidized RitR dimer ($RitR_{ox}$)** ..... 43

**2.2.3 Preparation of protein for structure determination** ..... 43

**2.2.4 Differential scanning fluorimetry** ..... 44

**2.2.5 Site-directed mutagenesis** ..... 46

**2.2.6 Determination of C128 $pK_a$ by DTNB assay [6, 7]** ..... 47

**2.2.7 Crystallization, structure determination, and model refinement** ..... 48

**2.2.8 Synthesis of binding site 3 (BS3) dsDNA oligonucleotides** ..... 52

**2.2.9 Size exclusion chromatography (SEC)** ..... 53

**2.2.10 Non-reducing SDS-PAGE and Native SDS-PAGE (NSDS)** ..... 54

**2.3 Results** ..... 55

**2.3.1 Determining the optimal RitR storage buffer for crystallization** ..... 55

**2.3.2 Monomeric structure of $RitR_{C128S}$** ..... 57

**2.3.3 The thiol group of the conserved C128 residue has a perturbed pKa** ..... 59

**2.3.4 The structure of $RitR_{ox}$** ..... 62

**2.3.5 RitR incubated with different metals** ..... 66

**2.3.6 Structural features important for RitR dimerization** ..... 69

**2.3.7 Mutations to the gate residues L86 and V93 result in an "extended" dimer** ..... 81

**2.3.8 Size exclusion chromatography of RitR : BS3 and $RitR_{L86A/V93A}$ : BS3** ..... 83

**2.3.9 Single mutants in helix α4 also bind to BS3-1** ..... 86

**2.3.10 Crystallization of $RitR_{L86A/V93A}$** ..... 87

**2.3.11 Shorten BS3-1 length for crystallization** ..... 89

**2.3.12 The ratio of $RitR_{L86A/V93A}$ : BS3-3 and $RitR_{L86A/V93A}$ : BS3-6 ..... 90**
**2.3.13 Structure of the $RitR_{L86A/V93A}$ REC domain ..... 92**
**2.3.14 Structure of the RD2LV REC domain construct ..... 97**
**2.3.15 RitR with GADDY motif ($RitR_{GADDY}$) ..... 99**
**2.3.16 The role of C128 in the $RitR_{L86A/V93A}$ variant ..... 101**
**2.4 Conclusions ..... 104**
**2.5 References ..... 110**
**Chapter 3 Uncharacterized Protein Q15Z91 from Pseudoalteromonas atlantica is an ALR-Regulated Diguanylate Cyclase**
**3.1 Introduction ..... 113**
**3.2 Methods ..... 114**
**3.2.1 Expression and purification of Q15Z91 ..... 114**
**3.2.2 Mutagenesis of Q15Z91 ..... 116**
**3.2.3 Crystallization, structure determination, and model refinement ..... 117**
**3.2.4 Quaternary structure characterization by size exclusion chromatography ..... 119**
**3.2.5 Size exclusion chromatography with multi-angle light scattering (SEC-MALS) ..... 119**
**3.2.6 Biofilm assay on borosilicate tubes ..... 120**
**3.2.7 Enzymatic assay ..... 121**
3.2.7.1 RP-HPLC based end-point assay ..... 121
3.2.7.2 Biomol Green microplate assay ..... 121
3.2.7.3 EnzCheck® Pyrophosphate Assay Kit (Sigma) ..... 122
**3.3 Results ..... 122**
**3.3.1 Q15Z91 is an ALR-regulated diguanylate cyclase ..... 122**
**3.3.2 Purification of Q15Z91 ..... 124**
**3.3.3 The structure of Q15Z91 with c-di-GMP and citrate bound ..... 125**
**3.3.4 Probing the roles of conserved residues by site-directed mutagenesis ..... 134**
**3.3.5 The oligomeric state of Q15Z91 ..... 136**
**3.3.6 Preliminary quantitation of biofilm phenotype ..... 139**
**3.3.7 Preliminary enzymatic activity ..... 142**
**3.4 Discussion ..... 144**
**3.5 References ..... 146**
**Chapter 4 An Unusual PLP-Dependent Enzyme in Enduracididine Biosynthesis**
**4.1 Introduction ..... 148**
**4.2 Biosynthesis of enduracididine ..... 154**
**4.3 Pyridoxial 5'-phosphate is a versatile cofactor ..... 159**
**4.4 Aminotransferases (ATase) ..... 166**
**4.4.1 The AATase active site ..... 167**
**4.4.2 Conformational changes associated with catalysis ..... 168**
**4.4.3 Dual substrate recognition ..... 169**
**4.5 L-3,4-dihydroxyphenylalanine (L-DOPA) decarboxylase ..... 172**
**4.5.1 Mechanisms of decarboxylation and oxidative deamination ..... 172**
**4.5.2 Structure of human DOPA decarboxylase ..... 174**

**4.6 References** ..... **177**

**Chapter 5 Streptomyces wadayamensis MppP is a PLP–Dependent L-Arginine Oxidase in the L-Enduracididine Biosynthetic Pathway**

**5.1 Background** ..... **183**

**5.2 Methods** ..... **188**

**5.2.1 Cloning, expression, and purification of *S. wadayamensis* and *Streptomyces globisporus* MppP** ..... **188**

**5.2.2 UV/Vis spectroscopy of SwMppP and its mutants reacting with L-Arginine and dioxygen** ..... **191**

**5.2.3 Characterization of MppP reaction products by NMR** ..... **191**

**5.2.4 Characterization of MppP reaction products by mass spectrometry** ..... **192**

**5.2.5 Ammonium detection by NADH based GDH assay[3]** ..... **193**

**5.2.6 Defining the relationship between $O_2$ usage and $H_2O_2$ formation** ..... **194**

**5.2.7 Reactions with $^{18}O_2$, $H_2{}^{18}O$** ..... **194**

**5.2.8 Crystallization of wild-type and mutant forms of SwMppP, as well as SgMppP** ..... **195**

**5.2.9 Preparation of 2-keto-arginine (3)** ..... **199**

**5.2.10 Steady State Enzyme Kinetics** ..... **199**

**5.2.11 The stoichiometry of L-Arg and $O_2$ in the reaction** ..... **200**

**5.2.12 SwMppP substrate specificity** ..... **200**

**5.2.13 Testing for communication between the two binding sites of $SwMppP_{D188A}$** ..... **202**

5.2.13.1 Isothermal Titration Calorimetry (ITC) ..... 202

5.2.13.2 Determination of binding constants by fluorescence titration ..... 202

**5.2.14 Pre-steady state enzyme kinetics** ..... **203**

**5.3 Results** ..... **205**

**5.3.1 The products of SwMppP with L-Arg and $O_2$** ..... **205**

**5.3.2 Ammonia is also a product of SwMppP with L-Arg and $O_2$** ..... **207**

**5.3.3 SwMppP is an oxidase and not an oxygenase** ..... **208**

**5.3.4 The structures of SwMppP** ..... **211**

**5.3.5 The structure of the SwMppP•L-Arg complex** ..... **217**

**5.3.6 Structures of SwMppP•product complexes** ..... **220**

**5.3.7 Characterization of N-terminus and active site residues** ..... **223**

**5.3.8 Characterization of SwMppP and mutants** ..... **224**

5.3.8.1 Stability of SwMppP and mutants by differential scanning fluorimetry ..... 224

5.3.8.2 Determination of the reaction products of the mutants ..... 224

5.3.8.3 The steady state parameters monitored by $O_2$ consumption ..... 227

**5.3.9 Full oxidation of L-Arg requires two equivalents of $O_2$** ..... **239**

**5.3.10 Substrate specificity** ..... **241**

**5.3.11 The structure of SwMppP with D-Arg** ..... **243**

**5.3.12 Proposed mechanism of SwMppP** ..... **247**

**5.3.13 Presteady state kinetics of SwMppP** ..... **248**

**5.3.14 Preliminary pre-steady state kinetics analysis of $SwMppP_{H29A}$** ..... **254**

**5.3.15 Preliminary pre-steady state kinetics analysis of $SwMppP_{\Delta 1\text{-}22}$** ..... **256**

**5.3.16 Independent binding between two binding sites of SwMppP** ..... **257**

**5.4 Discussion** ..... **260**

**5.5 Reference** ..... **265**

**Appendices** ..... **268**

**Appendix A: Crystallographic data collection and refinement statistics. .....268**
**Appendix B: Crystallographic data collection and refinement statistics. .....270**
**Appendix C: Crystallographic data collection and refinement statistics.....271**
**Appendix D: Proton NMR spectra for the products of SwMppP and its N-terminal mutants with L-Arg.....275**
**Appendix E: Proton NMR spectra for SwMppP active site mutants with L-Arg. .....277**
**Appendix F: Overlay the structure (A) and active site (B) of SwMppP•L-Arg with SwMppP•2.....279**
**Appendix G: Overlay the structure (A) and active site (B) of SwMppP•L-Arg with SwMppP•3.....279**

## LIST OF FIGURES

### Chapter 1


Figure 1-1 Schematic diagram of a typical two-component signal transduction system of the OmpR/PhoB family 2

Figure 1-2 Prototypical histidine kinase with its cognate RR 4

Figure 1-3 Schematic showing of VicK domain organization 6

Figure 1-4 PhoB dimerization mechanism 9

Figure 1-5 Structural comparison of 3 classes of full-length OmpR/PhoB subfamily 11

Figure 1-6 Overlay of the inactive CheY with $BeF_3$ activated CheY dimer 12

Figure 1-7 Conserved residues in phosphorylation-activated response regulators 15

Figure 1-8 The Structures of ChxR REC domain, full length ChxR dimer, and GlnR REC domain 17

Figure 1-9 Sequence Alignment of RitR and PhoB 21

Figure 1-10 The structure of the RitR receiver domain 22

Figure 1-11 The α4 helix of response regulator REC domains appears to be particularly malleable 23

Figure 1-12 Structure of the RitR "active site" 25

Figure 1-13 The structures of PleD monomer and dimer 28

Figure 1-14 The Wsp dimer, REC domain of WspR dimer and tetramer structure 32


### Chapter 2


Figure 2-1 The structure of full-length $RitR_{C128S}$ and a close-up view on the inter-domain interface 58

Figure 2-2 The pKa of conserved C128 in non-Group A/B subset of *Streptococcal* species by DTNB assay 61
Figure 2-3 Different amounts of oxidized RitR dimer in different buffer conditions 63
Figure 2-4 The structure of $RitR_{ox}$ 65
Figure 2-5 Oligomer state of RitR after incubated with different metals 67
Figure 2-6 Non-reducing-PAGE and native SDS-PAGE results of RitR treated with different metals 68
Figure 2-7 Cα trace of full-length $RitR_{C128S}$ structure with the sites chosen for mutagenesis marked as colored spheres 71
Figure 2-8 Oligomer states of wild-type RitR, K10D, N53D and N53A and the putative active site of RitR 73
Figure 2-9 Comparison of gate regions of two ALR REC domains, RitR and ChxR, and the canonical REC domains of PhoB and PhoP 75
Figure 2-10 Results of SEC experiments on the Y100A and D81A variants 76
Figure 2-11 Oligomer states of RitR mutants (F96G, Y102A, R113A, C128A and Y163F with or without DTT treatment 77
Figure 2-12 The effects of gate residues on RitR dimerization 80
Figure 2-13 SEC retention times of wild-type RitR, $RitR_{ox}$, and $RitR_{L86A/V93A}$ 82
Figure 2-14 Size exclusion chromatography results for RitR and $RitR_{L86A/V93A}$ with and without the BS3-1 dsDNA oligonucleotide 84
Figure 2-15 $T_m$ value change of RitR, RitRox, and $RitR_{L86A/V93A}$ after incubated with BS3-3 dsDNA 86
Figure 2-16 Gate residue variants bind to the dsDNA BS3-1 87

Figure 2-17 Complex peak area comparison of 216 μM $RitR_{L86A/V93A}$ with 100 μM of BS3-1, BS3-2, BS3-3, BS3-4 and BS3-5 89

Figure 2-18 Gel filtration results of different ratios of $RitR_{L86A/V93A}$ : BS3-3 and $RitR_{L86A/V93A}$ : BS3-6 91

Figure 2-19 Ribbon representation of the RDLV structures 94

Figure 2-20 Comparison of the active site and switch residues in the wild-type RitR REC domain and the RDLV variant 96

Figure 2-21 Ribbon representations of the RD2LV REC domain structure and the RD2LV asymmetric unit 97

Figure 2-22 Sequence alignment of RitR homologs with other DNA binding proteins in the OmpR family 99

Figure 2-23 Size exclusion chromatography results of the $RitR_{GADDY}$ mutant with or without $H_2O_2$ or DTT treatments 100

Figure 2-24 The LVC triple mutant still binds to the BS3-3 target dsDNA 102

Figure 2-25 Size exclusion chromatography results of $RitR_{C128D}$ and overlay of $RitR_{C128D}$ and $RitR_{C128S}$ structures 103

Figure 2-26 Proposed thiol group oxidation and reduction metabolism of RitR 106

Figure 2-27 The proposed RitR activation mechanism 109

**Chapter 3**

Figure 3-1 Sequence alignment of Q15Z91 with the RitR REC domain 123

Figure 3-2 The structure of Q15Z91 dimer with c-di-GMP and citrate bound 126

Figure 3-3 ALR domains of the Q15Z91 dimer and the overlay of the Q15Z91 and

RitR ALR domains 128

Figure 3-4 Two molecules of c-di-GMP dimerize through stacking of their bases and bind to the inhibitory sites on chain A and chain B 130

Figure 3-5 Citrate binds in slightly different orientations in the active sites of chain A and chain B 131

Figure 3-6 The structure of Q15Z91 with c-di-GMP and GTP bound 133

Figure 3-7 The affects of $H_2O_2$ or DTT treatment on the oligomeric states of Q15Z91 and $Q15Z91_{free}$ 136

Figure 3-8 SEC-MALS results for $Q15Z91_{free}$ 137

Figure 3-9 The oligomeric states of $Q15Z91_{I99A}$, c-di-GMP free $Q15Z91_{I99A}$, $Q15Z91_{G102A}$, c-di-GMP free $Q15Z91_{G102A}$, $Q15Z91_{C142S}$, and $Q15Z91_{R212N/D215A}$ with or without $H_2O_2$ or DTT treatment 139

Figure 3-10 Biofilm formation after IPTG induction in Origami2 cells with Q15Z91 related plasmids 141

Figure 3-11 Time courses for the reaction of Q15Z91 and $Q15Z91_{free}$ with 0.2 mM GTP in the absence or presence of $H_2O_2$ or DTT 143

**Chapter 4**

Figure 4-1 The numbers of new antibiotic compounds approved have been declining steadily since 1980 148

Figure 4-2 Comparison of the mannopeptimycin biosynthetic cluster with that of enduracidin (partial) and the corresponding sequence similarity of L-End biosynthetic genes 155

Figure 4-3 Ribbon diagrams of representative structures of the seven Fold Types of PLP-dependent enzymes 164

Figure 4-4 The reaction catalyzed by aspartate aminotransferase and the structure and active site of aspartate aminotransferase 166

Figure 4-5 Dual substrate recognition in lysine ε-aminotransferase from *Mycobacterium tuberculosis* 171

**Chapter 5**

Figure 5-1 Absorbance spectra recorded on a Hewlett- Packard 8453 diode array spectrophotometer for the reaction of 30 μM SwMppP with 2 mM L-Arg and ambient (~250 μM) $O_2$ 185

Figure 5-2 Proton NMR results of L-Arg and the reaction of 10 μM SwMppP with 2.0 mM L-Arg, both in 20 mM sodium phosphate pH 8.4 buffer 186

Figure 5-3 Compounds encountered in our studies of SwMppP 187

Figure 5-4 $^{13}C$-NMR spectrum of the reaction of 10 μM SwMppP with 2.0 mM L-Arg in 20 mM sodium phosphate pH 8.4 buffer 206

Figure 5-5 The ammonium formation in the reaction of SwMppP with L-Arg is proportional to the L-Arg concentration according to the GDH assay 208

Figure 5-6 $O_2$ regeneration after adding catalase into equilibrated SwMppP with varied [L-Arg] solutions 209

Figure 5-7 Mass spectrometric analysis of SwMppP with L-Arg in the presence of $^{18}O_2$ or $H_2{}^{18}O$ 210

Figure 5-8 The structure comparison between SwMppP and *E. coli* AATase 213

Figure 5-9 The active site of SwMppP 216

Figure 5-10 The structure and active site comparison between SwMppP and SwMppP•L-Arg 218

Figure 5-11 The external aldimine structure in active site of SwMppP•L-Arg 219

Figure 5-12 The active site of SwMppP•4HKA 221

Figure 5-13 The active site of SwMppP•2KA 222

Figure 5-14 Different residues in the active site of SwMppP•L-Arg 223

Figure 5-15 The active site of E15A•L-Arg 227

Figure 5-16 The spectrum of SwMppP and its N terminus mutants with L-Arg 230

Figure 5-17 The spectrum of H29A with L-Arg and overlay the active site of SwMppP and H29A 232

Figure 5-18 Overlaying the active site of H29A and H29A•L-Arg, H29A•L-Arg and SwMppP•L-Arg 234

Figure 5-19 The spectrum of F115Y with L-Arg and overlay the active site of SwMppP and F115Y 235

Figure 5-20 The spectrum of F191Y with L-Arg 237

Figure 5-21 The spectrum of D218S with L-Arg 238

Figure 5-22 The spectrum of SwMppP with L-arginine, L-ornithine, L-citrulline, L-canavanine, methyl-L-arginine and D-arginine 242

Figure 5-23 The active site of SwMppP•D-Arg 244

Figure 5-24 The D-Arg dissociation constant determination 245

Figure 5-25 Dissociation constant determination of D-Arg into SwMppP by fluorescence determination excited at 415 nm 246

Figure 5-26 Global fitting of pre-steady state kinetics data in KinTek Explorer 250

Figure 5-27 The model used for global fitting by simulation in KinTek Explorer 252

Figure 5-28 Accumulation of the fully oxidized 4-hydroxy-2-ketoarginine and the uncoupled 2-ketoarginine based on the global fitting by simulation 254

Figure 5-29 Comparison of fluorescence ($\lambda_{ex}$=415 nm) and absorbance (510 nm) of wild-type SwMppP and the H29A mutant reacting with L-Arg 255

Figure 5-30 Fluorescence excited at 415 nm of $SwMppP_{\Delta 1\text{-}22}$ with L-Arg substrate under anaerobic condition 256

Figure 5-31 Fluorescence change of $SwMppP_{D188A}$ with different concetrations of L-Arg and the fitting data at 480 nm 259

## LIST OF TABLES

### Chapter 2


Table 2-1 Primers used for mutagenesis 46

Table 2-2 Sequences of the BS3 variants used in RitR binding assays 53

Table 2-3 Compounds from the Solubility & Stability Screen (Hampton Research) giving the highest $T_m$ values in the DSF assay 56

Table 2-4 Buffers from the Slice pH Screen (Hampton Research) giving the highest $T_m$ values in the Thermofluor assay 56

Table 2-5 Summary of the rationale of each mutation 71

Table 2-6 Buffers from the Solubility & Stability Screen (Hampton Research) giving the highest $T_m$ values in the Thermofluor assay 82

Table 2-7 Buffers from the lice pH Screen (Hampton Research) giving the highest $T_m$ values in the Thermofluor assay 83


### Chapter 3


Table 3-1 Primers used for mutagenesis 117

Table 3-2 Buffers from the Solubility & Stability Screen giving the highest $T_m$ values in the DSF assay 124

Table 3-3 Buffers from the Slice pH Screen giving the highest Tm values in the DSF assay 125

Table 3-4 Characteristics of wild-type and mutant forms of Q15Z91 135

**Chapter 5**


Table 5-1 Primers used for mutagenesis 189

Table 5-2 $T_m$ values of SwMppP and mutants 224

Table 5-3 The products of SwMppP and its mutants with L-Arg and $O_2$ 225

Table 5-4 Steady state parameters monitored by $O_2$ consumption 228

Table 5-5 The ratio of [$O_2$ consumption]/[L-Arg added] of SwMppP and its mutants reactions 240

## LIST OF SCHEMES

### Chapter 1

Scheme 1-1 Metabolism of cyclic-di-GMP 27

Scheme 1-2 Schematic representation of the diguanylate cyclase reaction where two GTP molecules are condensed to form c-di-GMP 30

### Chapter 2

Scheme 2-1 The mechanism of DTNB assay 47

### Chapter 4

Scheme 4-1 Compounds mentioned in this chapter 4 150

Scheme 4-2 Enduracididine-containing natural products 152

Scheme 4-3 L-capreomycidine biosynthesis mechanism by VioD 157

Scheme 4-4 Some examples of reactions involving PLP 161

Scheme 4-5 Decarboxylation and oxidation deamination by DOPA decarboxylase 173

### Chapter 5

Scheme 5-1 Ammonia assay reaction 193

Scheme 5-2 Proposed mechanism of SwMppP 248

## LIST OF ABBREVIATIONS

| | |
|---|---|
| 2KA | 2-ketoarginine |
| 2KE | 2-ketoenduracididine |
| 4HKA | 4-hydroxy-ketoarginine |
| AATase | aspartate aminotransferase |
| ALR | aspartate-less receiver |
| APS | Advanced Photon Source |
| Atase | aminotransferase |
| c-di-GMP | bis-(3'-5')-cyclic dimeric guanosine monophosphate |
| CA | catalytic ATP/$Mg^{2+}$ binding site |
| D-βhEnd | D-β-hydroxyenduracididine |
| DBD | DNA-binding domain |
| DGC | diguanylate cyclase |
| DHp | dimerization interface and the phosphorylatable histidine residue |
| DSF | Differential scanning fluorimetry |
| DTNB | 5,5'-dithiobis-(2-nitrobenzoic acid) |
| DTT | dithiothreitol |
| EcAAT | *E. coli* aspartate aminotransferase |
| EMSA | electrophoretic mobility shift assay |
| ESI-MS | mass spectrometry with electrospray ionization |
| FDASIA | Food and Drug Administration Safety and Innovation Act |
| GAIN | Generating Antibiotic Incentives Now |
| GDH | L-glutamate dehydrogenase |

| | |
|---|---|
| GTP | guanosine triphosphate |
| HAMP | histidine kinase, adenylyl cyclases, methyl-accepting chemotaxis proteins, and phosphatase |
| HK | histidine kinase |
| HPt | histidine-containing phosphoryl transmitter domain |
| HTH | helix-turn-helix |
| IPTG | isopropyl β-D-1-thiogalactopyranoside |
| ITC | Isothermol titration Calorimetry |
| L-Cap | L-capreomycidine |
| L-DOPA | L-3,4-dihydroxyphenylalanine |
| L-End | L-enduracididine |
| L-βhEnd | L-β-hydroxyenduracididine |
| LAAO | L-amino acid oxidase |
| LCMS | Liquid Chromatograph Mass Spectrometer |
| LS-CAT | Life Science Collaborative Access Team |
| MCPs | methyl-accepting chemotaxis proteins |
| MESG | 2-amino-6-mercapto-7-methylpurine ribonucleoside |
| MRSA | methicillin-resistant *Staphylococcus aureus* |
| NADH | nicotinamide adenine dinucleotide |
| NMR | nuclear magnetic resonance |
| NSDS | native SDS-PAGE |
| OCST | one-component signal transduction |
| PAS | Per, ARNT and SIM |

| | |
|---|---|
| PEG | polyethylene glycol |
| pGpG | 5’-phosphoguanosylyl-(3’-5’)-guanosine |
| PLP | pyridoxal-5’-phosphate |
| PMP | pyridoxamine phosphate |
| PNP | purine nucleoside phosphorylase |
| Q1 | Quinonoid I |
| Q2 | Quinonoid II |
| RD2LV | RitR(L86A/V93A) REC domain, residues 1-132 |
| RDLV | RitR(L86A/V93A) REC domain, residues 1-124 |
| REC domain | receiver domain |
| RitR | repressor of iron transport regulator |
| rmsd | root-mean-square deviation |
| RP-HPLC | reverse phase high performance liquid chromatography |
| RR | response regulator |
| SAD | single-wavelength anomalous diffraction |
| SAXS | small-angle X-ray scattering |
| SDS-PAGE | sodium dodecyl sulfate–polyacrylamide gel electrophoresis |
| SEC | size exclusion chromatography |
| SEC-MALS | size exclusion chromatography with multi-angle light scattering |
| SSM | secondary structure matching |
| TCST | two-component signal transduction |
| TLS | translation-libration-screw |
| TNB- | 2-nitro-5-thiobenzoate |

| | |
|---|---|
| VRE | vancomycin-resistant enterococci |

**ACKNOWLEDGMENTS**

First and foremost, I would like to express my sincere gratitude to my advisor, Professor Nicholas R. Silvaggi, for giving me the opportunity to work on such interesting and exciting projects. He guided me through my PhD as a constructive, highly supportive mentor. I greatly appreciate his patient mentoring, excellent advice and professional training on crystallography. And also thank him for giving me chances to attend crystallography workshops and teaching me scientific writing skills. All of these would lead me become a real scientist. He always remains inspiring, active, and humorous, which makes our lab in a pleasant and relaxed environment. It is my great pleasure to be a member of the Silvaggi Lab.

I am very grateful to my committee, Professor Alexander A. Arnold, Professor Sonia Bardy, Professor David N. Frick, Professor Graham R. Moran and Professor Xiaohua Peng for their encouragement and insightful comments for my research and dissertation. I want to sincerely thank Professor Alexander A. Arnold for his kind collaboration and professional suggestions on my projects. Sincerely thank Professor David N. Frick for his support and suggestions on the DNA foot printing and ITC experiments. Sincerely thank Professor Xiaohua Peng for her support on the oligonucleotide synthesis. I also want to especially thank Professor Graham R. Moran for his great help on my SwMppP project, including the instruments training for enzyme kinetics, data analyzing, and answering my questions.

I also want to especially thank Dr. Kenneth Johnson for all suggestions on the global fitting of presteady state data. I want to thank Professor Andrew Ulijasz and Professor Alan

Schwabacher, our great collaborators, for sharing knowledge and experience to solve problems on my projects.

I want to greatly thank Spencer Anderson, Keith Brister, Joseph Brunzelle, Elena Kondrashkina, David Smith, and Zdzislaw Wawrzak from Life Sciences Collaborative Access Team, Advanced Photon Source in Argonne National Laboratory for their help in data collection and processing. Additionally, I am also grateful for the people who taught me new techniques: Dr. Frank Holger Foersterling (NMR), Revathi Kodali and Zhiqiang Wang (MS), Amber Bakkum and Dr. Blake Hill at the Medical college of Wisconsin (SEC-MALS).

I would like to thank all previous and current members of the Silvaggi Lab including Dr. Zahra Mashhadi, Dr. Lisa S. Mydy, Joshua Weiner, Alexander Gardner, Nemanja Vuksanovic and Lamia T. Badhon for their kind assistance and support in my study. I also would like to express my gratitude to the faculty members and staff of the Department of Chemistry and Biochemistry at University Wisconsin-Milwaukee.

I want to especially thank my husband, Yongtao Zhu, for his love, sharing on all ups and downs, indulgent to my every temper, unconditionally great support and encouragement all the time. I could not have accomplished this without his restless inspiration.

Last but not the least, thank my parents, Naiguo Han and Haimei Chen, for their understanding, support and love, which make it possible for me to reach this destination. I also want to thank my lovely son Leo J. Zhu, who gives me endless energy and happiness. I would also like to thank all my friends in Milwaukee, especially Guanguan Li, for all her help in these years.

# Chapter 1

## Introduction to Bacterial Signal Transduction

All cells sense and respond to environmental stimuli using signal transduction systems. In prokaryotes, these systems typically take the form of either one-component signal transduction (OCST) systems or two-component signal transduction (TCST) systems. OCST systems consist of one protein, which contains both input (sensory) and output (effector) domains, but lacks phosphotransfer domains[15]. The quorum-sensing protein TraR [16] from *Agrobacterium tumefaciens* is a one-component signaling system. When the autoinducer N-(3-oxo-octanoyl)-L-homoserine lactone binds to the N-terminal domain, TraR dimerizes and binds to DNA to activate expression of plasmid conjugal transfer genes [16, 17]. In contrast, the more common TCST systems usually consist of five parts: (1) a sensory protein to detect the stimulus, (2) an autophosphorylated histidine kinase (HK; often part of the sensory protein), (3) a response regulator (RR) that accepts the phosphoryl group from the HK, (4) a target that the response regulator acts on, and (5) a phosphatase to restore the RR to its inactive state. The name "two-component" signal transduction system refers to the histidine kinase/response regulator pair. A typical TCST system is illustrated schematically in Figure 1-1. The sensor domain of the transmembrane histidine kinase protein triggers autophosphorylation of a specific histidine side chain of the HK domain in response to the stimulus, which can be the binding of some ligand [18], changes in pH [19], osmolality [20], temperature [21] and nutrients [22]. The phosphoryl group on the HK is then transferred onto the conserved aspartate residue on the receiver (REC) domain of a cognate response regulator protein. This phosphotransfer reaction is catalyzed by the

response regulator itself and requires $Mg^{2+}$.

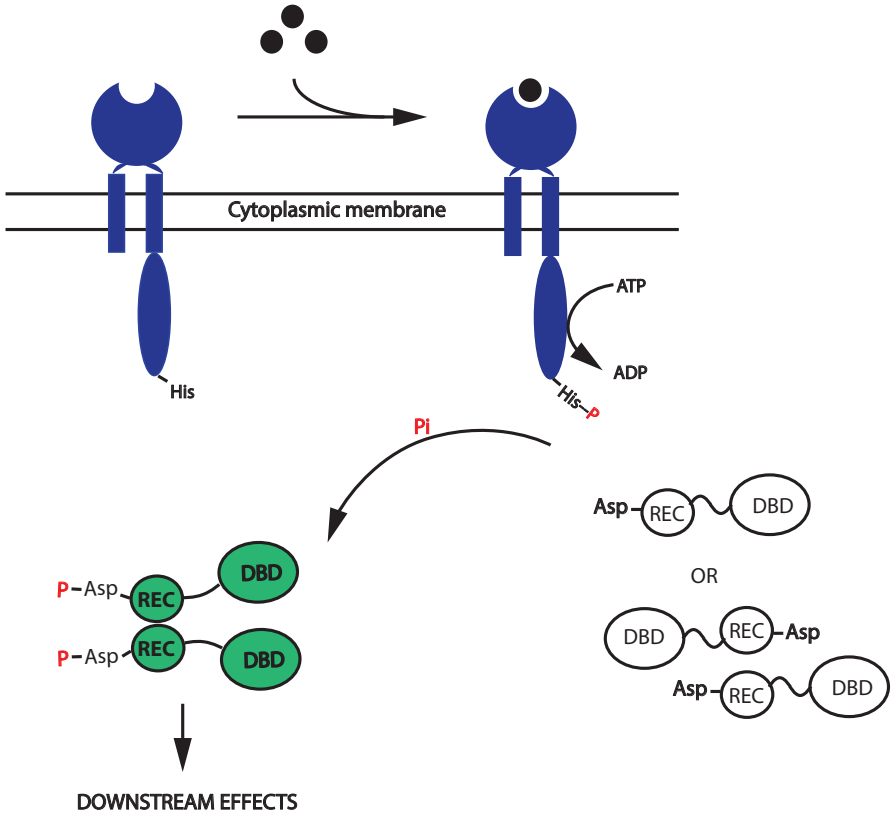


**Figure 1-1:** Schematic diagram of a typical two-component signal transduction system of the OmpR/PhoB family[5]. The stimulus (black solid circle) is represented as a small molecule that is recognized by the sensor-kinase (blue); ligand binding triggers autophosphorylation of the histidine kinase domain. The inactive response regulator (white) encounters the phosphorylation HK and transfers the phosphate group to an aspartate residue in the receiver domain (REC) of the response regulator. Inactive (unphosphorylated) response regulator proteins can exist as monomeric or inactive dimeric conformations. Phosphorylation of the REC domain causes conformational changes that result in formation of the active dimer conformation of the RR (green). The response regulator in this example has a DNA-binding domain (DBD) as the output domain, and activation would result in either up- or down-regulation of transcription from a specific gene locus.

Signal transduction systems in prokaryotes were recently found to be more complicated than originally thought due to the discovery of auxiliary factors [23] and diverse phosphotransmission pathways, such as the ArcB-ArcA anoxic redox control system in *E. coli* [24], the CheA-CheY/CheB chemotaxis system in *E. coli* [25], the KinA/KinB-Spo0F-Spo0B-Spo0A sporulation control system in *Bacillus subtilis* [7], and Ser/Thr and Tyr phosphorylation systems mediated by bacterial eukaryotic-like serine/threonine and tyrosine kinases and the cognate PP2C phosphatases[26-28].

### 1.1 Histindine Kinase

According to the domain compositions, HKs can be generally divided into two types: orthodox kinases and hybrid kinases. Orthodox histidine kinases typically contain a transmembrane domain, a four-helix coiled coil HAMP (histidine kinase, adenylyl cyclases, methyl-accepting chemotaxis proteins, and phosphatase) domain, a PAS (Per, ARNT and SIM) [29] domain, and a C-terminal transmitter domain. The transmitter domain contains the dimerization interface and the phosphorylatable histidine residue (DHp), and a catalytic ATP/$Mg^{2+}$ binding site (CA). EnvZ is an orthodox HK from *E. coli* that located in the inner membrane and contains two transmembran regions and a large cytoplasmic domain. It senses environmental osmolarity changes [1] and then phosphorylates the cognate RR protein OmpR, which ultimately regulates the expression of the outer membrane porins OmpF and OmpC [30] (Figure 1-2A). At high osmolality, OmpF is repressed and OmpC is the major outmembrane porin. It was also found that higher osmolality induces intra-helical H bonds, which enhances the H243 autophosphrylation and phosphoryl transfer to OmpR[31].

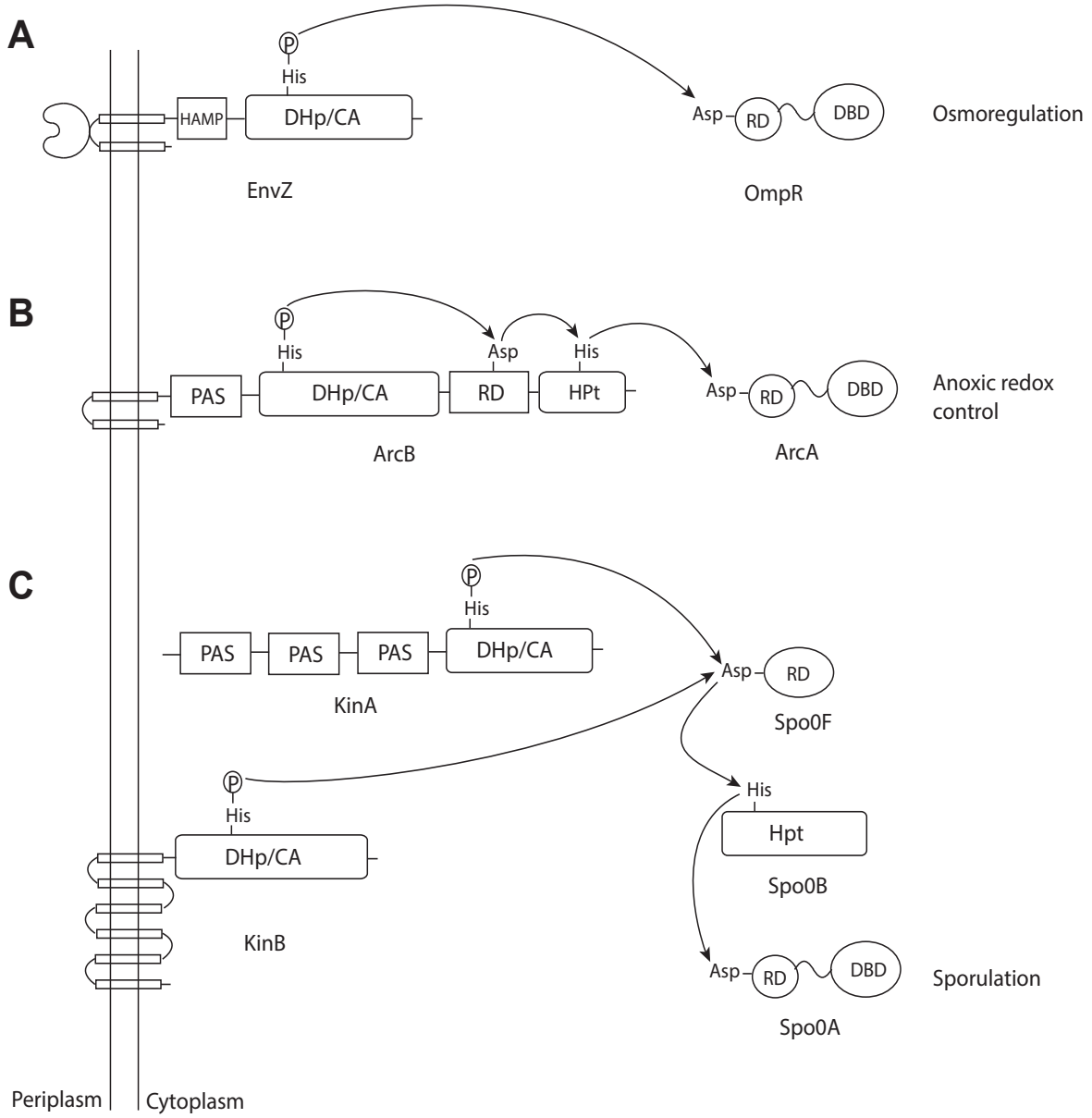


**Figure 1-2:** Prototypical histidine kinase with its cognate RR: Osmosis control (EnvZ [1]-OmpR) (A), a typical hybrid histidine kinase system, ArcB-ArcA [2] (B) and the KinA/KinB-Spo0F-Spo0B-Spo0A system [7] (C), which is involved in phosphor-relay control. HPt: Histidine-containing phosphoryl transmitter domain.

HKs usually have two or more transmembrane regions that separate the periplasmic sensor region from the cytoplasmic transmitter domain. Some orthodox HKs do not have a transmembrane region, like the chemotaxis kinase CheA[32] and the nitrogen regulatory kinase NtrB[33]. PAS domains are common in sensor proteins and can sense diverse environmental or internal signals, including ligands, light, oxygen level and redox change[34]. The architecture of proteins containing PAS domains is diverse, but the overall structures of PAS domains are conserved[35]. Most PAS domains contain a central antiparallel β sheet with several α helices packed against one face[35], as exemplified by VicK[36] from *Streptococcus mutans* (Figure 1-3). The PAS domain contains a five-stranded central β sheet surrounded by five α helices. The uppermost HAMP domain consists four parallel α helices from two chains. Deletion of HAMP and PAS domains impaired the phosphatase activity of VicK[37]. The dimerization domain is usually composed of two long α helices. The phosphoryl receptor histidine locates in the helix (H217 in VicK). The loop connecting the two α helices determines the specificity of the receptor for one or more specific RR proteins[38]. The main body of kinases CA domains is conserved, consisting of an α/β-sandwich fold with a five-stranded mixed β sheet and three α helices, as observed in DesK[39] and PhoQ[40]. This domain is structurally homologous to the ATPase domains of DNA gyrase B[41], MutL[42], and Hsp90[43].

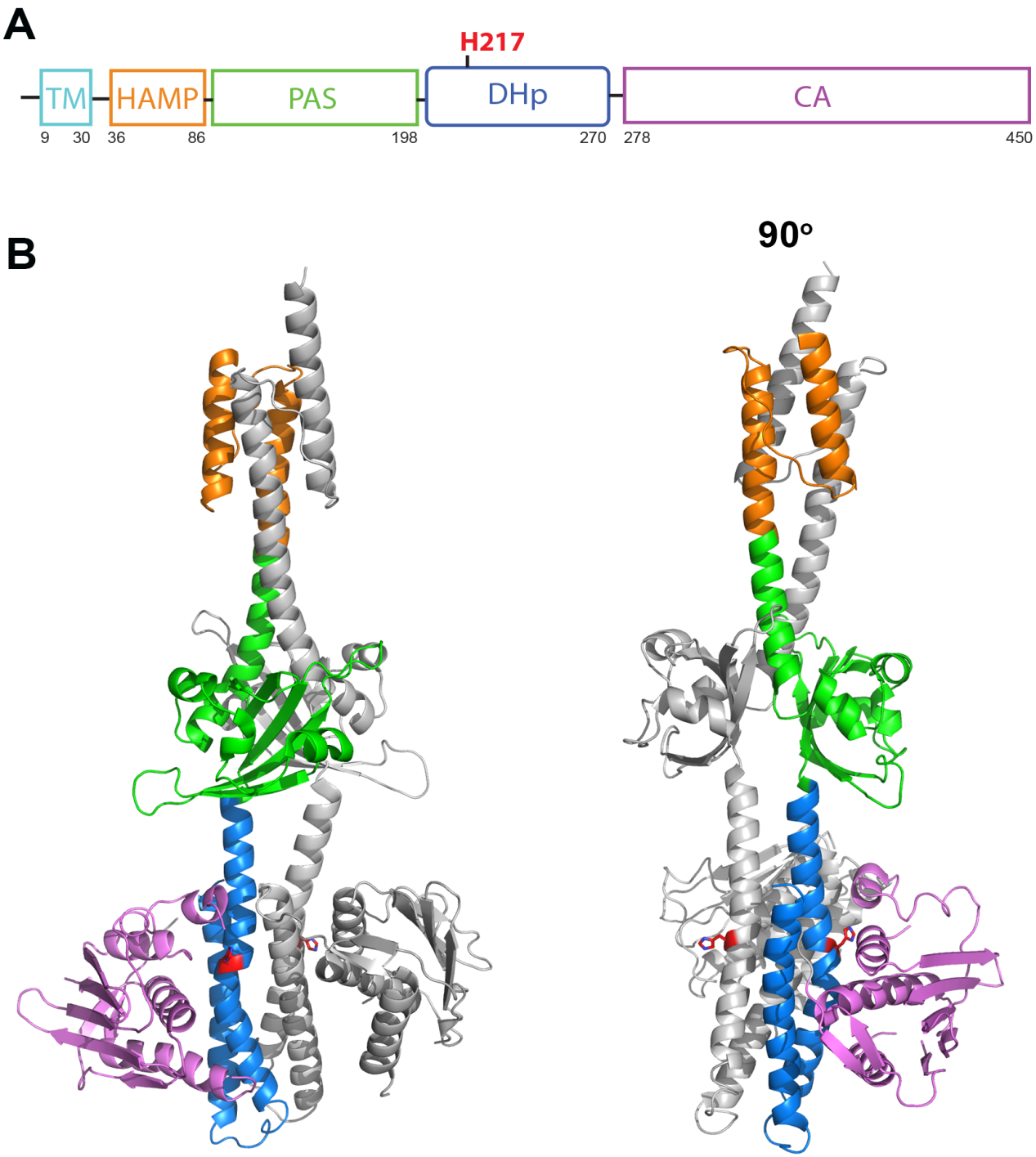


**Figure 1-3:** Schematic showing of VicK domain organization (A) and ribbon representation of VicK structure (PDB ID: 4I5S [36]) (the transmembrane domain is not included in the structure) (B). The colors of different domains in chain A are matching the schematic from A. Chain B is colored in grey. The conserved H217 residues in the DHp domain are shown in stick with red carbon atoms.

Hybrid kinases are found in some prokaryotes and almost all eukaryotes [44]. Hybrid kinases contain multiple phosphodonor and phosphoacceptor sites and undergo multi-step phospho transfer, such as ArcB [2, 24] (Figure 1-2B). ArcB from *E. coli* that is involved in anoxic redox control (Arc), is a typical HK of the hybrid kinase family. ArcB contains two N-terminal transmembrane regions, a kinase core, and a second His-containing phosphotransfer domain. Once the N-terminal transmembrane domain senses the stimulus, the signal is propagated into the transmitter domain by the HAMP domain, which triggers dimerization via the dimerization domain. The resulting four-helix bundle of the dimer is cross-phosphorylated on a conserved histidine residue of the dimerization domain using ATP and $Mg^{2+}$. The complexity of hybrid kinase structures allows different regulatory pathways.

## 1.2 Response regulators (RRs)

### 1.2.1 Activation mechanism of phosphorylation dependent RRs

In prokaryotic TCST systems, the most common and well-studied RRs are transcriptional regulators [15]. They have DNA-binding domains that bind specific DNA sequences, and usually function as homodimers. The largest subgroup of DNA binding RRs is OmpR/PhoB family. The RRs in OmpR/PhoB family are characterized with a REC domain and a winged helix-turn-helix domain connected by a linker [45].

X-ray crystal structures have been determined for a number of full-length RR proteins from the OmpR/PhoB family[10, 46-48]. In addition, the structures of some members of both

families have been determined in both the inactive, unphosphorylated and active, phosphorylated states. The latter is commonly approximated by $BeF_3$ adducts that mimic the actual phosphorylated protein, owing to the difficulty of producing fully phosphorylated (i.e. homogenous) protein for crystallization studies. The ability to compare the structures of unphosphorylated and "phosphorylated" RRs has allowed some insight into the phosphorylation-induced activation mechanisms in these proteins[14, 48].

The REC domains of OmpR/PhoB subfamily adopt a sandwich $(\beta/\alpha)_5$ topology with a central five-stranded parallel β sheet surrounded by 3 and 2 α helices on both sides (e.g. PhoB in Figure 1-4). The phosphorylatable aspartate usually located in the loop between β3 and α3, and the other two acidic residues usually located in the loop between β1 and α1. These three acidic triad residues are involved in the $Mg^{2+}$ coordination and phosphoryl transfer from cognate HK. They dimerize through α4-β5-α5 interface upon phosphorylation.

One well studied RR of OmpR/PhoB family is PhoB[5], which controls the cellular response to the phosphate-limitation in PhoR-PhoB[5] (known as PhoP in some organisms) TCST system in *E. coli* and *Bacillus subtilis*. PhoR is an autophosphorylated transmembrane histindine kinase. It has a N-terminal transmembrane region and a cytoplasmic domain consisting of PAS domain, DHp domain and CA domain[49]. PhoB (PhoP) is a transcriptional regulator that modulates the expression of *pho* regulon genes by binding to the "*pho* box" sequences of the promoters[50]. Both the inactive monomeric structure[9] and the active dimeric structure[14] of PhoB were determined (Figure 1-4).

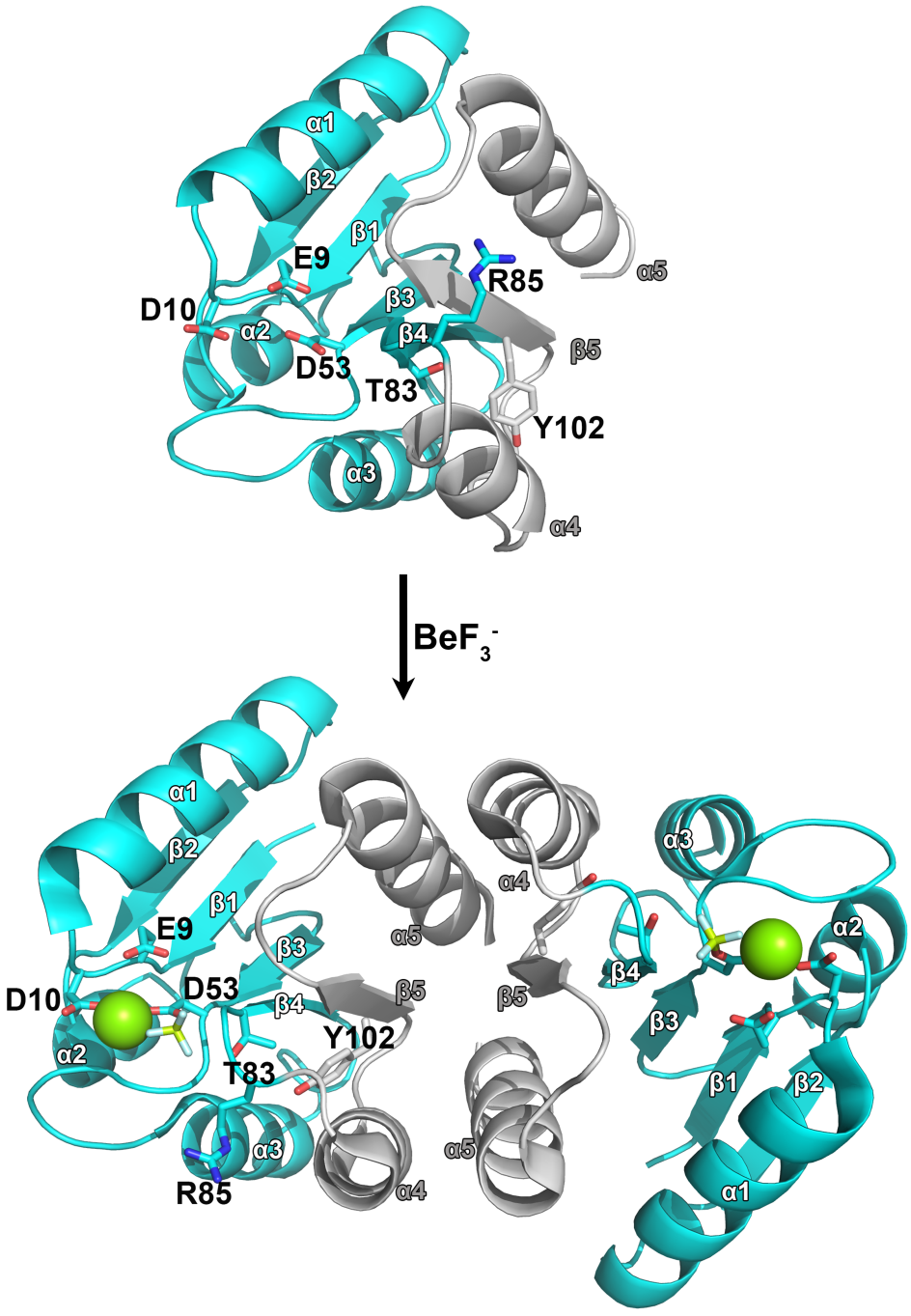


**Figure 1-4:** PhoB dimerization is triggered by beryllium trifluoride, a phosphoryl analog. The left side shows the structure of the inactive PhoB monomer (PDB ID: 1B00[9]), and the right side shows the $BeF_3$-activated dimer (PDB ID: 1ZES[14]). The acidic triad (E9, D10 and D53) and "switch" residues (T83 and Y102) are shown as sticks. The yellow-green sphere represents the magnesium ion required for the phosphotransfer reaction.

Once the aspartate residue accepts the phosphoryl group from histidine kinase, a subtle structural rearrangement brings the α3 helix closer to the active site. The α4 helix and β5 strand undergo a more pronounced conformational change. The side chain of T83 reorients and interacts with the phospho-Asp in the active site. In addition, the side chain of Y100 rotates around to fill the void left by the reorientation of T83. This reorientation of Y100 is thought to be an important factor in the formation of the α4-β5-α5 dimer interface[14]. Thus, T83 and Y100 have come to be thought of as the "switch residues" that are largely responsible for triggering dimerization by modulating the shape of the interacting surface of the REC domain.

Comparisons of some full-length RRs structures in OmpR/PhoB family and the autophosphorylation rate, it was found that the interdomain interactions between REC domain and DBD of the inactive RRs affect the autophosphorylation rate[51]. According to the extent of interdomain interactions, OmpR/PhoB subfamily RRs are indeed divided into three subclasses (Figure 1-5)[12]. As shown in Figure 1-5A, the α4-β5-α5 dimer interface of DrrB[3] REC domain interacts extensively with the DBD, which represents the "closed" subclass. DrrD[10] (Figure 1-5B) has less interdomain interactions and the DNA recognition helices are solvent accessible, which belongs to the "open" subclass. The representative of third subclasses is HP1043[11] (Figure 1-5C), which has little interdomain interactions and readily forms dimer through α4-β5-α5 dimer interface.

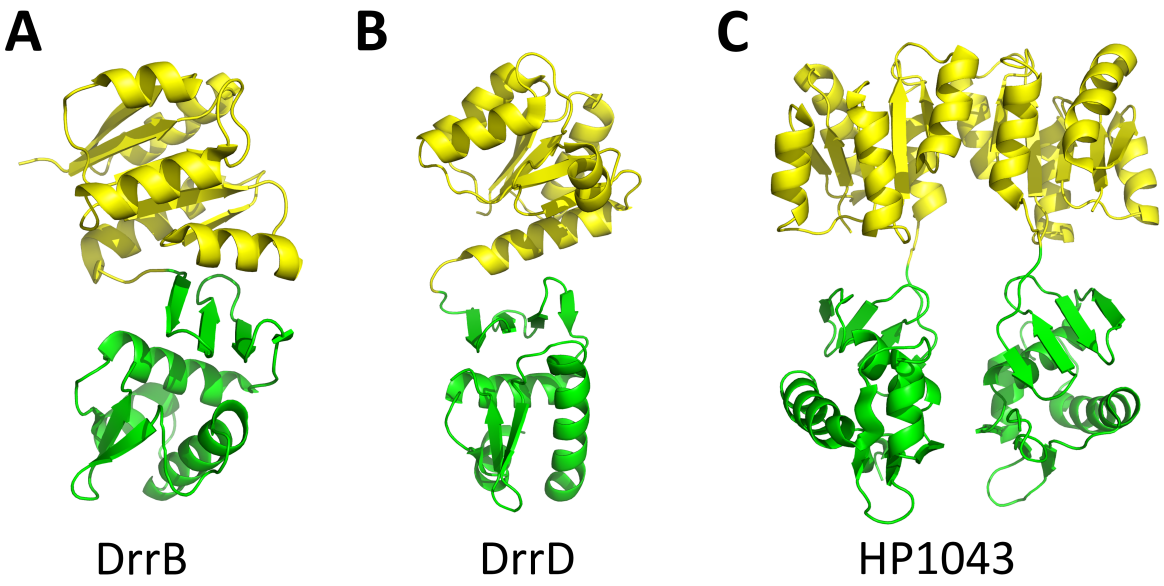


**Figure 1-5:** Structural comparison of various classes of full-length OmpR/PhoB subfamily structures. REC domains are colored in yellow, DBD colored in green. (A) The structure of DrrB (PDB ID: 1P2F [3]), representing the "closed" subclass that has extensively interdomain interactions. (B) The structure of DrrD (PDB ID: 1KGS [10]), representing the "open" subclass that has limited interdomain interactions (C) The structure of HP1043 (PDB ID: 2HQR [11]), representing the "free" subclass that completely lacks the interdomain interactions.

While DNA-binding effector domains are the most common, enzymatic domains (diguanylate cyclase, phosphatase, kinase etc), RNA binding domain and protein binding domain have also been observed in RRs[52]. Some RRs only have a REC domain and the regulatory function resides in the REC domain. For example, CheY is a chemotaxis-related regulator with a REC domain that directly regulates the direction of motor rotation of bacterial flagella after phosphorylation by binding to the rotor protein FliM and FliN[53, 54].

The chemotaxis system in *E. coli* mainly contains a transmembrane methyl-accepting chemotaxis proteins (MCPs), an adaptor CheW and the TCST system CheA-CheY/CheB. MCPs, including Tar, Tsr, Tap, Trg, Aer [55], can bind various chemicals (e.g. sugars, amino acids, $O_2$) and control the autophosphorylation of CheA via the adaptor protein CheW. CheA is a histindine kinase that lacks the periplasmic and transmembrane domains typically found in HKs [56, 57]. CheY, a response regulator with REC domain only and CheB, a glutamate methylesterase, compete for the phosphoryl group on CheA. Once phosphorylated, CheY binds to the switch protein on the flagella motor to change the rotation direction, while CheB controls the adaptation of the MCPs by demethylation. Demethylated MCPs are poor kinase activators[58], which result in less activated CheA and less phosphorylated CheY.

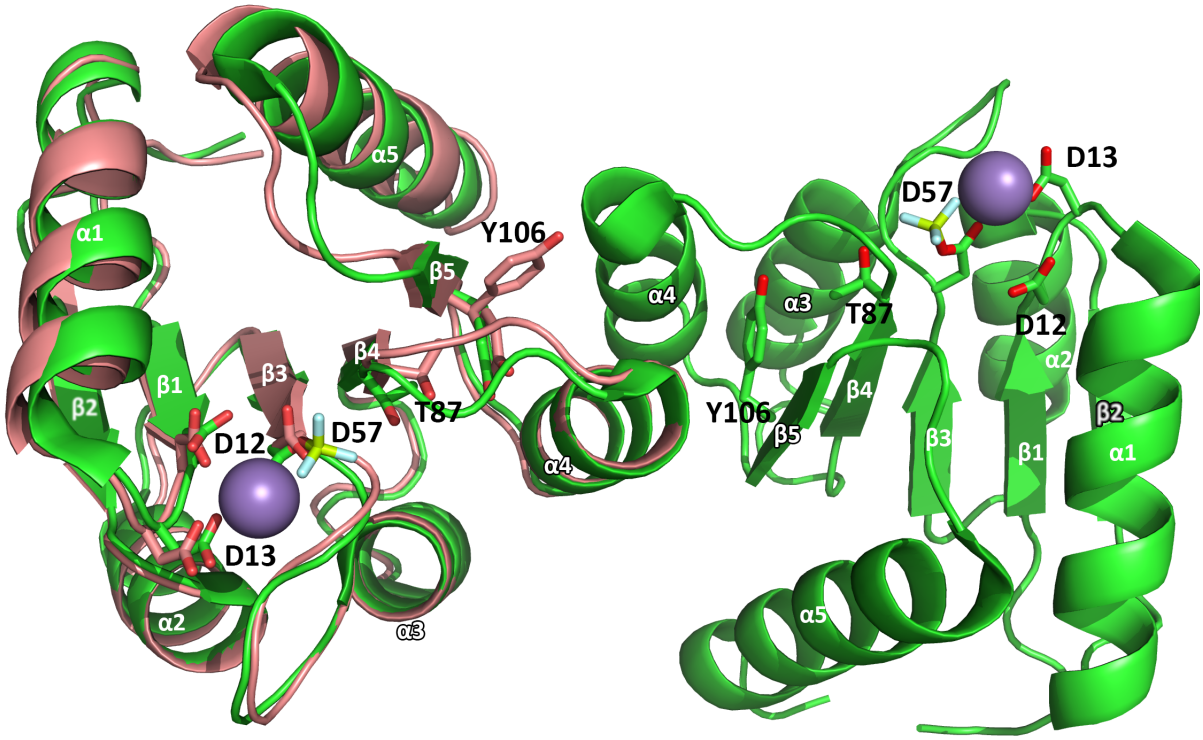


**Figure 1-6:** Overlay of the inactive CheY (light pink) with $BeF_3$ activated CheY dimer (green). Mn ions are represented in purple sphere. Acidic triad residues and switch residues are shown in stick.

Comparison of the inactive and $BeF_3^-$ activated mimic CheY structures[59-61] shows that CheY has a similar activation mechanism to that postulated for PhoB (Figure 1-4, Figure 1-6). Upon phosphorylation, the switch residue T87 of CheY rotates about to make a hydrogen bonding interaction with one of the fluoride atoms in the D57-$BeF_3$ adduct, analogous to one of the phosphate oxygen atoms. The side chain of Y106 also undergoes a conformational change, rotating inward to fill the void left by T87, where its phenolic oxygen makes a hydrogen bonding interaction with the main chain carbonyl O atom of E89 and the ring itself is buried in a hydrophobic pocket formed by residues on β4 and α4.

CheB has an N-terminal regulatory domain and a C-terminal methylesterase domain connected by a short linker. The regulatory domain of CheB is structurally homologous to CheY, but CheB contains a phosphorylation site and also an active site for auto-dephosphorylation on the REC domain[62]. The N-terminal REC domain inhibits the methylesterase activity in the inactive state, but after phosphorylation, the methylesterase activity will be transiently activated[62]. In addition, the inhibited full-length CheB structure is a "closed" conformation, because α4, α5 and β5 in the REC domain interact with the methylesterase domain and block the catalytic site[63]. Phosphorylation of D56 changes the conformations of α4 and α5, which disrupts the interdomain interactions and opens access to the catalytic site.

### 1.2.2 Conserved residues in phosphorylation-dependent RRs

Comparison of response regulator sequences (Figure 1-7) demonstrates that the

residues mentioned above, Ser/Thr and Tyr/Phe switch residues, the acidic triad residues including phosphorylatable aspartic acid are all highly conserved in phosphorylation-activated RRs. The acidic triad residues comprise a motif (Asp-Asp/Glu-Asp) that is essential for binding of the $Mg^{2+}$ (or other divalent metal ions) required for phosphoryl group transfer. The conserved phosphorylatable aspartate residue plays a key role in activation. Substitution of this aspartate residue by glutamate, which has been used as a phospho-Asp mimic to examine activation in CheY [64], RcsB [65] and NtrC [66], resulted in constitutive activation. In contrast, substitution by asparagine or alanine in RcsB[65] and NtrC [66] eliminated activation in these proteins. The switch residues Thr/Ser and Tyr/Phe are essential for forming the active dimer conformation in many RRs. Substitutions of these two switch residues (*e.g.* T87 into isoleucine or Y106 into trptophan) impairs activation in CheY and affects chemotaxis [67]. Likewise, mutation of T87 to isoleucine prevents the side chain of Y106 from adopting the "inward-facing" conformation even when CheY is phosphorylated [67].

In the REC domain of CheB [63], there is another important acidic residue E58. E58 is near the acidic triad and orients toward the metal-binding site. The E58K mutant of CheB exhibited a much slower rate of phosphoryl transfer from phospho-CheA and auto-dephosphorylation of CheB, which suggests that E58 contributes to the phosphoryl group transfer from CheA and autophosphotase activity of CheB. Phosphorylation-activated response regulators often have another conserved basic residue, a lysine, located near the phosphorylation site and interact with phospho-Asp.

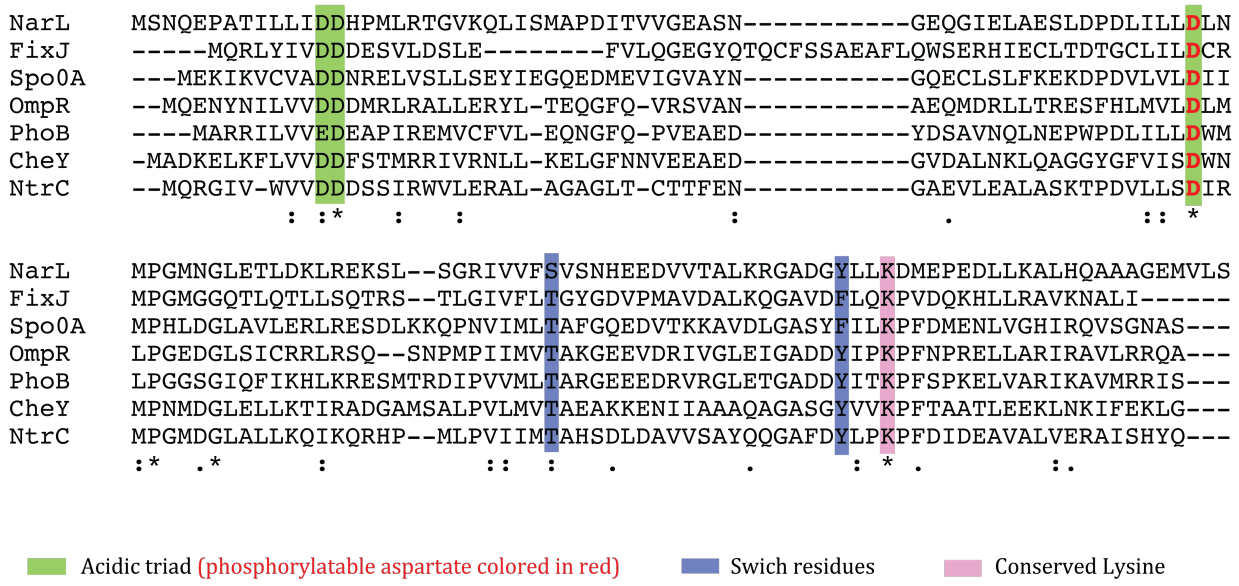


**Figure 1-7:** Conserved residues in phosphorylation-activated response regulators.

However, these highly conserved residues may have different roles in the transition to the activated state. In CheY, D57 is the conserved phosphorylatable residue[68]. *In vivo*, the CheY mutant D57N was phosphorylated at an alternative residue, S56, and still regulated the rotation of flagella[69]. However, a CheY D57E mutant, which in other systems has been thought to mimic phospho-Asp, exhibited no activity in *vivo*, although it was still phosphorylated by CheA. In NtrC (nitrogen regulatory protein C), the variant D54E mimics the phospho-Asp and has an NtrC+ phenotype[70]. *In vitro* phosphorylation studies verify that the NtrC D54E protein can still be phosphorylated even though not stable[71]. Like CheY, NtrC also has a serine residue (S53) adjacent to the conserved phospho-acceptor residue D54. However, the NtrC D54N mutant does not have any active phenotype[70, 71]. The conserved basic residue K109 in CheY interacts with the phospho-Asp and contributes to the phosphorylation by providing a simple electrostatic on-off switch[72-74]. While mutating

the analogous residue, K107 in CheB, to Arg does not affect the phosphorylation of D56, but it does slow down the dephosphorylation step[75]. The analogous residue in NtrC, K103, is also not required for phosphorylation [71].

### 1.2.3 Atypical, phosphorylation-independent RRs containing the conserved Asp residue

We talked about the phosphorylated RRs activation mechanism and the conserved residues above. For the remainder of this discussion, the phosphorylation-dependent response regulators will be referred to as "typical" or "canonical" RRs. Recently, a large group of RRs with atypical REC domains has been identified whose members respond to signals other than phosphorylation. For example, the regulators in MarR family can be activated by binding small molecules or oxidation of specific cysteine residues[76,96-98].

The orphan regulator NblR from *Synechococcus* that lacks the cognate histidine kinase, has the conserved phosphorylatable Asp residue, but it is not required for NblR function[77, 78]. Experiments with yeast and bacterial two-hybrid systems demonstrated that NblR does not interact with NblS (a conserved histidine kinase in Cyanobacteria), but rather with NarB (nitrate reductase).

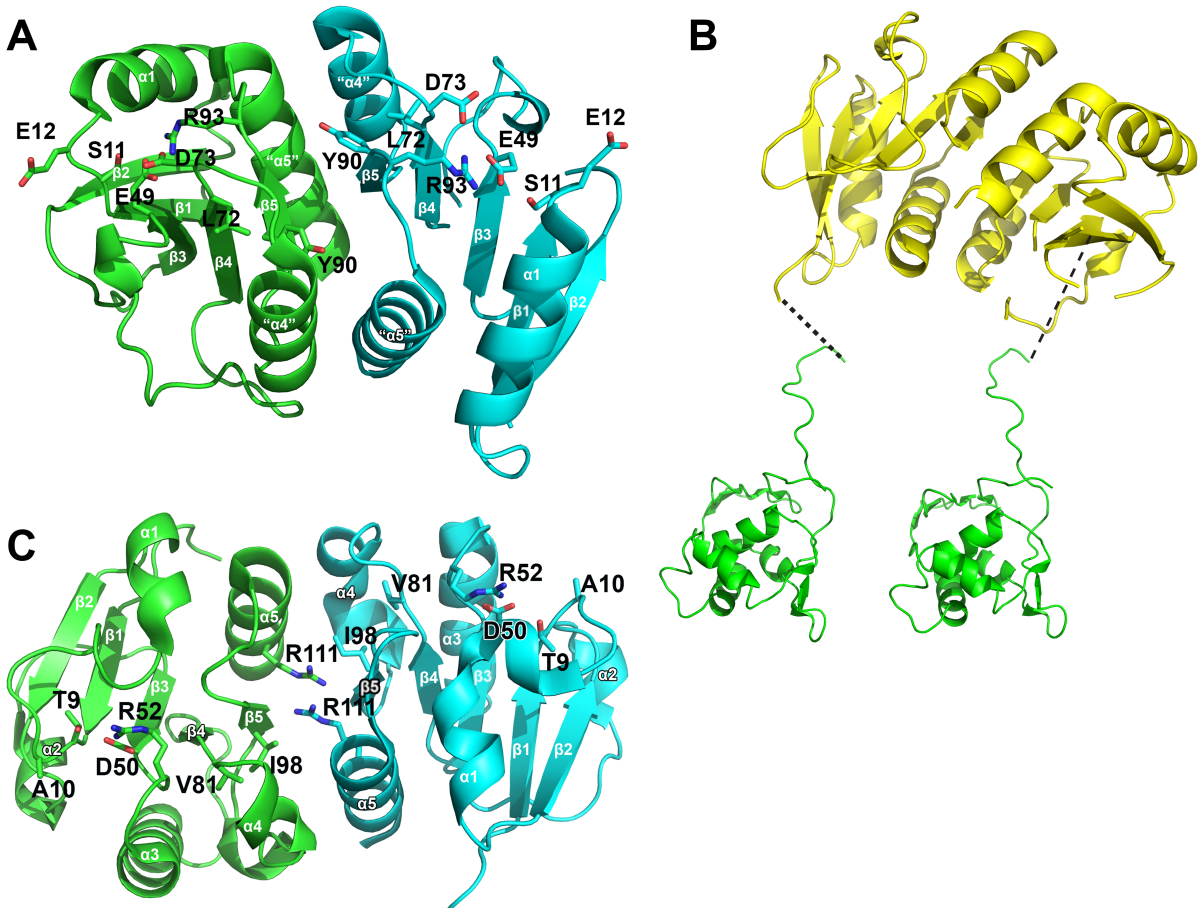


**Figure 1-8:** (A) The structure of ChxR REC domain (PDB ID: 3Q7R [8]). Chain A colored in green, chain B colored in cyan. In comparison with typical OmpR/PhoB RRs, ChxR lacks α2, α3 and the second and third helices are labeled as "α4" and "α5", respectively. (B) The model of full length ChxR dimer according to the best fit SAXS data [12] reflects a "free" conformation due to no interdomain interaction. The REC domains are linked with DBD by dash line. (C) The structure of GlnR REC domain (PDB ID: 4O1H [13]). Chain A colored in green, chain B colored in cyan. The putative acidic triad (except D50) and switch residues are all missing in GlnR.

ChxR from *Chlamydia trachomatis* exists as a constitutively active homodimer without phosphorylation[79]. First, the structure of the ChxR REC differs from those of typical (phosphorylation-dependent) RRs in that ChxR lacks two helices (α2 and α3) found in the

typical OmpR/PhoB-type regulators (Figure 1-8A)[8]. Second, ChxR does not have both of the Thr/Ser and Tyr/Phe switch residues. The tyrosine residue on β5 is present, but the Ser/Thr on β4 is missing. Furthermore, the two residues in ChxR equivalent to the switch residues (L72 and Y90) are oriented similarly to those of inactive OmpR/PhoB family regulators, which indicate ChxR has a different activation/dimerization mechanism. Based on small-angle X-ray scattering (SAXS) analysis of full-length ChxR (Figure 1-8B), ChxR belongs to the "free" subclass that lacks interdomain interaction between the REC domain and DBD [12], indicating that ChxR can bind to DNA in a phosphorylation-independent manner.

Another atypical regulator, GlnR from *Amycolatopsis mediterranei*, represses the expression of the glutamine synthetase gene and is thus involved in regulating nitrogen metabolism. GlnR is an orphan RR, because the cognate HK is not identified [80]. Like ChxR, GlnR also possesses the conserved phosphorylatable aspartate residue (D50), but functions as a homodimer without phosphorylation (Figure 1-8C). Interestingly, the other two acidic triad residues (E, D/E), the conserved Lys residue, and the switch residues (Ser/Thr, Tyr/Phe) are all not conserved in GlnR. In addition, Arg52 located on the loop between β3 and α3 (Lβ3α3) is essential for maintaining dimerization by occupying the "phosphorylation pocket" and interacting with the conserved D50 [13].

### 1.2.4 Aspartate-Less Regulators (ALR)

Among atypical RRs, there are many proteins lacking the phosphorylatable Asp residue,

such as the atypical response regulator HP1043 from *Helicobacter pylori*. HP1043 regulates the transcription of *tlpB* gene that encoding a methyl-accepting chemotaxis protein and is essential for cell growth [81]. In HP1043, a serine residue is substituted for the phosphorylatable Asp residue. The protein binds to DNA in a phosphorylation-independent way [11]. This raises the question of whether the loss of the phosphorylatable Asp residue is a common evolutionary theme in bacterial signal transduction. We recently defined a new subfamily of RR proteins with aspartate-less receiver (ALR) domains [6]. The ALR domains are common, accounting for ~4% of REC domain sequences in the Pfam database, and they are well distributed among bacteria, archaea, and eukaryotes. A large number (~28%) of ALR regulators have DNA-binding output domains. When compared to the entire class of RRs, the ALR domain-containing response regulators are enriched for enzymatic output domains, such as diguanylate cyclase (GGDEF) domains, Ser-Thr kinase, and phosphatase domains. Although these atypical receiver domains have been known to exist for some time, the molecular details of their regulatory mechanisms have remained unclear. In the next two chapters, the structure-function relationships of two ALR proteins will be explored: RitR (Repressor of iron transport regulator, Chapter 2) and Q15Z91 (diguanylate cyclase, Chapter 3).

#### 1.2.4.1 Repressor of iron transport regulator (RitR)

RitR is an orphan two-component signal transduction response regulator in *Streptococcus pneumoniae* R6. Analysis of the *S. pneumoniae* genome indicates that there are 13 pairs of TCST proteins (HK and RR) in this organism and a single orphan regulator,

RitR [82-84]. Searching the genome sequence, there is no kinase gene close to the *ritR* locus. Instead, the adjacent gene *gnd* encodes a 6-phosphogluconate dehydrogenase and is co-transcribed with *ritR*, as evidenced by Northern Blot analysis[85]. RitR represses iron uptake, activates some resistance proteins to oxidative stress, and is required for pathogenicity in a mouse lung model[85].

Analysis of REC domain sequences shows that RitR belongs to the OmpR/PhoB subfamily of RRs, and suggests that RitR likely has a similar tertiary structure to other OmpR/PhoB family members. A representative sequence alignment with the typical response regulator PhoB (Figure 1-9) shows that the conserved, phosphorylatable Asp residue in RitR is replaced by asparagine (N53; highlighted in yellow in Figure 1-9). Furthermore, RitR does not have any other residue near this position that would be capable of accepting a phosphate group, such as Ser56 in CheY. The absence of any obvious candidates for phosphorylation in the sequence suggests that RitR does not have a phosphorylatable site in the "active site". Further underscoring the likely functional differences between RitR and other PhoB-type RRs is the substitution of an aspartate residue in RitR for the Ser/Thr switch residue.

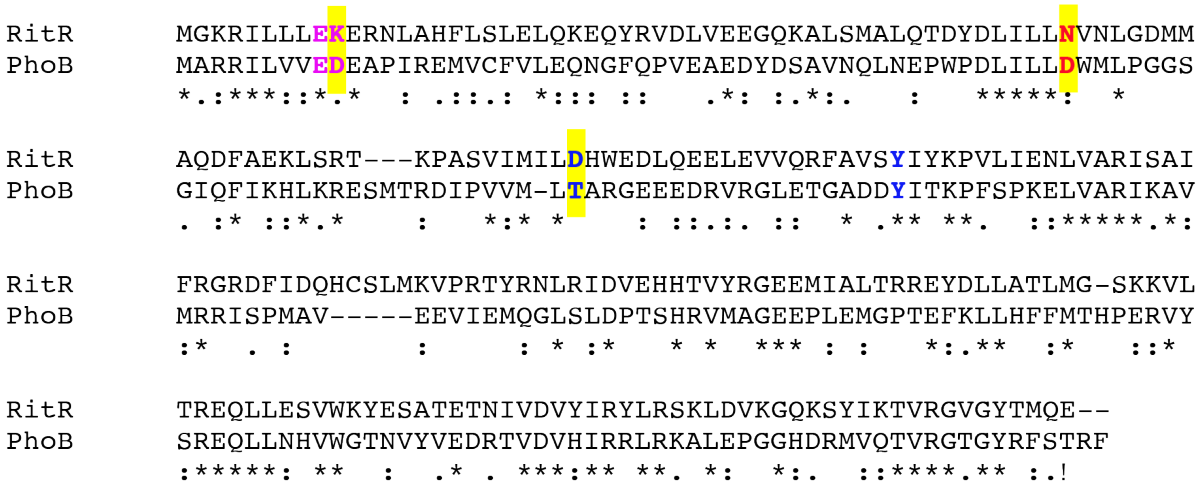


**Figure 1-9:** Sequence Alignment of RitR and PhoB. An "*" (asterisk) indicates positions which have same residue. A ":" (colon) indicates conservation between groups of strongly similar properties. A . (period) indicates conservation between residues of weakly similar properties. The acidic triad residues are colored magenta ($Mg^{2+}$-binding) and red (phosphorylation site). The conserved Asp residue is replaced by Asn in RitR. The two switch residues are colored blue. The yellow boxes mark the differences in conserved residues between RitR and PhoB.

The three-dimensional structure of the RitR receiver domain (PDB ID: 4LZL [6]) was obtained by molecular replacement (Figure 1-10). The RitR REC domain is monomeric, which means that this structure represents an inactive (no DNA binding) conformation. It has the same $(\beta/\alpha)_5$ topology observed in other OmpR/PhoB family members, with only subtle differences (see below).

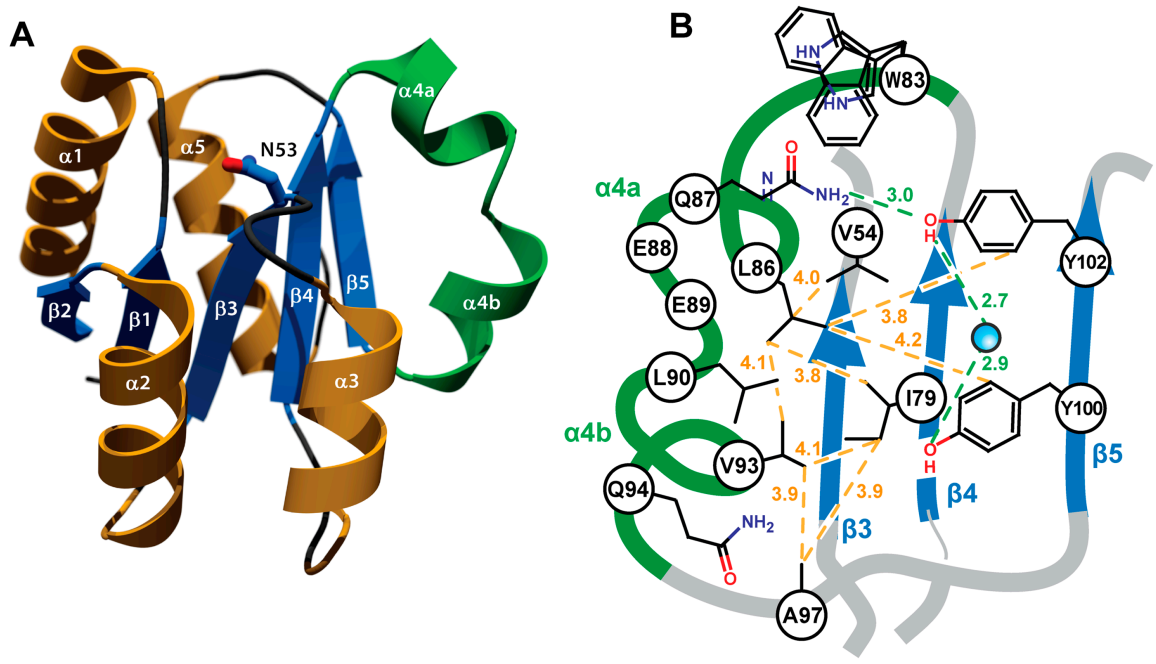


**Figure 1-10:** The structure of the RitR receiver domain (this figure is downloaded from PLOS Pathogens 11(4): e1004795 [6]). (A) Ribbon representation of the RitR REC domain with helices α1- α3 and α5 colored orange, the unusual α4 helix colored green, and the β-strands colored blue. N53 is shown in sticks. (B) Schematic view showing "hydrophobic interactions" (yellow dotted lines) and the hydrogen-bonding network (green dotted lines) in the "hydrophobic gate" region of the structure.

The most obvious difference is the broken α4 helix (colored green in Figure 1-10A), the pieces of which are labeled α4a and α4b, respectively. The hydrophobic residues on the α4 helix interact with residues on β3, β4 and β5, forming a hydrophobic core (as shown in Figure 1-10B). There are other RRs with unusual α4 helices, though none are "broken" like helix α4 of RitR. For example, DosR from *Mycobacterium tuberculosis* adopts an unusual $(\beta/\alpha)_4$ fold, where the canonical α4 helix and β5 strand have been lost [86] (Figure 1-11). Helix α4 in DosR is positioned where the canonical helix α5 is located in other NarL subfamily RR proteins. The conserved Y101 and K104 residues that are normally located

on strand β5 and the loop Lβ5α5, are instead located in linker helix α5 and far away from the phosphorylation site. In DrrD from *Thermotoga maritima*, helix α4 is roughly perpendicular rather than parallel to the other helices [3], as shown in Figure 1-11.

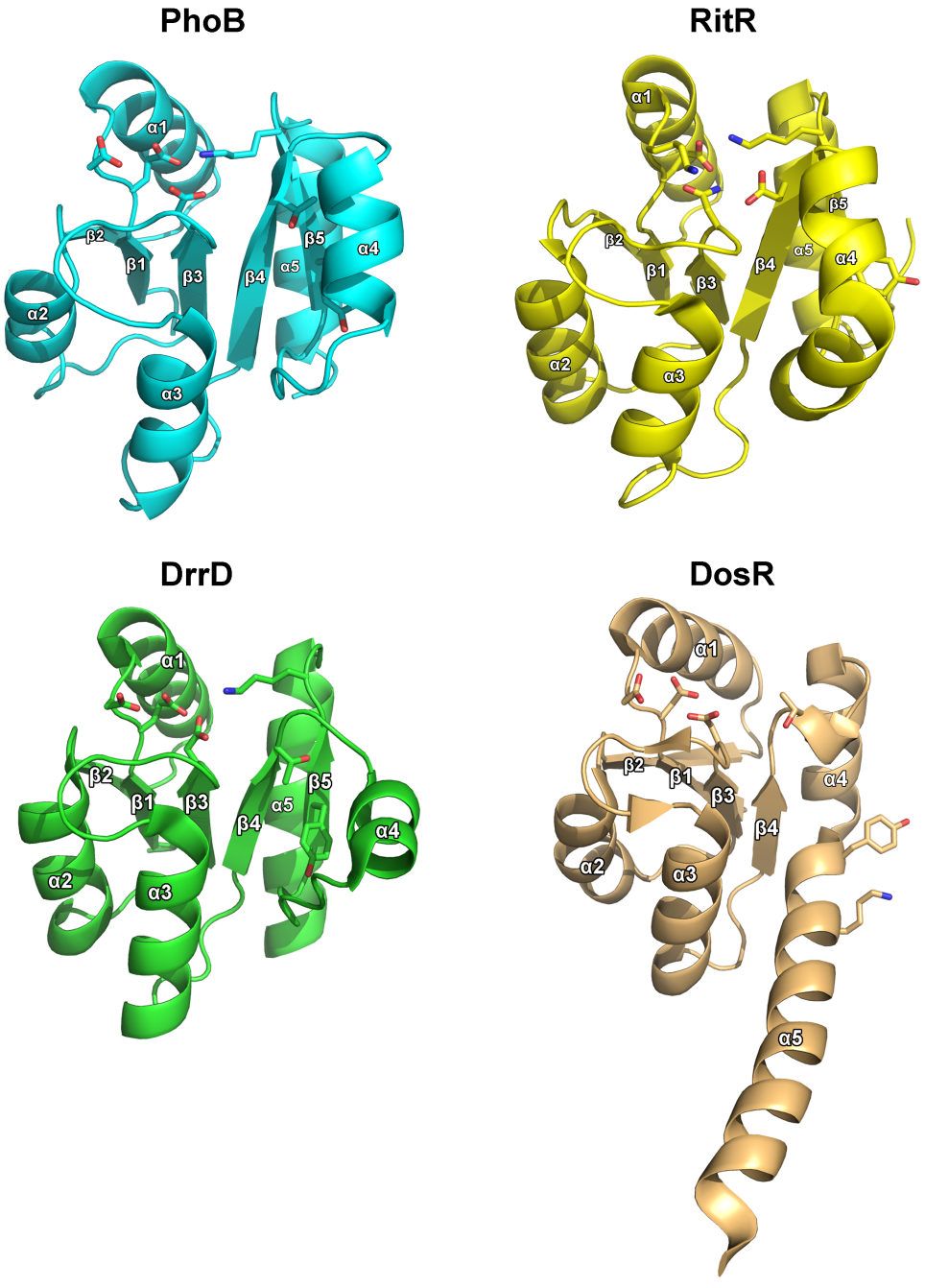


**Figure 1-11:** The α4 helix of response regulator REC domains appears to be particularly malleable. The

conserved residues equivalents are shown in stick. The typical topology where α4 is parallel to β5 and unbroken is exemplified by PhoB (PDB ID 1B00 [9]), Other RR proteins have unusual α4 helices. For example, helix α4 is broken into two pieces in RitR (PDB ID: 4LZL [6]), while that of DrrD (PDB ID: 1KGS [10]) is roughly perpendicular to strand β5. Finally, DosR (PDB ID: 3C3W [86]) has a completely different topology where α4 is missing entirely, as is strand β5.

In the so-called "active site" of RitR, the phosphorylatable aspartate is replaced with an asparagine residue and there is no bound metal (Figure 1-12A). In what would be the metal-binding site, E9 interacts with N53 and the conserved residue K103. The basic residue K10, which is normally one of the residues of the acidic triad, sits near the top of the putative phosphorylation site and disrupts the acidic environment that promotes metal binding. As shown in Figure 1-12B, not only is the acidic environment is disrupted, but also the cleft for $Mg^{2+}$ binding is eliminated in RitR. As mentioned above, RitR lacks a cognate histidine kinase. The lack of a cognate HK protein, together with the lack of key residues found in phosphorylation-dependent RRs makes it clear that RitR must be activated by a different mechanism from the typical, phosphorylation-dependent proteins.

Another noteable feature of RitR is the single cysteine, located in the linker region between REC domain and DBD. Bioinformatic results demonstrate that this cysteine128 is highly conserved in Streptococcus family. The specific role of this cysteine will be discussed in chapter 2.

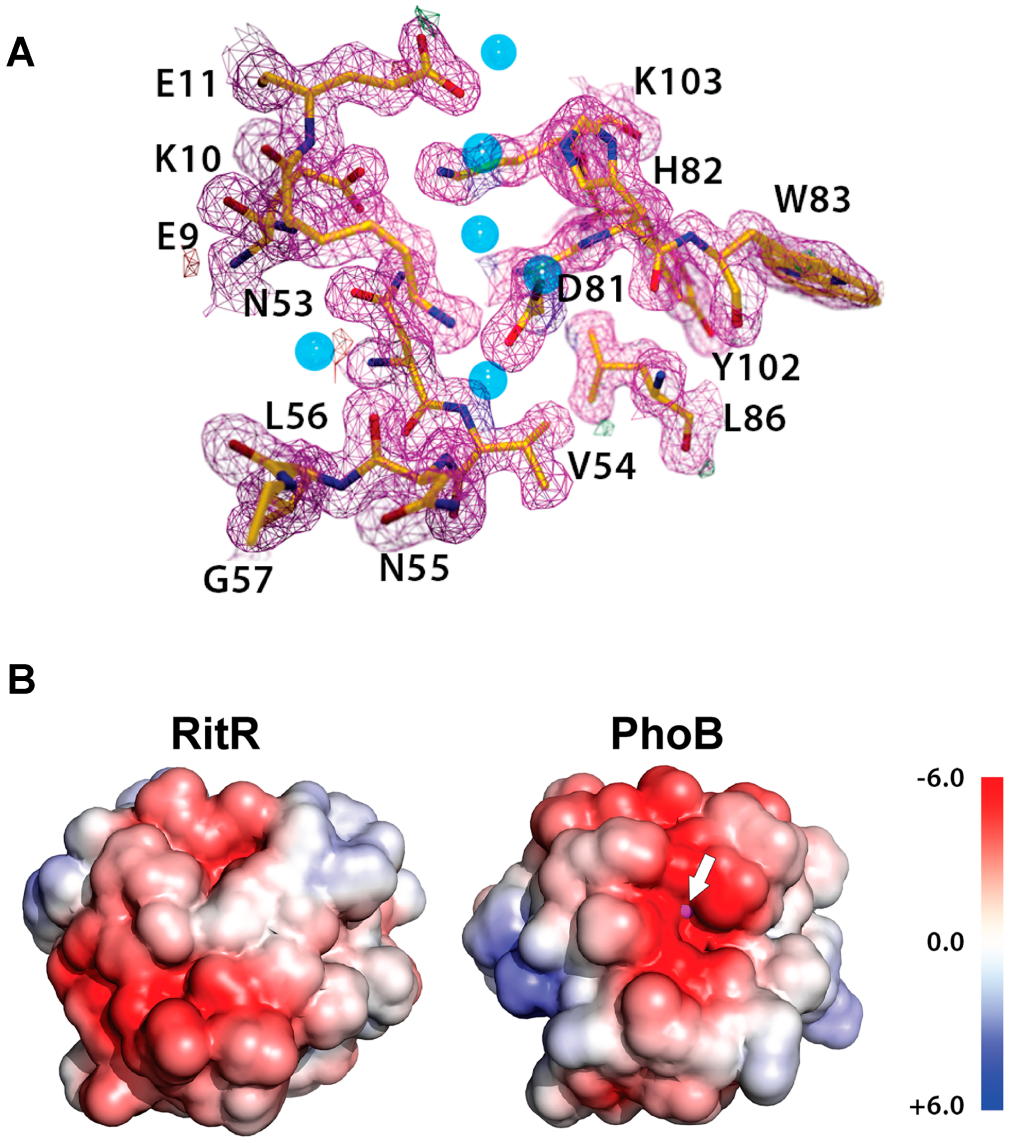


**Figure 1-12:** Structure of the RitR "active site" (this figure is downloaded from PLOS Pathogens 11(4): e1004795[6]). The stereoview of the $2|F_o|-|F_c|$ electron density in the RitR putative phosphorylation site (magenta mesh) contoured at 1.5 σ (A) shows the network of interactions and the lack of a large electron density peak that would indicate bound metal. Water molecules are shown as blue spheres. A comparison of the vacuum electrostatic surface potentials of the RitR and PhoB REC domains (B) highlights the differences in the surface properties of RitR that account for the loss of metal binding. The $Mg^{2+}$ in PhoB is shown as a magenta sphere and highlighted with a white arrow. Both the electronegative environment and the physical cleft for $Mg^{2+}$ binding are lost in the RitR putative phosphorylation site.

### 1.2.4.2 Diguanylate cyclase Q15Z91

A search of response regulator sequences for ALR proteins that also possess a cysteine residue at the C-terminal end of the linker helix (α5) and an enzymatic output domain led to the identification of a protein known only by its Uniprot accession code, Q15Z91. This putative regulatory protein from *Pseudoalteromonas atlantica* Tc6 contains an ALR domain linked to a diguanylate cyclase effector domain. This protein was chosen for study in order to explore the mechanism of ALR activation in the context of enzymatic activity rather than DNA binding. An enzymatic activity was preferred due to the facts that (1) it is simpler to conceptualize the active and inactive states of an enzyme and (2) it is significantly easier to quantify enzymatic activity than DNA-binding. A boon of the diguanylate cyclase domains in general is that the product, cyclic-di-guanosine monophosphate, is an important second messenger in biofilm formation. Thus, the biofilm phenotype is easily observed during heterologous expression in *E. coli* Origami™ 2 (DE3) cells, which will be discussed in detail in chapter 3.

The diguanylate cyclase (DGC) domain of Q15Z91 catalyzes the condensation of two molecules of GTP to yield bis-(3'-5')-cyclic dimeric guanosine monophosphate (c-di-GMP) (Scheme 1-1). A separate phosphodiesterase enzyme cleaves c-di-GMP to give 5'-phosphoguanosylyl-(3'-5')-guanosine (pGpG). Cyclic di-GMP is an important second messenger that regulates biofilm formation, cell adhesion, and induction of virulence factors in some bacteria [87-89].

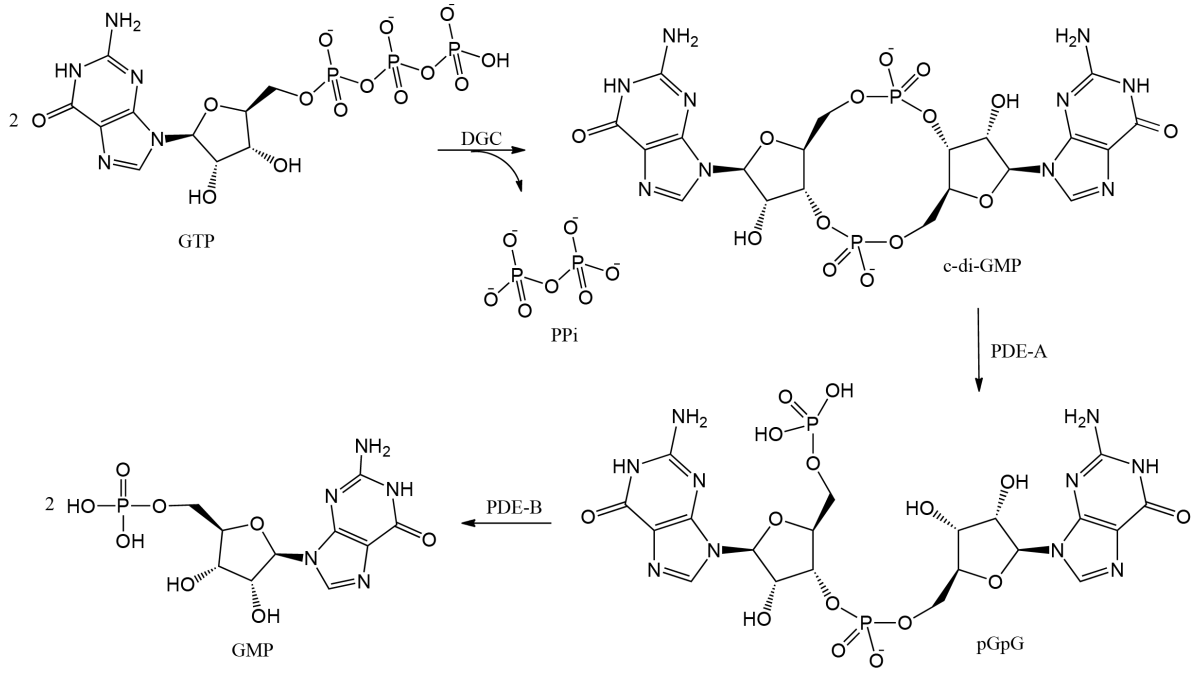


**Scheme 1-1:** Metabolism of cyclic-di-GMP. DGC: diguanylate cyclase; PDE-A: type A phosphodiesterase with EAL motif; PDE-B: type B phosphodiesterase with HD-GYP motif; pGpG: 5'-phosphoguanylyl-(3'-5')-guanosine.

The diguanylate cyclases usually contain a conserved GG(D/E)EF motif for catalysis and an RxxD motif for regulation of the DGC activity by product inhibition. A well-studied diguanylate cyclase, PleD from *Caulobacter crescentus*, is activated by phosphorylation[90]. As shown in Figure 1-13, PleD contains two CheY-like REC domains (a true receiver domain [D1] and an inactive "adapter" domain [D2]) and a DGC domain[91]. The receiver and adapter domains of PleD share the $(\beta/\alpha)_5$ topology common to typical OmpR/PhoB RRs. Upon phosphorylation of D53 in the acidic pocket of the REC domain (D1), the conserved switch residues T83 and F102 undergo a conformational change that triggers a rearrangement of the D1 and D2 domains relative to one another. This rearrangement optimizes one face of

the D1/D2 pair for dimerization between two PleD molecules[90, 92] (Figure 1-13A). Interestingly, the two REC domains (D1/D2) form an α4-β5-α5 dimer interface very similar to those seen in other OmpR/PhoB subfamily regulators, while the interactions between the PleD protomers includes residues from D1 domain (α1, β2, β3, α5) and D2 domain (α8 and α10).

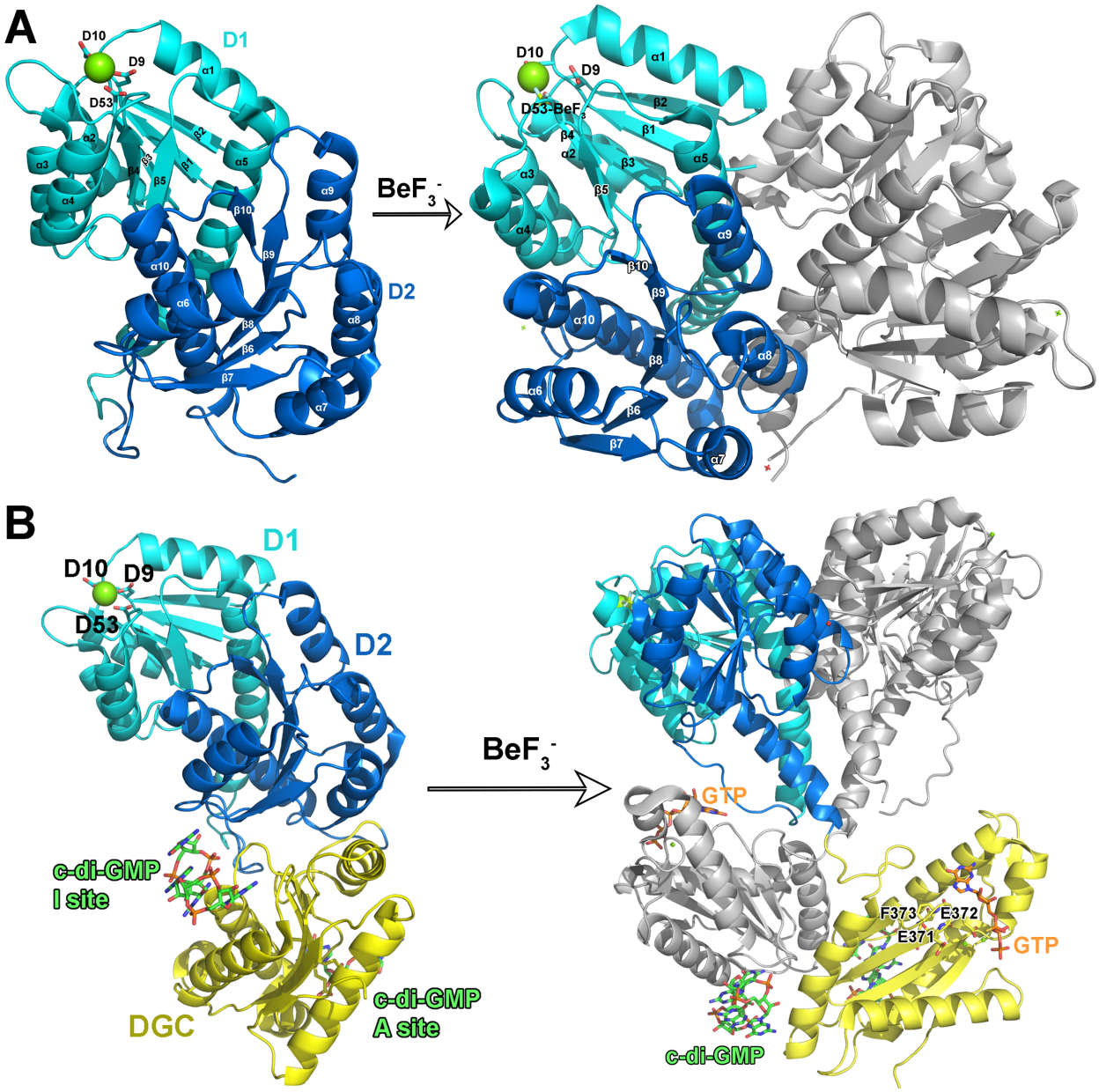

**Figure 1-13:** The receiver (D1) and adapter (D2) domains of PleD rearrange after $BeF_3^-$ treatment (A). $BeF_3^-$ was used to mimic phosphorylation of D53. The DGC domains were omitted for clarity. The acidic triad residues are shown as sticks. The $Mg^{2+}$ ions are shown as green spheres. The inactive form of PleD is shown on the left, and the $BeF_3$ activated mimic structure is shown on the right. The D1 domain is colored cyan, and the D2 adapter domain is colored blue. In the activated PleD structure, the D1 and D2 domains of the second protomer in the dimer are colored grey. After D53 accepts the phosphoryl group, $REC_1$ and $REC_2$ form a tighter dimer interface. PleD dimerization (B) is promoted by phosphorylation and c-di-GMP binding immobilizes the DGC domain against the D1 and D2 domains. As above, the inactive PleD structure is shown on the left and the activated mimic on the right. The c-diGMP molecules are shown as sticks. In the inactive structure, c-di-GMP is bound to both the inhibitory (I) and active (A) sites. In the $BeF_3$ phospho-mimic structure of the PleD dimer, c-di-GMP is still bound in the inhibitory site, which restricts DGC domains from catalysis. Two GTP molecules (shown in stick) bind in each active site respectively.

The conserved DGC domain (GGEEF motif) consists of a five-stranded central β sheet surrounded by α helices, which is similar to the structure of adenylate cyclase and type I DNA polymerase. A single DGC domain binds only one GTP molecule, which means that a single domain contains only half of an active site. As shown in Scheme 1-2, for reactions to happen, two GTP molecules from two DGC domains need to get closer and well aligned. Thus, activity requires the antiparallel association of two DGC domains, each with GTP bound. The regulatory logic is clear: antiparallel association of two DGC domains is much more likely in the dimeric form of PleD, where it is a unimolecular process, than it is in the case of free PleD monomers. In the active site of PleD, the conserved residues G368, G269 and E371 make key interactions for binding GTP, while E370 is essential for catalysis[91]. In PleD, inhibitory sites on the DGC domains, marked by an RxxD motif, bind intercalated c-di-GMP dimers that "pin" the DGC domains to the regulatory domains in the case of

unactivated PleD, or to each other in an unproductive back-to-back orientation in the case of activated (phosphorylated) PleD. This c-di-GMP dimer binding is the basis of the observed product inhibition that modulates DGC activity. Disruption of the inhibitory sites, for example by mutating the Arg or Gly residues of the RxxG motif, abrogates the product inhibition[93]. This allosteric feedback inhibition is not affected by phosphorylation status (Fig1-15B).

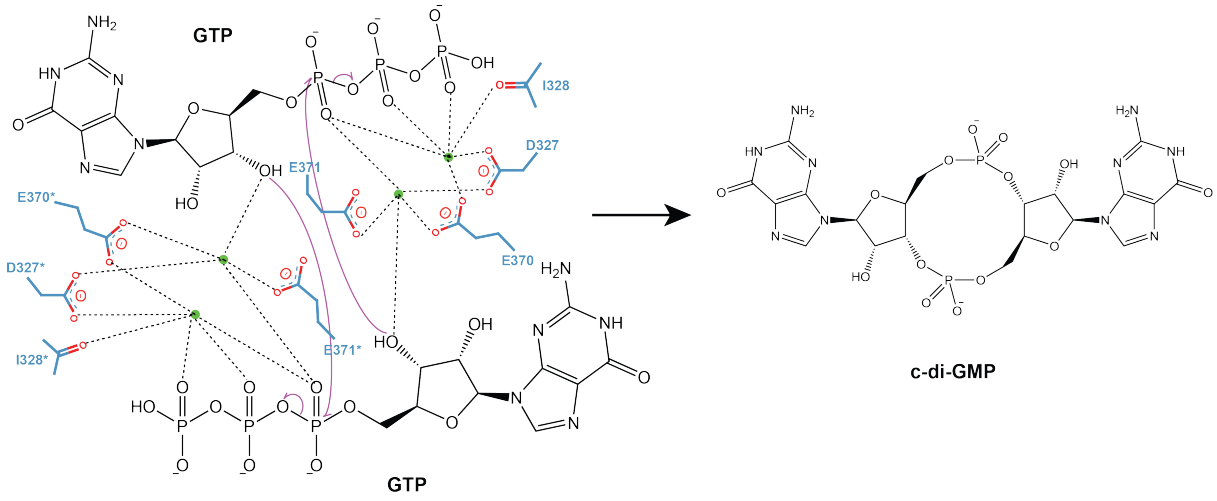


**Scheme 1-2:** Schematic representation of the diguanylate cyclase reaction where two GTP molecules are condensed to form c-di-GMP. The c-di-GMP contains two GMP moieties linked by O3'-P phosphodiester bonds. Four $Mg^{2+}$ ions are shown as green spheres. The two GTP molecules are held in close proximity and with the proper alignment by four $Mg^{2+}$ ions that are coordinated with the phosphate groups of GTP and the carboxyl groups of the conserved residues E370, E371, and D327. D327 is thought to promote deprotonation of the 3'-OH group of GTP to initiate the reaction. The deprotonated 3'-hydroxyl group would then attack the Pα-O bond, and release pyrophosphate (PPi). This is repeated in the other half of the active site so that a total of two molecules of PPi are released during each catalytic cycle.

The diguanylate cyclase WspR from *Pseudomonas aeruginosa* is very similar to PleD in that it is also regulated by feedback inhibition, though the exact mechanism differs[4]. WspR contains a single CheY-like REC domain and a DGC domain (Figure 1-14A). These two domains are linked by a long helix α5 [4]. The REC domain has a similar structure to those of activated OmpR/PhoB RRs. The switch residue Y117 adopts an inward conformation, promoting association through the commonly observed α4-β5-α5 dimer interface (Figure 1-14B). However, no post-translational modification of WspR, such as phosphorylation, has been observed in the structure. *In vitro* activity study of Wsp and phosphorylated WspR showed that unphosphorylated WspR can catalyze c-di-GMP formation but phosphorylated WspR exhibited faster DGC activity[94]. WspR from *P. aeruginosa* functions as a compact, c-di-GMP-free dimer. However, other WspR homologs, such as that from *P. syringae,* require phosphorylation-induced tetramerization for high cyclase activity[95]. This activated cyclase activity was only obtained by phosphodiesterase treatment of WspR to remove c-di-GMP, followed by phosphorylation-induced tetramerization[95]. Both WspR homologs exhibit product immobilization inhibition. WspR from *P. aeruginosa* is purified as a mixture of dimer and tetramer[4, 95]. In the crystal lattice, WspR formed a distinct 222-symmetric tetramer, and the long helix α5 facilitates the antiparallel tetramer formation[4, 95], as shown in Figure 1-14A. Molecules of c-di-GMP dimers bind to the specific I sites (RxxD motif) that composed by two protomers from different dimers (e.g. chain A and chain C) in the tetramer. The cross-linked DGC domains forced the active sites apart and prevent the cyclization of two GTP molecules.

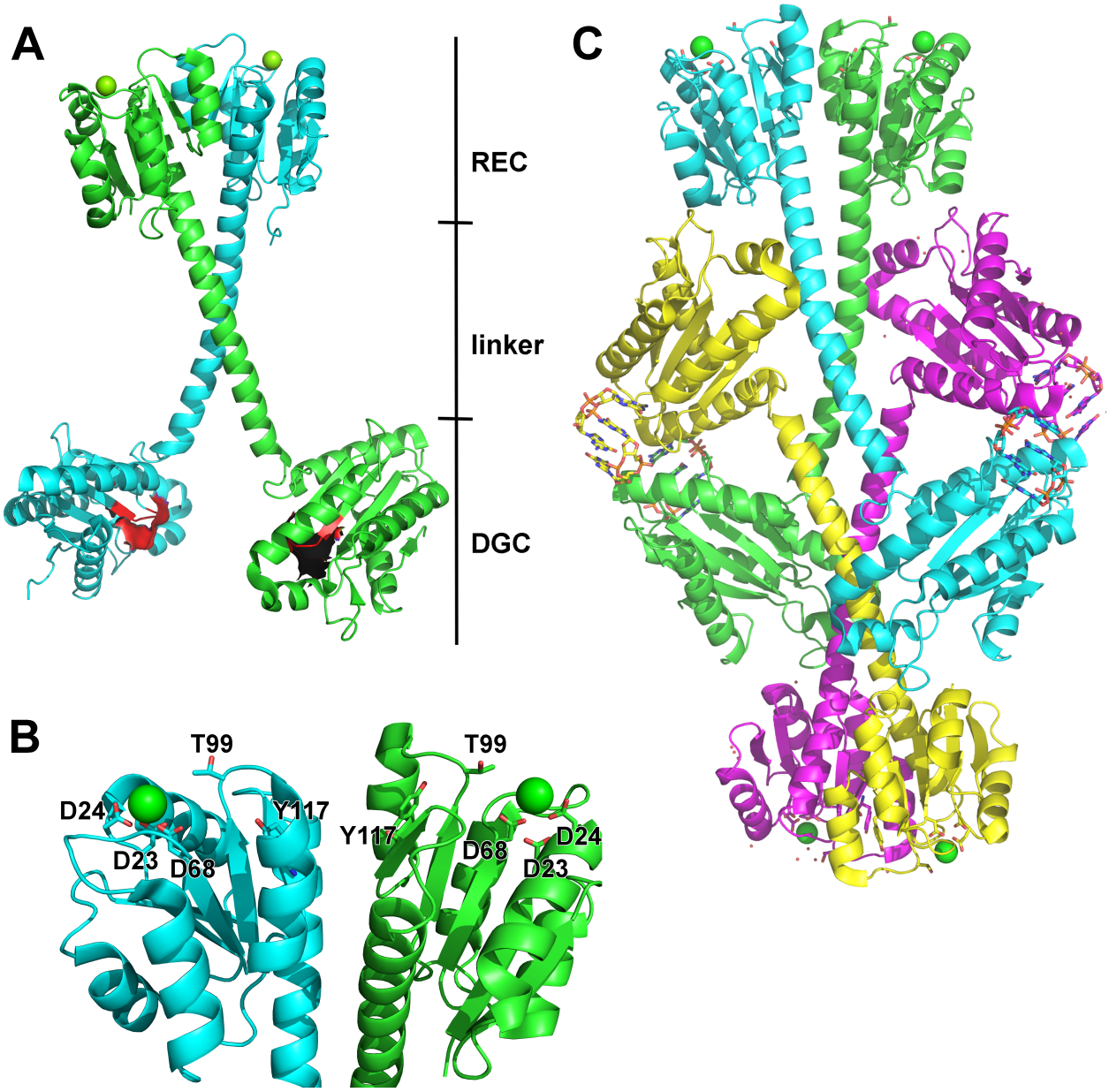


**Figure 1-14:** The Wsp dimer (A), REC domain of WspR dimer (B) and tetramer (C) structure from *Pseudomonas aeruginosa* (PDB ID: 3BRE [4]). Chain A is colored cyan, chain B is colored green, chain C is colored magenta, and chain D is colored yellow. Residues in phosphorylation site and switch residues are shown as sticks. The $Mg^{2+}$ ions are represented with green spheres. The GTP binding active site are shown in red sphere in (A). Four c-di-GMP dimers in (C) are shown as sticks. In the crystal, two WspR dimers packed in an antiparallel way to form the inactive tetramer with c-di-GMP bound.

Both of these diguanylate cyclases, PleD and WspR, have the structural features required for phosphorylation-dependent activation. In the case of PleD, phosphorylation has been shown to be the primary regulatory factor, whereas with WspR, phosphorylation accelerates the DGC activity. In contrast, Q15Z91 has lost these structural features, such as the conserved, phosphorylatable aspartate residue and the $Mg^{2+}$-binding site. This prompted us to ask, "what is the mechanism of activation of Q15Z91?" Is it also controlled by the non-competitive allosteric product inhibition? These questions will be addressed in Chapter 3.

In summary, ALRs exists in most classes of bacteria (averaging ~2 per genome), and are also prevalent in archaea, fungi, plants and possibly even insects and primitive animals. The key "invariant" catalytic and signaling residues required in canonical REC domains are found to be changed in many ALR sequences. Although these atypical REC domains has been known to exist for some time, it remain unknown that how they are regulated in the absence of the conserved Asp. Combining structural data with biochemical and genetic examination of two founding members of the ALR family, RitR and Q15Z91, we demonstrate that ALRs might have evolved to accommodate more diverse environmental signals, while largely retaining their time-tested ancestral post-input signaling mechanisms. This work also provides a foundation for future experimentation to decipher the largely unknown functional roles of these proteins.

## 1.3 References


[1] Yoshida, T., Phadtare, S., and Inouye, M. (2007) Functional and structural characterization of EnvZ, an osmosensing histidine kinase of E. coli, *Methods in enzymology 423*, 184-202.

[2] Matsushika, A., and Mizuno, T. (1998) A dual-signaling mechanism mediated by the ArcB hybrid sensor kinase containing the histidine-containing phosphotransfer domain in Escherichia coli, *Journal of bacteriology 180*, 3973-3977.

[3] Robinson, V. L., Wu, T., and Stock, A. M. (2003) Structural analysis of the domain interface in DrrB, a response regulator of the OmpR/PhoB subfamily, *Journal of bacteriology 185*, 4186-4194.

[4] De, N., Pirruccello, M., Krasteva, P. V., Bae, N., Raghavan, R. V., and Sondermann, H. (2008) Phosphorylation-Independent Regulation of the Diguanylate Cyclase WspR, *PLoS biology 6*, e67.

[5] Bachhawat, P., Swapna, G. V. T., and Stock, A. M. (2005) Mechanism of Activation for Transcription Factor PhoB Suggested by Different Modes of Dimerization in the Inactive and Active States, *Structure (London, England : 1993) 13*, 1353-1363.

[6] Maule, A. F., Wright, D. P., Weiner, J. J., Han, L., Peterson, F. C., Volkman, B. F., Silvaggi, N. R., and Ulijasz, A. T. (2015) The Aspartate-Less Receiver (ALR) Domains: Distribution, Structure and Function, *PLOS Pathogens 11*, e1004795.

[7] Stephenson, K., and Hoch, J. A. (2002) Evolution of signalling in the sporulation phosphorelay, *Molecular microbiology 46*, 297-304.

[8] Hickey, J. M., Lovell, S., Battaile, K. P., Hu, L., Middaugh, C. R., and Hefty, P. S. (2011) The Atypical Response Regulator Protein ChxR Has Structural Characteristics and Dimer Interface Interactions That Are Unique within the OmpR/PhoB Subfamily, *The Journal of biological chemistry 286*, 32606-32616.

[9] Sola, M., Gomis-Ruth, F. X., Serrano, L., Gonzalez, A., and Coll, M. (1999) Three-dimensional crystal structure of the transcription factor PhoB receiver domain, *Journal of molecular biology 285*, 675-687.

[10] Buckler, D. R., Zhou, Y., and Stock, A. M. (2002) Evidence of intradomain and interdomain flexibility in an OmpR/PhoB homolog from Thermotoga maritima, *Structure 10*, 153-164.

[11] Hong, E., Lee, H. M., Ko, H., Kim, D. U., Jeon, B. Y., Jung, J., Shin, J., Lee, S. A., Kim, Y., Jeon, Y. H., Cheong, C., Cho, H. S., and Lee, W. (2007) Structure of an atypical orphan response regulator protein supports a new phosphorylation-independent regulatory mechanism, *The Journal of biological chemistry 282*, 20667-20675.

[12] Barta, M. L., Hickey, J. M., Anbanandam, A., Dyer, K., Hammel, M., and Hefty, P. S. (2014) Atypical Response Regulator ChxR from Chlamydia trachomatis Is Structurally Poised for DNA Binding, *PLOS ONE 9*, e91760.

[13] Lin, W., Wang, Y., Han, X., Zhang, Z., Wang, C., Wang, J., Yang, H., Lu, Y., Jiang, W., Zhao, G. P., and Zhang, P. (2014) Atypical OmpR/PhoB subfamily response regulator GlnR of actinomycetes functions as a homodimer, stabilized by the unphosphorylated conserved Asp-focused charge interactions, *The Journal of biological chemistry 289*, 15413-15425.

[14] Bachhawat, P., Swapna, G. V., Montelione, G. T., and Stock, A. M. (2005) Mechanism of activation for transcription factor PhoB suggested by different modes of dimerization in the inactive and active states, *Structure 13*, 1353-1363.
[15] Ulrich, L. E., Koonin, E. V., and Zhulin, I. B. (2005) One-component systems dominate signal transduction in prokaryotes, *Trends in Microbiology 13*, 52-56.
[16] Vannini, A., Volpari, C., Gargioli, C., Muraglia, E., Cortese, R., De Francesco, R., Neddermann, P., and Di Marco, S. (2002) The crystal structure of the quorum sensing protein TraR bound to its autoinducer and target DNA, *The EMBO Journal 21*, 4393-4401.
[17] Zhu, J., Oger, P. M., Schrammeijer, B., Hooykaas, P. J., Farrand, S. K., and Winans, S. C. (2000) The bases of crown gall tumorigenesis, *Journal of bacteriology 182*, 3885-3895.
[18] Salvi, M., Schomburg, B., Giller, K., Graf, S., Unden, G., Becker, S., Lange, A., and Griesinger, C. (2017) Sensory domain contraction in histidine kinase CitA triggers transmembrane signaling in the membrane-bound sensor, *Proceedings of the National Academy of Sciences 114*, 3115-3120.
[19] Müller, S., Götz, M., and Beier, D. (2009) Histidine Residue 94 Is Involved in pH Sensing by Histidine Kinase ArsS of Helicobacter pylori, *PLoS ONE 4*, e6930.
[20] Moker, N., Reihlen, P., Kramer, R., and Morbach, S. (2007) Osmosensing properties of the histidine protein kinase MtrB from Corynebacterium glutamicum, *The Journal of biological chemistry 282*, 27666-27677.
[21] Braun, Y., Smirnova, A. V., Weingart, H., Schenk, A., and Ullrich, M. S. (2007) A temperature-sensing histidine kinase: function, genetics, and membrane topology, *Methods in enzymology 423*, 222-249.
[22] Zhang, X. X., Gauntlett, J. C., Oldenburg, D. G., Cook, G. M., and Rainey, P. B. (2015) Role of the Transporter-Like Sensor Kinase CbrA in Histidine Uptake and Signal Transduction, *Journal of bacteriology 197*, 2867-2878.
[23] Buelow, D. R., and Raivio, T. L. (2010) Three (and more) component regulatory systems - auxiliary regulators of bacterial histidine kinases, *Molecular microbiology 75*, 547-566.
[24] Kwon, O., Georgellis, D., and Lin, E. C. C. (2000) Phosphorelay as the sole physiological route of signal transmission by the arc two-component system of Escherichia coli, *Journal of bacteriology 182*, 3858-3862.
[25] Thakor, H., Nicholas, S., Porter, I. M., Hand, N., and Stewart, R. C. (2011) Identification of an anchor residue for CheA-CheY interactions in the chemotaxis system of Escherichia coli, *Journal of bacteriology 193*, 3894-3903.
[26] Dworkin, J. (2015) Ser/Thr phosphorylation as a regulatory mechanism in bacteria, *Current opinion in microbiology 24*, 47-52.
[27] Pereira, S. F. F., Goss, L., and Dworkin, J. (2011) Eukaryote-Like Serine/Threonine Kinases and Phosphatases in Bacteria, *Microbiology and Molecular Biology Reviews : MMBR 75*, 192-212.
[28] Kalantari, A., Derouiche, A., Shi, L., and Mijakovic, I. (2015) Serine/threonine/tyrosine phosphorylation regulates DNA binding of bacterial transcriptional regulators, *Microbiology 161*, 1720-1729.

[29] Nambu, J. R., Lewis, J. O., Wharton, K. A., and Crews, S. T. (1991) The Drosophila single-minded gene encodes a helix-loop-helix protein that acts as a master regulator of CNS midline development, *Cell 67*, 1157-1167.
[30] Yoshida, T., Cai, S. j., and Inouye, M. Interaction of EnvZ, a sensory histidine kinase, with phosphorylated OmpR, the cognate response regulator.
[31] Wang, L. C., Morgan, L. K., Godakumbura, P., Kenney, L. J., and Anand, G. S. (2012) The inner membrane histidine kinase EnvZ senses osmolality via helix‐coil transitions in the cytoplasm, *The EMBO Journal 31*, 2648.
[32] Stock, A., Chen, T., Welsh, D., and Stock, J. (1988) CheA protein, a central regulator of bacterial chemotaxis, belongs to a family of proteins that control gene expression in response to changing environmental conditions, *Proceedings of the National Academy of Sciences of the United States of America 85*, 1403-1407.
[33] MacFarlane, S. A., and Merrick, M. (1985) The nucleotide sequence of the nitrogen regulation gene ntrB and the glnA-ntrBC intergenic region of Klebsiella pneumoniae, *Nucleic acids research 13*, 7591-7606.
[34] Taylor, B. L., and Zhulin, I. B. (1999) PAS Domains: Internal Sensors of Oxygen, Redox Potential, and Light, *Microbiology and Molecular Biology Reviews 63*, 479-506.
[35] Möglich, A., Ayers, R. A., and Moffat, K. (2009) Structure and Signaling Mechanism of Per-ARNT-Sim Domains, *Structure 17*, 1282-1294.
[36] Wang, C., Sang, J., Wang, J., Su, M., Downey, J. S., Wu, Q., Wang, S., Cai, Y., Xu, X., Wu, J., Senadheera, D. B., Cvitkovitch, D. G., Chen, L., Goodman, S. D., and Han, A. (2013) Mechanistic insights revealed by the crystal structure of a histidine kinase with signal transducer and sensor domains, *PLoS biology 11*, e1001493.
[37] Gutu, A. D., Wayne, K. J., Sham, L. T., and Winkler, M. E. (2010) Kinetic characterization of the WalRKSpn (VicRK) two-component system of Streptococcus pneumoniae: dependence of WalKSpn (VicK) phosphatase activity on its PAS domain, *Journal of bacteriology 192*, 2346-2358.
[38] Casino, P., Miguel-Romero, L., and Marina, A. (2014) Visualizing autophosphorylation in histidine kinases, *5*, 3258.
[39] Trajtenberg, F., Grana, M., Ruetalo, N., Botti, H., and Buschiazzo, A. (2010) Structural and enzymatic insights into the ATP binding and autophosphorylation mechanism of a sensor histidine kinase, *The Journal of biological chemistry 285*, 24892-24903.
[40] Marina, A., Waldburger, C. D., and Hendrickson, W. A. (2005) Structure of the entire cytoplasmic portion of a sensor histidine-kinase protein, *Embo j 24*, 4247-4259.
[41] Wigley, D. B., Davies, G. J., Dodson, E. J., Maxwell, A., and Dodson, G. (1991) Crystal structure of an N-terminal fragment of the DNA gyrase B protein, *Nature 351*, 624-629.
[42] Ban, C., and Yang, W. (1998) Crystal Structure and ATPase Activity of MutL: Implications for DNA Repair and Mutagenesis, *Cell 95*, 541-552.
[43] Prodromou, C., Roe, S. M., O'Brien, R., Ladbury, J. E., Piper, P. W., and Pearl, L. H. (1997) Identification and structural characterization of the ATP/ADP-binding site in the Hsp90 molecular chaperone, *Cell 90*, 65-75.
[44] Wolanin, P. M., Thomason, P. A., and Stock, J. B. (2002) Histidine protein kinases: key signal transducers outside the animal kingdom, *Genome Biology 3*, reviews3013.3011-reviews3013.3018.

[45] Martínez-Hackert, E., and Stock, A. M. (1997) Structural relationships in the OmpR family of winged-helix transcription factors11Edited by M. Gottesman, *Journal of molecular biology 269*, 301-312.
[46] King-Scott, J., Nowak, E., Mylonas, E., Panjikar, S., Roessle, M., Svergun, D. I., and Tucker, P. A. (2007) The structure of a full-length response regulator from Mycobacterium tuberculosis in a stabilized three-dimensional domain-swapped, activated state, *The Journal of biological chemistry 282*, 37717-37729.
[47] Menon, S., and Wang, S. (2011) Structure of the response regulator PhoP from Mycobacterium tuberculosis reveals a dimer through the receiver domain, *Biochemistry 50*, 5948-5957.
[48] Park, A. K., Lee, J. H., Chi, Y. M., and Park, H. (2016) Structural characterization of the full-length response regulator spr1814 in complex with a phosphate analogue reveals a novel conformational plasticity of the linker region, *Biochemical and biophysical research communications 473*, 625-629.
[49] Gardner, S. G., Miller, J. B., Dean, T., Robinson, T., Erickson, M., Ridge, P. G., and McCleary, W. R. (2015) Genetic analysis, structural modeling, and direct coupling analysis suggest a mechanism for phosphate signaling in Escherichia coli, *BMC Genetics 16*, S2.
[50] Qi, Y., Kobayashi, Y., and Hulett, F. M. (1997) The pst operon of Bacillus subtilis has a phosphate-regulated promoter and is involved in phosphate transport but not in regulation of the pho regulon, *Journal of bacteriology 179*, 2534-2539.
[51] Barbieri, C. M., Mack, T. R., Robinson, V. L., Miller, M. T., and Stock, A. M. (2010) Regulation of response regulator autophosphorylation through interdomain contacts, *The Journal of biological chemistry 285*, 32325-32335.
[52] Galperin, M. Y. (2010) Diversity of structure and function of response regulator output domains, *Current Opinion in Microbiology 13*, 150-159.
[53] Wadhams, G. H., and Armitage, J. P. (2004) Making sense of it all: bacterial chemotaxis, *Nature reviews. Molecular cell biology 5*, 1024-1037.
[54] Sarkar, M. K., Paul, K., and Blair, D. (2010) Chemotaxis signaling protein CheY binds to the rotor protein FliN to control the direction of flagellar rotation in Escherichia coli, *Proceedings of the National Academy of Sciences 107*, 9370-9375.
[55] Greer-Phillips, S. E., Alexandre, G., Taylor, B. L., and Zhulin, I. B. (2003) Aer and Tsr guide Escherichia coli in spatial gradients of oxidizable substrates, *Microbiology 149*, 2661-2667.
[56] Bourret, R. B., Davagnino, J., and Simon, M. I. (1993) The carboxy-terminal portion of the CheA kinase mediates regulation of autophosphorylation by transducer and CheW, *Journal of bacteriology 175*, 2097-2101.
[57] Griswold, I. J., Zhou, H., Matison, M., Swanson, R. V., McIntosh, L. P., Simon, M. I., and Dahlquist, F. W. (2002) The solution structure and interactions of CheW from Thermotoga maritima, *Nat Struct Mol Biol 9*, 121-125.
[58] Borkovich, K. A., Alex, L. A., and Simon, M. I. (1992) Attenuation of sensory receptor signaling by covalent modification, *Proc Natl Acad Sci U S A 89*, 6756-6760.
[59] Lee, S.-Y., Cho, H. S., Pelton, J. G., Yan, D., Henderson, R. K., King, D. S., Huang, L.-s., Kustu, S., Berry, E. A., and Wemmer, D. E. (2001) Crystal structure of an activated response regulator bound to its target, *Nat Struct Mol Biol 8*, 52-56.

[60] Lee, S. Y., Cho Hs Fau - Pelton, J. G., Pelton Jg Fau - Yan, D., Yan D Fau - Berry, E. A., Berry Ea Fau - Wemmer, D. E., and Wemmer, D. E. Crystal structure of activated CheY. Comparison with other activated receiver domains.
[61] Volz, K., and Matsumura, P. (1991) Crystal structure of Escherichia coli CheY refined at 1.7-A resolution, *The Journal of biological chemistry 266*, 15511-15519.
[62] Lupas, A., and Stock, J. (1989) Phosphorylation of an N-terminal regulatory domain activates the CheB methylesterase in bacterial chemotaxis, *The Journal of biological chemistry 264*, 17337-17342.
[63] Djordjevic, S., Goudreau, P. N., Xu, Q., Stock, A. M., and West, A. H. (1998) Structural basis for methylesterase CheB regulation by a phosphorylation-activated domain, *Proceedings of the National Academy of Sciences of the United States of America 95*, 1381-1386.
[64] Bourret, R. B., Hess, J. F., and Simon, M. I. (1990) Conserved aspartate residues and phosphorylation in signal transduction by the chemotaxis protein CheY, *Proc Natl Acad Sci U S A 87*, 41-45.
[65] Gupte, G., Woodward, C., and Stout, V. (1997) Isolation and characterization of rcsB mutations that affect colanic acid capsule synthesis in Escherichia coli K-12, *Journal of bacteriology 179*, 4328-4335.
[66] Klose, K. E., Weiss, D. S., and Kustu, S. (1993) Glutamate at the site of phosphorylation of nitrogen-regulatory protein NTRC mimics aspartyl-phosphate and activates the protein, *Journal of molecular biology 232*, 67-78.
[67] Zhu, X., Rebello, J., Matsumura, P., and Volz, K. (1997) Crystal structures of CheY mutants Y106W and T87I/Y106W. CheY activation correlates with movement of residue 106, *The Journal of biological chemistry 272*, 5000-5006.
[68] Sanders, D. A., Gillece-Castro, B. L., Stock, A. M., Burlingame, A. L., and Koshland, D. E., Jr. (1989) Identification of the site of phosphorylation of the chemotaxis response regulator protein, CheY, *The Journal of biological chemistry 264*, 21770-21778.
[69] Appleby, J. L., and Bourret, R. B. (1999) Activation of CheY mutant D57N by phosphorylation at an alternative site, Ser-56, *Molecular microbiology 34*, 915-925.
[70] Klose, K. E., Weiss, D. S., and Kustu, S. (1993) Glutamate at the Site of Phosphorylation of Nitrogen-regulatory Protein NTRC Mimics Aspartyl-Phosphate and Activates the Protein, *Journal of molecular biology 232*, 67-78.
[71] Moore, J. B., Shiau, S. P., and Reitzer, L. J. (1993) Alterations of highly conserved residues in the regulatory domain of nitrogen regulator I (NtrC) of Escherichia coli, *Journal of bacteriology 175*, 2692-2701.
[72] Lee, S. Y., Cho, H. S., Pelton, J. G., Yan, D., Berry, E. A., and Wemmer, D. E. (2001) Crystal structure of activated CheY. Comparison with other activated receiver domains, *The Journal of biological chemistry 276*, 16425-16431.
[73] Drake, S. K., Bourret, R. B., Luck, L. A., Simon, M. I., and Falke, J. J. (1993) Activation of the phosphosignaling protein CheY. I. Analysis of the phosphorylated conformation by 19F NMR and protein engineering, *The Journal of biological chemistry 268*, 13081-13088.
[74] Lukat, G. S., Lee, B. H., Mottonen, J. M., Stock, A. M., and Stock, J. B. (1991) Roles of the highly conserved aspartate and lysine residues in the response regulator of bacterial chemotaxis, *The Journal of biological chemistry 266*, 8348-8354.

[75] Stewart, R. C. (1993) Activating and inhibitory mutations in the regulatory domain of CheB, the methylesterase in bacterial chemotaxis, *The Journal of biological chemistry 268*, 1921-1930.
[76] Hao, Z., Lou, H., Zhu, R., Zhu, J., Zhang, D., Zhao, B. S., Zeng, S., Chen, X., Chan, J., He, C., and Chen, P. R. (2013) The multiple antibiotic resistance regulator MarR is a copper sensor in Escherichia coli, *Nature Chemical Biology 10*, 21.
[77] Ruiz, D., Salinas, P., Lopez-Redondo, M. L., Cayuela, M. L., Marina, A., and Contreras, A. (2008) Phosphorylation-independent activation of the atypical response regulator NblR, *Microbiology 154*, 3002-3015.
[78] Kato, H., Chibazakura, T., and Yoshikawa, H. (2008) NblR Is a Novel One-Component Response Regulator in the Cyanobacterium <I>Synechococcus elongatus</I> PCC 7942, *Bioscience, Biotechnology, and Biochemistry 72*, 1072-1079.
[79] Hickey, J. M., Weldon, L., and Hefty, P. S. (2011) The atypical OmpR/PhoB response regulator ChxR from Chlamydia trachomatis forms homodimers in vivo and binds a direct repeat of nucleotide sequences, *Journal of bacteriology 193*, 389-398.
[80] Malm, S., Tiffert, Y., Micklinghoff, J., Schultze, S., Joost, I., Weber, I., Horst, S., Ackermann, B., Schmidt, M., Wohlleben, W., Ehlers, S., Geffers, R., Reuther, J., and Bange, F. C. (2009) The roles of the nitrate reductase NarGHJI, the nitrite reductase NirBD and the response regulator GlnR in nitrate assimilation of Mycobacterium tuberculosis, *Microbiology 155*, 1332-1339.
[81] Schar, J., Sickmann, A., and Beier, D. (2005) Phosphorylation-independent activity of atypical response regulators of Helicobacter pylori, *Journal of bacteriology 187*, 3100-3109.
[82] Lange, R., Wagner, C., de Saizieu, A., Flint, N., Molnos, J., Stieger, M., Caspers, P., Kamber, M., Keck, W., and Amrein, K. E. (1999) Domain organization and molecular characterization of 13 two-component systems identified by genome sequencing of Streptococcus pneumoniae, *Gene 237*, 223-234.
[83] Tettelin, H., Nelson, K. E., Paulsen, I. T., Eisen, J. A., Read, T. D., Peterson, S., Heidelberg, J., DeBoy, R. T., Haft, D. H., Dodson, R. J., Durkin, A. S., Gwinn, M., Kolonay, J. F., Nelson, W. C., Peterson, J. D., Umayam, L. A., White, O., Salzberg, S. L., Lewis, M. R., Radune, D., Holtzapple, E., Khouri, H., Wolf, A. M., Utterback, T. R., Hansen, C. L., McDonald, L. A., Feldblyum, T. V., Angiuoli, S., Dickinson, T., Hickey, E. K., Holt, I. E., Loftus, B. J., Yang, F., Smith, H. O., Venter, J. C., Dougherty, B. A., Morrison, D. A., Hollingshead, S. K., and Fraser, C. M.
[84] Throup, J. P., Koretke, K. K., Bryant, A. P., Ingraham, K. A., Chalker, A. F., Ge, Y., Marra, A., Wallis, N. G., Brown, J. R., Holmes, D. J., Rosenberg, M., and Burnham, M. K. (2000) A genomic analysis of two-component signal transduction in Streptococcus pneumoniae, *Molecular microbiology 35*, 566-576.
[85] Ulijasz, A. T., Andes, D. R., Glasner, J. D., and Weisblum, B. (2004) Regulation of iron transport in Streptococcus pneumoniae by RitR, an orphan response regulator, *Journal of bacteriology 186*, 8123-8136.
[86] Wisedchaisri, G., Wu, M., Sherman, D. R., and Hol, W. G. J. (2008) Crystal Structures of the Response Regulator DosR from Mycobacterium tuberculosis Suggest a Helix Rearrangement Mechanism for Phosphorylation Activation, *Journal of molecular biology 378*, 227-242.

[87] Jenal, U., and Malone, J. (2006) Mechanisms of cyclic-di-GMP signaling in bacteria, *Annual review of genetics 40*, 385-407.
[88] Tischler, A. D., and Camilli, A. (2004) Cyclic diguanylate (c-di-GMP) regulates Vibrio cholerae biofilm formation, *Molecular microbiology 53*, 857-869.
[89] Ryan, R. P. (2013) Cyclic di-GMP signalling and the regulation of bacterial virulence, *Microbiology 159*, 1286-1297.
[90] Paul, R., Abel, S., Wassmann, P., Beck, A., Heerklotz, H., and Jenal, U. (2007) Activation of the diguanylate cyclase PleD by phosphorylation-mediated dimerization, *The Journal of biological chemistry 282*, 29170-29177.
[91] Chan, C., Paul, R., Samoray, D., Amiot, N. C., Giese, B., Jenal, U., and Schirmer, T. (2004) Structural basis of activity and allosteric control of diguanylate cyclase, *Proc Natl Acad Sci U S A 101*, 17084-17089.
[92] Wassmann, P., Chan, C., Paul, R., Beck, A., Heerklotz, H., Jenal, U., and Schirmer, T. (2007) Structure of BeF3−-Modified Response Regulator PleD: Implications for Diguanylate Cyclase Activation, Catalysis, and Feedback Inhibition, *Structure 15*, 915-927.
[93] Christen, B., Christen, M., Paul, R., Schmid, F., Folcher, M., Jenoe, P., Meuwly, M., and Jenal, U. (2006) Allosteric control of cyclic di-GMP signaling, *The Journal of biological chemistry 281*, 32015-32024.
[94] Hickman, J. W., Tifrea, D. F., and Harwood, C. S. (2005) A chemosensory system that regulates biofilm formation through modulation of cyclic diguanylate levels, *Proc Natl Acad Sci U S A 102*, 14422-14427.
[95] De, N., Navarro, M. V., Raghavan, R. V., and Sondermann, H. (2009) Determinants for the activation and autoinhibition of the diguanylate cyclase response regulator WspR, *Journal of molecular biology 393*, 619-633.
[96] Perera, I. C., Lee, Y. H., Wilkinson, S. P., and Grove, A. (2009) Mechanism for attenuation of DNA binding by MarR family transcriptional regulators by small molecule ligands, *Journal of molecular biology 390*, 1019-1029.
[97] Chang, Y. M., Chen, C. K., Ko, T. P., Chang-Chien, M. W., and Wang, A. H. (2013) Structural analysis of the antibiotic-recognition mechanism of MarR proteins, *Acta crystallographica. Section D, Biological crystallography 69*, 1138-1149.
[98] Zorn, J. A., and Wells, J. A. (2010) Turning enzymes ON with small molecules, *Nat Chem* Biol 6, 179-188.

# Chapter 2

# The Atypical Response Regulator Protein Repressor of Iron Transport Regulator (RitR) Exhibits an Alternative Mechanism of Activation

## 2.1 Background

RitR is an orphan response regulator in *S. pneumonia* R6 that has been shown to down-regulate the expression of iron-transport proteins to avoid oxidative damage during aerobic growth [1, 2]. RitR differs from typical two-component systems in that 1) it lacks a cognate HK protein, 2) the conserved phosphorylatable aspartate residue (D53) is substituted with asparagine, and 3) the binding site for $Mg^{2+}$, which is required for the phosphorylation reaction, is apparently disrupted in RitR. Together, these differences suggest that RitR cannot be phosphorylated and, thus, must use a different mechanism of activation. So my work is using biophysical tools to determine the regulatory mechanisms of proteins with ALR domains.

## 2.2 Methods

### 2.2.1 Cloning, expression, and purification of wild-type and mutant RitR

The gene encoding wild-type RitR from *Streptococcus pneumoniae* strain R800 was amplified and cloned into the pE-$SUMO_{kan}$ expression vector (LifeSensors Inc, Malvern, PA) using primers containing BsaI and XbaI restriction sites. The $His_6$-tagged SUMO-RitR fusion protein was expressed from *E. coli* BL21 Star (DE3) cells (Invitrogen Inc, Carlsbad, CA)

carrying the pE-SUMO-RitR plasmid. Cultures were grown in Luria-Bertani medium with 50 μg/mL kanamycin at 37 °C with agitation at 250 rpm. When the cultures reached an $OD_{600}$ of ~1.0, protein expression was induced with 0.4 mM IPTG. The temperature was then reduced to 16 °C and the cultures were grown overnight. Cells were harvested by centrifugation, resuspended in 5 mL/g of buffer A (25 mM TRIS pH 8.0, 300 mM NaCl, 10 mM imidazole) supplemented with 0.1 mg/mL DNAse I (Worthington Biochemical Corp., Lakewood, NJ). Cells were lysed using a Branson Sonifier S-450 cell disruptor (Branson Ultrasonics Corp., Danbury, CT) for a total of 5 min of sonication at 60% amplitude with 30 s pulses separated by 50 s rest periods. The temperature was maintained at or below 4 °C by suspending the steel beaker in an ice bath directly over a spinning stir bar. The lysate was clarified by centrifugation at 39,000 x g for 45 minutes and then applied to a 5 mL HisTrap column (GE Lifesciences, Piscataway, NJ) at a flow rate of 5 mL/min to isolate the $His_6$-SUMO-RitR fusion protein. The protein was eluted by a 4-step gradient of buffer B (25 mM TRIS pH 8.0, 300 mM NaCl, and 250 mM imidazole; 5, 15, 50, and 100% B). The $His_6$-SUMO-RitR fusion protein eluted in the third and fourth steps and was ~90% pure, as judged on coomassie-stained SDS-PAGE gels. Peak fractions were pooled and dialyzed overnight against 4 L of 25 mM TRIS pH 8.0, 150 mM NaCl, and ~3 μM SUMO protease (LifeSensors Inc). The dialysate was passed through the HisTrap column a second time to remove the cleaved $His_6$-SUMO tag as well as the protease. The resulting RitR preparation was >95% pure according to SDS-PAGE results. The protein was desalted using a HiTrap Desalting column (GE Lifesciences) into storage buffer (pH 6.5, 25 mM TRIS, 150 mM NaCl, 100 mM Malic acid) and stored at -80 °C. All mutants mentioned in the chapter 2 were expressed and purified using the same protocol as the wild type RitR.

### 2.2.2 Preparation of purification of the oxidized RitR dimer ($RitR_{ox}$)

$RitR_{ox}$ was prepared by treating purified, wild-type RitR with 1 mM hydrogen peroxide for 3 h, followed by size exclusion chromatography to obtain the oxidized dimer. A HiPrep 26/60 Sephacryl S100 HR column was equilibrated with 2 column volumes of buffer C (pH 6.5, 20 mM TRIS, 150 mM NaCl, 100 mM malic acid, 1 mM $H_2O_2$). The first peak to elute from the column, which was consistent in size with the dimer (~60 kDa), contained the dimeric $RitR_{ox}$ protein.

### 2.2.3 Preparation of protein for structure determination

The mutant SeMet labeled $RitR_{C128S}$ from T7 Express Crystal cells (New England BioLabs, Ipswich, MA) carrying the pE-SUMO-C128S plasmid. Cells were grown in SelenoMethionine Medium Complete (Molecular Dimensions, Newmarket, Suffolk, UK) with 50 μg/mL kanamycin. This selenomethionine-labelled $RitR_{C128S}$ mutant was purified using the same protocol described for RitR. But it was stored in 25 mM TRIS pH 8.0, 5 mM DTT for crystallization. The mutant $RitR_{C128D}$ was purified using the same protocol described for RitR. But it was stored in 10 mM ADA pH 7.0 buffer.

Two forms of a $RitR_{L86A/V93A}$ ALR domain were devised to probe the structural consequences of this double mutation: one corresponding to the original RitR ALR domain structure, which ends well before the putative redox-active C128 residue ($RitR_{L86A/V93A}$ residues 1-124; RDLV) and a longer version that included the entire α5 helix (residues 1-132; RD2LV). Selenomethionine-labelled protein was prepared for both double mutants

from T7 Express Crystal cells (New England BioLabs, Ipswich, MA) carrying the pE-SUMO-RDLV or pE-SUMO-RD2LV plasmid. Cells were grown in SelenoMethionine Medium Complete (Molecular Dimensions, Newmarket, Suffolk, UK) with 50 μg/mL kanamycin. Both selenomethionine-labelled double mutant $RitR_{L86A/V93A}$ REC domains were purified using the same protocol described for RitR.

### 2.2.4 Differential scanning fluorimetry

Differential scanning fluorimetry (DSF) was used to search for buffer conditions where the relatively unstable WT RitR might be stable enough to crystallize. Wild-type RitR was diluted to 20 μM with water (1.1ml final volume) and 2μl of SYPRO Orange dye was added. This protein solution (10 μl) was mixed 1:1 with the Slice pH buffer screen (Hampton Research) in a 96-well PCR plate. The plate was heated from 20 °C to 95 °C in 1 °C steps in an Eppendorf RealPlex real-time PCR machine. At each temperature step, the fluorescence signal from the SYPRO Orange dye (ThermoFisher Scientific) in each well of the plate was monitored. Plotting the second derivative of the fluorescence intensity vs temperature plot gives a peak corresponding to the $T_m$ of the protein in that buffer. Buffers showing at least a 2-3 °C upward shift in the $T_m$ were investigated as storage buffers for RitR.

DSF was also used to assess the ability of RitR and various mutants to bind to DNA by monitoring the ability of DNA to stabilize the proteins. To test the buffer and pH effects on the $T_m$, RitR and $RitR_{L86A/V93A}$ were incubated with a dsDNA oligo corresponding to the putative primary RitR binding site in *S. pneumoniae* R6 (BS3-3: 5'-

ATGAAACTTTCTCATTATTTAATTGGCTTACTTCT-3') in different buffers at different pH. Firstly, 1500 µl solution containing 200 µM protein and 100 µM BS3-3 was incubated at room temperature for 2 hours. Then 2 µl of the protein/BS3-3 mixture was mixed with 18 µl of different buffers at different pH containing the SYPRO Orange dye. Protein-only negative controls were prepared by mixing 200 µM RitR or $RitR_{L86A/V93A}$ protein with different buffers only containing SYPRO Orange dye.

Finally, DSF was used to double check the gel shift results by looking at the shifts in $T_m$ when different forms of RitR were incubated with BS3-3 in the binding buffer[1] (20 mM HEPES pH 7.2, 5 mM $MgCl_2$, 1 mM $CaCl_2$, 0.1 mM EDTA) and with the optimal protein:DNA ratio for binding (protein:DNA = 4:1). The protein variants investigated included $RitR_{ox}$, $RitR_{L86A/V93Aox}$ and $RitR_{L86A/V93A/C128Sox}$. Oxidized proteins were prepared by incubating with 1mM $H_2O_2$ at 4 $^oC$ overnight. Each RitR variant (RitR, RitRox, $RitR_{L86A/V93A}$, $RitR_{L86A/V93Aox}$, $RitR_{L86A/V93A/C128S}$, and $RitR_{L86A/V93A/C128Sox}$) was mixed with BS3-3 at final concentrations of 400 µM protein and 100 µM DNA in 25 mM TRIS pH 8.0, 150 mM NaCl buffer for 2 hours at room temperature. Then 2 µl of each protein/BS3-3 mixture was mixed with 18 µl of different buffers (buffer 1: 20 mM TRIS pH 6.5, 150 mM NaCl, 100 mM Malic acid; buffer 2: binding buffer; or buffer 3: binding buffer supplemented with 150 mM NaCl) containing SYPRO Orange dye. The protein-only controls were prepared by mixing 400 µM protein with buffer with SYPRO™ orange fluorescent dye.

### 2.2.5 Site-directed mutagenesis

The K10A, N53A, N53D, D81A, L86A, L90A, V93A, L86A/V93A, F96G, Y100A, Y102A, R113A, C128A, C128S, C128Dand Y163F mutants were prepared by the Ulijasz lab. Other mutants, L86A/V93A/C128S, RDLV and RD2LV, were constructed as part of this work. The full-length mutants were obtained by the Quick-Change™ mutagenesis method using the primers listed in Table 2-1. The Quick-Change™ protocol used the Pfusion DNA polymerase and the high fidelity (HF) master mix (New England Biolabs, Ipswich, MA). The PCR program included an initial denaturing step at 98 $^{o}$C for 30 s, followed by the cyclic portion of the program (denature at 98 $^{o}$C for 10 s, anneal at ($T_m$ of primer pair – 2) $^{o}$C for 25 s, extend for 210 s at 72 $^{o}$C; 17 cycles), and a final extension step at 72 $^{o}$C for 10 min. After PCR, DpnI (20 U) was added to the 50 µl PCR reaction to digest the methylated template DNA at 37 $^{o}$C for 1 h. The DpnI-treated PCR reaction (5 µl) was used to transform NEB5α competent *E. coli* (New England Biolabs, Ipswich, MA). Transformants were sequenced to confirm the presence of the mutation. The genes of two ALR domains of $RitR_{L86A/V93A}$ were amplified from pSUMO-$RitR_{L86A/V93A}$ plasmid. After BsaI and XbaI digestion, the genes were ligated into XbaI digested pSUMO kan plasmid. The success of ligation was checked by sequencing.

**Table 2-1:** Primers used for mutagenesis

| Names | Primer sequence |
|---|---|
| sumo-RitRL86A_RD_Fwd | GCGGTCTCAAGGTATGGGGAAACGGATTTTAT |
| sumo-RitRL86A_RD_Rev | GCTCTAGATTAAATGAAGTCCCGACCTCGG |

| | |
|---|---|
| sumo-RitR$_{C128S}$_Fwd | GACTTCATTGATCAACACAGCAGTCTGATGAAAGTTC |
| sumo-RitR$_{C128S}$_Rev | GAACTTTCATCAGACTGCTGTGTTGATCAATGAAGTC |
| sumo-RDLV_Rev | GCTCTAGATTAAATGAAGTCCCGACCTCGG |
| sumo-RD2LV_Rev | GCTCTAGATTATTTCATCAGACTGCAGTGTTGATC |
| sumo-RitR$_{C128D}$_Fwd | GACTTCATTGATCAACACGACAGTCTGATGAAAGTTC |
| sumo-RitR$_{C128D}$_Rev | GAACTTTCATCAGACTGTCGTGTTGATCAATGAAGTC |

### 2.2.6 Determination of C128 pK$_a$ by DTNB assay [6, 7]

The thiol-reactive reporter compound 5,5'-dithiobis-(2-nitrobenzoic acid) (DTNB) can be used to determine the number of free, solvent-exposed thiol groups in a protein or to estimate the pK$_a$ in cases where a single thiol group is present. The assay is based on the formation of 2-nitro-5 thiobenzoate (TNB$^-$) upon reaction of DTNB with thiol groups. The ionized reporter group, TNB$^{2-}$ absorbs UV light at 412 nm (Scheme 2-1).

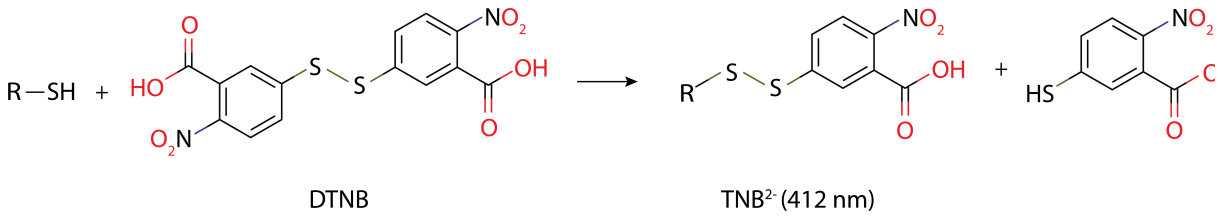


**Scheme 2-1**: The mechanism of DTNB assay

Reactions contained 5 μM RitR and 20 μM DTNB in 50 mM CHB buffer (50 mM citric acid, 50 mM HEPES, 50 mM Bicine, 150 mM NaCl, with pH adjusted by titration with NaOH

or HCl as appropriate) at pH values ranging from 4 to 9. The reactions were conducted at room temperature (~21 °C) in an Evolution™ 300 UV-Vis spectrophotometer (Thermo Scientific). The absorption at 412 nm was recorded until it plateaued. Then the pH-dependent rate of each reaction $k_{(pH)}$ was determined by fitting the time course to the following equation:

$$A_{412}(t) = A_{412,0} + \Delta A_{412}(1 - e^{-k(pH)t}) \quad \text{Equation 1}$$

Since $k_{(pH)}$ is directly dependent on the proportion of the cysteine thiolate group, the $pK_a$ of the C128 thiol was obtained by fitting the plot of $k_{(pH)}$ vs pH to the following equation:

$$k_{(pH)} = \frac{k}{1+10^{pK_{a,thiol}-pH}} \quad \text{Equation 2}$$

where $k_{(pH)}$ is the observed rate constant at a particular pH value, and k is the maximal rate of $TNB^{2-}$ formation at high pH.

### 2.2.7 Crystallization, structure determination, and model refinement

Crystals of selenomethionine (SeMet)-substituted $RitR_{C128S}$ were grown by the vapor diffusion method with hanging drop geometry. Drops were comprised of equal parts protein solution (20 mg/ml $RitR_{C128S}$ in 25 mM TRIS, pH 8.0) and crystallization solution (25% (w/v) polyethylene glycol (PEG) 3350, 0.1 M ammonium acetate). Partially-hollow rods appeared after several days at 16°C. Crystals were prepared for flash-cooling by sequential soaks in solutions containing 25% PEG (w/v) 3350, 0.2 M ammonium acetate, and 5, 10, or 20% glycerol (v/v).

Crystals of $RitR_{C128D}$ were grown by the same method, except with hanging drops composed of 1 µl of protein solution (15.3 mg/mL $RitR_{C128D}$ in 10 mM ADA pH 7.0) and 1 µl of crystallization solution (0.1 M HEPES pH 7.5, 22.5% Jeffamine ED-2001 pH 7.0). Long rod-shaped crystals grew after 3 days at 16 °C. Crystals were prepared for flash-cooling by sequential soaks in solutions containing 0.1 M HEPES pH 7.5, 22.5% Jeffamine ED-2001 pH 7.0, and 5, 10, or 20% glycerol (v/v).

Crystals of $RitR_{ox}$ were grown by the hanging-drop, vapor diffusion method with drops consisting of 2 µl of protein solution (6 mg/ml $RitR_{ox}$ in pH 6.5, 20 mM TRIS, 150 mM NaCl, 100 mM malic acid, 1 mM $H_2O_2$) and 1 µl of crystallization solution (10% (w/v) PEG 3350, 0.3 M magnesium sulfate). Prism-shaped crystals appeared after several days at 16 °C. Crystals were prepared for flash-cooling by soaking in a solution containing 10% (w/v) PEG 3350, 0.3 M magnesium sulfate, and 20% glycerol (v/v).

Crystals of RitR oxidized by treatment with $CuCl_2$ rather than $H_2O_2$ were grown from drops containing 1 µl of protein solution (5 mg/mL $RitR_{CuOX}$ in pH 6.5, 25 mM TRIS, 150 mM NaCl, 100 mM Malic acid, 1 mM $CuCl_2$) and 1 µl of microseeding solution (4% Tacsimate pH 6.0, 7.5% PEG 3350 containing microseeds derived from its own crystals). Single prism-shaped crystals grew after several days at 16 °C. Crystals were prepared for flash-cooling by sequential soaking in solutions containing 4% Tacsimate pH 6.0, 7.5% PEG 3350, and 5, 10, or 20% glycerol (v/v).

Crystals of selenomethionine-substituted $RitR_{L86A/V93A}$ REC domain, residues 1-124 (RDLV), were grown in drops consisting of equal parts of protein solution (4.4 mg/ml RDLV in 10 mM TRIS pH 8.5, 50 mM Succinic acid) and crystallization solution (20% (w/v) PEG

3350, 0.2 M magnesium sulfate, 0.1 M TRIS pH 8.5, 1 mM DTT). Small rods appeared after several days at 16 $^{o}$C. Crystals were prepared for flash-cooling by sequential soaks in solutions containing 20% PEG (w/v) 3350, 0.2 M magnesium sulfate, 0.1 M TRIS pH 8.5, and 5, 10, or 20% glycerol (v/v).

Crystals of SeMet-substituted $RitR_{L86A/V93A}$ REC domain, residues 1-132 (RD2LV), were grown by the hanging-drop, vapor diffusion method in drops comprised of equal parts of protein solution (19 mg/ml RD2LV in 10 mM glycine pH 8.8, 25 mM L-Arg) and crystallization solution (22.5% (w/v) polyethylene glycol (PEG) 3350, 12% Tacsimate pH 8.2). Small plate-shaped crystals appeared after several days at 16 $^{o}$C. Crystals were prepared for flash-cooling by sequential soaks in solutions containing 22.5% (w/v) PEG 3350, 12% Tacsimate pH 8.2, and 5, 10, or 20% glycerol (v/v).

X-ray diffraction data for SeMet $RitR_{C128S}$ were collected at beamline 21-ID-F of the Life Science Collaborative Access Team (LS-CAT) at the Advanced Photon Source (APS), Argonne National Laboratory. The $RitR_{C128D}$ data set was collected at LS-CAT beamline 21-ID-G. The $RitR_{ox}$ data set was collected at LS-CAT beamline 21-ID-F. The SeMet RDLV data was collected at LS-CAT beamline 21-ID-G. The SeMet RD2LV data were collected at LS-CAT beamline 21-ID-D. All data sets were processed with HKL2000[8].

The structure of $RitR_{C128S}$ was determined by the single-wavelength anomalous diffraction (SAD) method using 1.5 Å-resolution data collected from a single crystal of SeMet-substituted $RitR_{C128S}$ at 0.97889 Å, 61.0 eV below the tabulated K-edge wavelength for Se (0.97950Å). The program autoSHARP[9] was used to solve the Se substructure, which contained 16 of the 18 Se atoms in the asymmetric unit, and to calculate density-modified

electron density maps. An initial model comprising ~90 % of the asymmetric unit contents was built using BUCCANEER[10].

The structure of RDLV was determined by the single-wavelength anomalous diffraction (SAD) method using 1.9 Å-resolution data collected from a single crystal of SeMet-substituted proteins at 0.97857 Å, 61.0 eV below the tabulated K-edge wavelength for Se (0.97950Å). The program autoSHARP[9] was used to solve the Se substructure, which contained 16 of the 18 Se atoms in the asymmetric unit, and to calculate density-modified electron density maps. An initial model comprising ~90 % of the asymmetric unit contents was built using BUCCANEER[10]. The structure of RD2LV was determined by the single-wavelength anomalous diffraction (SAD) method using 2.6 Å-resolution data collected from a single crystal of SeMet-substituted proteins at 0.97872 Å, 61.0 eV below the tabulated K-edge wavelength for Se (0.97950Å). The program autoSHARP[9] was used to solve the Se substructure, which contained 16 of the 18 Se atoms in the asymmetric unit, and to calculate density-modified electron density maps. An initial model comprising ~90 % of the asymmetric unit contents was built using BUCCANEER[10].

Chain A of this model was used as the search model for molecular replacement in PHASER[11] to phase the $RitR_{ox}$ structure. Both models were subjected to iterative cycles of manual model building in COOT[12] and maximum likelihood-based refinement using the PHENIX package (phenix.refine[13]). Ordered solvent molecules were added automatically in phenix.refine and culled manually in COOT. Hydrogen atoms were added to the model using phenix.reduce[14] and were included in the later stages of refinement to improve the stereochemistry of the model. Positions of H atoms were refined using the riding model

with a global B-factor. Regions of the model for translation-libration-screw (TLS) refinement were identified using phenix.find_tls_groups (P.V. Afonine, unpublished work) and the TLS parameters were refined in phenix.refine. Once the refinement converged, the model was validated using the tools implemented in COOT and PHENIX [15, 16]. Sections of the backbone with missing or uninterpretable electron density were not included in the final model. Data collection and model refinement statistics are listed in Appendix A. Coordinates and structure factors for both $RitR_{C128S}$ and $RitR_{ox}$ models have been deposited in the Protein Data Bank (www.rcsb.org) with accession codes 5U8K and 5U8M.

### 2.2.8 Synthesis of binding site 3 (BS3) dsDNA oligonucleotides

Early footprinting experiments detected 3 binding sites for RitR(BS1-BS3)[1]. Since RitR was deemed to have the highest affinity for BS3, this sequence was used to investigate the DNA-binding activity of RitR and its variants. To facilitate co-crystallization of RitR bound to DNA, different lengths of BS3 were designed (Table 2-2), since the length of the oligonucleotide is a key parameter in the crystallization of protein:DNA complexes. Both strands of BS3-1, BS3-2, BS3-3, BS3-4, and BS3-5 were synthesized by Integrated DNA Technologies (Coralville, IA). Both strands of BS3-6 were synthesized via standard automated DNA synthesis techniques in a 1.0 μM scale using commercial 1000 Å CPG-succinyl-nucleoside supports. Deprotection of the nucleobases and phosphate moieties as well as cleavage of the linker were carried out under mild deprotection conditions using a mixture of 40% aq. $MeNH_2$ and 28% aq. $NH_3$ (1:1) at room temperature for 2 h. Oligonucleotides were purified by 20% denaturing polyacrylamide gel electrophoresis.

Quantification of oligonucleotides was carried out using a Phosphorimager equipped with ImageQuant Version 5.2 software. Double-stranded DNA was obtained by mixing the two single-stranded oligonucleotides in 250 mM TRIS pH 6.5, 150 mM NaCl buffer and heating to 90 $^{o}$C for 5 min, followed by slow cooling to room temperature.

**Table 2-2:** Sequences of the BS3 variants used in RitR binding assays.

| Name | Sequence | Length (bp) |
|---|---|---|
| BS3-1 | 5'-GGTATGAAACTTTCTCATTATTTAATTGGCTTACTTCT-3'<br>3'-CCATACTTTGAAAGAGTAATAAATTAACCGAATGAAGA-5' | 38 |
| BS3-2 | 5'-GGTATGAAACTTTCTCATTATTTAATTGGCTTAC-3'<br>3'-CCATACTTTGAAAGAGTAATAAATTAACCGAATG-5' | 34 |
| BS3-3 | 5'-ATGAAACTTTCTCATTATTTAATTGGCTTACTTCT-3'<br>3'-TACTTTGAAAGAGTAATAAATTAACCGAATGAAGA-5' | 35 |
| BS3-4 | 5'-AAACTTTCTCATTATTTAATTGGCTTACTTCT-3'<br>3'-TTTGAAAGAGTAATAAATTAACCGAATGAAGA-5' | 32 |
| BS3-5 | 5'-CTTTCTCATTATTTAATTGGCTTACTTCT-3'<br>5'-GAAAGAGTAATAAATTAACCGAATGAAGA-3' | 29 |
| BS3-6 | 5'-CTTTCTCATTATTTAATTGGCTTA-3'<br>3'-GAAAGAGTAATAAATTAACCGAAT-5' | 24 |

### 2.2.9 Size exclusion chromatography (SEC)

The oligomeric states of wild-type and mutant forms of RitR were assessed by size exclusion chromatography (SEC). All separations were carried out using an Agilent 1220

Compact HPLC equipped with a 250 x 4.6 mm BioBasic SEC-300 column equilibrated with pH 6.5, 10 mM TRIS, 150 mM NaCl, and 100 mM malic acid. The column was calibrated with the Gel Filtration Molecular Weight Marker kit from Sigma-Aldrich (Cytochrome C (12.4 kDa), Carbonic Anhydrase (29 kDa), Bovine Serum Albumin (66 kDa), and Sweet Potato Amylase (200 kDa)). The $H_2O_2$- or $CuCl_2$- treated RitR proteins were injected (5 µl of 4 mg/mL proteins) onto the column and separated at a flow rate of 0.5 ml/min at ambient temperature. Wild-type and mutant forms of RitR was assayed for DNA-binding activity by mixing 260 µM protein (RitR, $RitR_{L86A/V93A}$, $RitR_{L86A/V93A/C128S}$ and other mutants) with 100 µM each of the BS3 variant oligonucleotides (BS3-1, BS3-2, BS3-3, BS3-4, BS3-5, BS3-6). SEC experiments were carried out under the same conditions used for the RitR proteins in the absence of DNA.

### 2.2.10 Non-reducing SDS-PAGE and Native SDS-PAGE (NSDS)

Proteins were incubated with different metals for 2 hours at room temperature. These samples were then mixed with SDS loading dye lacking reducing agent, boiled for 5 min, and loaded on 12% SDS polyacrylamide gel. Proteins were revealed by staining with GelCode™ Blue Safe Protein Stain (Thermo SCIENTIFIC, Rockford, IL) for 1 h and destained in MilliQ $H_2O$. The slightly modified protocol for running native SDS-PAGE is followed as previously described by Nowakowski AB[17].

## 2.3 Results

### 2.3.1 Determining the optimal RitR storage buffer for crystallization

Like many DNA-binding proteins, such as the γδ resolvase[18], MarA[19], and MarR[20], the full-length RitR protein is not stable in low ionic strength buffers. In low ionic strength buffers like 25 mM TRIS pH 8.0, RitR precipitated out as a flocculent white solid, and this precipitate could be redissolved by addition of NaCl. Since it is generally preferred to search for crystallization conditions with the protein in a dilute, low ionic strength buffer, we performed experiments to find the lowest NaCl concentration where RitR would be stable. To begin, purified RitR was desalted into 25 mM TRIS pH 8.0, with concentrations of NaCl ranging from 50 to 200 mM in 50 mM steps. Samples were incubated overnight at 4 °C and the amount precipitate was assessed qualitatively. The lowest NaCl concentration tested that did not give visible precipitate was 150 mM. With the ionic strength optimized, we set about exploring the effect of buffer identity and pH on RitR stability. This was done using differential scanning fluorimetry together with the Solubility & Stability and Slice pH screens (Hampton research). The Solubility and Stability Screen, which is a collection of 96 small-molecule additives, was run in the 25 mM TRIS pH 8.0, 150 mM NaCl buffer. The top 10 conditions from the Solubility & Stability and the Slice pH screens, as judged by the degree of increase in the $T_m$ above the average $T_m$, are shown in Table 2-3 and Table 2-4, respectively.

**Table 2-3:** Compounds from the Solubility & Stability Screen (Hampton Research) giving the highest $T_m$ values in the DSF assay

| $T_m - T_{m,averaged}$ (°C) | Additive |
|---|---|
| 6.2 | Spermine tetrahydrochloride |
| 4.8 | GSH, GSSG |
| 4.7 | Choline acetate |
| 4.7 | Ammonium sulfate |
| 4.6 | Succinic acid pH 7.0 |
| 4.4 | Sodium malonate pH 7.0 |
| 4.4 | Sodium sulfate decahydrate |
| 4.3 | L-Arginine, L-Glutamic acid |
| 4.1 | 1-Ethyl-3-methylimidazolium acetate |
| 4.0 | Sodium chloride |

**Table 2-4:** Buffers from the Slice pH Screen (Hampton Research) giving the highest $T_m$ values in the Thermofluor assay

| $T_m - T_{m,averaged}$ (°C) | Additive |
|---|---|
| 4.6 | DL-malic acid pH 5.6 |
| 4.4 | Succinic acid pH 6.0 |
| 4.2 | DL-malic acid pH 5.3 |
| 4.0 | Succinic acid pH 5.7 |
| 3.5 | BIS-TRIS propane pH 7.3 |
| 3.4 | BIS-TRIS pH 6.6 |
| 3.3 | ADA pH 7.0 |
| 3.3 | HEPES sodium pH 6.6 |
| 3.2 | MES monohydrate pH 6.5 |
| 3.1 | Sodium cacodylate trihydrate pH 6.1 |

Since malonate is used as a cryo-protecting agent for protein crystals, 100mM malonate was added to the protein storage buffer. The agents with similar structures, such as DL-malic acid (ACROS Organics) and citric acid (ACROS Organics), were also used for wild-type RitR protein storage and crystallization.

According to the Slice pH screen results, the optimal pH is ~6 to 6.5. We chose pH 6.5, 25 mM Tris, 150 mM NaCl, 100 mM malonic acid/DL-malic acid/citric acid buffers to store wild-type RitR. RitR in these three buffers were crystallized. Crystals were obtained at all these buffers. But better crystals were obtained in DL-malic buffer, so the final RitR storage buffer I used is pH 6.5, 25 mM Tris, 150 mM NaCl, 100 mM DL-malic acid buffer.

### 2.3.2 Monomeric structure of $RitR_{C128S}$

Gel filtration chromatography suggests that inactive RitR is predominantly monomeric, but a second species, consistent in size with a dimer, is also present and accounts for ~10-20% of the sample. Likely because of this heterogeneity, the full-length, wild-type RitR proved impossible to crystallize. To facilitate crystallization, the only cysteine residue (C128) was mutated to serine ($RitR_{C128S}$). This variant proved to be 100% monomeric as judged by gel filtration chromatography and native-PAGE.

The structure of $RitR_{C128S}$ was determined to 1.7 Å resolution by using phases derived from SeMet single-wavelength anomalous diffraction (Se-SAD)(Figure 2-1). It is a monomer, which is in agreement with biochemical data mentioned above. There are two monomers in the asymmetric unit. But these two monomers do not form a dimer, nor with

their symmetry mates. RitR$_{C128S}$ contains regulatory ALR domain and DNA binding domain (DBD). The only cysteine residue in RitR, C128, is located at the C-terminal end of the long α5 linker helix, which connects the ALR domain with the DBD. The ALR domain structure is same with the earlier solved RitR ALR domain only structure (PDB ID: 4LZL[3], Figure 1-10). DBD has the helix-turn-helix (HTH) motif, which is the simplest and most common motif in prokaryotes and eukaryotes[21]. This HTH motif contains two fixed angled helices connected by a small loop. The more C-terminal helix (colored in red in Figure 2-1) is the recognition helix that used for contacting with specific DNA major groove.

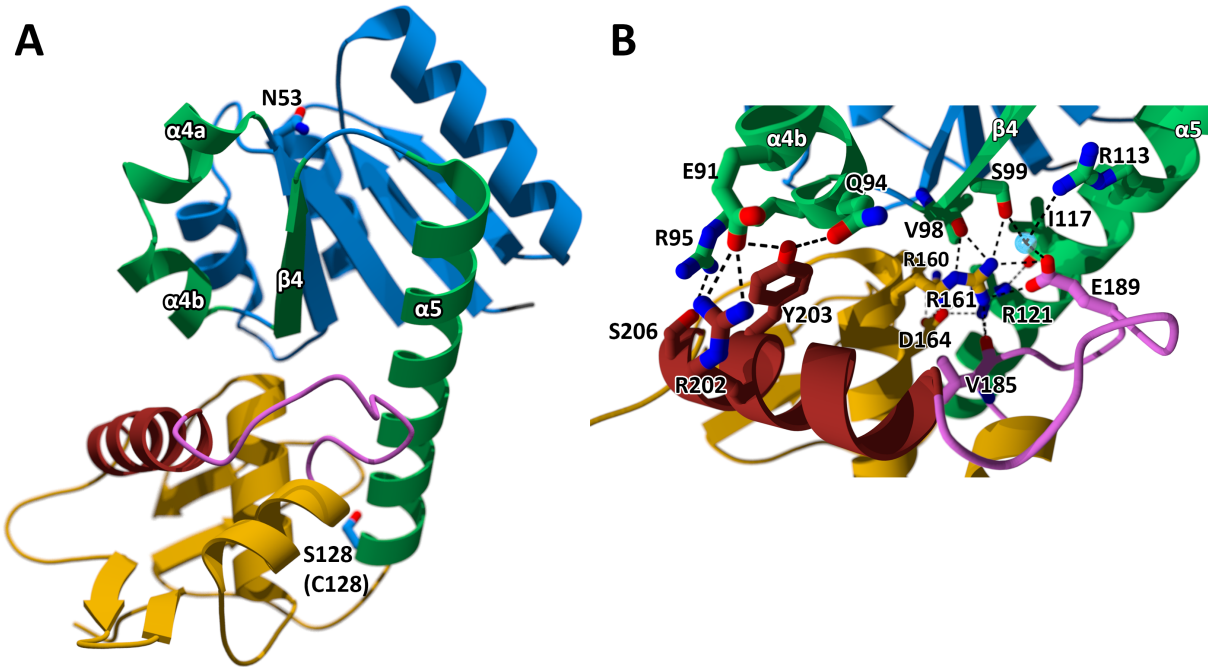


**Figure 2-1:** Ribbon representation of the structure of full-length RitR$_{C128S}$ (A) and a close-up on the inter-domain interface (B). Important amino acid side chains are shown as sticks. The regulatory domain is shown in blue, except for the putative α4-β5-α5 dimer interface, which is colored green. The DNA-binding domain is colored yellow, except for the DNA-contacting helix and trans-activation loop, which are colored red and magenta, respectively.

There is an extensive network of salt bridges and hydrogen bonds between the regulatory ALR domain and DBD, with each domain contributing a surface area of approximately ~850 Å$^2$ (Figure 2-1B). E91 makes salt bridges with R202 (3.1 Å). E91 and Q94 make hydrogen bonds to Tyr203 with distances of 2.0 Å and 2.2 Å, respectively). R95 interacts with S206 (2.5 Å), residues that are found on the DNA-contacting helix of the DBD, helix α4b, and helix α5 of the ALR domain. Both α4 and α5 are contributed to the dimerization interface in other OmpR/PhoB type response regulator proteins. The DNA-contacting helix interacts with helix α4b and is thus not free to interact with DNA. Additionally, the trans-activation loop is involved in the interdomain interface and would thus be unavailable to interact with RNA polymerase. All of these facts demonstrate that this monomeric conformation is not the active, DNA-binding conformation of RitR.

### 2.3.3 The thiol group of the conserved C128 residue has a perturbed pKa

We assumed that, like most DNA-binding RR proteins, the active DNA-binding form of RitR is a homodimer. Comparing the sequences of all RitR homologs in the *Streptococci* (Figure 2-2A) shows that this Cys residue is strictly conserved. This raises the possibility that RitR could be a redox-responsive response regulator protein. In other cysteine-based redox sensor proteins, the side chain thiol groups of the key cysteine residues have been found to have significantly depressed $pK_a$ values[22, 23]. In order to ascertain whether or not the C128 thiol group also has a perturbed $pK_a$, and could thus be expected to be redox active under physiological conditions, the $pK_a$ of C128 was determined using the DTNB assay. The rate of reaction of DTNB with thiol groups depends directly on the proportion of

thiols that are present as the thiolate anion. The reaction (Scheme 2-1) releases $TNB^-$, which readily deprotonates to give $TNB^{2-}$, a species that absorbs at 412 nm. By monitoring the rate of the DTNB reaction at different pH values, it is possible to derive an estimate of the $pK_a$ of the thiol group. Reactions containing 20 μM DTNB in a buffer system consisting of citric acid, HEPES, and bincine (50mM each) were initiated by the addition of 5 μM RitR, and the absorbance at 412 nm was monitored (Figure 2-2 B). Nonlinear fitting of these progress curves to Equation 1 gave estimates of the pH-dependent rate constant of the reaction, $k_{(pH)}$. These values were plotted as a function of pH, and then fit to Equation 2 (Figure 2-2C) to gives an estimate of the $pK_a$ of C128 of 7.2 ± 0.2. This is slightly decreased from the thiol $pK_a$ of cysteine in solution, which is generally quoted above 8.3. Different buffer systems were tested for this assay, giving a $pK_a$ range for C128 of 6.9-7.5. The perturbed $pK_a$ of C128 suggests that this residue is more reactive than a typical surface-exposed cysteine residue and thus may be part of a redox-sensing switch mechanism in RitR.

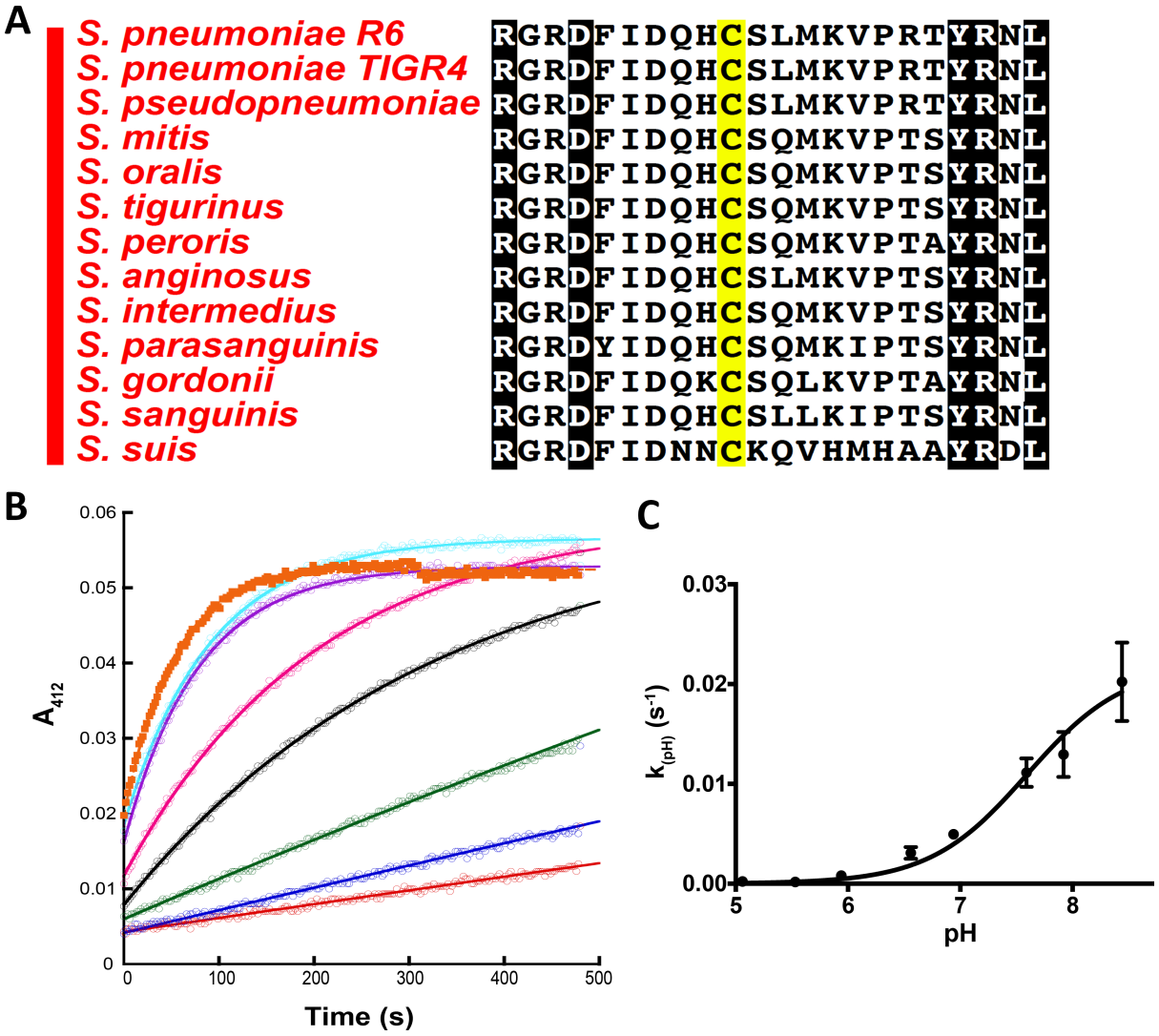


**Figure 2-2:** (A) Sequence alignment of RitR homolog in a non Group A/B subset of Streptococcal species demonstrated a conservation of redox sensor C128. (B) The absorbance at 412 nm (dots) and fitting lines at pH 5.1 (red), 5.5 (blue), 6.0 (green), 6.6 (black), 6.9 (magenta), 7.6 (cyan), 7.9 (purple) and 8.4 (orange). (C) The pH dependence of the rate constants of C128 with DTNB.The plot of rate constants ($k_{(pH)}$) vs pH gives the C128 pKa of 7.2 ± 0.2.

### 2.3.4 The structure of $RitR_{ox}$

RitR is a transcriptional regulator with a DNA-binding effector domain, which suggests that RitR probably functions as a homodimer, since oligomerization is an extremely common feature of DNA-binding proteins, and of response-regulators in particular. The depressed $pK_a$ of C128 suggested the possibility of a redox-based activation mechanism in RitR. Accordingly, the consequences of $H_2O_2$-mediated oxidation of RitR with respect to the oligomeric state and structure were investigated by size exclusion chromatography and X-ray crystallography.

Initial experiments showed that brief incubations of $H_2O_2$ with RitR failed to produce any change in the oligomeric state of the protein (Figure 2-3A). Using different buffers for the oxidation, such as citric acid, malic acid, or malonic acid, all at 50mM and pH 6.5, likewise did not alter the oligomeric state when RitR was treated with 1 mM $H_2O_2$ (Figure 2-3B). Extending the oxidation time to 19h did increase the proportion of dimer present, the maximum proportion of dimer (~90%) was only obtained when the SEC running buffer contained 1 mM $H_2O_2$. Once the optimal oxidation conditions were established, a preparative scale Sephacryl S-200 10/300 column was used to prepare samples of RitR dimer (*i.e.* $RitR_{ox}$) for crystallization. The dimer peak from the S-200 column was collected and stored in pH 6.5, 25 mM TRIS, 150 mM NaCl, 100 mM malic acid, and 1 mM $H_2O_2$. This material was concentrated to 10 mg/ml and subjected to screening for crystallization conditions.

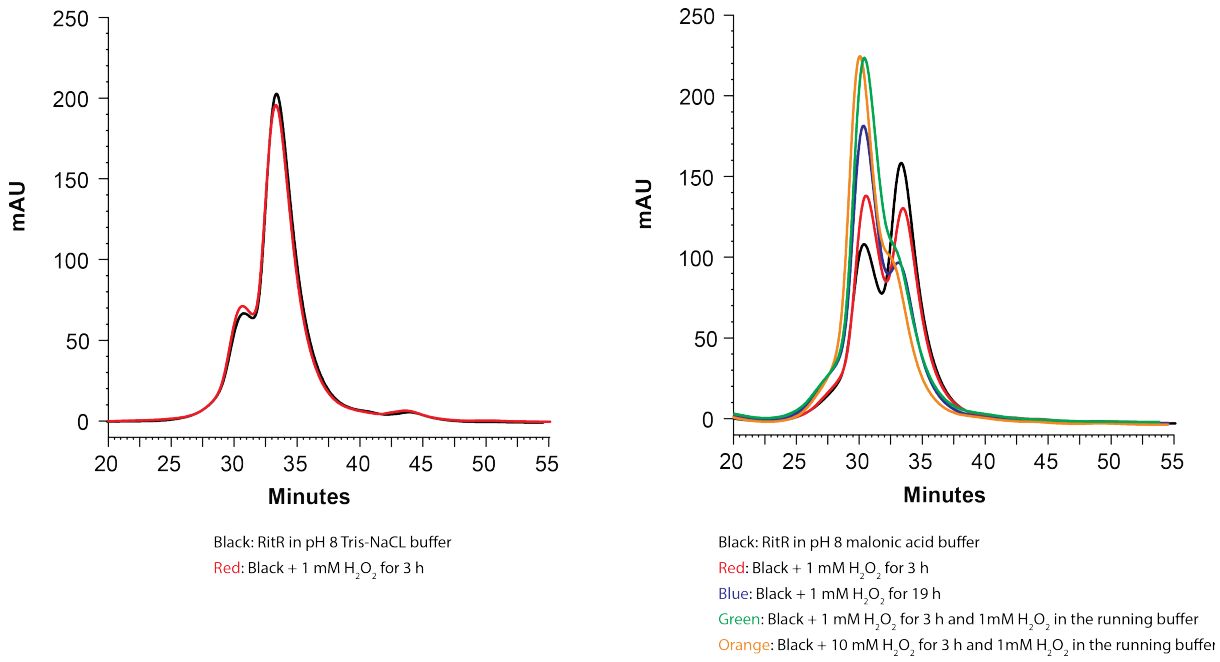


**Figure 2-3:** Different amounts of oxidized RitR dimer in different buffer conditions were determined by gel filtration on a Sephacryl S-200 10/300 column. (A) The gel filtration results of RitR in pH8, 25 mM Tris, 150 mM NaCl buffer. Black line represents no $H_2O_2$ treatment, while red line represents 1 mM $H_2O_2$ treatment. (B) The gel filtration results of RitR in pH 8, 25 mM Tris, 150 mM NaCl, 100 mM malonic acid buffer with different $H_2O_2$ treatment conditions. Black line represents no $H_2O_2$ treatment. Red line represents RitR was treated with 1 mM $H_2O_2$ for 3 h. Blue line represents RitR was treated with 1 mM $H_2O_2$ for 19 h. Green represents RitR was treated with 1 mM $H_2O_2$ for 3 h and containing 1mM $H_2O_2$ in the running buffer. Orange represents RitR was treated with 10 mM $H_2O_2$ for 3 h and containing 1mM $H_2O_2$ in the running buffer. The maximum amounts of $RitR_{ox}$ were obtained with 1 mM $H_2O_2$ in the running buffer.

Diffraction-quality crystals of $RitR_{ox}$ were obtained from a hanging drop containing 2 µl of protein solution (6 mg/ml $RitR_{ox}$ in pH 6.5, 20 mM TRIS, 150 mM NaCl, 100 mM malic acid, 1 mM $H_2O_2$) and 1 µl of crystallization solution (10% (w/v) PEG 3350, 0.3 M magnesium sulfate. The structure was determined to 1.7 Å resolution by using $RitR_{C128S}$ as

the model. The structure of $RitR_{ox}$ shows that the tertiary structures of the individual domains do not change significantly. However, the two chains present in the asymmetric unit form a domain-swapped dimer (Figure 2-4A). Upon oxidation, the DNA-binding domain must be released from the REC domain. The structural change that triggers release of the DNA-binding domain may be a rearrangement of the C-terminal end of the long α5 linker helix, which appears to unwind upon oxidation of C128 (Figure 2-4B) to form an inter-chain disulfide bond. Since there is no DNA to bind, and the restricted conformation imposed by the inter-chain disulfide bond, the DNA-binding domain of one protomer interacts with the REC domain from the other protomer to almost perfectly recapitulate the inactive, monomeric structure (Figure 2-4D). Overlaying the REC domain of chain A together with the DBD of chain B onto the $RitR_{C128S}$ monomer gives a root-mean-square deviation for aligned Cα atoms of 0.7 Å. This inactive "cross-dimer" conformation may be an intermediate that forms before the oxidized dimer encounters its cognate DNA sequence, or it may indicate that oxidation of C128 is not the entire signal.

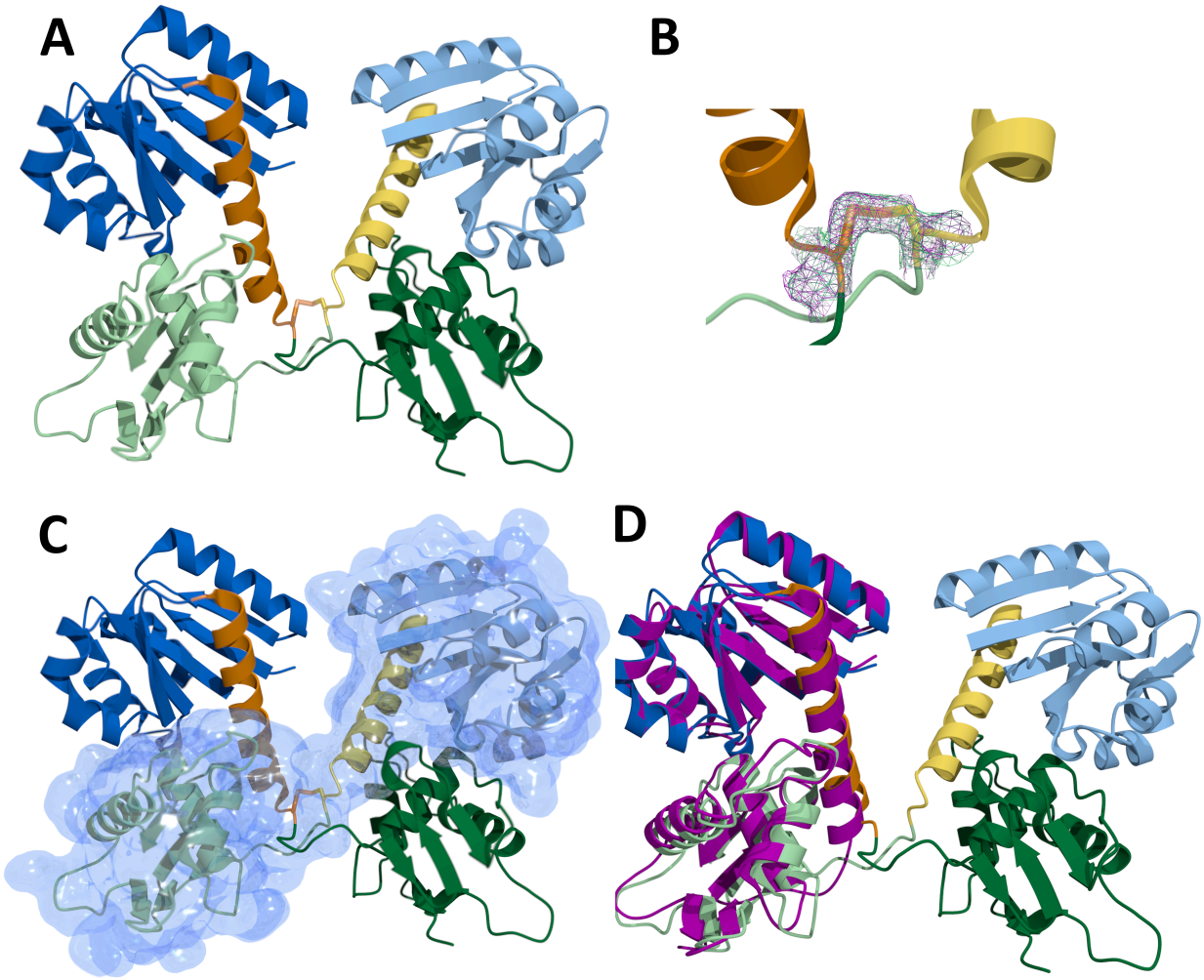


**Figure 2-4:** The structure of $RitR_{ox}$. (A) Ribbon representation of the $RitR_{ox}$ structure, Rec domain colored in blue (dark blue in chain A and light blue in chain B); α5 helix colored in orange (dark orange in chain A and light yellow in chain B); DNA binding domain colored in green (dark green in chain A and light green in chain B). (B) Close up view of disulfide bond. The $2|F_o|-|F_c|$ electron density map contoured at 1.0σ is shown as magenta mesh, and the $2|F_o|-|F_c|$ composite omit map, also contoured at 1.0σ is shown as green mesh. (C) RitRox structure with transparent blue surface in chain B. (D) Superimpose RitRox with inactive monomeric $RitR_{C128S}$ (purple). RMSD = 0.7 Å

### 2.3.5 RitR incubated with different metals

Because RitR is the repressor of iron transport, we hypothesized that iron or another divalent metal might be involved in the activation mechanism of RitR. To study the effect of metals on RitR dimerization, RitR was treated with $Fe^{III}Cl_3$, $Fe^{II}SO_4$, $MgCl_2$, $MnCl_2$, $CaCl_2$, $CuCl_2$, or $ZnCl_2$, all in pH 6.5, 20 mM TRIS, 150 mM NaCl, 100 mM malic acid buffer. Size exclusion chromatography was used to check the oligomeric state, and the results are shown in Figure 2-5.

**Figure 2-5:** Oligomer state of RitR after incubated with different metals. Blue line represents RitR only. Cyan line represents $RitR_{L86A/V93A}$ only. This mutant represented an extended dimer, which will be discussed below. Magenta line represents RitR with 1 mM metals. (A) RitR were incubated with $CuCl_2$. (B) RitR were incubated with $Fe^{III}Cl_3$ with DTT. (C) RitR were incubated with $Fe^{III}Cl_3$ (D) RitR were incubated with $Fe^{II}SO_4$ with 0.1 N HCl. (E) RitR were incubated with $MgCl_2$. (F) RitR were incubated with $ZnCl_2$. (G) RitR were incubated with $CaCl_2$. (H) RitR were incubated with $MnCl_2$.

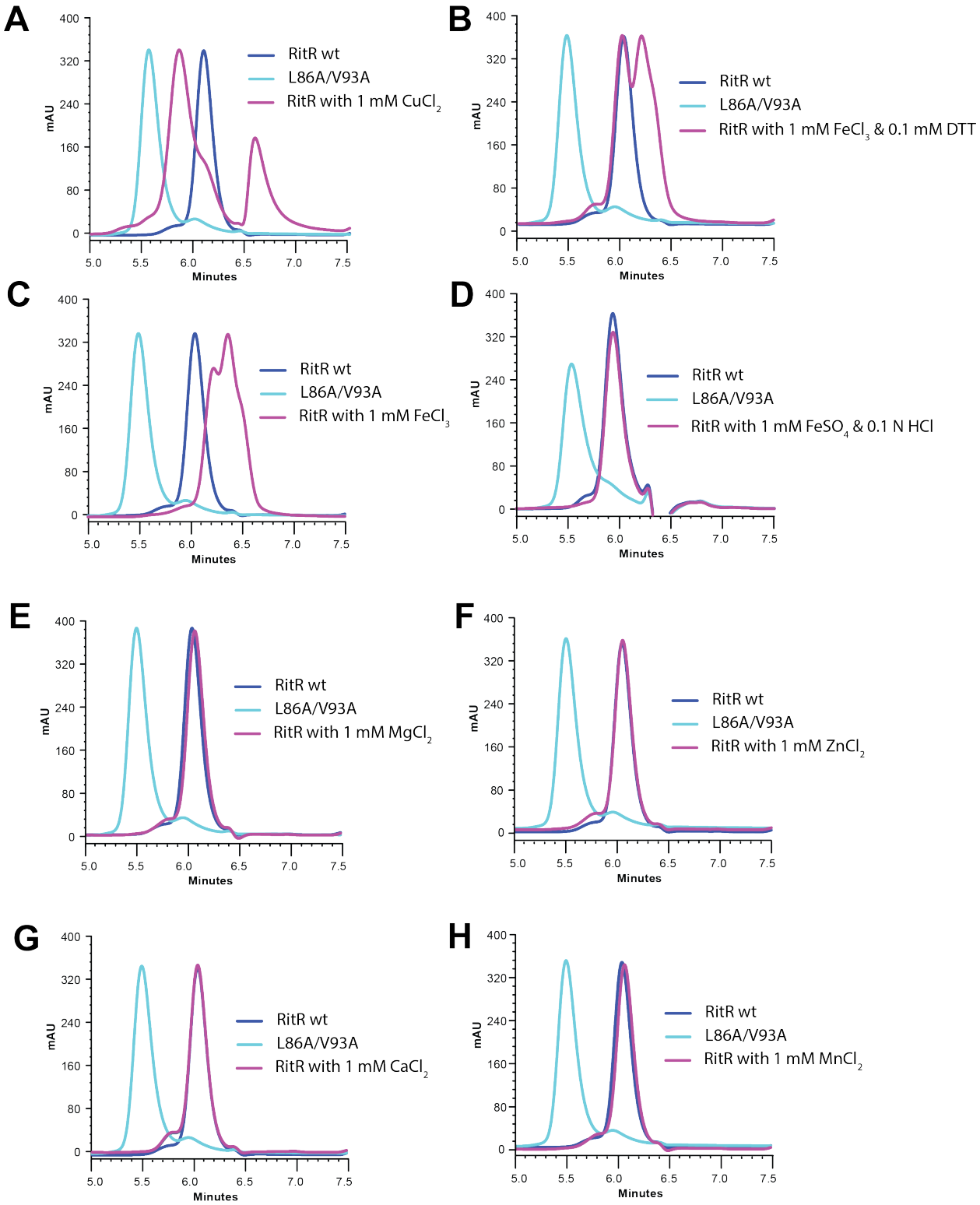
A
RitR wt
L86A/V93A
RitR with 1 mM CuCl2
B
RitR wt
L86A/V93A
RitR with 1 mM FeCl3 & 0.1 mM DTT
C
RitR wt
L86A/V93A
RitR with 1 mM FeCl3
D
RitR wt
L86A/V93A
RitR with 1 mM FeSO4 & 0.1 N HCl
E
RitR wt
L86A/V93A
RitR with 1 mM MgCl2
F
RitR wt
L86A/V93A
RitR with 1 mM ZnCl2
G
RitR wt
L86A/V93A
RitR with 1 mM CaCl2
H
RitR wt
L86A/V93A
RitR with 1 mM MnCl2
mAU
Minutes

SDS-PAGE, non-reducing-PAGE, and native SDS-PAGE were also used to check the oligomeric state after treatment with the various metals. The results of these experiments are shown in Figure 2-6.

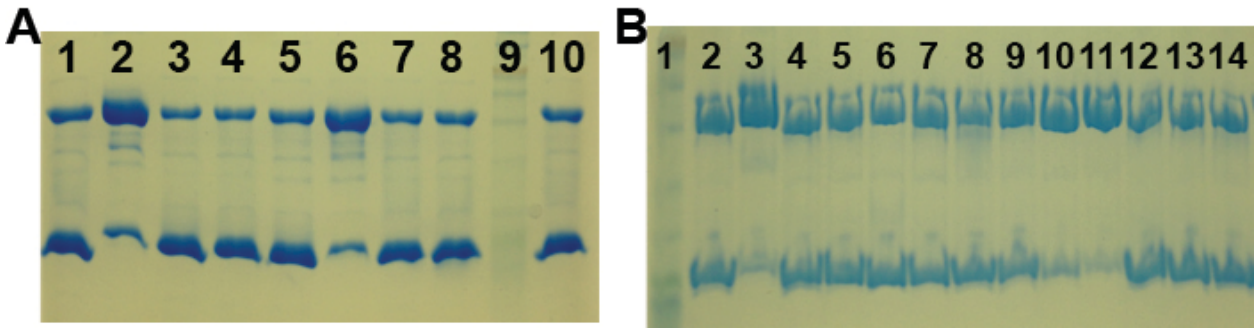


**Figure 2-6:** (A) Non-reducing-PAGE results of RitR treated with different metals. 1, wild-type RitR; 2, $RitR_{L86A/V93A}$; 3, RitR with 1 mM $Fe^{III}Cl_3$; 4, RitR with 10 mM $MgCl_2$; 5, RitR with 10 mM $MnCl_2$; 6, RitR with 1 mM $CuCl_2$; 7, RitR with 10 mM $CuCl_2$; 8, RitR with 1 mM $ZnCl_2$; 9, Marker; 10, RitR with 10 mM $ZnCl_2$. (B) Native SDS-PAGE results of RitR treated with different metals. 1, Marker; 2, wild-type RitR; 3, $RitR_{L86A/V93A}$; 4, RitR with 1 mM $Fe^{III}Cl_3$; 5, RitR with 10 mM $MgCl_2$; 6, RitR with 10 mM $MnCl_2$; 7, RitR with 1 mM $CaCl_2$; 8, RitR with 10 mM $ZnCl_2$; 9, RitR with 10 μM $CuCl_2$; 10, RitR with 100 μM $CuCl_2$; 11, RitR with 1 mM $CuCl_2$; 12, RitR with 10 μM $Fe^{III}Cl_3$ with 0.1 mM DTT; 13, RitR with 100 μM $Fe^{III}Cl_3$ with 0.1 mM DTT; 14, RitR with 1 mM $Fe^{III}Cl_3$ with 0.1 mM DTT. Top bands located around the 50 kD marker, corresponding to dimer, while the bottom bands located around the 25 kD marker, corresponding to monomer.

When the metal-treated samples of RitR were run on a non-reducing gel (Figure 2-6A) to preserve any disulfide bonds, wild-type RitR runs mainly as a monomer, while the double mutant $RitR_{L86A/V93A}$ runs mainly as a dimer. This constitutively dimeric double mutant will be discussed in detail below. Treatment of the wild-type RitR with $Fe^{3+}$, $Fe^{2+}$, $Mg^{2+}$, $Mn^{2+}$, $Zn^{2+}$, did not alter the dimer/monomer ratio. However, treatment with $Cu^{2+}$

promoted dimerization of RitR as judged from the non-denaturing SDS-PAGE gel. This result was confirmed by native SDS-PAGE (nSDS-PAGE). Increasing the $CuCl_2$ concentration increased the proportion of dimer obtained (lane 10 and lane 11 in Figure 2-6B). These results indicated that $Cu^{2+}$ induced the dimerization of RitR.

The structure of RitR dimer by $CuCl_2$ treatment (data not shown) is same with $RitR_{ox}$ by $H_2O_2$ treatment, because copper also can oxidize the cysteine residue to form disulfide bond [24-26]. So the structure of $RitR_{ox,CuCl_2}$ is also an inactive conformation.

### 2.3.6 Structural features important for RitR dimerization

The active, DNA-binding form of RitR is hypothesized to be a homodimer, which binds to specific sequences in the *piu* promotor and represses the expression of genes associated with iron uptake and up-regulates the expression of genes involved in the response to oxidative stress. We saw above that the DBD of the RitR dimer obtained by oxidation alone (*i.e.* in the absence of DNA) is characterized by a conformational change at the C-terminal end of α5 and a domain-swapping arrangement that matches almost perfectly with the inactive monomeric structure. There is virtually no contact between the ALR domains in this so-called "cross dimer." By analogy to other RR proteins whose active structures are known, we hypothesize that the ALR domains will dimerize in the active, DNA-binding state, likely through the same α4-β5-α5 interface that interacts with the DBD in the inactive structure. Again, by analogy to other RRs, there is likely to be a conformational change that makes formation of this ALR dimer more favorable in the activated state. To investigate

what residues are involved in the disruption of the ALR-DBD interface, and thus facilitate dimerization of the ALR domains, site-directed mutagenesis was employed. Specific point mutants were chosen based on the $RitR_{C128S}$ and $RitR_{ox}$ structures and are concentrated in regions of the structure known to be important in other RRs, or in regions that are particularly unusual in RitR. For example, residues in the active site that differentiate RitR from typical REC domains were investigated (K10D, N53D and N53A, D81A). Likewise, residues on the unusual α4 helix that were hypothesized to be part of a "hydrophobic gate" that could influence dimerization were also mutated (L86A, L90A, V93A, L86A/V93A, F96G). Residues on β5 that are involved in dimerization in other RRs were targeted (Y100 and Y102), since these residues make extensive interactions with the DBD in both structures. Finally, we tested the effects of mutating residues in the α5 linker helix that make key interactions in the ALR-DBD interface (R133A). C128 was targeted due to its central hypothesized role in redox-based sensing (C128A, C128S, C128D) and Y163 was mutated to Phe to break the water-mediated interaction with C128. The locations of the mutagenesis sites are shown in Figure 2-7, and the rationale for each is given in Table 2-5.

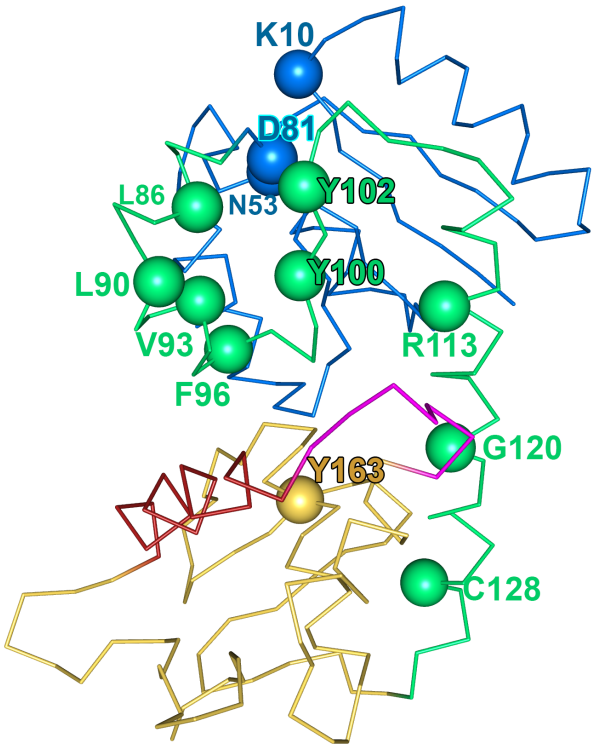


**Figure 2-7:** Cα trace of full-length RitR$_{C128S}$ structure with the sites chosen for mutagenesis marked as colored spheres. The ALR domain is colored blue, except for the α4-β5-α5 face, which is colored green. The DBD is colored pale yellow, except for the DND-contacting helix (red) and the trans-activation loop (magenta).

**Table 2-5:** Summary of the rationale of each mutation

| Mutation Site | Reason for mutation |
|---|---|
| K10 | Basic residue in the putative phosphorylation site, usually acidic residue in typical RRs. |
| N53 | Phosphorylatable site |
| D81 | Switch residue |
| Y100 | Switch residue |
| F96 | Hydrophobic core and impede the Y100 reorientation for dimerization |
| Y102 | Point outward and affect the dimer interface formation |
| R113 | Interact with Y100 and impede the Y100 reorientation for dimerization |
| C128 | Redox sensing |
| Y163 | Interact with S128(C) through a water |
| L86 | Hydrophobic core and impede the Y100 reorientation for dimerization |
| L90 | Hydrophobic core and impede the Y100 reorientation for dimerization |
| V93 | Hydrophobic core and impede the Y100 reorientation for dimerization |

The oligomeric state of each of the mutants was assessed by size exclusion chromatography in the hope of finding at least one variant that was dimeric even in the fully reduced state. Accordingly, each mutant was analyzed on the BioBasic SEC-300 column in the presence or absence of dithiothreitol (DTT). Wild-type RitR mainly exists as monomer, with a small portion of dimer (green trace in Figure 2-8A), which disappears when DTT is added (red trace). According to the sequence alignment in Figure 1-3, one of the acidic triad residues of typical response regulators is replaced with a basic residue, lysine, in RitR (K10; Figure 2-8B). The side chain of K10 disrupts both the acidic environment and the cleft for $Mg^{2+}$ binding. The mutant K10D, which partially reconstitutes the $Mg^{2+}$-binding site, like the wild-type protein, exists mainly as monomer (Figure 2-8C). Interestingly, changing N53, which in typical RRs is the phosphorylatable aspartic acid residue, leads to a shift in the oligomeric state in the N53A variant (Figure 2-8D). This protein has a greater proportion of dimer than the wild-type, but monomer is still the major species. Changing N53 back to Asp (N53D) leads to an unstable and likely mostly unfolded protein (Figure 2-8E).

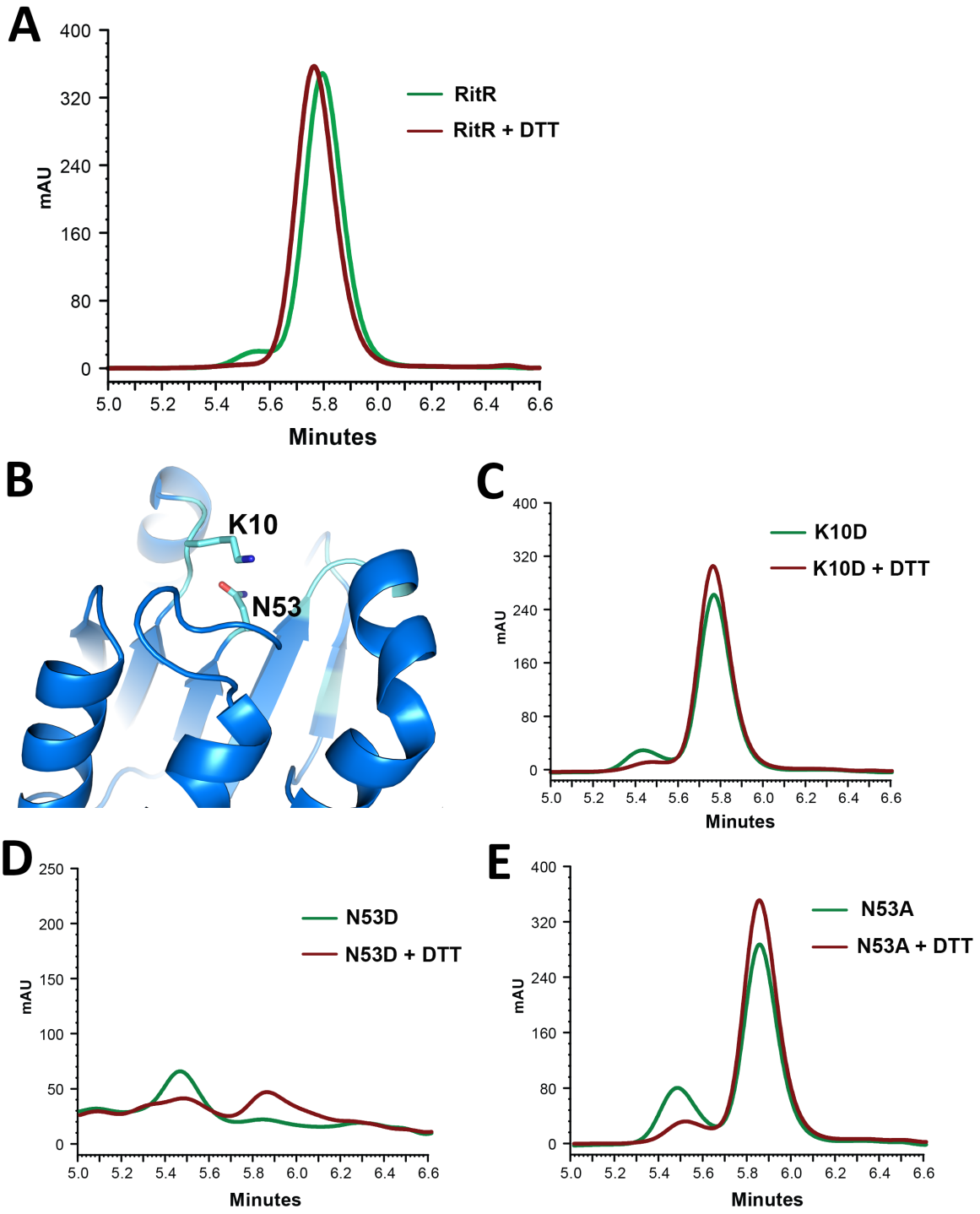


**Figure 2-8:** Oligomer states of wild-type RitR (A), $RitR_{K10D}$ (C), $RitR_{N53D}$ (D) and $RitR_{N53A}$ (E) without any treatment (green) or with 10 mM DTT treatment (red). (B) The putative active site of RitR. K10 and N53 are shown in stick.

In RitR, the residue that is equivalent to the threonine of the Y/T switch found in typical RRs is D81. This residue is oriented toward N53 and is held there by interactions with a number of active site residues (Figure 2-9). Compared with the corresponding residue in atypical regulator ChxR (L72) and typical regulator PhoP (T79), D81 in RitR represents the active conformer (Figure 2-9). This conformation of D81 is reminiscent of the interaction between T83 and the phospho-Asp side chain in activated PhoB[27] (Figure 1-4). In the inactive state, L72 in ChxR and T79 in PhoP forms part of gate residues, but in RitR, D81 points toward the putative active site and leaves L86 replacing the corresponding position. Some other atypical RRs that have been studied, such as ChxR, have a leucine residue at this position. It also shifts away from the active site.

The hydroxyl group of tyrosine of inactive ChxR and PhoB point outward from the domain, which interrupts the dimer interface formation. In the structure of non-phosphorylated PhoP (Figure 2-9), even it forms a similar "active" dimer with the switch residue Y98 pointing outward, but this dimer was obtain at high crystallization concentration and the helix α4 exhibits very high flexibility, which suggests this high concentration induced dimer is not a stable dimer. The phosphorylation-induced dimerization of PhoP (PDB ID: 2PL1[5]) is stable with Y98 side chain pointing inward. So in RitR structure, Y/T switch is effectively "uncoupled", where Asp81 is in the active form but Tyr100 is in the inactive form.

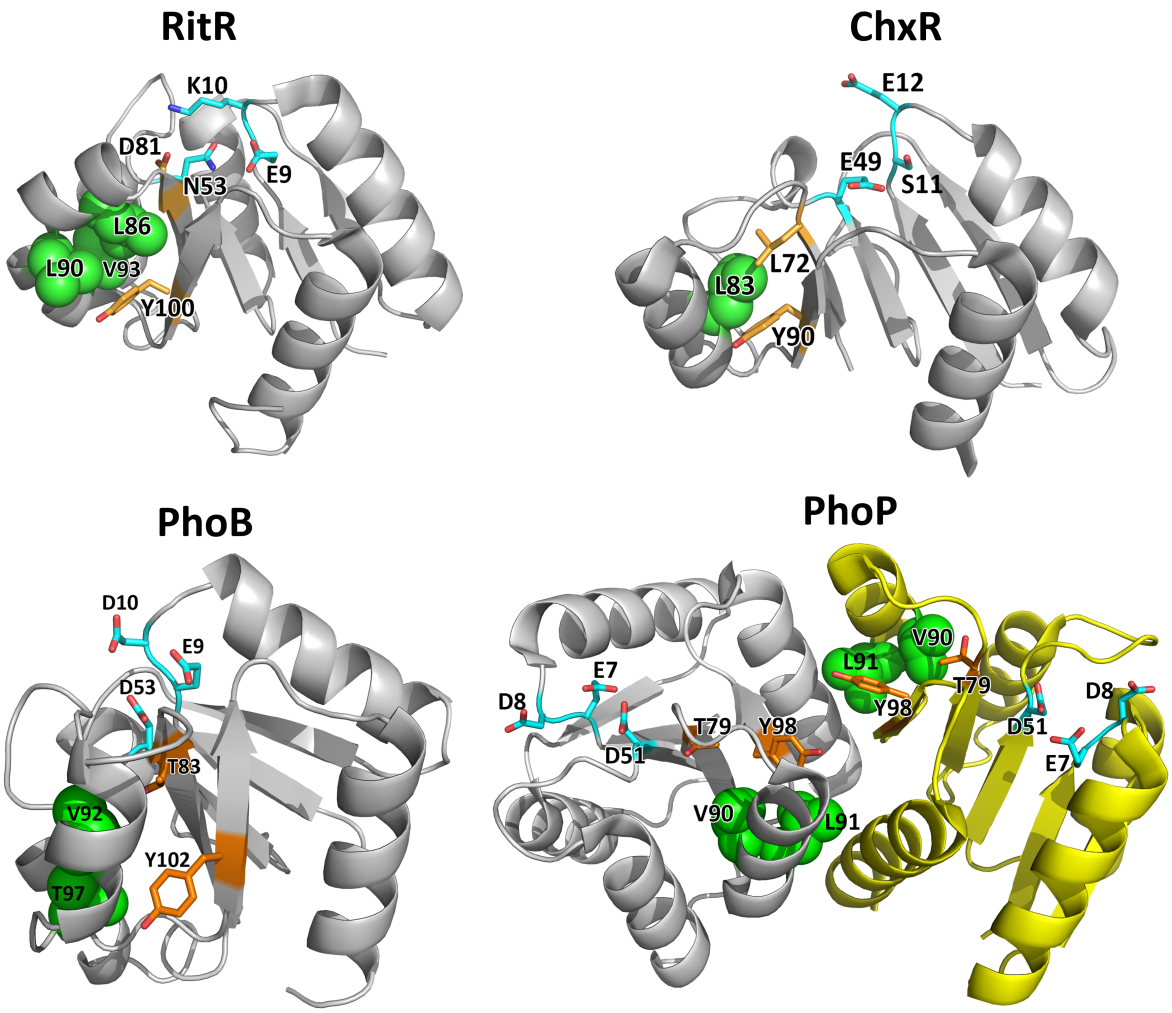


**Figure 2-9:** Comparison of gate regions of two ALR REC domains, RitR (PDB ID 4LZL[3]) and ChxR (PDB ID 3Q7T[4]), and the canonical REC domain of PhoB (PDB ID 1B00) and PhoP (PDB ID 2PKX[5]). These structures are all in an inactive state according to the positions of their Y/T switch residues. Even PhoP forms a dimer (Chain A colored in grey, chain B colored in yellow), but the dimer is a high protein concentration induced, unstable dimer. The activated dimer of PhoP is a more stable dimer with the switch residues shift inward. Gate residues are represented in green spheres, Y/T switch residues are shown as sticks with orange carbon atoms, and important catalytic residues are shown as sticks with cyan carbon atoms. Note that the Y/T switch residues L72 in ChxR, T83 in PhoB and T79 in PhoP form part of the gate, whereas D81 in RitR does not and is turned toward N53, resembling the active conformation of PhoB. In RitR, the switch residue side chain position is substituted by gate residue L86, which is strategically placed in front of tyrosine 100, allowed by the unusual formation of the kinked α4 helix in RitR.

In order to determine whether or not D81 and Y100 act similarly to the switch residues in other RR proteins, both residues were mutated (singly) to alanine and the effects on the oligomeric state assessed by SEC. Substitution of Y100 with Ala does not significantly increase the proportion of RitR in the dimeric conformation (Figure 2-10A). After treatment with DTT, there was no evidence of the dimer form of the Y100A variant. In contrast, the D81A variant exists as 65% dimer and 35% monomer (Figure 2-10B). After treatment with DTT, the proportion of dimer is less (~50%), but still represents a significant portion of the sample.

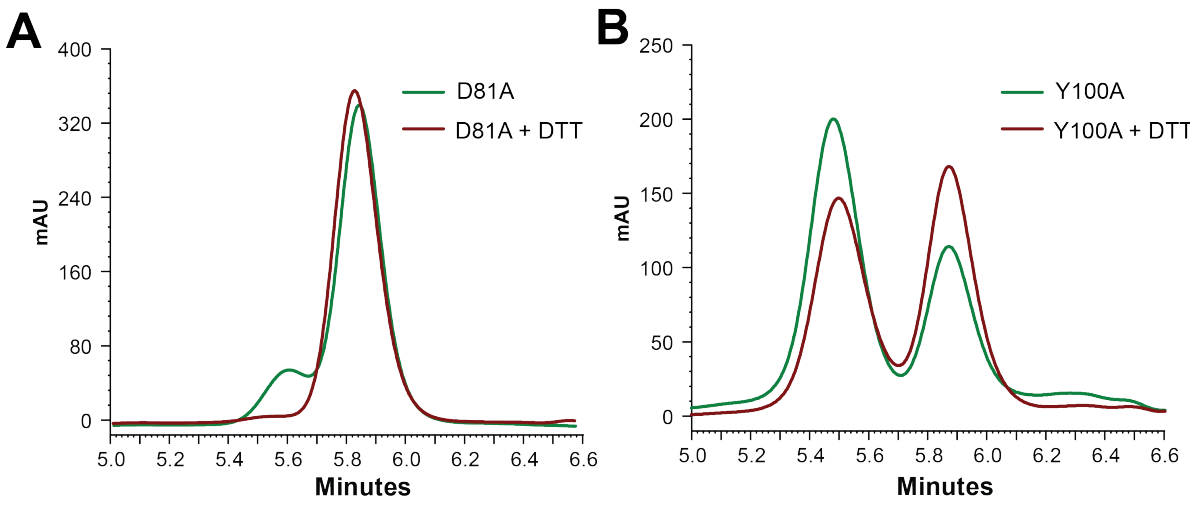


**Figure 2-10:** Results of SEC experiments on the Y100A (A) and D81A (B) variants. The green traces show the results in the absence of DTT treatment, and the red traces show the data after treatment with 10 mM DTT.

As shown in Figure 2-11, F96, which is located at the C-terminal end of helix α4b, is involved in the hydrophobic interactions within the hydrophobic core (β3, α3, β4). Substituting Gly for Phe at position 96 does increase the proportion of dimer compared to the wild type, but after DTT treatment, there was no dimer detectable. Also, the F96G

variant was not stable in solution.

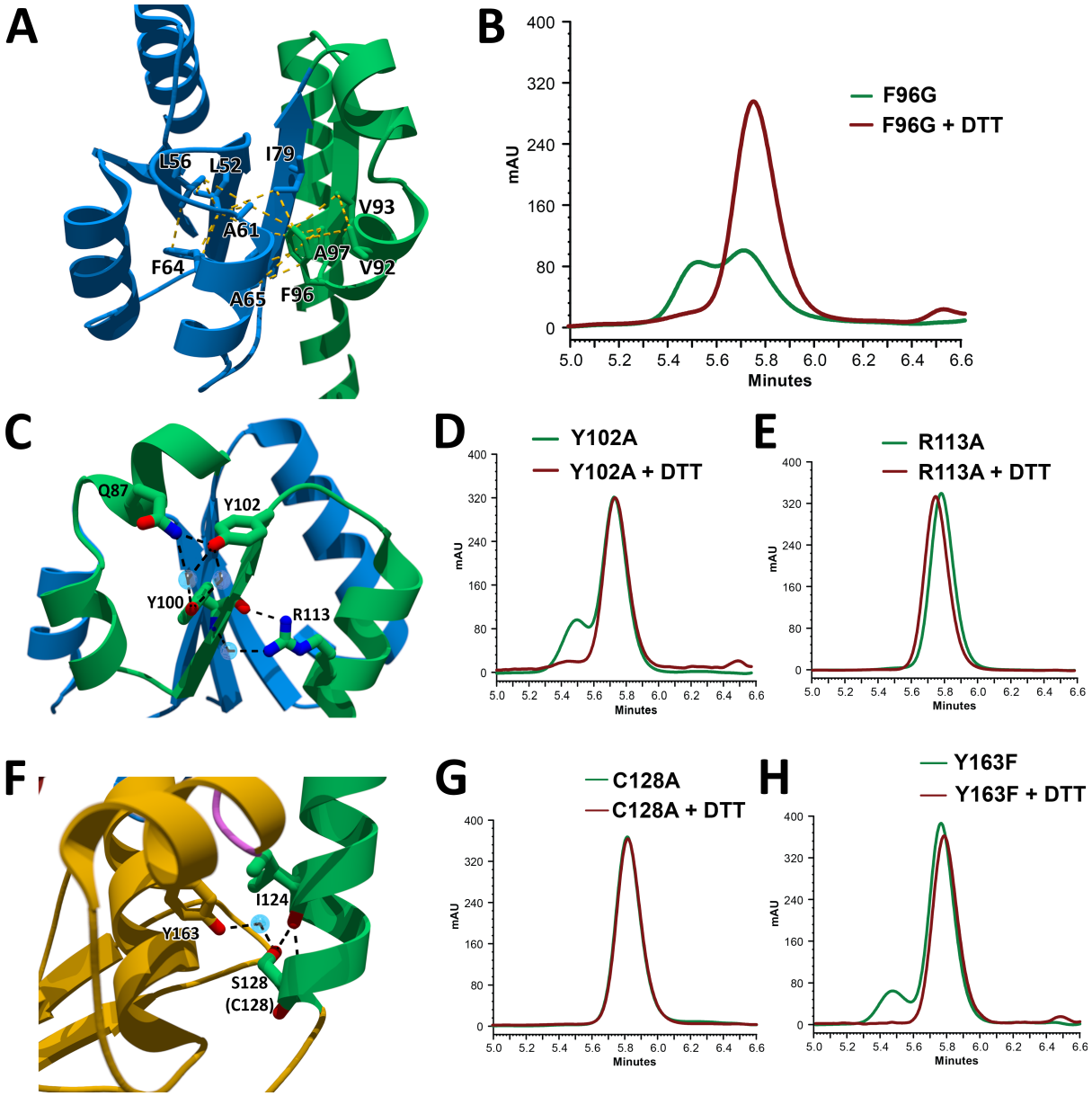


**Figure 2-11:** (A) F96 residue is involved in the hydrophobic interactions within hydrophobic core. (B) Oligomer states of RitR$_{F96G}$ (B), RitR$_{Y102A}$ (D), RitR$_{R113A}$ (E), RitR$_{C128A}$ (G) and RitR$_{Y163F}$ (H) with or without DTT treatment. Green represents no DTT treatment; brown red represents proteins were treated with 10 mM DTT. (C) Y102 and R113 both interact with the switch residue Y100 through water molecules. (F) Y163 interacts with serine in redox sensor C128 position through a water molecule.

Like Y100 discussed above, Y102 also points outward, away from the core of the ALR domain and projects out from the α4-β5-α5 face of the protein (Figure 2-11C), which may interfere with formation of the dimer interface. In addition, Y102 forms hydrogen bonds with Q87 and Y100 (through a water molecule), which likely impedes the reorientation of the Y100 side chain. When Y102 is mutated to Ala, there is little effect on the monomer-dimer equilibrium. The slight increase in the proportion of dimer becomes undetectable after treatment with 10 mM DTT by analytical SEC (Figure 2-11D). R113, which is located on the α5 linker helix, is also involved in interactions with Y100 and also makes a key interaction with the DBD in the inactive structures. Substitution of R113 with Ala results in a protein that is purely monomeric, whether or not it is treated with DTT (Figure 2-11E).

As expected, the C128 mutants (C128A) are purely monomeric (Figure 2-11G). The hydroxyl group of Y163 forms a water-mediated hydrogen bonding interaction with the hydroxyl group of S128 in the C128S variant (Figure 2-11F). This interaction could potentially be involved in the $pK_a$ perturbation of C128. To test this idea, Y163 was mutated to Phe to remove the hydroxyl group. This change has very little effect on the monomer-dimer equilibrium. There is a slight increase in the proportion of dimer compared to the wild-type (Figure 2-11H), and treatment with DTT pushes the protein fully toward the monomeric form.

One feature of the RitR ALR domain that distinguishes it from typical OmpR/PhoB-type RRs is the kinked α4 helix. Helix α4 is broken in two, with an approximately $100^{o}$ angle between the helical axes of the two pieces (α4a and α4b). No REC domain has been shown to have a similar conformation of helix α4. Three hydrophobic residues located in α4a

(L86), the short stretch of helix between α4a and α4b (L90), and in α4b (V93), pack against the central β sheet and make van der Waals interactions with V54 (Lβ3α3), I79 (β4), A97 (Lα4β5), Y100 (β5) and Y102 (β5) to form the hydrophobic core of this part of the protein (Figure 2-12A). This solidly packed core would seem to be a mechanical barrier impeding the reorientation of Tyr100 as seen in the structures of activated REC domains: a sort of "hydrophobic gate." If reorientation of Y100 is required for RitR dimerization as seen in other RRs, and if the hydrophobic gate residues do influence the conformation of Y100, then mutating these residues should have an impact on dimerization.

To test this idea, a series of mutants was constructed, including L86A, L90A, and V93A. The oligomeric state of each mutant was analyzed by size exclusion chromatography. The mutant L90A exists as a roughly equal mixture of monomer and dimer, and treatment with DTT shifts the equilibrium toward the monomeric form (~30% dimer; Figure 2-12B). Interestingly, $RitR_{L86A}$ and $RitR_{V93A}$ both exist as predominantly dimer in solution, and the response of each of these mutants to DTT is quite different (Figure 2-121C, D). The $RitR_{L86A}$ variant is nearly insensitive to DTT, with only slightly more monomer present after treatment with 10mM of the reductant. On the other hand, the V93A variant shifted dramatically, becoming predominantly monomeric after DTT treatment. Since they had the greatest amount of dimer of any mutants tested, the $RitR_{L86A}$ and $RitR_{V93A}$ mutants were combined ($RitR_{L86A/V93A}$; Figure 2-12E). The double mutant was slightly more stable to DTT treatment than the $RitR_{L86A}$ variant. In all, Ala substitution on any of the three hydrophobic gate residues dramatically increases the proportion of RitR dimers. The $RitR_{L86A/V93A}$ double mutant was purified in large quantities for crystallographic structure determination.

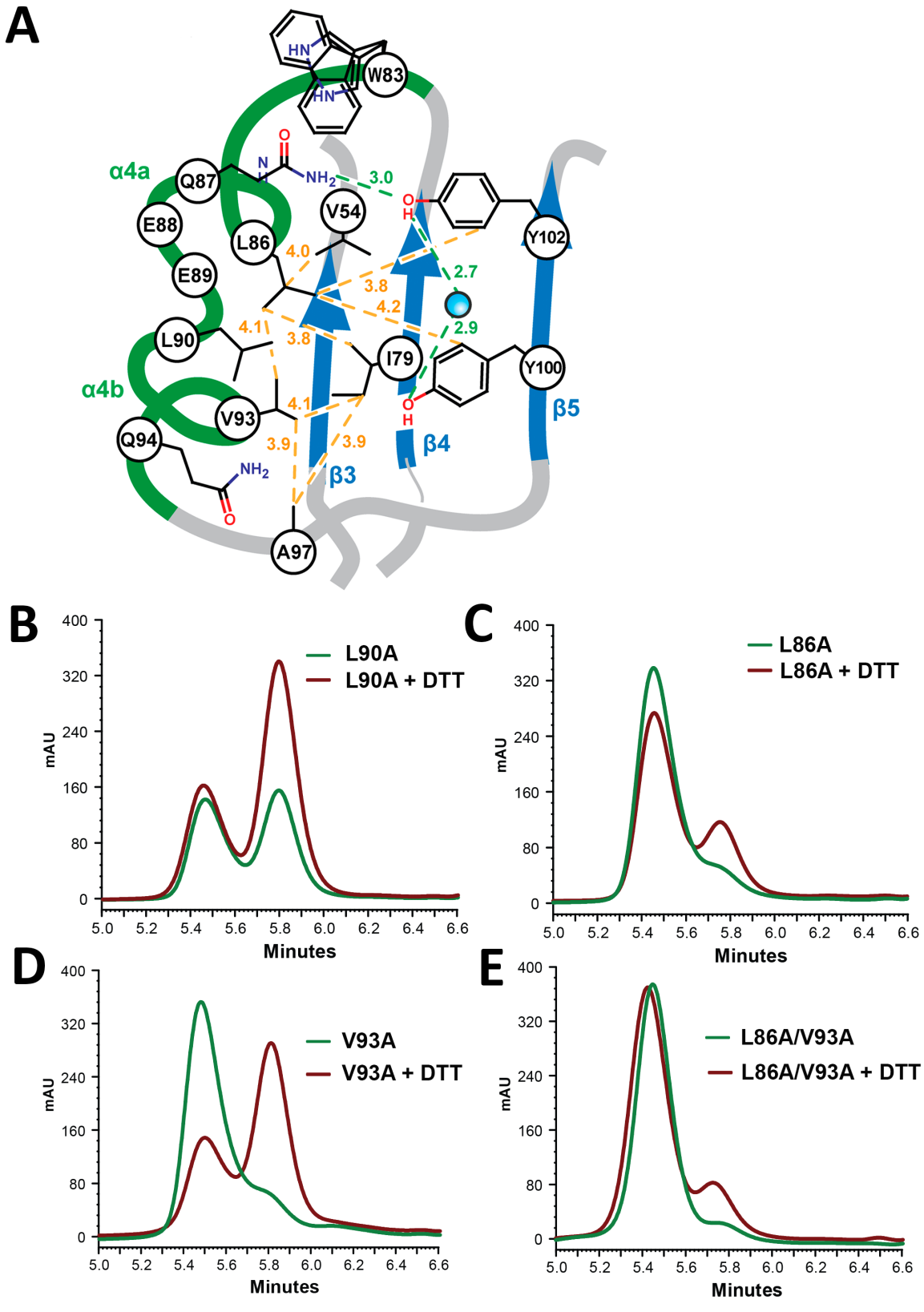


**Figure 2-12:** The effects of gate residues on RitR dimerization. (A) Schematic view of RitR gate residues van

der Waals interactions (yellow dotted lines) and hydrogen-bonding network (green dotted lines) in the dimer/gate region. Oligomer states of wild-type RitR, $RitR_{L90A}$ (B), $RitR_{L86A}$ (C), $RitR_{V93A}$ (D) and $RitR_{L86A/V93A}$ (E) without any treatment (green) or with 10 mM DTT treatment (red).

### 2.3.7 Mutations to the gate residues L86 and V93 result in an "extended" dimer

We were surprised to learn that the retention time of the $RitR_{L86A/V93A}$ dimer was significantly earlier (5.4 min) than that of the "cross dimer" conformation (5.6 min) observed for the wild-type protein oxidized with $H_2O_2$ (Figure 2-13). In addition, the tiny monomer peak of the $RitR_{L86A/V93A}$ variant eluted earlier than that of the wild-type RitR monomer. Both of these observations suggest that the conformation of $RitR_{L86A/V93A}$ is more extended, making it behave like a larger protein on the SEC column. This led us to believe that the inter-domain interactions between the $RitR_{L86A/V93A}$ ALR domain and the DNA-binding domain are disrupted. This is supported by the small difference in thermal stability between the double mutant and the wild-type protein measured by differential scanning fluorimetry. The average $T_m$ value (46.6°C) measured for $RitR_{L86A/V93A}$ is lower than that of wild-type RitR (52.2 °C), which suggests that $RitR_{L86A/V93A}$ is less stable than RitR. The D,L-malic acid buffer used for storage of the wild-type protein is still a good buffer to store $RitR_{L86A/V93A}$ (Table 2-6 and Table 2-7).

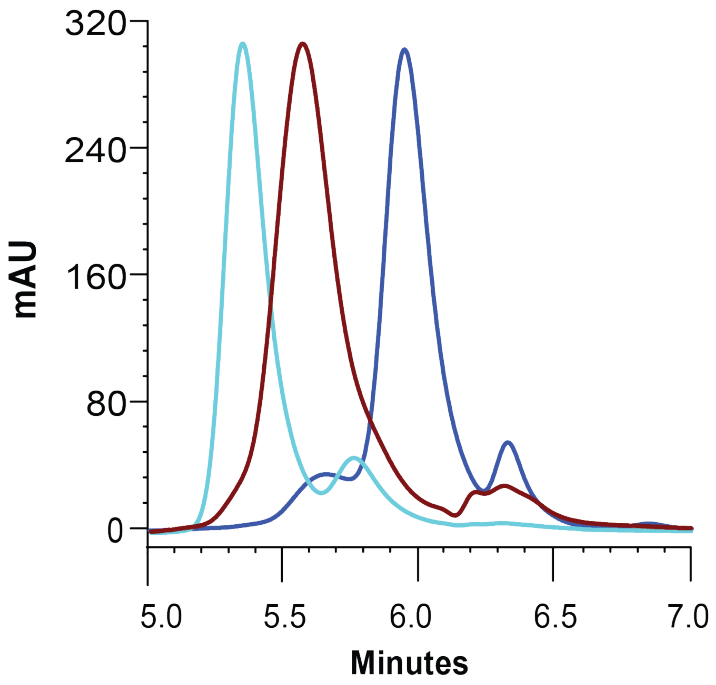


**Figure 2-13:** SEC retention times of wild-type RitR (as purified, colored in blue), wild-type treated with $H_2O_2$ ($RitR_{ox}$, colored in brown), and the $RitR_{L86A/V93A}$ variant (colored in cyan).

**Table 2-6:** Buffers from the Solubility & Stability Screen (Hampton Research) giving the highest $T_m$ values in the Thermofluor assay.

| N.O. | $T_m$ - $T_{m,averaged}$ (°C) | Buffer |
|---|---|---|
| 1 | 4.3 | Sodium phosphate monobasic, Potassium phosphate dibasic |
| 2 | 3.5 | Methyl α-D-glucopyranoside |
| 3 | 3.3 | Lithium citrate tribasic tetrahydrate |
| 4 | 3.2 | Sodium sulfate decahydrate |
| 5 | 3.1 | Sucrose |
| 6 | 2.9 | Succinic acid pH 7.0 |
| 7 | 2.7 | Spermine tetrahydrochloride |
| 8 | 2.6 | Sodium malonate pH 7.0 |
| 9 | 2.5 | DL-Malic acid pH 7.0 |

**Table 2-7:** Buffers from the lice pH Screen (Hampton Research) giving the highest $T_m$ values in the Thermofluor assay.

| N.O. | $T_m$ (°C) | Buffer |
|---|---|---|
| 1 | 3.0 | DL-malic acid pH 5.3 |
| 2 | 2.7 | DL-malic acid pH 5.9 |
| 3 | 2.7 | Succinic acid pH 6.0 |
| 4 | 2.5 | Succinic acid pH 5.7 |

### 2.3.8 Size exclusion chromatography of RitR : BS3 and $RitR_{L86A/V93A}$ : BS3

Since the two domains in the double mutant appeared to be dissociated from one another, while still allowing the protein to dimerize, it is possible that the $RitR_{L86A/V93A}$ mutant dimer conformation is the active conformation. To ascertain whether or not this variant is active, the DNA-binding ability of $RitR_{L86A/V93A}$ to bind to DNA was assessed by SEC. RitR is known to directly bind and repress *piu* transcription, and three binding sites (BS1-3) were identified by electrophoretic mobility shift assay (EMSA)[1]. Due to the much higher affinity of RitR for BS3, we concentrated on this target sequence. In this thesis, I tested the affinity of six lengths of BS3 for crystallization (Table 2-1). And BS3 is called BS3-1 in this thesis.

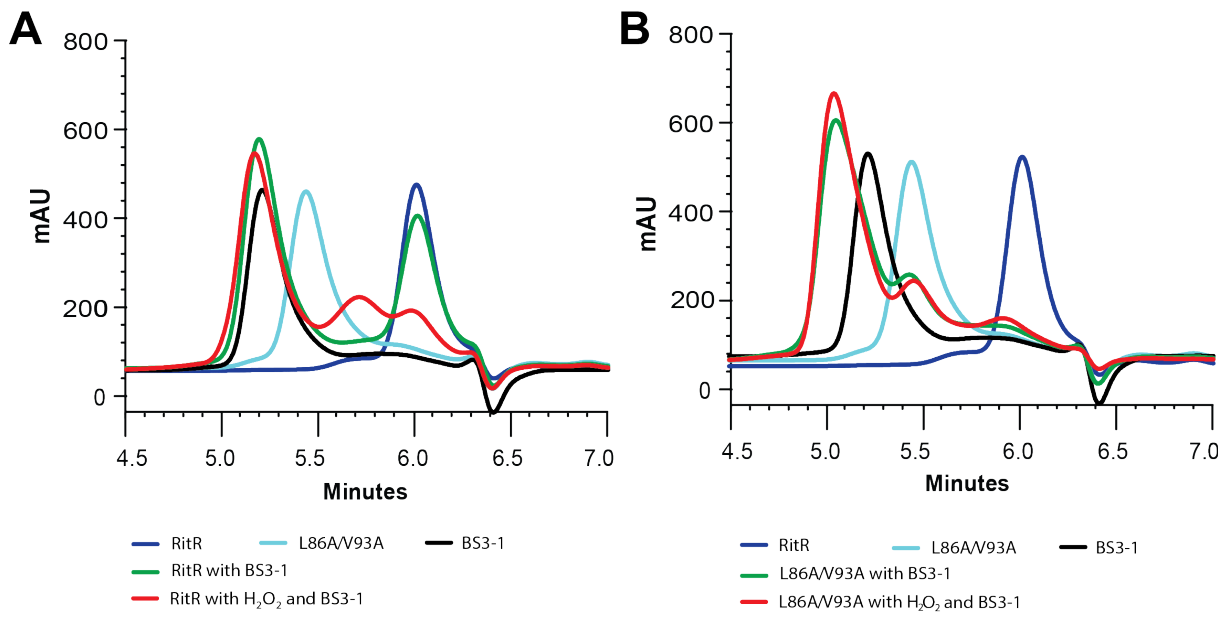


**Figure 2-14:** Size exclusion chromatography results for RitR with and without the BS3-1 dsDNA oligonucleotide (A) and $RitR_{L86A/V93A}$ with and without BS3-1 (B). In both panels, the traces for the wild-type RitR protein alone are blue, the $RitR_{L86A/V93A}$ protein alone cyan, BS3-1 alone black, RitR or $RitR_{L86A/V93A}$ with BS3-1 without $H_2O_2$ green, and with 1 mM $H_2O_2$ red. For the mixture of RitR or $RitR_{ox}$ with BS3-1, dsDNA BS3-1 and proteins were eluted separately. For the mixture of $RitR_{L86A/V93A}$ with BS3-1, the $RitR_{L86A/V93A}$:BS3-1 complex was eluted, as indicated by the earlier elution time when compared to the BS3-1-only and protein-only peaks.

As shown above, and in Figure 2-14A above, RitR exists mainly as a monomer in the absence of any oxidant. Incubating the wild-type protein with the BS3-1 olignucleotide did not result in formation of a stable RitR:BS3-1 complex. Oxidation of RitR with 1 mM $H_2O_2$ for several hours prior to the addition of BS3-1 DNA, resulted in about 60% RitR forming the "cross dimer" $RitR_{ox}$ conformation. There is no peak corresponding to the $RitR_{ox}$:BS3-1 complex. The $RitR_{L86A/V93A}$ variant, on the other hand, is present almost exclusively as the

extended dimer, and when DNA was added, the majority of the protein elutes as a complex with the BS3-1 oligonucletide (retention time ~5.1 min). Oxidation of $RitR_{L86A/V93A}$ with $H_2O_2$ did not significantly alter the oligomeric state of the double mutant or its ability to bind to the BS3-1 DNA. To verify the binding of $RitR_{L86A/V93A}$ to BS3-3 while the wildtype RitR protein does not, differential scanning fluorimetry was used. When the protein bound to BS3-3, the protein would get stabilized and resulted in a higher $T_m$ value. But if the protein cannot bind to the DNA, $T_m$ value would not be affected. In all three buffers I tried, $T_m$ of RitR value does not change significantly, while the $T_m$ value of mutant $RitR_{L86A/V93A}$ significantly increases (Figure 2-15). These results show that wild-type RitR in both its reduced and oxidized forms is not able to bind to the dsDNA oligonucleotide BS3-1. However, there is a complex peak formed for the sample $RitR_{L86A/V93A}$ with dsDNA BS3-1, while $RitR_{L86A/V93A}$ with its presumed altered conformation, is able to do so, whether or not it is treated with $H_2O_2$. This suggests that the L86A/V93A substitutions bypass the intiatory C128-mediated redox-sensing trigger, resulting in a constitutively active form of RitR.

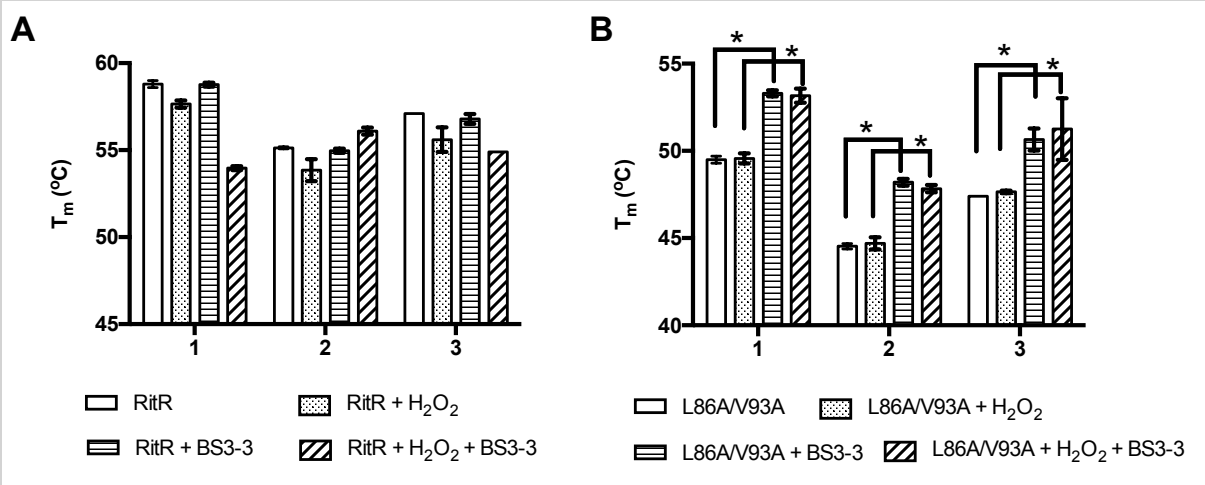


**Figure 2-15:** $T_m$ value change of (A) RitR, $RitR_{ox}$ and (B) $RitR_{L86A/V93A}$ after incubated with BS3-3 dsDNA. **1**: pH 6.5, 25 mM TRIS, 150 mM NaCl, 100 mM DL-malic acid; **2**: 20 mM HEPES pH 7.2, 5 mM $MgCl_2$, 1 mM $CaCl_2$, 0.1 mM EDTA; **3**: 20 mM HEPES pH 7.2, 5 mM $MgCl_2$, 1 mM $CaCl_2$, 0.1 mM EDTA, 150 mM NaCl. After incubated with BS3-3, RitR $T_m$ did not change significantly in three different buffers. Similar results were obtained for $RitR_{ox}$. But the mutant $RitR_{L86A/V93A}$ $T_m$ value increased significantly in all three buffers.

### 2.3.9 Single mutants in helix α4 also bind to BS3-1

The studies above verified that mutagenesis on both L86 and V93 that located in the kinked α4 helix bind to the target DNA BS3-1. To investigate the binding ability of three single mutants (L86A, L90A, V93A) in α4 helix, the oligomer states of these mutants with BS3-1 were determined by SEC. The results were shown in Figure 2-16. These three single mutants on α4 helix all bind to BS3-1, because a complex peak eluted earlier than BS3-1 only peak.

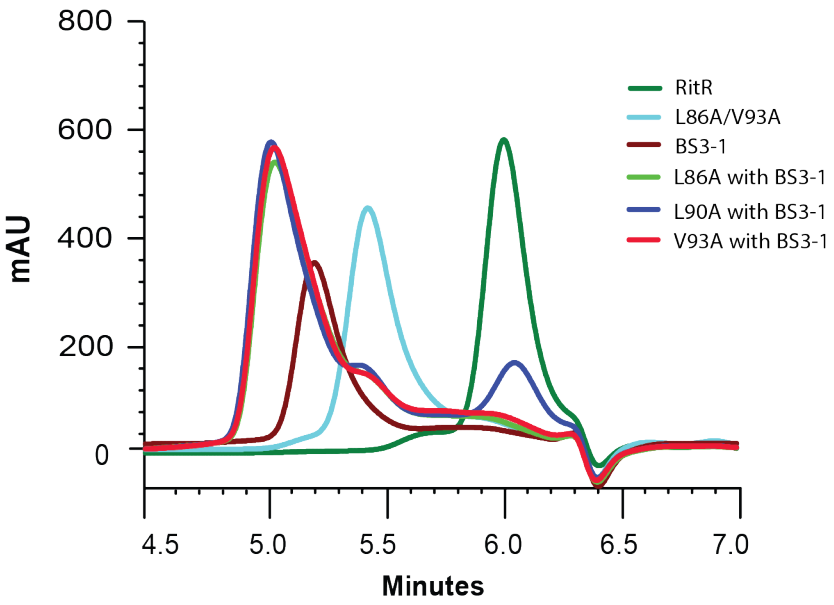


**Figure 2-16:** Gate residue variants bind to the dsDNA BS3-1 due to a complex peak eluted. In the panel, the traces for the wild-type RitR protein alone are green, the $RitR_{L86A/V93A}$ protein alone cyan, BS3-1 alone brown, $RitR_{L86A}$ with BS3-1 green, $RitR_{L90A}$ with BS3-1 blue and $RitR_{V93A}$ with BS3-1 red.

### 2.3.10 Crystallization of $RitR_{L86A/V93A}$

$RitR_{L86A/V93A}$ is almost entirely dimeric as observed by SEC, but there are detectable amounts of monomer. Since this heterogeneity would make the protein difficult to crystallize, the dimer form was purified by preparative SEC with the same protocol used to purify the $RitR_{ox}$ dimer (with the exception of the $H_2O_2$ treatment). The fractions containing the $RitR_{L86A/V93A}$ dimer were concentrated to 7.2, 10.1, or 34.0 mg/ml and used to set up sparse matrix screens for the identification of crystallization conditions (Index, PEG/Ion, SaltRx, and PEGRx from Hampton Research). These screens resulted in only clear drops, phase separation, or amorphous precipitate; no conditions resulted in crystalline protein.

Examination of the conditions that gave phase separation (super-concentrated protein) showed that the protein favors neutral pH (HEPES or BIS-TRIS at pH 6.5-7.5), PEG3350, and a variety of salts having monovalent cations (ammonium sulfate, lithium sulfate, sodium formate, sodium malonate). These conditions were optimized with different $RitR_{L86A/V93A}$ concentrations on both sitting drop and hanging drop methods at different temperatures (room temperature, 16 $^{o}$C, 22 $^{o}$C). Considering the protein crystallization diagram, increase the protein concentration (supersaturation) was necessary for nucleation. So the highest protein concentration I tried was 88 mg/mL. However, there was no crystal formed and only stronger phase separation was obtained. To get nucleation or crystals on those phase separation conditions, additive screen (Hampton) was also tried. There was no crystal formed either. I also tried to use some other protein crystals as microseeds (SbADC, $RitR_{ox}$, $RitR_{C128D}$) to crystallize the $RitR_{L86A/V93A}$ protein, but none succeeded.

Some proteins only crystallize with the cognate DNA, for example, AmrZ in *Pseudomonas aeruginosa*[28]. Based on the shorter retention time on size exclusion column, $RitR_{L86A/V93A}$ is assumed to be an extended dimer. Because it's so hard to crystallize $RitR_{L86A/V93A}$ protein, $RitR_{L86A/V93A}$ probably is the protein that only crystallizes with cognate DNA. Then I tried to co-crystallize $RitR_{L86A/V93A}$ with dsDNA.

### 2.3.11 Shorten BS3-1 length for crystallization

One variable of protein-DNA complex crystallization is the length of DNA. The general principle is "smallest functional". So different lengths of oligonucleotides were designed to provide blunt-ended dsDNA fragments. In addition, the ratio of protein to DNA is also important for successful crystallization. This ratio relates directly to the shape of the protein component, rather than the oligonucleotide, because the overall shape of the B-DNA is regular and cylindrical.

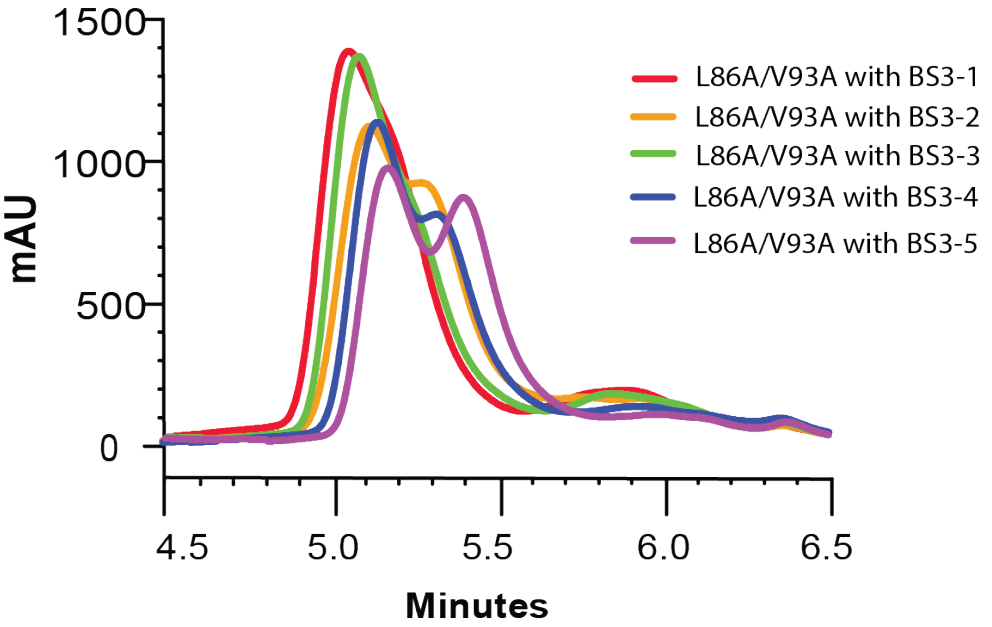


**Figure 2-17:** Complex peak area comparison of 216 µM $RitR_{L86A/V93A}$ with 100 µM of BS3-1 (38 bp, red), BS3-2 (34 bp, orange), BS3-3 (35 bp, green), BS3-4 (32 bp, blue) and BS3-5 (29 bp, purple).

To find out which blunt-ended dsDNA at what ratio to $RitR_{L86A/V93A}$ protein gives the most quantity of protein-DNA complex for crystallization, the complex peak area of

different ratios of $RitR_{L86A/V93A}$ to dsDNA (BS3-1 to BS3-5) was determined by SEC. $RitR_{L86A/V93A}$ protein (216 μM) was mixed with 100 μM of dsDNA (BS3-1 to BS3-5). The results were shown in Figure 2-17. Comparing the complex absorbance at 280 nm of $RitR_{L86A/V93A}$ with different lengths of DNA, BS3-3 with 35 bp nucleotides gives the most quantity of protein-DNA complex.

### 2.3.12 The ratio of $RitR_{L86A/V93A}$ : BS3-3 and $RitR_{L86A/V93A}$ : BS3-6

Based on the above results, BS3-3 gives the most quantity of protein-DNA complex, so BS3-3 was chosen to cocrystallize with $RitR_{L86A/V93A}$. Another shorter dsDNA (BS3-6, 24 bp) was also used in cocrystallization with $RitR_{L86A/V93A}$ protein. Because the dsDNA is limiting, to get the maximum protein-DNA complex, the "best" ratio of $RitR_{L86A/V93A}$ over BS3-3/BS3-6 was determined by comparing the absorbance of complex peak at different protein : DNA conditions. According to the gel filtration results shown in Figure 2-18, the absorbance of protein-DNA complex increases as the protein to DNA ratio increases. For $RitR_{L86A/V93A}$ with BS3-3 (Figure 2-18A), the maximum complex was obtained at the ratio of 4 : 1 with the excess protein. Increasing the ratio to 10:1 does not increase the protein-DNA complex peak absorbance. For $RitR_{L86A/V93A}$ with BS3-6 (Figure 2-18B), the BS3-6 DNA peak overlaps with the $RitR_{L86A/V93A}$ protein only peak. The binding affinity is lower than that of BS3-3, because even treated with 10 fold more protein, the complex absorbance still not get maximum. So the maximum ratio of 10 : 1 with the excess protein was used. The two conditions were used for incubating protein with DNA, and then the complex was separated on a HiPrep™ 26/60 Sephacryl® S100 HR column. Before making the

crystallization tray, extra BS3-3/BS3-6 DNA was added into the complex solution. But there is no crystal was obtained but salt crystals.

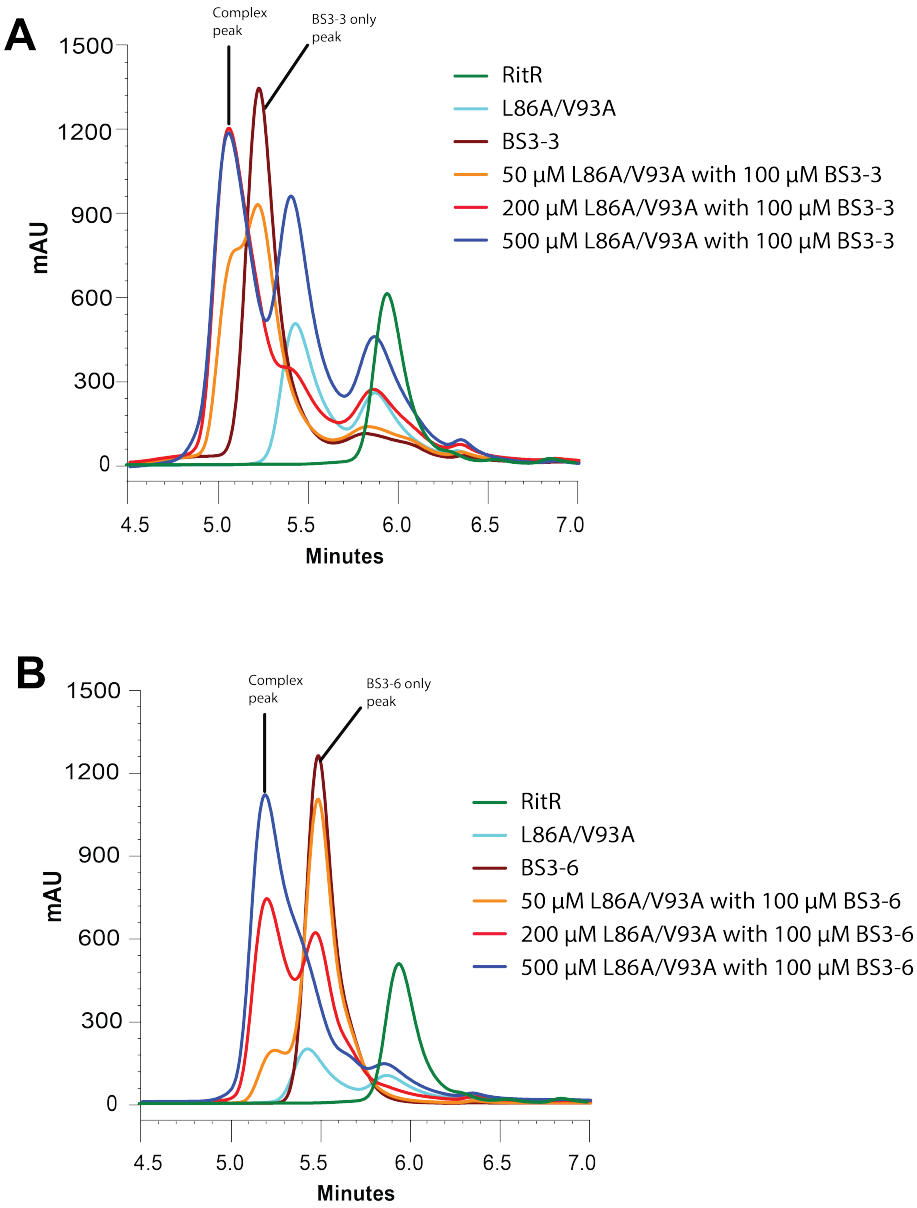


**Figure 2-18:** Gel filtration results of different ratios of $RitR_{L86A/V93A}$ : BS3-3 (A) and $RitR_{L86A/V93A}$ : BS3-6 (B). In both panels, the traces for the $RitR_{L86A/V93A}$ protein alone are dark green, the $RitR_{L86A/V93A}$ protein alone cyan, BS3-3 or BS3-6 alone brown, 100 µM BS3-3 or BS3-6 were incubated with 50 µM (orange), 200 µM (red) and 500 µM (blue) of $RitR_{L86A/V93A}$.

### 2.3.13 Structure of the $RitR_{L86A/V93A}$ REC domain

Likely owing to the higher degree of flexibility in the "extended dimer" of the $RitR_{L86A/V93A}$, we were not successful in obtaining diffraction-quality crystals of the full-length protein. Attempts to "lock down" the DNA-binding domains by co-crystallizing a number of BS3 variants with the double mutant. This was also unsuccessful. In order to determine whether or not the ALR domains of $RitR_{L86A/V93A}$ formed a stable dimer, an expression construct was prepared that included only residues 1-124 (RDLV; the same residues used in the original wild-type ALR domain structure). Diffraction-quality crystals were obtained from hanging drops containing 1 µl protein solution (4.4 mg/ml RDLV in 10 mM TRIS pH 8.5, 50 mM Succinic acid) and 1 µl crystallization solution (20% (w/v) PEG 3350, 0.2 M magnesium sulfate, 0.1 M TRIS pH 8.5), which diffracted to 1.8 Å resolution. The crystals belonged to space group $P222_1$ (a = 50.1 Å, b = 62.9 Å, and c = 80.3 Å) and contained 2 chains per asymmetric unit. We expected that the structure would be solved easily by molecular replacement, since the structure of the wild-type ALR domain was known. However, the molecular replacement calculation consistently failed, no matter which REC domain structure was used as the search model. SeMet-substituted RDLV was prepared, and it crystallized in the same condition used for the native protein, except 1 mM DTT was added to prevent heterogeneity due to oxidation of the SeMet residues. The data extended to 1.9 Å resolution and the anomalous signal from the 14 Se atoms provided excellent initial phase estimates that allowed Autobuild[29] to build an approximately 74% complete model. The two chains in the asymmetric unit form a dimer, which is consistent with the size exclusion chromatography results (data not shown). There are numerous hydrogen bonds between two chains, with an interface area of approximately 2,261 $Å^2$.

Shockingly, the topology of the $RitR_{L86A/V93A}$ ALR dimer is drastically altered from the $(\beta/\alpha)_5$ topology seen in all previous REC domain structures (Figure 2-19, Figure 2-10). There are two primary differences between the RDLV and all other REC domain structures. First, the kinked α4 helix rearranges to form an extension of strand β4 and a long loop leading into β5. Owing to the loss of α4, β5 is no longer parallel to β4. Thus the central sheet in the RDLV ALR domain is mixed rather than parallel as it is in the wild-type ALR. Second, "α5," which is technically the 4$^{th}$ α-helix in the structure, is no longer docked with β5 and the rest of the domain, but rather participates in a domain-swapping interaction with the other protomer of the dimer. The two protomers literally swap their "α5" helices, and other than coming from the opposite dimer, there is little difference in the positions of "α5" of the RDLV and α5 of the monomeric ALR with respect to the rest of the tertiary structure.

**Figure 2-19:** Ribbon representation of the RDLV structure (A) showing the arrangement of the secondary structure elements. Chain A of the RDLV dimer is colored dark blue and dark orange (the rearranged β4, β5 and α5); chain B is colored light blue.and yellow (the rearranged β4, β5 and α5). The Y100 residues of each chain (shown as sticks) stack with each other in the dimer interface. Note the loss of the α4 helix, which becomes part of β4 and a long loop leading into β5. This reverses the direction of strand β5 and results in a mixed β sheet structure, rather than the parallel sheet typical of REC domains. The "α5" helices are swapped between the two chains, but occupy a position in the structure very similar to that of α5 in the monomeric RitR REC domain. (B) The overlay of the RDLV structure (chain A, colored in dark blue) onto the wild-type RitR REC domain structure (colored in grey) highlights the extent of the structural rearrangements leading to this dimeric form of the ALR domain.

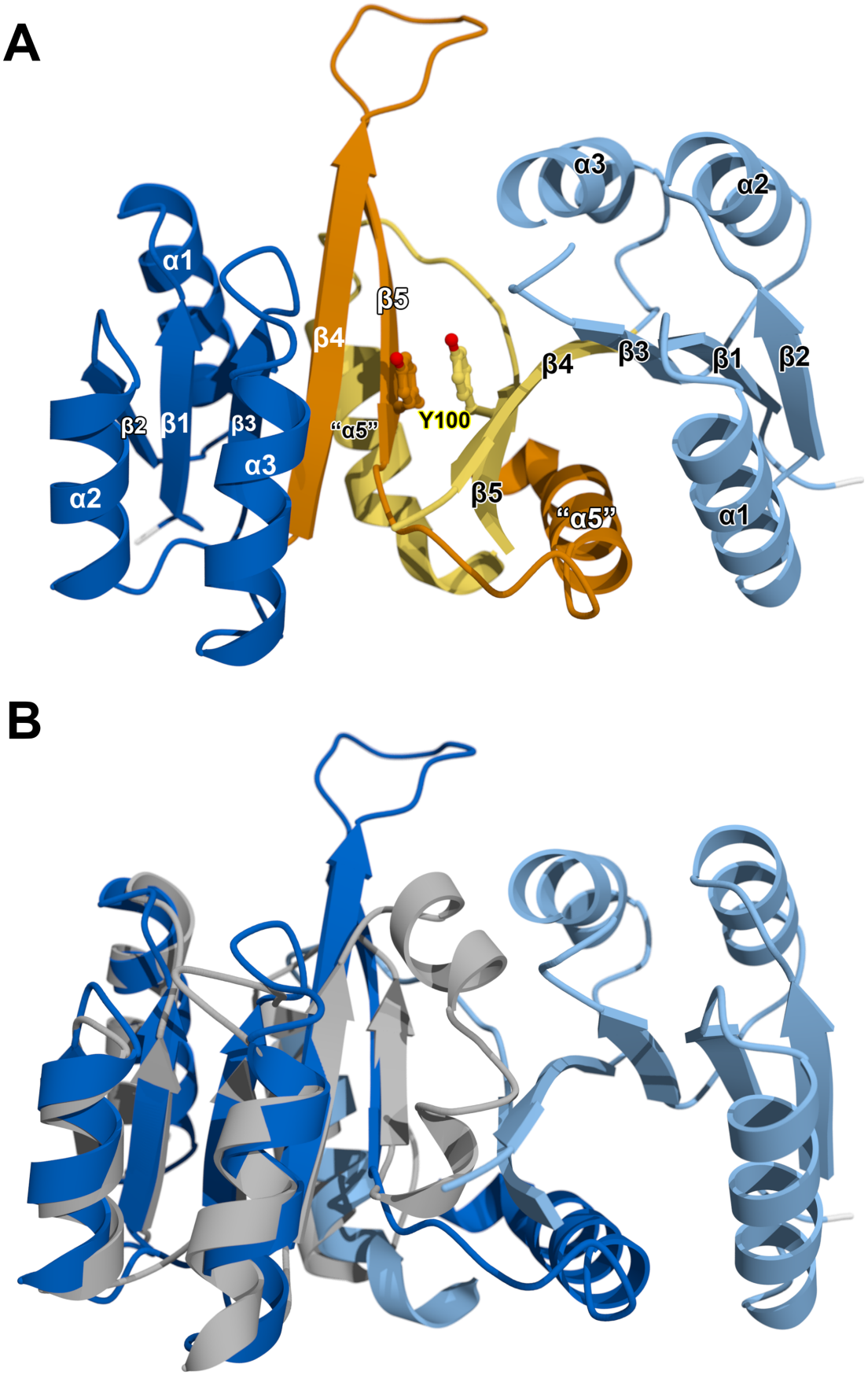
A
α1
β5
β4
β3
β1
β2
α3
α2
β2
β1
β3
α3
α2
"α5"
Y100
β4
β5
"α5"
α1
B

Of course, the pronounced changes in the topology of the RDLV REC domain lead to serious changes in the active site and switch residues (D81 and Y100; Figure 2-20). With the rearrangement of the hydrophobic core in the β4-α4 region of the protein, the side chains of N53 and N55, which point away from each other in the wild-type structure, both rotate ~180° to participate in a hydrogen bonding network that includes the amide nitrogen of V54. The side chain of the switch residue D81, which makes a hydrogen bonding interaction with the V54 amide nitrogen atom in the wild-type REC domain moves slightly in the RDLV REC domain so that it no longer interacts with V54. The other switch residue, Y100, also has an ~180° change in the orientation of its side chain, though in this case it is due to the "flipping" of the β5 strand rather than a simple rotation about the Cα-Cβ bond. In this orientation, the rings of Y100 from each protomer stack against one another at the heart of the dimer interface.

**Figure 2-20:** Comparison of the active site and switch residues in the wild-type RitR REC domain (A) and the RDLV variant (B). The wild-type REC domain is colored grey; RDLV dimer is colored in dark blue (chain A) and light blue (chain B). Because the kinked α4 helix forms the loop between β4 and β5 and changes the orientation of β5, the loop between β3 and α3 then moves due to the changed interactions. The N55 side chain flips and occupies the space occupied by K10 in the wild-type RitR REC domain.

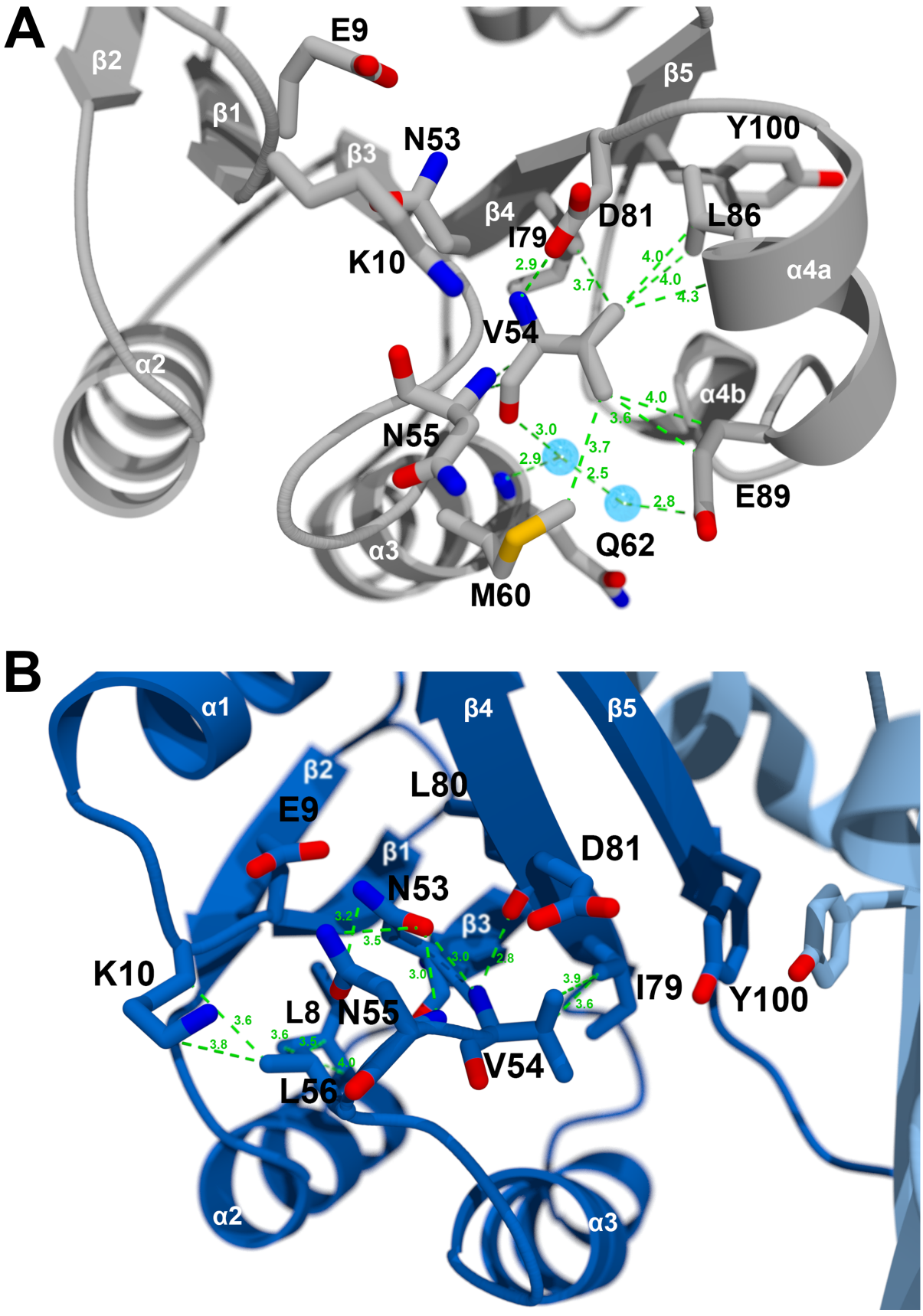
A
β2
β1
E9
β3
N53
β5
Y100
β4
D81
L86
I79
K10
α4a
V54
α2
α4b
N55
E89
α3
Q62
M60
B
α1
β4
β5
β2
L80
E9
β1
D81
N53
β3
K10
I79
Y100
L8
N55
V54
L56
α2
α3

### 2.3.14 Structure of the RD2LV REC domain construct

Because of the radical nature of the structural changes observed in the RDLV variant, we thought it important to confirm that the structure is not affected or induced by crystallization. To this end, we constructed a slightly longer form of the RDLV REC domain that includes the putative redox-sensing C128. This longer construct was dubbed RD2LV. SeMet-substituted protein was produced and diffraction-quality crystals were obtained from Hanging drops containing 1 µl of protein solution (19 mg/ml RD2LV in 10 mM glycine pH 8.8, 25 mM L-Arg) and 1 µl of crystallization solution (22.5% (w/v) polyethylene glycol (PEG) 3350, 12% Tacsimate pH 8.2).. These crystals diffracted to 2.6 Å resolution. They belonged to space group $P2_12_12$ with a = 115.3 Å, b = 125.4 Å, and c = 40.2 Å. The asymmetric unit contained four molecules arranged as two homodimers (Figure 2-21B).

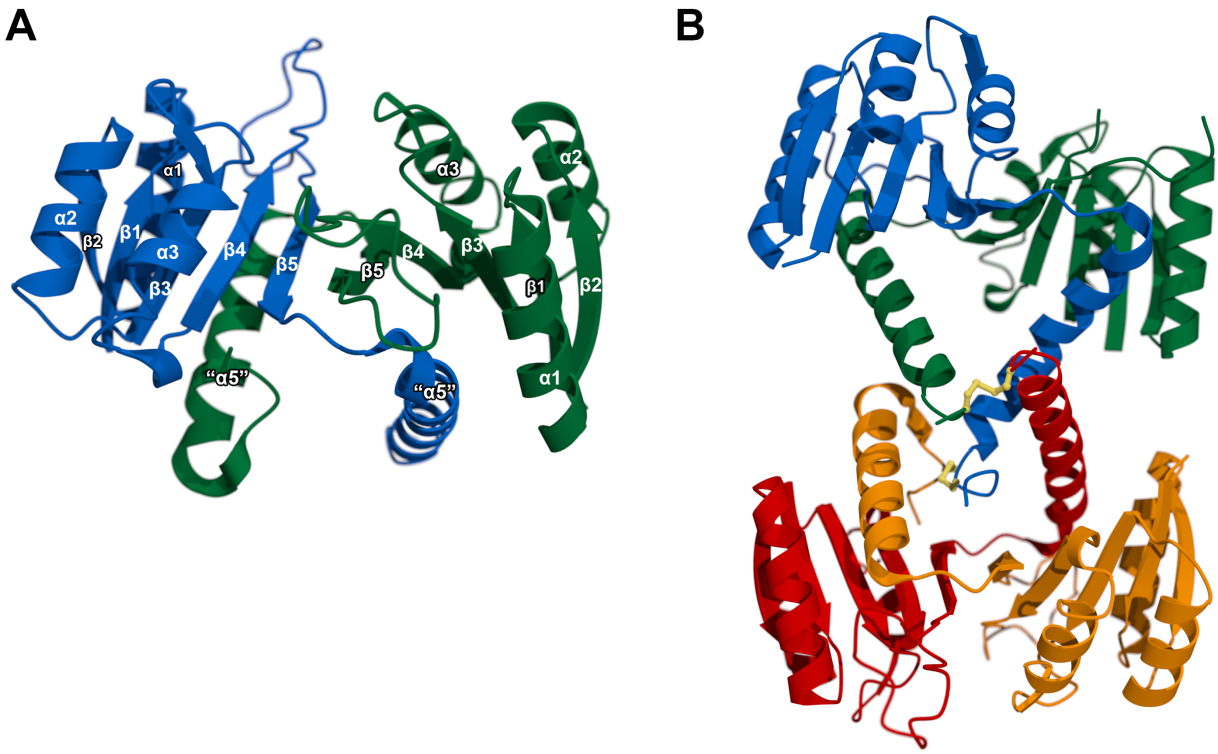

**Figure 2-21:** Ribbon representations of the RD2LV REC domain structure (A) and the RD2LV asymmetric unit (two dimers). The presence of C128 does not alter the domain swapped dimer, which is nearly identical in both structures. There are inter-dimer disulfide bonds that technically turn this into a tetramer. This appears to be an artifact of crystallization, as no tetramer is detectable in SEC traces of RD2LV (data not shown).

The structure of RD2LV is nearly identical to that of the shorter RDLV protein, both in terms of the tertiary structure of the protomer as well as the quaternary structure of the dimer (Figure 2-21A). The largest difference between the two structures is the fact that the "α5" helix is longer in RD2LV, which is not unexpected. This leads both to a modest increase in the number of hydrogen bonds and salt bridges between two chains, while the buried surface area of the interface is nearly unchanged (2,272 $Å^2$ vs 2,261 $Å^2$). More importantly, there are two disulfide bonds between the C128 residues of the two dimers (Figure 2-21B). The inter-dimer disulfide bonds are likely an artifact of the high concentrations required for crystallization, since there is not clear evidence of tetramerization in the analytical SEC data for the RD2LV variant (data not shown). Presumably, the α5 helices of the two protomers in a single dimer could also become disulfide linked, and this would hold the two DBDs in the proper orientation for DNA binding. The arrangement of the α5 helices in the RD2LV dimer suggests that the highly unusual REC domain structure observed here may be biologically relevant.

### 2.3.15 RitR with GADDY motif (RitR$_{GADDY}$)

A comprehensive investigation of OmpR family proteins[30] shows that RitR homologs have lost not only the phosphorylatable Asp residue, but also several highly conserved acidic residues that comprise the REC "GADDY motif" (see residues highlighted with red in Fig. 2-22), which is begins in the loop between α4 and β5 (Lα4β5) and ends near the middle of strand β5. The GADDY motif contributes to hydrogen bonding in the dimer interface of canonical REC domains [3, 31]. The terminal Tyr residue of the GADDY motif is the Y/T couple residue. We hypothesized that the loss of the GADDY motif in RitR (the motif becomes (F/Y)AVSY in RitR homologs) may explain why it only forms dimers in response to Cys128 oxidation.

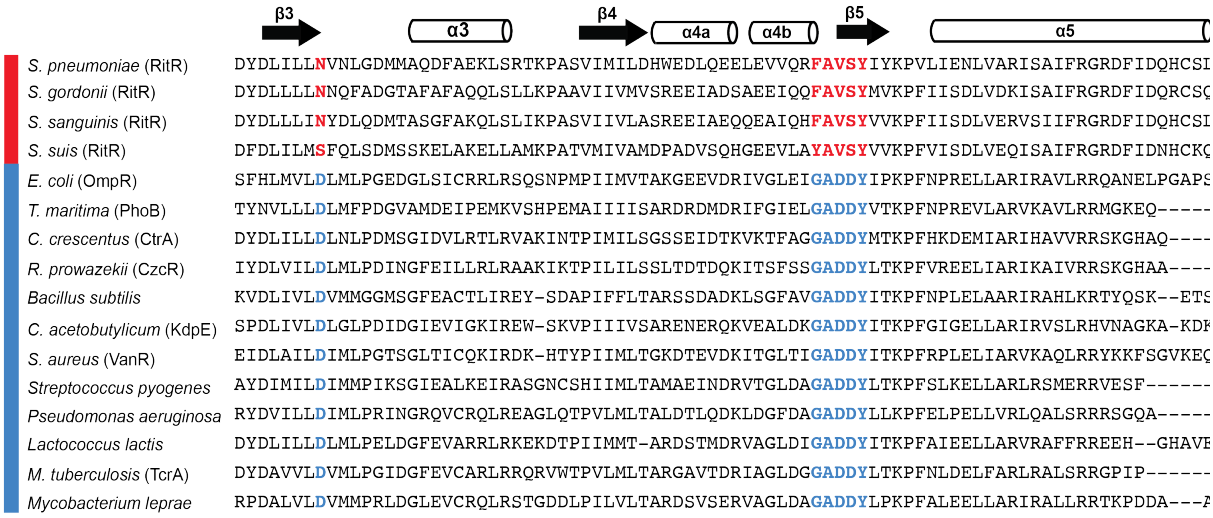


**Figure 2-22:** Sequence alignment of RitR homologs with other DNA binding proteins in the OmpR family. The major differences in the Streptococcal RitR homologs and the typical REC domain proteins are labeled in red. Asn/Ser substitutes for the phosphorylatable Asp residue, and the conserved GADDY motif is replaced with (F/Y)AVSY in RitR proteins.

To explore the hypothesis, we constructed a triple mutant of RitR where the equivalent "FAVSY" sequence is changed to GADDY ($RitR_{GADDY}$). The oligomeric state of $RitR_{GADDY}$ was investigated by SEC and the results are shown in Figure 2-23. The $RitR_{GADDY}$ variant has significantly more dimer than wild-type RitR protein in the absence of added oxidant. The retention time of the $RitR_{GADDY}$ dimer is the same as that of RDLV, but earlier than the $RitR_{ox}$ cross dimer. The retention time of the $RitR_{GADDY}$ monomer is also earlier than that of the wild-type RitR monomer. These observations suggest that both the dimeric and monomeric forms of $RitR_{GADDY}$ are more "extended" than the wild-type, likely due to dissociation of the ALR and DBD domains. The dimer/monomer ratio in $RitR_{GADDY}$ is still dependent on the redox state of C128. After treatment with 1 mM $H_2O_2$, $RitR_{GADDY}$ forms pure extended dimer, while it forms pure extended monomer after treatment with DTT (Figure 2-23).

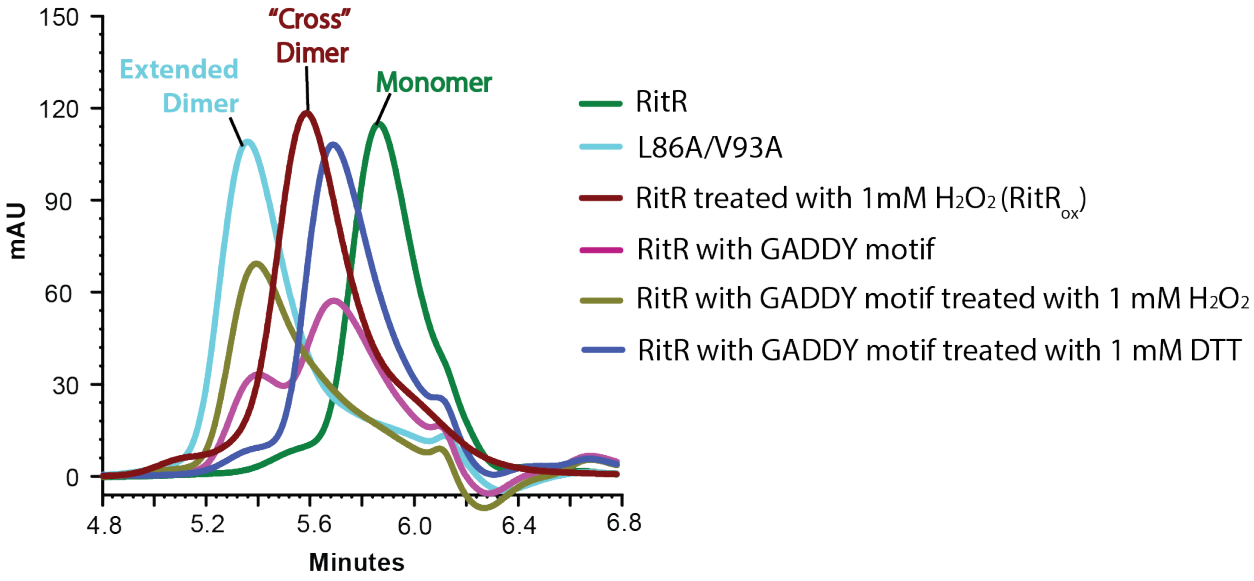


**Figure 2-23:** Size exclusion chromatography results of the $RitR_{GADDY}$ mutant with or without $H_2O_2$ or DTT treatments. The mutant $RitR_{GADDY}$ protein (magenta) exists as a mixture of extended dimer and extended monomer. After treatment with $H_2O_2$ (red), it forms almost pure dimer. And after DTT treatment (dark blue),

it forms almost pure monomer. The $RitR_{ox}$ "cross dimer" is dark red, the $RitR_{L86A/V93A}$ ("extended dimer") is cyan, wild-type RitR is green.

### 2.3.16 The role of C128 in the $RitR_{L86A/V93A}$ variant

C128 in RitR is highly conserved among a non-Group A/B subset of streptococcal species. To check if C128 has a role in the DNA-binding activity of RitR, we mutated C128 to Ser in the $RitR_{L86A/V93A}$ variant. The $RitR_{L86A/V93A}$ variant was used for these experiments, since it is the only form of RitR that we are reliably able to bind to DNA. The affinity of this $RitR_{L86A/V93A/C128S}$ triple mutant (LVC) for the BS3 target sequence was qualitatively assessed by SEC and differential scanning fluorimetry. As is evident in Figure 2-24, the LVC mutant binds to the BS3 forming protein-DNA complex. There is a peak corresponding to the complex with a retention time of 5.1 min, and stability of the protein significantly increased in the presence of DNA. As expected from the results above, it seems that oxidation of C128 is only the beginning of the signal, and some other factor is required to trigger the structural rearrangement of the α4-β5-α5 face of the REC domain that leads to dimerization, and it would seem, to DNA binding.

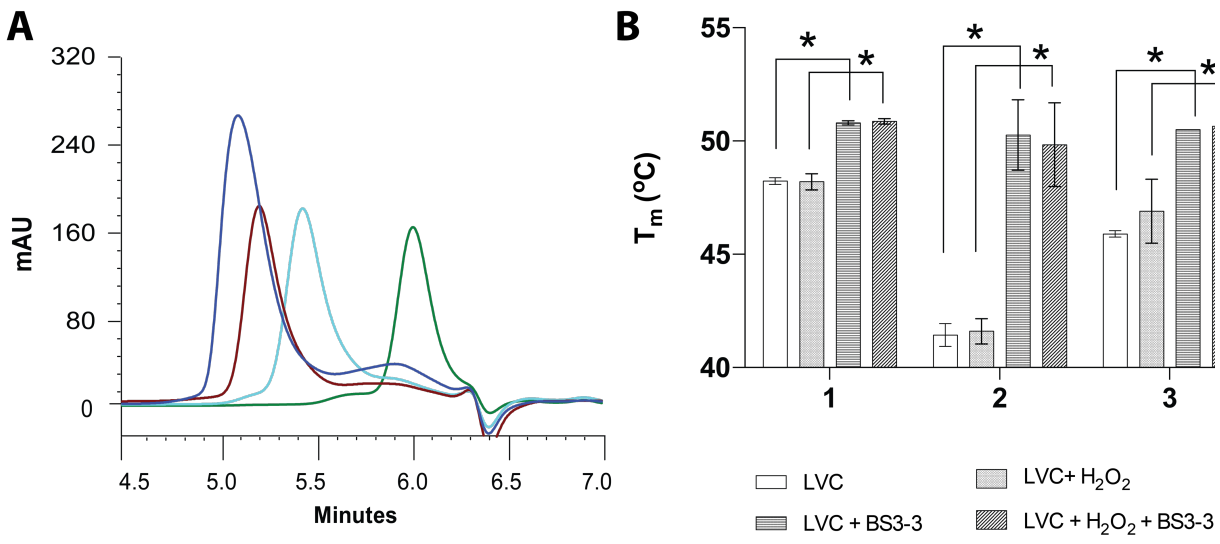


**Figure 2-24:** The LVC triple mutant still binds to the BS3-3 target dsDNA. Size exclusion chromatography results of LVC in the presence of BS3-3 (A) show that a peak eluted at 5.1 min that is not present in traces of either the protein or DNA alone and likely corresponds to the complex between the two. The presence of BS3-3 also significantly increased the stability of LVC as judged by differential scanning fluorimetry (B). **1**: pH 6.5, 25 mM TRIS, 150 mM NaCl, 100 mM DL-malic acid; **2**: 20 mM HEPES pH 7.2, 5 mM $MgCl_2$, 1 mM $CaCl_2$, 0.1 mM EDTA; **3**: 20 mM HEPES pH 7.2, 5 mM $MgCl_2$, 1 mM $CaCl_2$, 0.1 mM EDTA, 150 mM NaCl.

Our collaborators in the Ulijasz laboratory at Loyola University Chicago constructed three C128 mutants in the natural chromosomal position in *Streptococcus pneumoniae* strain R800 and D39: C128A (sensory dead), C128S (reduced mimetic) and C128D (oxidized mimetic). They found that the C128A mutant strain exhibited significantly impaired growth under aerobic conditions, whereas the C128S exhibited an intermediate growth defect. Conversely, the C128D mutant grew faster than the wild type. The results of the streptonigrin killing assay, which is an indirect indicator of cellular iron concentrations,

suggest that these effects are due to RitR-mediated repression of iron transport (to be published).

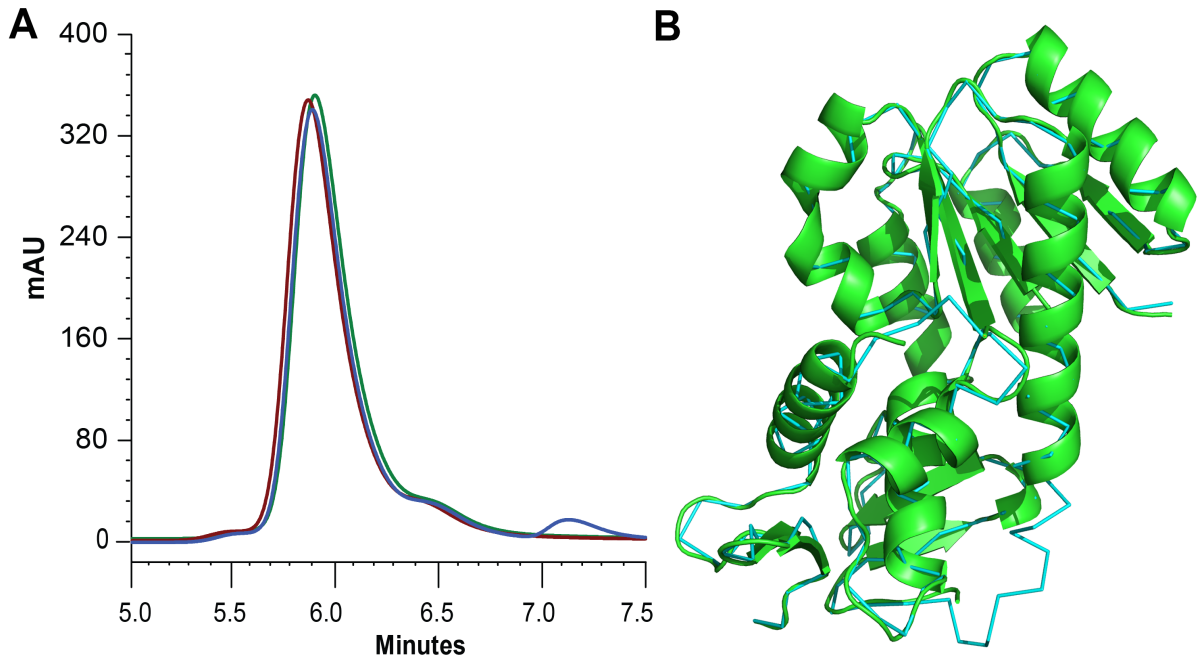


**Figure 2-25:** (A) Size exclusion chromatography results of $RitR_{C128D}$ with 1 mM $H_2O_2$ or 1mM DTT. The traces of $RitR_{C128D}$ only colored in blue, $H_2O_2$ treatment colored in red and DTT treatment colored in green. (B) Overlay of $RitR_{C128D}$ and $RitR_{C128S}$ structures. $RitR_{C128D}$ is colored green, while the $RitR_{C128S}$ structure is colored cyan. The rmsd for the matched Cα atoms in the two structures is 0.30 Å.

To investigate the structure and function relationship of the $RitR_{C128D}$ mutant, the oligomeric state and the protein structure were determined. The results are shown in Figure 2-25. The $RitR_{C128D}$ mutant exists as monomer, even after treatment with 1 mM $H_2O_2$ for several days. The structure of $RitR_{C128D}$ is very similar to that of the $RitR_{C128S}$ structure. Superposition of the $RitR_{C128S}$ and $RitR_{C128D}$ structures using secondary structure matching

(SSM)[32] gives a root-mean-square deviation (rmsd) of 0.3 Å for 220 of the 229 Cα atoms in the $RitR_{C128S}$ chain A. This indicates that the two structures are essentially identical. The long α5 linker helix still connects the REC and DBD domains of the protein and runs almost the entire length of the protein. However, the C-terminal end of this helix is disordered in the $RitR_{C128D}$ variant. This suggests that the Cys > Asp substitution mimics the oxidized form of RitR at least enough to trigger the disordering of the C-terminal end of α5 that was observed in the $RitR_{ox}$ structure, even though it was apparently not enough to trigger dissociation of the domains.

## 2.4 Conclusions

To propagate a signaling response, the typical TCST system employs a sensory histidine kinase that phosphorylates a receiver domain on a conserved aspartate residue. However, RitR is an orphan TCST response regulator in *Streptococcus pneumonia* R6 that lacks a cognate histidine kinase. In addition, there are some other characteristics suggesting that RitR has a different activation mechanism: the phosphorylatable aspartate is replaced by asparagine in RitR; D10 in the acidic triad is substituted by basic lysine; one switch residue T83 is substituted with D81; and there is a conserved cysteine residue near the DBD, C128, that is not present in other response regulators. This cysteine residue appears to be redox active and to influence the quaternary structure of RitR.

Analogy to other DNA-binding response regulators suggests that the active form of RitR binds to DNA as a dimer. As purified, RitR exists as a monomer in equilibrium with a very

small amount of homodimer. To get homogenous protein for crystallization, C128 was mutated to serine; the resulting C128S variant is purely monomeric. The structure of RitR(C128S) showed that the ALR domain and the DNA-binding domain are linked by an unusually long α-helix that runs the length of the entire protein, with C128 near the C-terminal end. Bioinformatic analysis of all streptococcal RitR homologs showed that C128 is strictly conserved, suggesting that RitR may be a novel redox sensor. The environment of the cysteine thiol group, as inferred from the position of S128 Oγ is quite polar (Figure 2-11F). Thus there is no clear indication why the C128 thiol group has a $pK_a$ of 7.2 (Figure 2-2), which is significantly lower than the $pK_a$ of free cysteine in aqueous solution. It is possible that other hydrogen bonding interactions, *e.g.* the water-mediated hydrogen bond to Y163, as well as the concentration of basic amino acids toward the C-terminus of α5 (H127, H147, and R160, as well as R135, which is located on the loop after α5) might mitigate the unfavorable interaction between a cysteine thiolate and the helix dipole. However, what is evident is that the C-terminus of helix α5, despite an extensive hydrogen bonding network around C128 that includes H147, D115, R160 and D164, is one of the more dynamic regions of the structure. The last few turns of helix α5 become disordered in the $H_2O_2$-oxidized protein, as well as the oxidized (sulfenate/sulfinate)-mimetic mutant RitR(C128D) (Figure 2-4 and Figure 2-25). Cysteine sulfenic acid (Cys-SOH) is a not-uncommon feature in redox-active proteins. For example, sulfenic acid was found to be an intermediate for disulfide bond formation *in vitro*[33]. The dramatically faster growth phenotype of the C128D mutant strain of *S. pneumoniae* verifies that the disordering of the C-terminal end of α5 is one step of RitR activation.

Iron is an important micronutrient in bacteria, which influences cell growth, virulence and metabolism. To stop the repressor signal, the *gnd* gene that co-transcribed with RitR, may be involved in the shutdown of oxidization-induced RitR activation. The *gnd* encodes a 6-phosphogluconate dehydrogenase that catalyzes NADPH formation. NADPH is, in turn, the cosubstrate of glutathione reductase, which may be involved in repressing RitR activation by reducing the sulfenic acid or disulfide bond into the reduced thiol group (Figure 2-26).

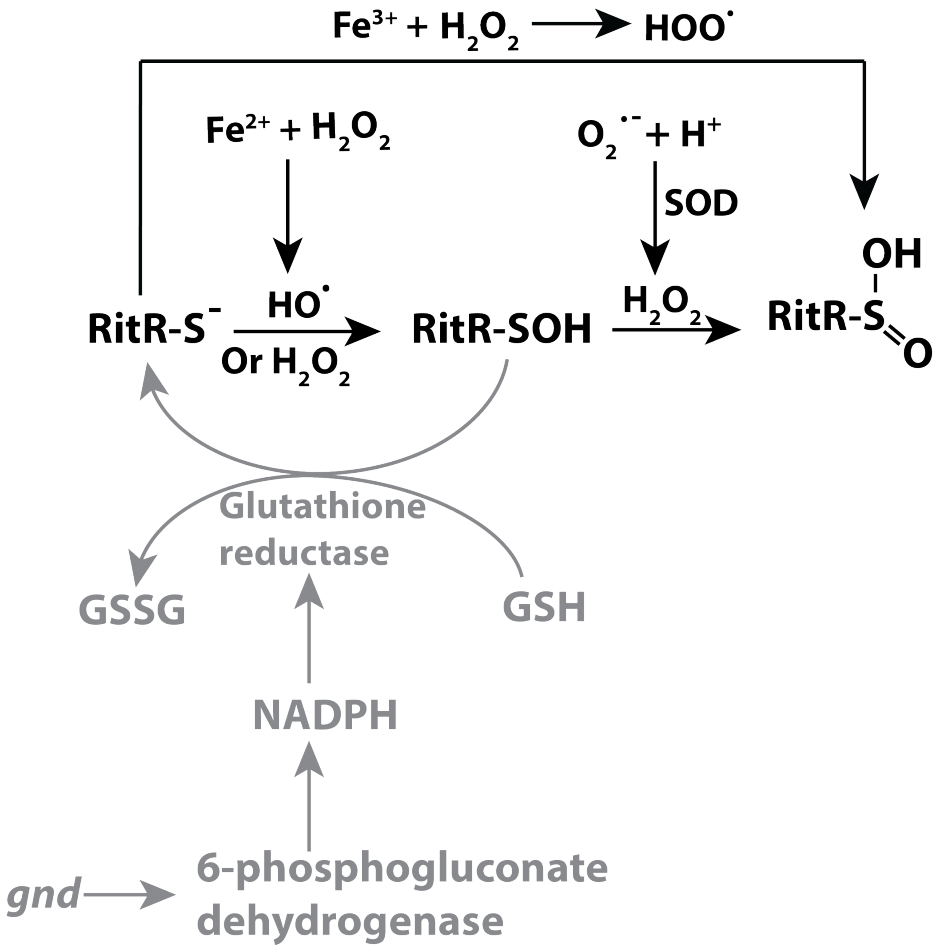


**Figure 2-26:** Proposed thiol group oxidation and reduction metabolism of RitR.

The structure of an oxidized, dimeric form of RitR was determined by X-ray crystallography. Oxidation of C128 to the disulfide caused a conformational change that caused the DBD to release from the ALR domain. Surprisingly, the freed DBD was observed bound to the ALR domain of the other, disulfide-linked molecule of RitR, recapitulating almost exactly the structure of the inactive, monomeric protein.

A second dimeric conformation was found in the RitR(L86A/V93A) variant. L86 and V93 were both mutated to Ala. These residues are found in the kinked α4 helix that interacts with the DBD and form part of the hydrophobic core of this region of the protein. RitR(L86A/V93A) elutes significantly earlier than the "cross-dimer" conformation of the oxidized, inactive wild-type RitR, suggesting that it has a different, likely more extended, overall shape. This "extended-dimer" binds to the target DNA according to gel filtration and differential scanning fluorimetry.

Attempts to crystallize the full-length RitR(L86A/V93A) protein alone, or in complex with oligonucleotides of various lengths were unsuccessful. Only blunt-ended dsDNA was tested in these experiments; it is possible that sticky-end dsDNA might promote crystallization of the protein:DNA complex by forming long, repeating assemblies of oligonucleotides[34]. Because the protein component is usually globular, packing of the bound protein within the lattice formed by neighboring DNA oligonucleotide assemblies can be important for growth of a three-dimensional crystal.

Since the full-length protein did not crystallize readily, we targeted the isolated RitR(L86A/V93A) REC domain for crystallization. The crystal structures of two constructs were determined: a 1-124 version that matches the original wild-type REC domain

construct (RDLV) and a longer 1-132 version that includes the putative redox-active C128 (RD2LV). Both RDLV and RD2LV exhibited the same unprecedented conformational change for a response regulator protein, where helix α4 is disordered and the two protomers swap their "α5" helices to form the dimer. The α5 helices point in opposite directions, which would place the DNA-binding domains far apart and give the extended shape suggested by gel filtration.

The fact that strains harboring a reduced mimetic RitR mutants (e.g. C128S) have a growth defect phenotype, it seems that oxidation of C128 is part of the activation mechanism. The $RitR_{ox}$ structure demonstrates that the dissociation of the REC domain from the DBD upon oxidation, but the dissociated DBD re-binds to the REC domain of the other protomer. So there must be an additional factor that leads to dimerization of the ALR domains, the active form of which likely has a similar structure to the RitR(L86A/V93A) REC domain.

Based on these studies, we propose a model for RitR activation, as shown in Figure 2-27. Under reducing conditions, RitR mainly exists as inactive monomer. Upon oxidation, as might happen during the oxidative burst phase of the *pneumococcus* growth where millimolar amounts of $H_2O_2$ are produced [35], RitR favors the dissociated and extended conformation. In the absence of target DNA, RitR would eventually form the inactive cross-dimer. In the presence of DNA, it may bind to DNA at low affinity. Under the influence of some still-unknown factor, the ALR domain of RitR would undergo a conformational rearrangement of the α4-β5-α5 region to promote dimerization and place the two DBDs far from the ALR domains. In that way, RitR can keep the extended, active conformation to

bind to DNA with high affinity. Alternatively, the ALR domains might be triggered to dimerize before binding to DNA, and only bind to target DNA when the active conformation has been obtained.

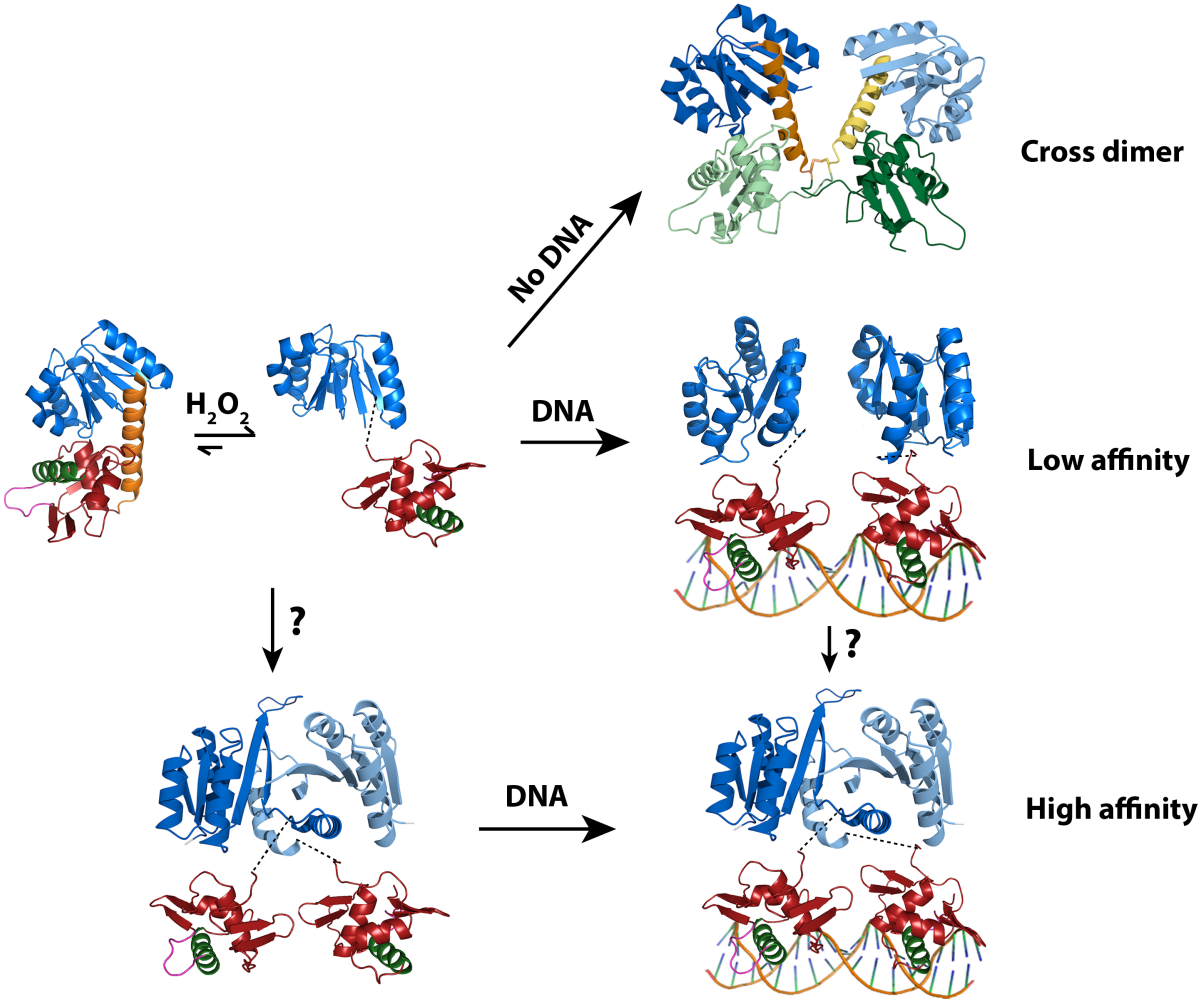


**Figure 2-27:** The proposed RitR activation mechanism.

Comparative transcriptome analysis demonstrated that, in addition to repressing expression of the *piu* iron transport genes, RitR also activates expression of bacterial ferritin, several genes involved in sugar uptake and other genes involved in DNA repair [1].

To check whether up-regulated sugars might contribute to RitR activation (dimerization), co-incubation of RitR with several carbohydrates (sucrose, sorbitol, mannitol, glucose, isoleucine) was conducted at room temperature for several hours. Size exclusion chromatography results showed that no oligomer state change was observed. So future studies on finding the trigger for RitR ALR domain dimerization are still needed to explore.

## 2.5 References


[1] Ulijasz, A. T., Andes, D. R., Glasner, J. D., and Weisblum, B. (2004) Regulation of iron transport in Streptococcus pneumoniae by RitR, an orphan response regulator, *Journal of bacteriology 186*, 8123-8136.

[2] Ong, C. L., Potter Aj Fau - Trappetti, C., Trappetti C Fau - Walker, M. J., Walker Mj Fau - Jennings, M. P., Jennings Mp Fau - Paton, J. C., Paton Jc Fau - McEwan, A. G., and McEwan, A. G. Interplay between manganese and iron in pneumococcal pathogenesis: role of the orphan response regulator RitR.

[3] Maule, A. F., Wright, D. P., Weiner, J. J., Han, L., Peterson, F. C., Volkman, B. F., Silvaggi, N. R., and Ulijasz, A. T. (2015) The Aspartate-Less Receiver (ALR) Domains: Distribution, Structure and Function, *PLOS Pathogens 11*, e1004795.

[4] Hickey, J. M., Lovell S Fau - Battaile, K. P., Battaile Kp Fau - Hu, L., Hu L Fau - Middaugh, C. R., Middaugh Cr Fau - Hefty, P. S., and Hefty, P. S. The atypical response regulator protein ChxR has structural characteristics and dimer interface interactions that are unique within the OmpR/PhoB subfamily.

[5] Bachhawat, P., and Stock, A. M. Crystal structures of the receiver domain of the response regulator PhoP from Escherichia coli in the absence and presence of the phosphoryl analog beryllofluoride.

[6] Palm, G. J., Khanh Chi, B., Waack, P., Gronau, K., Becher, D., Albrecht, D., Hinrichs, W., Read, R. J., and Antelmann, H. (2012) Structural insights into the redox-switch mechanism of the MarR/DUF24-type regulator HypR, *Nucleic acids research 40*, 4178-4192.

[7] Winther, J. R., and Thorpe, C. (2014) Quantification of Thiols and Disulfides, *Biochimica et biophysica acta 1840*, 10.1016/j.bbagen.2013.1003.1031.

[8] Otwinowski Z Fau - Minor, W., and Minor, W. Processing of X-ray diffraction data collected in oscillation mode.

[9] Vonrhein, C., Blanc, E., Roversi, P., and Bricogne, G. (2007) Automated structure solution with autoSHARP, *Methods in molecular biology (Clifton, N.J.) 364*, 215-230.

[10] Cowtan, K. (2006) The Buccaneer software for automated model building. 1. Tracing protein chains, *Acta crystallographica. Section D, Biological crystallography 62*, 1002-1011.
[11] McCoy, A. J., Grosse-Kunstleve, R. W., Adams, P. D., Winn, M. D., Storoni, L. C., and Read, R. J. (2007) Phaser crystallographic software, *Journal of applied crystallography 40*, 658-674.
[12] Emsley, P., Lohkamp, B., Scott, W. G., and Cowtan, K. (2010) Features and development of Coot, *Acta crystallographica. Section D, Biological crystallography 66*, 486-501.
[13] Afonine, P. V., Mustyakimov, M., Grosse-Kunstleve, R. W., Moriarty, N. W., Langan, P., and Adams, P. D. (2010) Joint X-ray and neutron refinement with phenix.refine, *Acta crystallographica. Section D, Biological crystallography 66*, 1153-1163.
[14] Word, J. M., Lovell, S. C., Richardson, J. S., and Richardson, D. C. (1999) Asparagine and glutamine: using hydrogen atom contacts in the choice of side-chain amide orientation11Edited by J. Thornton, *Journal of molecular biology 285*, 1735-1747.
[15] Adams, P. D., Afonine, P. V., Bunkóczi, G., Chen, V. B., Davis, I. W., Echols, N., Headd, J. J., Hung, L.-W., Kapral, G. J., Grosse-Kunstleve, R. W., McCoy, A. J., Moriarty, N. W., Oeffner, R., Read, R. J., Richardson, D. C., Richardson, J. S., Terwilliger, T. C., and Zwart, P. H. (2010) PHENIX: a comprehensive Python-based system for macromolecular structure solution, *Acta Crystallographica Section D: Biological Crystallography 66*, 213-221.
[16] Urzhumtseva, L., Afonine Pv Fau - Adams, P. D., Adams Pd Fau - Urzhumtsev, A., and Urzhumtsev, A. Crystallographic model quality at a glance.
[17] Nowakowski, A. B., Wobig Wj Fau - Petering, D. H., and Petering, D. H. Native SDS-PAGE: high resolution electrophoretic separation of proteins with retention of native properties including bound metal ions.
[18] Rimphanitchayakit, V., Hatfull, G. F., and Grindley, N. D. (1989) The 43 residue DNA binding domain of gamma delta resolvase binds adjacent major and minor grooves of DNA, *Nucleic acids research 17*, 1035-1050.
[19] Rhee, S., Martin, R. G., Rosner, J. L., and Davies, D. R. (1998) A novel DNA-binding motif in MarA: the first structure for an AraC family transcriptional activator, *Proc Natl Acad Sci U S A 95*, 10413-10418.
[20] Alekshun, M. N., Levy, S. B., Mealy, T. R., Seaton, B. A., and Head, J. F. (2001) The crystal structure of MarR, a regulator of multiple antibiotic resistance, at 2.3 A resolution, *Nat Struct Mol Biol 8*, 710-714.
[21] Chaffey, N. (2003) Alberts, B., Johnson, A., Lewis, J., Raff, M., Roberts, K. and Walter, P. Molecular biology of the cell. 4th edn, *Annals of Botany 91*, 401-401.
[22] Paulsen, C. E., and Carroll, K. S. (2013) Cysteine-Mediated Redox Signaling: Chemistry, Biology, and Tools for Discovery, *Chemical Reviews 113*, 4633-4679.
[23] Roos, G., Foloppe N Fau - Messens, J., and Messens, J. Understanding the pK(a) of redox cysteines: the key role of hydrogen bonding.
[24] Hiniker, A., Collet, J. F., and Bardwell, J. C. (2005) Copper stress causes an in vivo requirement for the Escherichia coli disulfide isomerase DsbC, *The Journal of biological chemistry 280*, 33785-33791.
[25] Matsui Lee, I. S., Suzuki, M., Hayashi, N., Hu, J., Van Eldik, L. J., Titani, K., and Nishikimi, M. (2000) Copper-Dependent Formation of Disulfide-Linked Dimer of S100B Protein, *Archives of Biochemistry and Biophysics 374*, 137-141.

[26] Pecci, L., Montefoschi, G., Musci, G., and Cavallini, D. (1997) Novel findings on the copper catalysed oxidation of cysteine, *Amino Acids 13*, 355-367.
[27] Bachhawat, P., Swapna, G. V., Montelione, G. T., and Stock, A. M. (2005) Mechanism of activation for transcription factor PhoB suggested by different modes of dimerization in the inactive and active states, *Structure 13*, 1353-1363.
[28] Pryor, E. E., Jr, Wozniak, D. J., and Hollis, T. (2012) Crystallization of Pseudomonas aeruginosa AmrZ protein: development of a comprehensive method for obtaining and optimization of protein-DNA crystals, *Acta Crystallographica Section F 68*, 985-993.
[29] Terwilliger, T. C., Grosse-Kunstleve, R. W., Afonine, P. V., Moriarty, N. W., Zwart, P. H., Hung, L.-W., Read, R. J., and Adams, P. D. (2008) Iterative model building, structure refinement and density modification with the PHENIX AutoBuild wizard, *Acta Crystallographica Section D 64*, 61-69.
[30] Marchler-Bauer, A., Bo, Y., Han, L., He, J., Lanczycki, C. J., Lu, S., Chitsaz, F., Derbyshire, M. K., Geer, R. C., Gonzales, N. R., Gwadz, M., Hurwitz, D. I., Lu, F., Marchler, G. H., Song, J. S., Thanki, N., Wang, Z., Yamashita, R. A., Zhang, D., Zheng, C., Geer, L. Y., and Bryant, S. H. (2017) CDD/SPARCLE: functional classification of proteins via subfamily domain architectures, *Nucleic acids research 45*, D200-d203.
[31] Toro-Roman, A., Mack Tr Fau - Stock, A. M., and Stock, A. M. Structural analysis and solution studies of the activated regulatory domain of the response regulator ArcA: a symmetric dimer mediated by the alpha4-beta5-alpha5 face.
[32] Krissinel, E., and Henrick, K. (2004) Secondary-structure matching (SSM), a new tool for fast protein structure alignment in three dimensions, *Acta crystallographica. Section D, Biological crystallography 60*, 2256-2268.
[33] Rehder, D. S., and Borges, C. R. (2010) Cysteine sulfenic acid as an intermediate in disulfide bond formation and non-enzymatic protein folding, *Biochemistry 49*, 7748-7755.
[34] Pio, F., Ni, C.-Z., Mitchell, R. S., Knight, J., McKercher, S., Klemsz, M., Lombardo, A., Maki, R. A., and Ely, K. R. (1995) Co-crystallization of an ETS Domain (PU.1) in Complex with DNA: ENGINEERING THE LENGTH OF BOTH PROTEIN AND OLIGONUCLEOTIDE, *Journal of Biological Chemistry 270*, 24258-24263.
[35] Pericone, C. D., Bae, D., Shchepetov, M., McCool, T., and Weiser, J. N. (2002) Short-sequence tandem and nontandem DNA repeats and endogenous hydrogen peroxide production contribute to genetic instability of Streptococcus pneumoniae, *Journal of bacteriology 184*, 4392-4399.

# Chapter 3

# Uncharacterized Protein Q15Z91 from *Pseudoalteromonas atlantica* is an ALR-Regulated Diguanylate Cyclase

## 3.1 Introduction

Aspartate-less receiver (ALR) proteins are a subclass of response regulator proteins in bacterial signal transduction systems. In typical two-component signaling systems, the receiver domain of the regulator would be phosphorylated in the conserved aspartate residue by the cognate histidine kinase. In ALR-containing response regulators, there is no conserved Asp residue for phosphorylation, which means that ALRs must necessarily respond to different regulatory stimuli. Chapter 2 described my work aimed at elucidating the activation mechanism of an ALR protein, RitR. I showed that it functions as an "extended dimer" where the DNA-binding domains are released from the ALR domain, partly in response to oxidation of C128. Owing to its activity as a DNA-binding protein, it was difficult to make quantitative studies of RitR activation. The assays used to detect DNA binding often gave contradictory results and could be highly dependent on the experimental system (*e.g.* choice of buffer, salt concentration, and temperature). For this reason, we chose to study an ALR-containing response regulator whose effector domain has an enzymatic activity, which would allow a much more nuanced and quantitative assessment of activation. We identified just such a protein through BLAST[2, 3] searches using

residues 1-132 of RitR, which comprise the ALR domain and the extended α5 helix that contains the redox-active cysteine (C128). By manually filtering the results of the BLAST search for sequences that contained the same "HCS" motif found in RitR, we found an uncharacterized protein from *Pseudoalteromonas atlantica* TC6, which is known only by its UNIPROT accession code, Q15Z91, which catalyzes the formation of the bacterial second messenger molecule bis-(3'-5')-cyclic dimeric guanosine monophosphate (c-di-GMP) from two molecules of GTP. In this chapter I describe my structural and enzyme kinetics studies of Q15Z91.

## 3.2 Methods

### 3.2.1 Expression and purification of Q15Z91

The coding sequence of Q15Z91 (Genbank locus ID Patl_0265) was optimized for expression in *E. coli* and synthesized by GenScript Inc (Piscataway, NJ). The synthetic gene was sub-cloned into the pE-SUMO kan expression vector (LifeSensors Inc, Malvern, PA) using primers containing BsaI and XbaI restriction sites (Q15Z91 forward: 5'-GGTCTCAAGGTATGCAAAATCCGGAAAGTGC-3', Q15Z91 reverse: GCTCTAGATCATTATGACACCAGACGGTTACGA-3'). The $His_6$-tagged SUMO-Q15Z91 fusion protein was expressed from Origami2 *E. coli* cells (Invitrogen Inc, Carlsbad, CA) carrying the pE-SUMO-Q15Z91 plasmid. Cultures were grown in Luria-Bertani medium with 50 μg/mL kanamycin at 37 °C. When the cultures reached an $OD_{600nm}$ of ~0.7, protein expression was induced with 0.4 mM IPTG. The temperature was reduced to 16 °C and the

cultures were grown overnight with shaking at 250 rpm. Cells were harvested by centrifugation, resuspended in 5 mL of buffer A (25 mM TRIS pH 8.0, 300 mM NaCl, 10 mM imidazole) supplemented with 1 mg/mL hen egg lysozyme (Hampton Research) and 0.1 mg/mL DNAse I (Worthington Biochemical Corp., Lakewood, NJ) per gram wet weight of cells. Cells were lysed using a Branson Sonifier S-450 cell disruptor (Branson Ultrasonics Corp., Danbury, CT) for a total of 10 min of sonication at 60% amplitude with 30 s pulses separated by 50 s rest periods. The temperature was maintained at or below 4 °C by suspending the steel beaker in an ice bath directly over a spinning stir bar. The lysate was clarified by centrifugation at 39,000 x g for 45 minutes and then applied to a 5 mL HisTrap column (GE Lifesciences, Piscataway, NJ) at a flow rate of 5 mL/min to isolate the $His_6$-SUMO-Q15Z91 fusion protein. The protein was eluted by a 4-step gradient of buffer B (25 mM TRIS pH 8.0, 300 mM NaCl, and 250 mM imidazole; 5, 15, 50, and 100%). The $His_6$-SUMO-Q15Z91 fusion protein eluted in the third step and was ~90 % pure, as judged on coomassie-stained SDS-PAGE gels. Fractions corresponding to $A_{280nm}$ peaks on the chromatogram were pooled ~3 μM SUMO protease (LifeSensors Inc) were added. The sample was loaded into SnakeSkin dialysis tubing and dialyzed overnight against 4 L of SUMO protease digestion buffer (25 mM TRIS pH 8.0, 150 mM NaCl). The dialysate was passed through the HisTrap column a second time to remove the cleaved $His_6$-SUMO tag as well as the protease. The resulting Q15Z91 preparation was > 95% pure. The protein was desalted using a 2x5 mL HiTrap Desalting column (GE Lifesciences) equilibrated with 25 mM TRIS pH 7.5, 150 mM NaCl and stored at -80 °C. The mutants described below were purified using the same protocol as the wild type protein.

Q15Z91 co-purified with c-di-GMP as determined by spectroscopy and crystallography. To get c-di-GMP-free Q15Z91 protein, SadR, a phosphodiesterase from *Pseudomonas aeruginosa*, was used to linearize the c-di-GMP. The SadR expression construct was a kind gift of professor Holger Sondermann in the Department of Molecular Medicine, College of Veterinary Medicine, Cornell University. The $His_6$-tagged SadR protein was purified as described by De, et al[4], omitting the precision protease cleavage step. SadR treatment results in the degradation of c-di-GMP to free pGpG, which is easily removed by gel filtration. The $His_6$-tagged SadR protein was added to the purified Q15Z91 and dialyzed in 4 L of 50 mM TRIS pH 8.0, 150 mM NaCl, 2 mM $MgCl_2$ buffer at 4 $^oC$ overnight. The dialysate was passed through the HisTrap column a third time to separate c-di-GMP free Q15Z91 ($Q15Z91_{free}$) from the $His_6$-tagged SadR. The resulting Q15Z91 protein was desalted using a HiTrap Desalting column equilibrated with 25 mM TRIS pH 7.5, 150 mM NaCl and stored at -80 °C. In the desalt step, the free pGpG would be separated from protein. The c-di-GMP free mutants described below were purified using the same protocol as $Q15Z91_{free}$.

### 3.2.2 Mutagenesis of Q15Z91

The full-length mutants were obtained using the Q5 site-directed mutagenesis kit (New England Biolabs, Ipswich, MA) as described for RitR in Chapter 2. The sequences of the mutagenic PCR primers are listed in Table 3-1.

**Table 3-1:** Primers used for mutagenesis

| Name | Primer sequence |
|---|---|
| sumo-Q15Z91_C142S_Fwd | CCTGATTTCTTCCACCGATGGCC |
| sumo-Q15Z91_C142S_Rev | GCCAGGGTGCGCAGTTTC |
| sumo-Q15Z91_R212N/D215A_Fwd | TCTGCTGCGATGGGCCGCTACGGC |
| sumo-Q15Z91_R212N/D215A _Rev | TTCATTCTGCAGGCTAGCTTCAATCGTGGTTG |
| sumo-Q15Z91_I99A _Fwd | GAAATCACTGGCTCTGTCGGGCC |
| sumo-Q15Z91_I99A _Rev | GGGGTGTCTTTGCCATAC |
| sumo-Q15Z91_G102A _Fwd | GATTCTGTCGGCCCTGGAAGCGG |
| sumo-Q15Z91_G102A _Rev | AGTGATTTCGGGGTGTCTTTG |

### 3.2.3 Crystallization, structure determination, and model refinement

Crystals of Q15Z91 alone were grown by the vapor diffusion method with sitting-drop geometry. Crystals formed in many different conditions. The highest quality crystals formed in drops comprised of equal parts protein solution (8 mg/ml Q15Z91 in 10 mM TRIS/100mM citric acid pH 4.5, 150 mM NaCl, and crystallization solution (20% (w/v) PEG 3350, and 0.2 M sodium citrate tribasic dehydrate). Cube-shaped crystals appeared after several months at 4$^{o}$C and were prepared for flash-cooling by soaks in solutions containing 2 µl of well solution and 0.7 µl of glycerol (~26%). Crystals of Q15Z91 without GTP bound were grown by mixing 1 µl of 8 mg/mL Q15Z91 that pre-incubated with 5mM $MgCl_2$, 200 µM $ZnCl_2$, 3 mM GTP with crystallization solution (8% v/v Tacsimate pH 7.0, 20% w/v Polyethylene glycol (PEG) 3,350). Cube-shaped crystals appeared after several months at 4 $^{o}$C. Crystals were prepared for flash-cooling in the same way as Q15Z91 alone crystals.

X-ray diffraction data were collected from crystals of Q15Z91 at beamline 21-ID-D of the Life Science Collaborative Access Team (LS-CAT) at the Advanced Photon Source (APS). Data were collected from crystals of the protein with GTP at LS-CAT beamline 21-ID-G. Data were processed with HKL2000 [5]. The structure of Q15Z91 was determined by molecular replacement using 3BRE REC domain and effector domain as two ensembles in Phaser[5]. The initial model comprising 88% of the asymmetric unit contents was built by Autobuild[6]. Chain A of this model was used as the search model for molecular replacement in PHASER[7] to phase the Q15Z91 with GTP bound structure. Both models were subjected to iterative cycles of manual model building in COOT[8] and maximum likelihood-based refinement using the PHENIX package (phenix.refine[9]). Ordered solvent molecules were added automatically in phenix.refine and culled manually in COOT. Hydrogen atoms were added to the model using phenix.reduce[10] and were included in the later stages of refinement to improve the stereochemistry of the model. Positions of H atoms were refined using the riding model with a global B-factor. Regions of the model for translation-libration-screw (TLS) refinement were identified using phenix.find_tls_groups (P.V. Afonine, unpublished work) and the TLS parameters were refined in phenix.refine. Once the refinement converged, the model was validated using the tools implemented in COOT and PHENIX[9, 11]. Sections of the backbone with missing or uninterpretable electron density were not included in the final model. Data collection and model refinement statistics are listed in Table 3-2. Coordinates and structure factors for both Q15Z91 and Q15Z91 with GTP models will be deposited in the Protein Data Bank (www.rcsb.org).

### 3.2.4 Quaternary structure characterization by size exclusion chromatography

SEC experiments were carried out using an Agilent 1220 Compact HPLC equipped with a 250 x 4.6 mm BioBasic SEC-300A column equilibrated with 25 mM TRIS pH 7.5, 150 mM NaCl. The column was calibrated with the Gel Filtration Molecular Weight Marker kit from Sigma-Aldrich (Cytochrome C (12.4 kDa), Carbonic Anhydrase (29 kDa), Bovine Serum Albumin (66 kDa), and Sweet Potato Amylase (200 kDa)). Q15Z91 was pre-incubated with 1 mM $H_2O_2$ or 1mM DTT and 5 µl of the treated proteins were injected onto the column and separated at a flow rate of 0.5 ml/min at ambient temperature. The separation was monitored using a variable wavelength UV-visible detector set to 280 nm.

### 3.2.5 Size exclusion chromatography with multi-angle light scattering (SEC-MALS)

To confirm the molecular weights estimated from the calibrated SEC runs of Q15Z91 on the BioBasic SEC-300A column, the separations were repeated on the SEC-MALS system in the laboratory of Dr. Blake Hill at the Medical college of Wisconsin. The multiple-angle light scattering detector provides a direct estimate of the molecular weights of particles eluting from the column that is independent of the retention time. The same 250 x 4.6 mm BioBasic SEC-300A column was used with 24-hour equilibration in 25 mM TRIS pH 7.5, 150 mM NaCl at 0.5 ml/min. The running buffer is same as used above, except that it was filtered through a 0.022 µm filter, rather than a 0.22 µm filter. Due to the relatively low sensitivity of the MALS detector the separation was done with 100-200µg of Q15Z91, rather than the ~15 µg used for the UV/vis-monitored separations. The concentrated

proteins were centrifuged at 16,900 x g for 20 min at 4°C before loading.

### 3.2.6 Biofilm assay on borosilicate tubes

Assays to quantify the degree of biofilm formation in *E. coli* expressing wild-type or mutant forms of Q15Z91 were performed as a way to assess the *in vivo* activity of the proteins. Overnight cultures of Origami2 *E. coli* carrying the pSUMO-Q15Z91 (or mutant) plasmids were adjusted to the same inoculum amounts in 3 ml of fresh LB broth with 50 µg/ml kanamycin in 14 ml borosilicate glass tubes. After growth with rotating at 37 °C for ~5 hours, the cultures were equalized by adding extra fresh $LB_{kan}$ medium and then protein expression was induced by the addition of 0.4 mM IPTG. The cultures were allowed to rotate overnight at 25°C. The next day, the cultures were removed from their respective test tubes, which were washed three times with tap water. After washing, crystal violet was used to stain any biofilm that had been deposited on the walls of the tubes. After staining, the culture tubes were washed with tap water five times. The culture tubes were then dried and the residual stain – that bound in the biofilm – was dissolved in 2 mL of 80% (v/v) ethanol/20% (v/v) acetone. The absorbance at 540 nm was measured on a spectrometer and taken to be a qualitative indicator of the degree of biofilm formation induced by wild-type Q15Z91 or the various mutants tested.

### 3.2.7 Enzymatic assay

#### 3.2.7.1 RP-HPLC based end-point assay

As a convenient check for catalytic activity of the various forms of Q15Z91 studied here, protein was incubated for a set period of time with GTP and $MgCl_2$ and the reaction mixtures were characterized by reverse phase high performance liquid chromatography (RP-HPLC). Each 200 µl reaction contained 20 µM enzyme, 25 mM TRIS pH 7.5, 150 mM NaCl, 2mM $MgCl_2$, and 0.5 mM GTP. The GTP was prepared fresh as a 100 mM stock in $mqH_2O$. Reactions were incubated at room temperature for 30 min, and then quenched by boiling for 5 min. After centrifugation at 30,000 x g for 10 min, the supernatants were analyzed on a 150 x 3 mm Aquasil C18 column (Thermo Scientific). Buffer A was 10 mM $NaH_2PO_4/K_2HPO_4$ pH 6.3, and buffer B was 30% (v/v) methanol, 70% (v/v) buffer A. The gradient from 5% to 100% B over 28 min, then held at 100% B for 5 min, 5% buffer B for 5 min. All separations were run at 50 °C and were monitored at 254 nm.

#### 3.2.7.2 Biomol Green microplate assay

Reactions were prepared in a volume of 500 µl and contained 10 µM enzyme, 25 mM TRIS pH 7.5, 150 mM NaCl, 2 mM $MgCl_2$, and 0.5 mM GTP. Reactions were initiated with the addition of GTP. Aliquots were taken at set intervals and quenched by boiling for 5 min. After centrifugation at 30,000 x g for 10 min, the supernatants were kept at 4 $^{o}$C. The negative control was the reaction buffer containing GTP. The amount of pyrophosphate released was quantified by adding 0.005 U pyrophosphatase (Thermo Scientific) to each

reaction, followed by a 1.5 h incubation room temperature. Then 50 µl of the pyrophosphatase-treated reaction mixture were mixed with 100 µl Biomol Green reagent and incubated at room temperature for 20 min. The absorbance of the mixtures at 620 nm was recorded and converted to concentration of phosphate via a standard curve prepared with 0.03125 nM-2 nM inorganic phosphate.

#### 3.2.7.3 EnzCheck® Pyrophosphate Assay Kit (Sigma)

This assay was conducted by following the optimized procedure published by Webb[12, 13]. Pyrophosphatase can catalyze pyrophosphate into 2 molecules of inorganic phosphate. In the presence of inorganic phosphate, purine nucleoside phosphorylase (PNP) catalyzes 2-amino-6-mercapto-7-methylpurine ribonucleoside (MESG) into ribose 1-phosphate and 2-amino-6-mercapto-7-methylpurine that absorbs maximally at 360 nm. Each 1 mL reaction contained 1 µM enzyme with 2-amino-6-mercapto-7-methylpurine ribonucleoside (MESG), purine nucleoside phosphorylase in the reaction buffer was incubated at 22 $^{o}$C for 10 min. The reactions were initiated with the addition of GTP and the absorbance at 360 nm was monitored. The concentrations of GTP tested range from 50 µM to 1000 µM.

## 3.3 Results

### 3.3.1 Q15Z91 is an ALR-regulated diguanylate cyclase

Q15Z91 is 310 amino acids long (34.6 kDa) and consists of an N-terminal ALR domain

fused to a diguanylate cyclase domain. Alignment of the RitR and Q15Z91 sequences shows that the phosphorylatable aspartate residue is replaced by arginine in Q15Z91 (Figure 3-1). The conserved C128 that has been shown to play an important role in RitR activation is retained in Q15Z91, though the residues flanking it are different between the two proteins. The effector domain contains the GGEEF motif characteristic of diguanylate cyclase enzymes.

```
Q15Z91      MQNPESANVLKQTLLVVDNPGEMLKALTRQF-STSFHLLVCNDNEEVLKLALNAPIDLVL
RitR        ---------MGKRILLLEKERNLAHFLSLELQKEQYRVDLVEEGQKALSMALQTDYDLIL
                     : : :*::::  :: : *: :: . .::: : ::.::.*.:**::  **:*

Q15Z91      IRVSPRDSDWLLICTRLKQHPLTIDIPLILYGKDTPKSLIL--SGLE----------AGA
RitR        LNVNLGDMMAQDFAEKL--------------SRTKPASVIMILDHWEDLQEELEVVQRFA
            :.*.  *     :. :*               .: .* *:*:  .  *            *

Q15Z91      LDFVELPTDIAMLNIKIRNHMQVSAKLRTLALIS--CTDGLTGVPNRMQLDTTYNRFWYA
RitR        VSYIYKPVFIENLVA------RISAIFRGRDFIDQHCS--LMKVPR------TY------
            :.::  *. *  *        ::** :*   :*.      *  **.      **

Q15Z91      AIRGQHELSVLMIDIDFFKGFNDTYGHVAGDECLKKVATTIEASLQRESDAMGRYGGEEF
RitR        ------------------------------------------------------------

Q15Z91      LVLLPFTDKVGAQKIAEMILRNIEALDIKNKASTVNGKVTVSVGAATLKLHDINDHTFNH
RitR        ------------------------------------------------------------

Q15Z91      PEFLVEQADRCLYQAKKQGRNRLVS
RitR        -------------------------
```

**Figure 3-1**: Sequence alignment of Q15Z91 with the RitR REC domain. Arginine (colored in red) substitutes the conserved aspartate residue of the typical response regulator proteins (N53 in RitR). The conserved Cys128 of RitR is colored in orange; the GGEEF motif of Q15Z91 is colored blue.

### 3.3.2 Purification of Q15Z91

The pSUMO-Q15Z91 plasmid was transformed into BL21 Star (DE3) cells, T7 LysY/Iq cells (New England Biolabs, Ipswich, MA), and Origami2 cells (Novagen) Single colonies were used to inoculate large-scale expression cultures, which were grown at 37 °C to an $OD_{600nm}$ of ~0.7, at which point protein expression was induced by the addition of 0.4 mM IPTG. Three strains were attempted to express Q15Z91, but only the Origami2 cells expressed soluble proteins and exhibited an obvious biofilm phenotype. Induction at higher or lower $OD_{600nm}$ resulted in lower yields of soluble protein.

**Table 3-2**: Buffers from the Solubility & Stability Screen giving the highest $T_m$ values in the DSF assay.

| $T_m - T_{m,averaged}$ (°C) | Additive |
|---|---|
| 8.4 | Adipic acid |
| 6.7 | Ethylenediaminetetra acetic acid disodium |
| 5.9 | TCEP hydrochloride |
| 5.9 | Sodium phosphate monobasic, potassium phosphate dibasic |
| 5.6 | Ammonium sulfate |
| 5.5 | L-Argininamide dihydrochloride |
| 5.1 | Ethylenediamine dihydrochloride |
| 5.1 | Magnesium sulfate hydrate |

Q15Z91 was not stable in the purification buffers. To find the optimal storage buffer and pH, the Solubility & Stability Screen (Hampton research) and Slice pH (Hampton research) were used in differential scanning fluorimetry assays. The results showed that Q15Z91 is not stable, its average $T_m$ being 33°C; this is not surprising given that *P. atlantica*

is a psychrophilic bacterium. The top 10 conditions as judged by their increase in the $T_m$ above the average, are shown in Table 3-2 and Table 3-3. Based on these data, 25mM TRIS/100mM citric acid pH 4.5, 150 mM NaCl was chosen as the storage buffer for Q15Z91.

**Table 3-3:** Buffers from the Slice pH Screen giving the highest $T_m$ values in the DSF assay.

| $T_m - T_{m,averaged}$ (°C) | Additive |
|---|---|
| 5.5 | Sodium citrate tribasic dihydrate pH 4.5 |
| 4.9 | Citric acid pH 4.4 |
| 4.7 | DL-malic acid pH 4.7 |
| 4.6 | Sodium citrate tribasic dihydrate pH 4.2 |
| 4.6 | DL-malic acid pH 5.0 |
| 4.3 | DL-malic acid pH 5.3 |
| 4.3 | Succinic acid pH 5.1 |
| 4.1 | Citric acid pH 4.1 |
| 4.1 | Succinic acid pH 4.8 |
| 4.1 | Succinic acid pH 5.4 |

### 3.3.3 The structure of Q15Z91 with c-di-GMP and citrate bound

The structure of Q15Z91 was determined by molecular replacement using 2.0 Å resolution data. The model contains residues 11-310, as well as two citrate molecules and two c-di-GMP dimers. As shown in Figure 3-2A, Q15Z91 is a dimer, with citrate bound at the active sites (A site) of the diguanylate cyclase (DGC) domains, and c-di-GMP dimers at the inhibitory sites (I site). Chain A (light green) has no inter-domain interface, while chain

B (light blue) has a weak interface. And there is a S-S bond between two chains. We can see clear electron density for the disulfide bond (Figure 3-2B). This Q15Z91 dimer structure is an inactive conformation, because the c-di-GMP bound in the I sites immobilizes the two DGC domains in an unproductive back-to-back orientation.

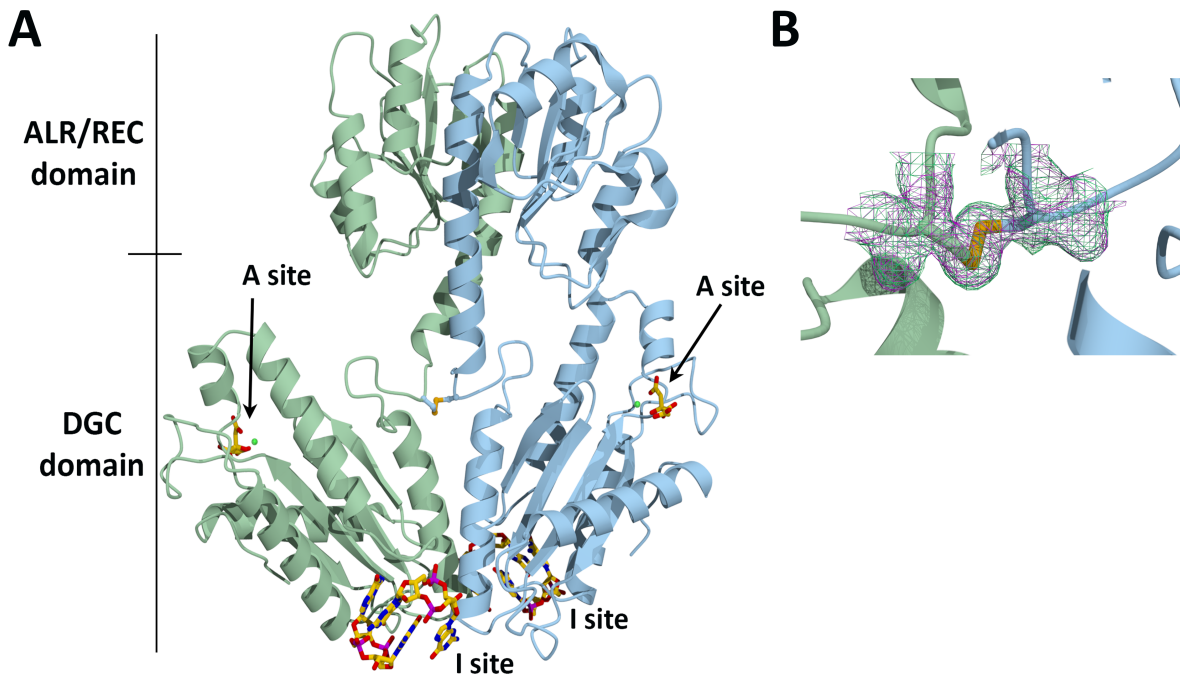


**Figure 3-2:** The structure of Q15Z91 dimer with c-di-GMP and citrate bound (A). The two protomers are colored light green and light blue. The ALR domain of Q15Z91 is at the top of the image, and the DGC catalytic effector domain is at the bottom. Citrate and c-di-GMP are shown as sticks with yellow carbon atoms. $Mg^{2+}$ ions are shown as small green spheres associated with the tri-phosphate moieties of the citrate molecules. The citrate molecules from crystallization buffer are bound in the active sites (A site) and the c-di-GMP dimers are bound in the inhibitory sites (I site) of the DGC domain. The two polypeptides comprising the dimer are linked by a disulfide bond formed between C142 on both chains (B). The $2|F_o|-|F_c|$ electron density map contoured at 1.0σ is shown as a magenta mesh, and the $2|F_o|-|F_c|$ composite omit map, also contoured at 1.0σ, is shown as a green mesh.

The ALR domain of Q15Z91 has the same $(\beta/\alpha)_5$ topology and α4-β5-α5 dimer interface (Figure 3-3) characteristic of typical OmpR/PhoB RRs. As shown in Figure 3-3B, the switch residue F110 (equivalent to Y100 of RitR) is oriented inward, which is the conformation associated with the activated forms of typical OmpR/PhoB RRs and is thought to facilitate dimer formation. However, the other Ser/Thr switch residue is replaced by G91 in Q15Z91. In the phosphorylation-dependent RRs, phosphorylation induces a conformational change of the Ser/Thr switch residue that results in the reorientation of the Tyr/Phe switch residue to facilitate dimerization. In Q15Z91, the residue that is equivalent to the Ser/Thr switch residue in typical RRs is G91, so obviously side chain reorientation cannot be an integral part of the activation mechanism in Q15Z91. This is similar to what was seen in RitR, where the Ser/Thr switch equivalent, D81, had a minimal impact on dimerization. In addition, R61 in Q15Z91 replaces the phosphorylatable aspartate residue of the typical RRs. Comparison of the Q15Z91 and RitR ALR domains shows that the side chain of R61 takes the place of the "lid residue" K10 of RitR and that the loop between β1 and α1 shifts away from the "phosphorylation site" comparison with that in RitR. It seems that the ALR domain of Q15Z91 has evolved to be an obligate dimer, and that activation may be subtler than a change from monomer to dimer as has been seen for the DNA-binding RR proteins.

**Figure 3-3:** ALR domains of the Q15Z91 dimer (A) and the overlay of the Q15Z91 and RitR ALR domains (PDB ID 4LZL[1]) (B). Chain A of Q15Z91 ALR domain colored in light green, chain B colored in blue. RitR ALR domain is colored cyan. The active site residues and switch residues equivalent are shown in stick. The Cα atom of G91 (Ser/Thr switch residue equivalent) in Q15Z91 is shown in sphere.

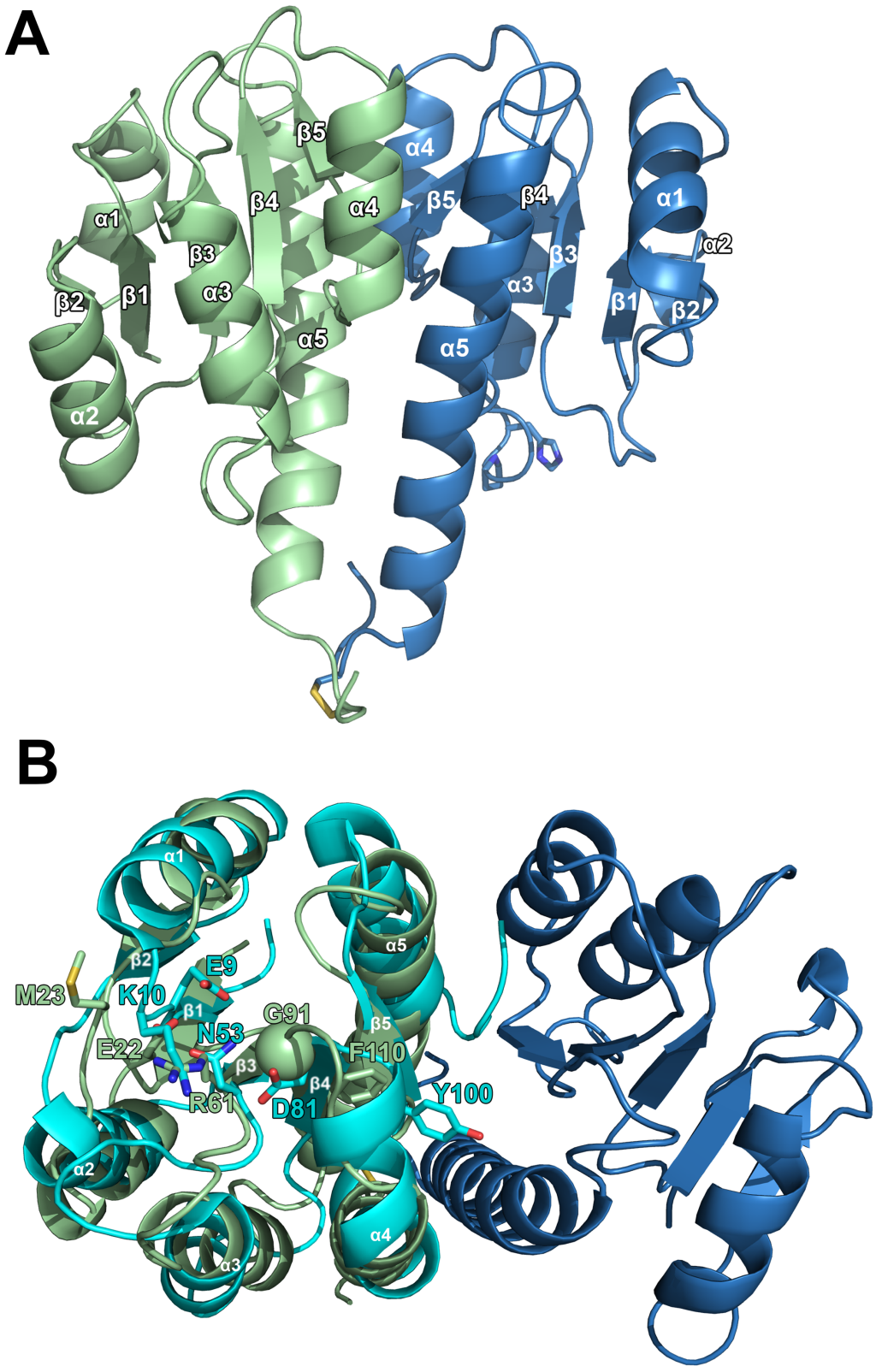
A
β5
α4
β4
α4
β5
β4
α1
α1
α2
β3
β3
α3
β2
β1
α3
β1
β2
α5
α5
α2
B
α1
α5
β2
E9
M23
K10
β1
G91
β5
N53
E22
F110
β3
β4
Y100
R61
D81
α2
α4
α3

The active site of each DGC domain has one molecule of citrate and a $Mg^{2+}$ ion bound (Figure 3-4). Due to the asymmetric arrangement of the domains—the lack of any inter-domain interface in chain A, and the weak interface between the ALR and DGC domains in chain B—there some differences in the way GTP binds to the two DGC domains. In chain A, there are no contacts between the ALR domain and the citrate. Without GTP addition in the crystallization condition, the structure of purified Q15Z91 alone has c-di-GMP bound, which must have co-purified during the protein expression in cells. In the I site, c-di-GMP forms a dimer through stacking their guanosine rings, interactions between phosphate group with N11 and N21 on the Hoogsteen-edge of the guanine base of the other chain and hydrogen bond between O61 with N7 of the other c-di-GMP (Figure 3-4).

The DGC domains found in other response regulator proteins also have a Rxx(D/E) motif that is associated with the inhibitory site. In Q15Z91, the residues of this Rxx(D/E) motif are R212 and D215. A shown in Figure 3-4, R212 interacts with the O6 and N7 atoms on the Hoogsteen-edge of the guanine base of one c-di-GMP molecule with 2.9 Å and 3.0 Å, respectively. The gunidinium group of R212 also interacts with the phosphate group of the second c-di-GMP within the c-di-GMP dimer at a distance of 2.8 Å. The carboxyl group of D215 forms hydrogen bonds with the N1 and N2 atoms on the Watson-Crick-edge of the guanine base of the second c-di-GMP molecule. There are also many other residues contributing to interacting with c-di-GMP dimer, including T232-N2 of the second c-di-GMP (2.7 Å), R168-posphate group of the c-di-GMP (2.8 Å), E213-posphate group of the c-di-GMP (2.9 Å).

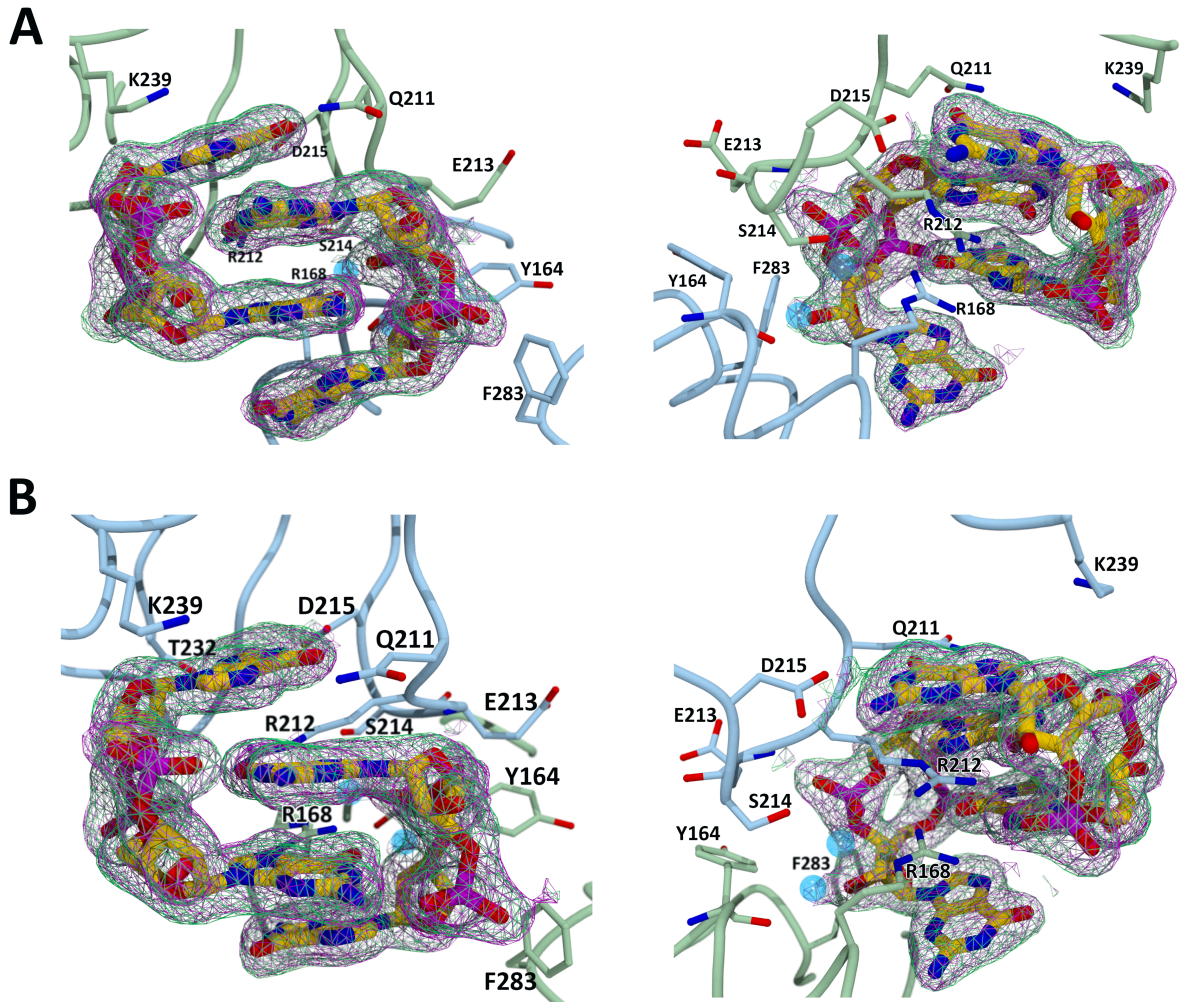


**Figure 3-4:** Two molecules of c-di-GMP dimerize through stacking of their bases and bind to the inhibitory sites on chain A (A) and chain B (B). The c-di-GMP dimers are shown as sticks with yellow carbon atoms. R212 and D215 are the most conserved residues in the I site. The $2|F_o|-|F_c|$ electron density map, contoured at 1.0σ, is shown as magenta mesh, and the $2|F_o|-|F_c|$ composite omit map, also contoured at 1.0σ, is shown as green mesh.

In addition to the I site with Rxx(D/E) motif, DGC has two active sites (A site) with GGEEF motif. In the structure of Q15Z91, two citrate molecules form the protein storage

buffer binds in the two A site respectively (Figure 3-5). E223, D179, carbonyl group of I180 and the citrate coordinate the $Mg^{2+}$ ion. The basic residues K301 and R305, as well as the amide N atoms of F182, F183 and K184 interact with two carboxyl groups of citrate. In chain B, where there is a small interface between the ALR and DGC domains, Q78 from the ALR domain interacts with H192, which takes on multiple conformations. Due to the small interaction interface, this interdomain construction is probably caused by the whole geometry of this c-di-GMP inhibited dimer.

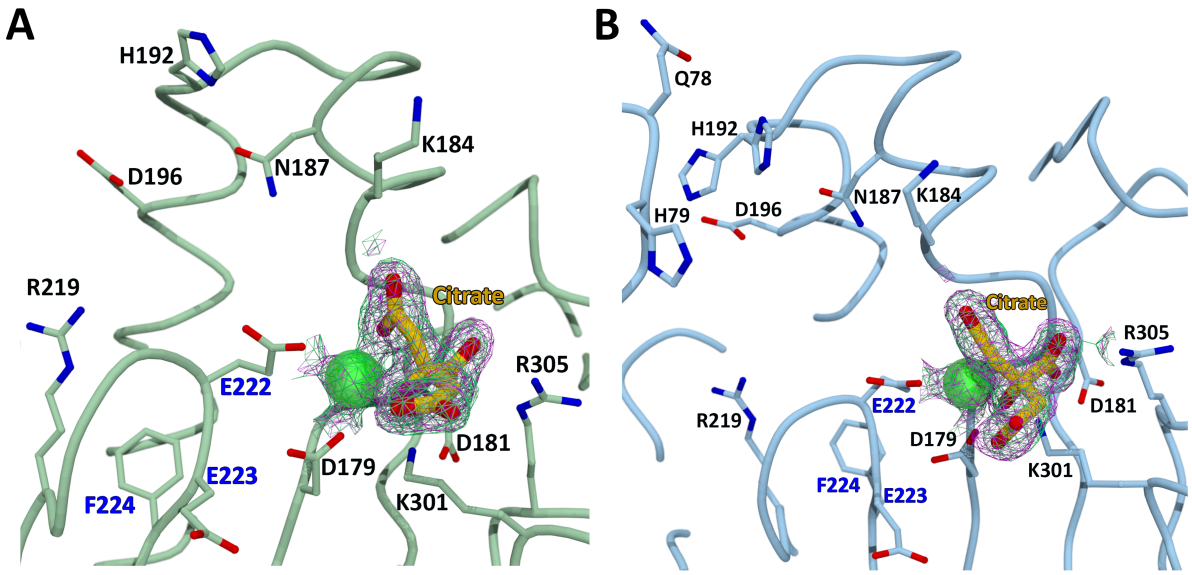


**Figure 3-5:** Citrate binds in slightly different orientations in the active sites of chain A (A) and chain B (B). Citrate is shown as sticks with yellow carbon atoms. The residues in the A site are also shown as sticks, with carbons colored according to the chain color. The labels of the conserved GGEEF residues are colored in blue. The $2|F_o|-|F_c|$ electron density map, contoured at 1.0σ, is shown as magenta mesh, and the $2|F_o|-|F_c|$ composite omit map, also contoured at 1.0σ, is shown as green mesh.

The structure of Q15Z91 with the substrate GTP was also determined with 1.8 Å data (Figure 3-6). The structure of Q15Z91 with GTP and c-di-GMP is same with the structure of Q15Z91 with citrate and c-di-GMP, except the GTP molecules bound in the A sites. The imidazole of H192 packs on top of the 6-membered ring of the nucleotide. The carboxyl group of D196 interacts with N2 of the guanosine. The guanidine group of R219 interacts with O6 of GTP. K184 forms a hydrogen bonding interaction to the 3' hydroxyl of GTP in chain B, while it interacts with 2'-OH of GTP in chain A. E223, D179, and the phosphate groups of GTP coordinate the $Mg^{2+}$ ion; the metal, therefore, serves to anchor the tri-phosphate moiety of GTP to the enzyme. The basic residues K301 and R305 interact with the terminal phosphate group. In chain B, where there is an interface between the ALR and DGC domains, Q78 from the ALR domain interacts with H192, which takes on multiple conformations and appears to have less of an interaction with the GTP. The relative interactions between D196, K184, and the GTP are different from those observed in chain A: K184 makes a hydrogen bonding interaction with the 3' hydroxyl of GTP rather than the 2' hydroxyl, and D196 loses the interactions with H192 due to the inter-domain interaction between Q78 and H192.

Comparison with the structure of diguanylate cyclase PleD (PDB ID 2V0N[14]), the structure of Q15Z91 with GTP and c-di-GMP is more likely an activated but product-inhibited form of Q15Z91.

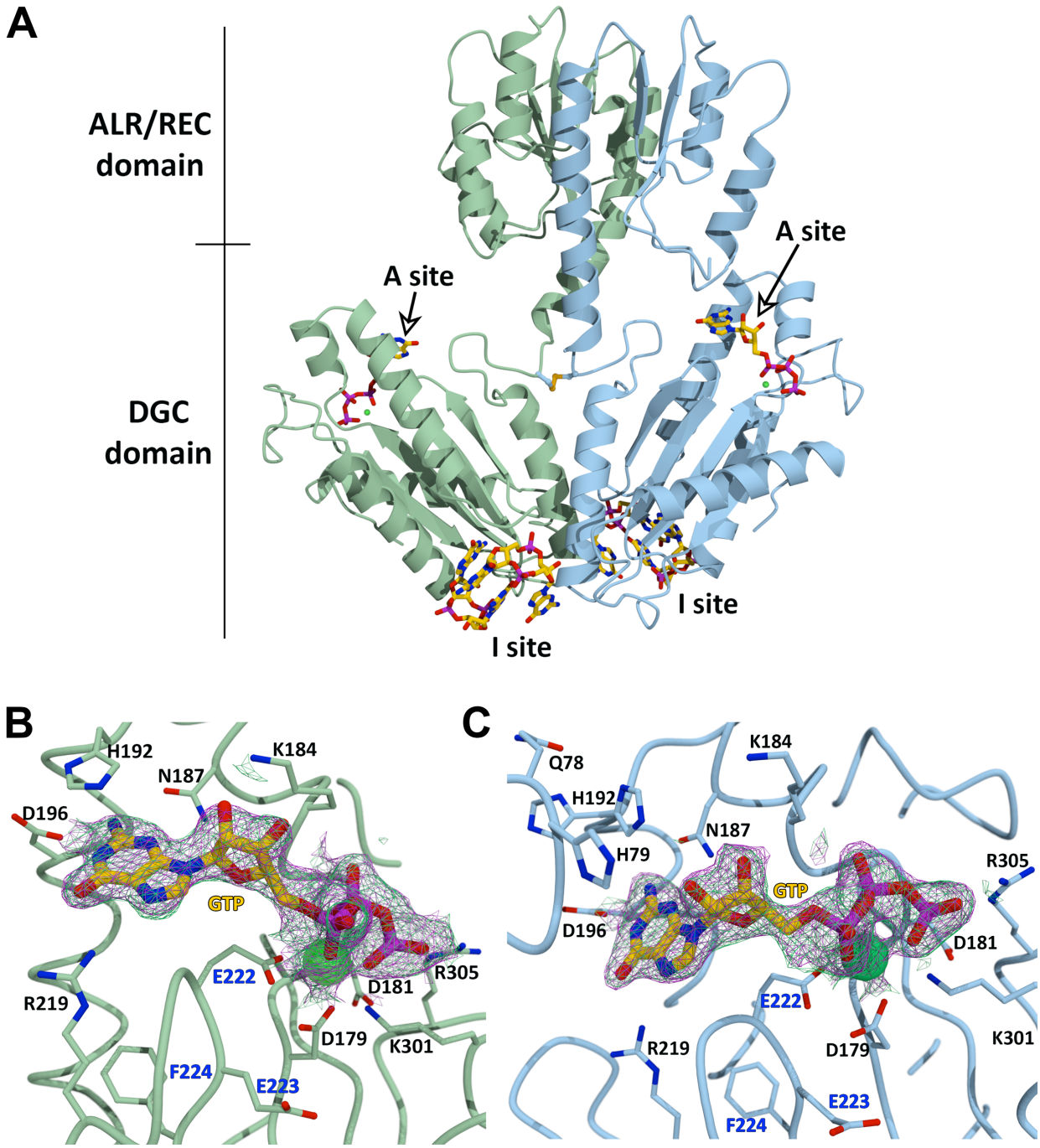


**Figure 3-6:** The structure of Q15Z91 with c-di-GMP and GTP bound (A). Chain A is colored in light green, while chain B is colored in light blue. Citrate and c-di-GMP are shown as sticks with yellow carbon atoms. GTP binds in slightly different orientations in the active sites of chain A (B) and chain B (C). GTP is shown as sticks with yellow carbon atoms. The residues involved in GTP interactions are also shown as sticks, with carbons colored according to the chain color. The labels of the conserved GGEEF residues are colored in blue. The

$2|F_o|-|F_c|$ electron density map, contoured at 1.0σ, is shown as magenta mesh, and the $2|F_o|-|F_c|$ composite omit map, also contoured at 1.0σ, is shown as green mesh.

It was not possible to obtain crystals of the un-inhibited (c-di-GMP-free) Q15Z91 and the $Q15Z91_{C142S}$ variant discussed below. The flexible conformation of the two catalytic domains without the product binding and disulfide bond may be one reason for the failures in crystallization of both c-di-GMP-free Q15Z91 and $Q15Z91_{C142S}$.

### 3.3.4 Probing the roles of conserved residues by site-directed mutagenesis

As mentioned in Chapter 2, the RitR double mutant $RitR_{L86A/V93A}$ exhibited activated characteristics (extended conformation and the ability to bind DNA). So the equivalent residues of Q15Z91, I99 and G102, were targeted for mutagenesis. C128 of RitR plays an important role in redox control. To determine whether or not the equivalent residue of Q15Z91, C142, has a similar role, this residue was changed to serine (C142S). Finally, R212 and D215 in the Rxx(D/E) I-site motif were mutated to Asn and Ala to determine the effect of disrupting the I-sites required for product inhibition. As described above, Q15Z91 and its variants only fold correctly in Origami2 *E. coli* cells, which have been engineered to have a less reducing environment in the cytoplasm and thus promote formation of disulfide bonds. After IPTG induction, biofilm formation was observed for in cultures expressing all forms of Q15Z91 we tested (Table 3-4). The fact that all of the Q15Z91 variants promoted biofilm formation indicates that none of them has been inactivated or catastrophically destabilized by the mutations.

**Table 3-4:** Characteristics of wild-type and mutant forms of Q15Z91.

| Proteins | Biofilm formation | c-di-GMP |
|---|---|---|
| Q15Z91 | + | + |
| I99A | + | + |
| G102A | + | + |
| C142S | + | - |
| R212N/D215A | + | - |

The c-di-GMP produced during expression binds so well to the I-site that it co-purifies with Q15Z91, even persisting through dialysis and desalting steps. To remove the product inhibition, we used the phosphodiesterase SadR from *Pseudomonas aeruginosa* to linearize c-di-GMP into pGpG, which is easily removed by gel filtration. This c-di-GMP-free protein is called $Q15Z91_{free}$. To determine whether or not the mutants had c-di-GMP bound, the absorbance at 260 nm (due to the nucleotide) was measured for Q15Z91 and each of the mutants. The results demonstrate that only the C142S and R212N/D215A variants do not have c-di-GMP bound. This was expected for the double mutant, since both of those residues are involved in key interactions with the c-di-GMP dimer in the I-site. The fact the loss of C142S impacts product binding to the I-site as drastically it does was surprising and likely indicates that reduction of the C142-mediated disulfide bond increases Q15Z91-catalyzed DGC activity by relieving the product inhibition.

### 3.3.5 The oligomeric state of Q15Z91

As shown in Figure 3-7, Q15Z91 mainly exists as a dimer with c-di-GMP bound (retention time 5.2 min). The peak with a retention time of ~6.2 min is due to c-di-GMP, which is verified by the higher absorption at 260 nm than at 280 nm. After treatment with SadR and gel filtration, $Q15Z91_{free}$ still mainly exists as a dimer; the absence of the peak at ~6.2 min is further evidence that that peak is due to c-di-GMP. The $Q15Z91_{free}$ protein is considerably less stable than Q15Z91 (with c-di-GMP bound), as evidenced by the greater proportion of aggregated protein seen in the chromatogram. The retention time of the Q15Z91 dimer was longer than expected based on the molecular weight standards. This may be due to shape effects or direct interactions between the protein and column matrix.

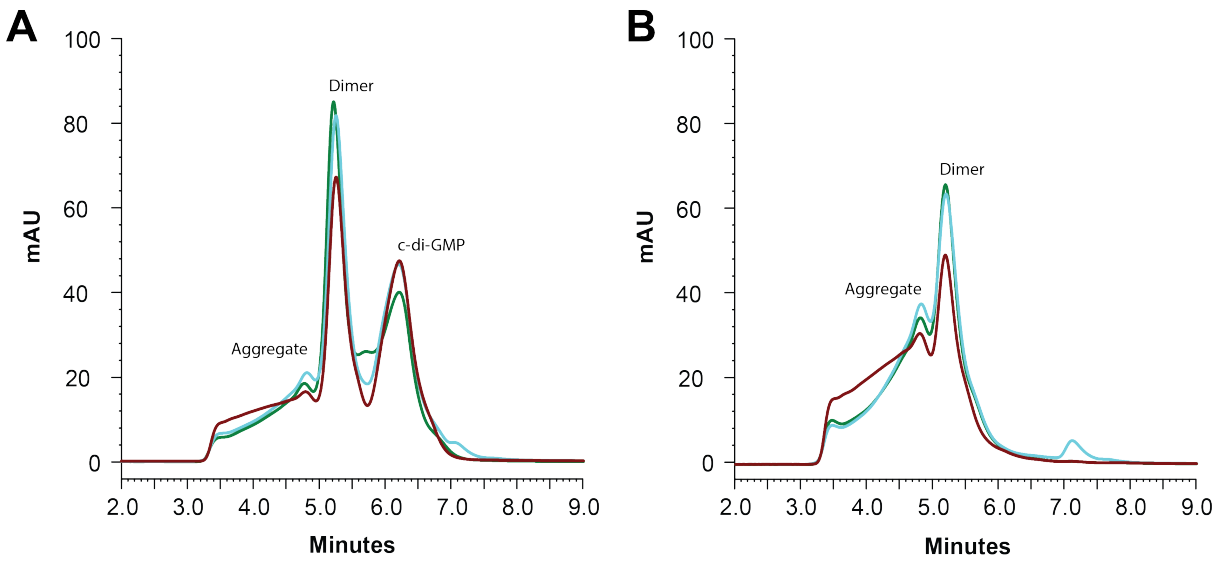


**Figure 3-7:** The affects of $H_2O_2$ or DTT treatment on the oligomeric states of Q15Z91 (A) and $Q15Z91_{free}$ (B) were analyzed by SEC. The traces of protein only colored in green, protein with 1 mM $H_2O_2$ treatment colored in brown red and protein with 1 mM DTT treatment is colored in cyan.

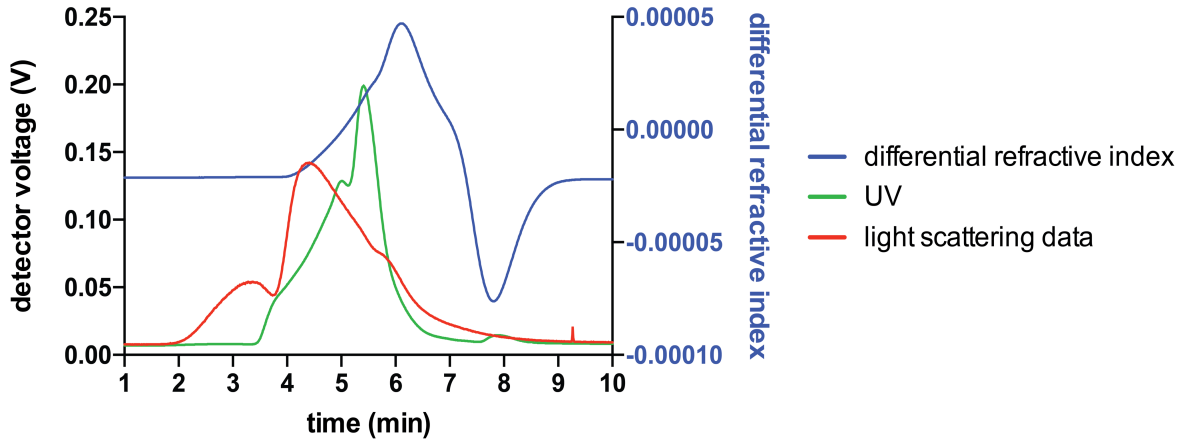


| Elution time (min) | 2.7-3.1 | 3.4-4.0 | 4.2-4.9 | 5.1-5.7 | 6.0-6.3 |
|---|---|---|---|---|---|
| Molar mass (kDa) | 101.8e+3 | 984.3 | 219.4 | 79.1 | 64.7 |

**Figure 3-8:** SEC-MALS results for $Q15Z91_{free}$.

In order to get a more accurate mass estimate for the molecule responsible for the peak at 5.2 min, $Q15Z91_{free}$ was analyzed by size exclusion chromatography with multi-angle static light scattering (SEC-MALS). The chromatograms were analyzed using the ASTRA software package (Figure 3-8). The major peak in the UV trace (retention time range 5.1-6.3 min) has a mass of 65-79 kDa, which is close to the mass of the Q15Z91 dimer. The peaks that elute earlier than 5 min were verified to be high molecular weight aggregates. To check the effects of reducing or oxidizing agents on the oligomeric state, DTT and $H_2O_2$ were added to Q15Z91 and $Q15Z91_{free}$ samples (1 mM each). SEC analysis (Figure 3-7) shows that oxidizing and reducing C142 have no effect on the oligomeric state of either form of the protein (free or product-inhibited).

The oligomeric state of each of the Q15Z91 point mutants was also checked by size exclusion chromatography (Figure 3-9). The mutants I99A and G102A both existed as dimers with c-di-GMP bound. Like the wild-type protein, both mutants existed as dimers after treatment with SadR to remove the c-di-GMP. Interestingly, in spite of being treated in exactly the same way, SadR was apparently not able to remove all of the c-di-GMP from the I99A mutant. Consistent with the UV/vis data, the other two mutants C142S and R212N/D215A, existed as dimers without c-di-GMP bound. Neither of these mutants is affected by treatment with DTT or $H_2O_2$.

**Figure 3-9:** The oligomeric states of $Q15Z91_{I99A}$ (A), c-di-GMP-free $Q15Z91_{I99A}$ (B), $Q15Z91_{G102A}$ (C), c-di-GMP-free $Q15Z91_{G102A}$ (D), $Q15Z91_{C142S}$ (E), $Q15Z91_{R212N/D215A}$ (F) with or without $H_2O_2$ or DTT treatment were analyzed by SEC. The traces of protein only colored in green, protein with 1 mM $H_2O_2$ treatment colored in brown red and protein with 1 mM DTT treatment is colored in cyan.

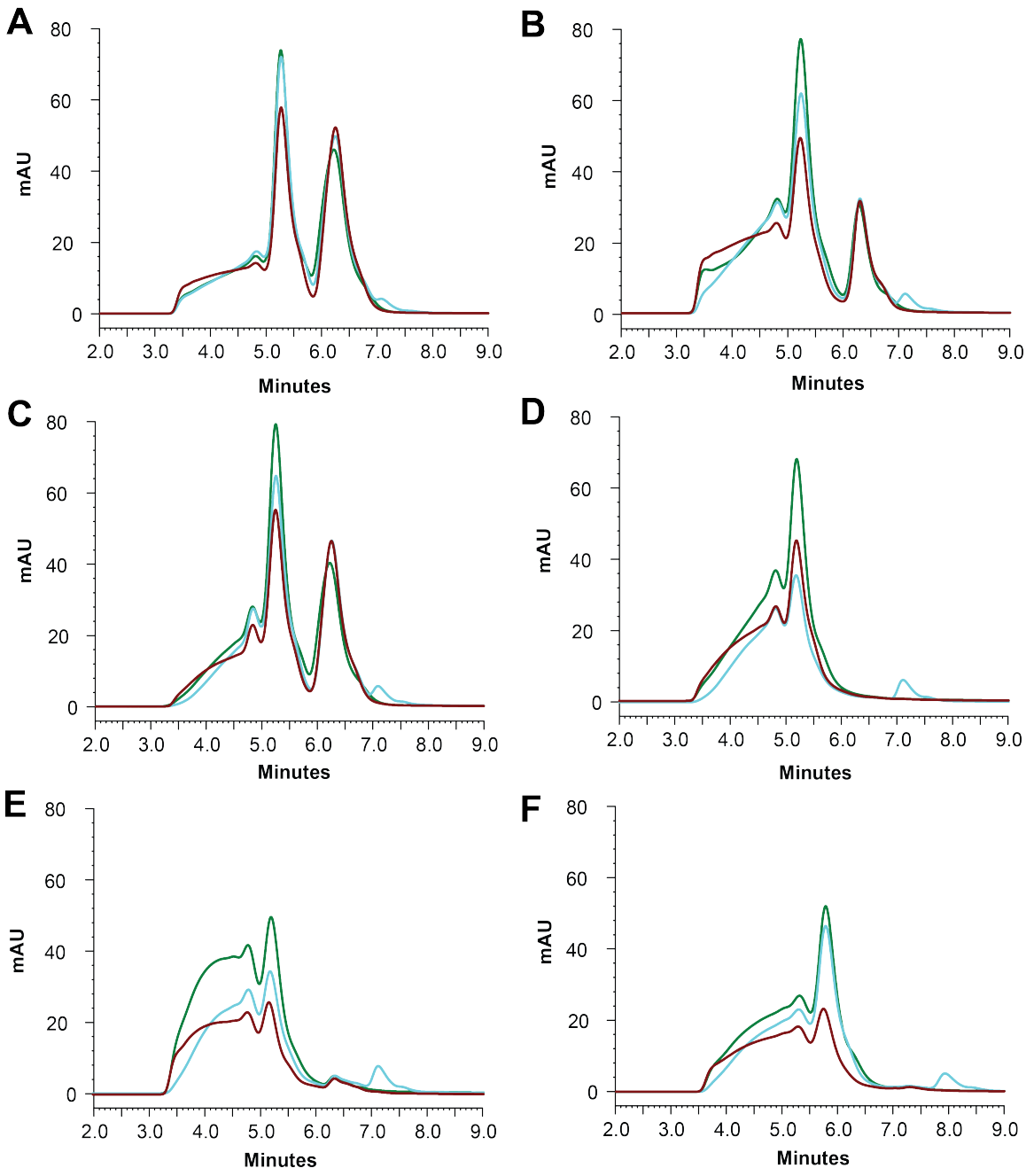


### 3.3.6 Preliminary quantitation of biofilm phenotype

In order to quantify the observed biofilm formation phenotype of Origami2 cells expressing Q15Z91 or its mutants, the amount of biofilm material deposited on the walls of

culture tubes was measured by the degree of staining with crystal violet as described in the methods section. All proteins were expressed as $His_6$-SUMO fusion proteins; the fact that biofilm formation was observed in response to Q15Z91 expression is evidence that the SUMO tag does not affect the catalytic activity of the protein. After dissolving the crystal violet-stained biofilm in a mixture of ethanol and acetone, the absorbance at 540 nm was measured. The amount of dye, and thus the absorbance, is proportional to the amount of biofilm present. Cultures were induced at an $OD_{600nm}$ of ~0.7, except for the $Q15Z91_{C142S}$ culture in LB with kanamycin. After growing for 7 hours at 37 °C, the $OD_{600nm}$ of C142S mutant in kanamycin-containing culture was still about 0.3, so 0.4 mM IPTG was added to induce SUMO-$Q15Z91_{C142S}$ expression. It is circumstantial, but this result may suggest that the C142S variant is constitutively active, and therefore, that the reduced form of the protein is the activated form.

In Figure 3-10A, it is clear that all of the other mutants formed biofilm and that the cells are evenly distributed in the medium. The cells carrying the pSUMO-C142S plasmid aggregated at the bottom of the culture tube. The $A_{540}$ of the biofilm extract from the $Q15Z91_{C142S}$ culture is the highest one. The double mutant R212N/D215A only formed a small amount of biofilm, which suggests that the I-site is also important for the cyclase activity.

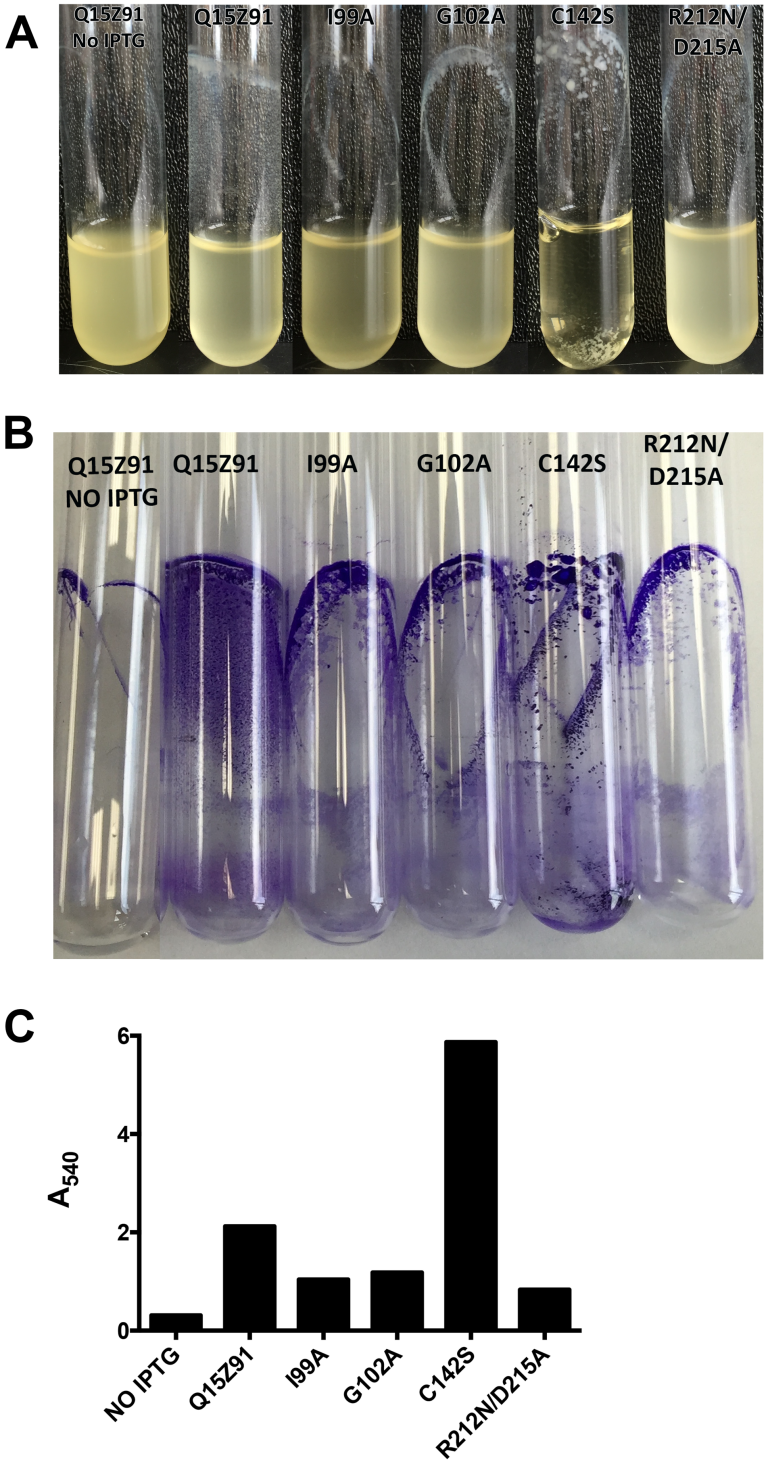


**Figure 3-10:** Biofilm formation after IPTG induction in Origami2 cells with Q15Z91 related plasmids. (A) cultures photo (B) After crystal violet stain. (C) Biofilm amounts are quantified by absorbance at 540 nm. The biofilm formed in Q15Z91$_{C142S}$ is significantly higher than others.

### 3.3.7 Preliminary enzymatic activity

Three different assays were attempted in order to characterize the diguanylate cyclase activities of Q15Z91 and $Q15Z91_{free}$ in the presence and absence of DTT and $H_2O_2$. The first was an end-point assay where the proteins were incubated for 30 min in the presence of GTP and $MgCl_2$. The reaction products were then characterized by reverse-phase HPLC. Extensive method development work failed to identify combinations of stationary and mobile phases whereby GTP could be separated from the product c-di-GMP. In all of the methods tested, the analytes were not retained on the columns.

The second assay used the Biomol Green reagent to quantify the inorganic pyrophosphate released by the DGC. Since Biomol Green can only detect $P_i$, pyrophosphotase was used to digest the $PP_i$ into two equivalents of $P_i$. The reactions contained 10 μM Q15Z91 or $Q15Z91_{free}$, 0.2 mM GTP, and 2 mM $MgCl_2$, and were incubated at RT for a total of 180 min. Aliquots were quenched at specific time points and the $P_i$ content was measured to build a time course of the reaction. The preliminary results for Q15Z91 and $Q15Z91_{free}$ with GTP are shown in Figure 3-11. Both and $Q15Z91_{free}$ exhibit a very low rate of $PP_i$ release. This is not unexpected, since Q15Z91protein purify as its product-inhibited form and $Q15Z91_{free}$ may form disulfide bond and immobilize the DGC domains. Consistent with the SEC results above, the addition of 1 mM DTT results in a much more rapid reaction. The reaction is so rapid, in fact, that it was complete by the time the first aliquot was taken (10 min). The effect of DTT is especially pronounced with the $Q15Z91_{free}$ enzyme, likely because this reaction is not contaminated with c-di-GMP.

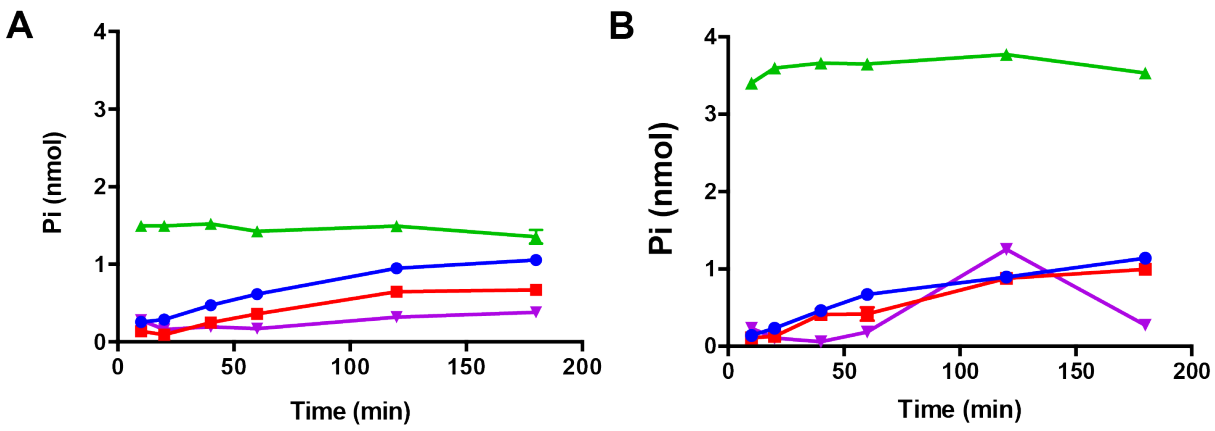


**Figure 3-11:** Time courses for the reaction of Q15Z91 (A) and Q15Z91$_{free}$ (B) with 0.2 mM GTP in the absence or presence of $H_2O_2$ or DTT. Blue line represents enzyme Q15Z91 or Q15Z91$_{free}$ only. Red line represents 1 mM $H_2O_2$ treatment. Green line represents 1 mM DTT treatment. Purple line represents the reaction conducted at 4 $^{o}$C.

Due to the speed of the reaction with the DTT-treated protein, we sought a direct assay that would allow us to monitor earlier time points. The EnzCheck assay kit (Sigma) allows the real-time monitoring of phosphate release by coupling it to purine nucleoside phosphorylase-catalyzed phosphorylation of the synthetic nucleotide MESG, which absorbs light at 360 nm. The first experiments with this assay were inconclusive, since the 10 min pre-incubation with MESG, purine nucleoside phosphorylase appeared to destabilize the enzyme, resulting in extremely small rates.

## 3.4 Discussion

Q15Z91 is a diguanylate cyclase that is regulated by an ALR domain. Key residues for the phosphorylation-dependent activation of typical response regulator receiver domains, particularly the acidic triad residues, have been lost in Q15Z91. The phosphorylatable aspartate is replaced by arginine, and the other two acidic triad residues are replaced with Met and Glu. These changes exclude the possibility of phosphorylation-dependent activation of Q15Z91. In spite of this, the positions of the switch residues positions and the dimer interface of Q15Z91 are similar to those of the typical, phosphorylation-dependent OmpR/PhoB RRs. Q15Z91, like RitR, the other ALR domain-containing protein discussed here, also has a conserved cysteine residue in the linker between the ALR and effector domains.

Q15Z91 purifies as a product-inhibited form with c-di-GMP bound. The Q15Z91 structure, as well as the SEC results, demonstrates that Q15Z91 exsits as a dimer. After removal of c-di-GMP, it maintains this dimer conformation. Neither $H_2O_2$ nor DTT have any effect on the oligomeric state of Q15Z91. Preliminary activity tests show that the activities of Q15Z91 and $Q15Z91_{free}$ are dramatically increased in the presence of DTT. To check the role of the conserved cysteine residue, Cys142 was mutated into serine. The variant $Q15Z91_{C142S}$ is also dimeric, providing ample evidence that Q15Z91 is not regulated by a switch between dimer and monomer as RitR is. Interestingly, the C142S mutant is no longer able to bind c-di-GMP, or at least only with much reduced affinity compared with the wild-type protein. Cyclic di-GMP, as an important second messenger, regulates biofilm formation, which is an important phenotype to check the cyclase activity in heterogeneous

cell systems. According to the results of our biofilm assays, there is a significant increment of biofilm formation for Q15Z91$_{C142S}$ mutant. In other words, the variant C142S seems to greatly reduce product inhibition by c-di-GMP, which means the disulfide bond formation is likely essential for c-di-GMP binding. In summary, we propose that C142 of Q15Z91 is not essential for dimerization, but involved in facilitating c-di-GMP binding and product feedback inhibition.

In RitR, the C128 functions as redox sensor to control the inter-domain interactions for later dimerization and activation. Considering the dimer structure of Q15Z91, Q15Z91 appears to be constitutively active and this activity is modulated by product inhibition. Under oxidizing conditions, where the C142 disulfide bond is formed, product inhibition is potent and the DGC activity of Q15Z91 is low. Under reducing conditions, the C142 disulfide bond is broken, decreasing the affinity for c-di-GMP and largely removing the product inhibition. Taken together, the cysteine located at the C-terminal end of the α5 linker helix is important for the activation mechanism of Q15Z91. This is a departure from the well-studied phosphorylation-dependent diguanylate cyclases PleD[14-16] and WspR[4], where product inhibition is modulated by changes in the oligomeric state (dimer-tetramer equilibrium) that are influenced by additional domains. In short, Q15Z91 replaces the extra domain of PleD and WspR with a redox-active cysteine that directly influences product inhibition.

There are about fifty DGCs in *P. atlantica* T6c. These DGCs tend to be fused to PAS or GAF sensor domains, to additional regulatory domains, or to phosphodiesterase domains. These apparent redundancies but with different activation mechanisms DGCs/PDEs raises

a question that how the small molecule c-di-GMP to regulate the activities of these different diguanylate cyclase enzymes. By studying Q15Z91, we find that c-di-GMP inhibition regulation is dependent on the C142 disulfide bond formation. So we can assume that there are definitely other mechanisms combining with product binding to regulate specific DGC/PDE activity upon different environmental stimulation.

### 3.5 References


[1] Maule, A. F., Wright, D. P., Weiner, J. J., Han, L., Peterson, F. C., Volkman, B. F., Silvaggi, N. R., and Ulijasz, A. T. (2015) The Aspartate-Less Receiver (ALR) Domains: Distribution, Structure and Function, *PLOS Pathogens 11*, e1004795.

[2] Altschul, S. F., Gish, W., Miller, W., Myers, E. W., and Lipman, D. J. (1990) Basic local alignment search tool, *Journal of molecular biology 215*, 403-410.

[3] States, D. J., and Gish, W. (1994) Combined use of sequence similarity and codon bias for coding region identification, *Journal of computational biology : a journal of computational molecular cell biology 1*, 39-50.

[4] De, N., Pirruccello, M., Krasteva, P. V., Bae, N., Raghavan, R. V., and Sondermann, H. (2008) Phosphorylation-Independent Regulation of the Diguanylate Cyclase WspR, *PLoS biology 6*, e67.

[5] Otwinowski, Z., and Minor, W. (1997) Processing of X-ray diffraction data collected in oscillation mode, *Methods in enzymology 276*, 307-326.

[6] Terwilliger, T. C., Grosse-Kunstleve, R. W., Afonine, P. V., Moriarty, N. W., Zwart, P. H., Hung, L.-W., Read, R. J., and Adams, P. D. (2008) Iterative model building, structure refinement and density modification with the PHENIX AutoBuild wizard, *Acta Crystallographica Section D 64*, 61-69.

[7] McCoy, A. J., Grosse-Kunstleve, R. W., Adams, P. D., Winn, M. D., Storoni, L. C., and Read, R. J. (2007) Phaser crystallographic software, *Journal of applied crystallography 40*, 658-674.

[8] Emsley, P., Lohkamp, B., Scott, W. G., and Cowtan, K. (2010) Features and development of Coot, *Acta crystallographica. Section D, Biological crystallography 66*, 486-501.

[9] Adams, P. D., Afonine, P. V., Bunkóczi, G., Chen, V. B., Davis, I. W., Echols, N., Headd, J. J., Hung, L.-W., Kapral, G. J., Grosse-Kunstleve, R. W., McCoy, A. J., Moriarty, N. W., Oeffner, R., Read, R. J., Richardson, D. C., Richardson, J. S., Terwilliger, T. C., and Zwart, P. H. (2010) PHENIX: a comprehensive Python-based system for macromolecular structure solution, *Acta Crystallographica Section D: Biological Crystallography 66*, 213-221.

[10] Word, J. M., Lovell, S. C., Richardson, J. S., and Richardson, D. C. (1999) Asparagine and glutamine: using hydrogen atom contacts in the choice of side-chain amide orientation11Edited by J. Thornton, *Journal of molecular biology 285*, 1735-1747.
[11] Urzhumtseva, L., Afonine Pv Fau - Adams, P. D., Adams Pd Fau - Urzhumtsev, A., and Urzhumtsev, A. Crystallographic model quality at a glance.
[12] Upson, R. H., Haugland, R. P., Malekzadeh, M. N., and Haugland, R. P. (1996) A spectrophotometric method to measure enzymatic activity in reactions that generate inorganic pyrophosphate, *Analytical biochemistry 243*, 41-45.
[13] Webb, M. R. (1992) A continuous spectrophotometric assay for inorganic phosphate and for measuring phosphate release kinetics in biological systems, *Proceedings of the National Academy of Sciences 89*, 4884-4887.
[14] Wassmann, P., Chan, C., Paul, R., Beck, A., Heerklotz, H., Jenal, U., and Schirmer, T. (2007) Structure of BeF3−-Modified Response Regulator PleD: Implications for Diguanylate Cyclase Activation, Catalysis, and Feedback Inhibition, *Structure 15*, 915-927.
[15] Chan, C., Paul, R., Samoray, D., Amiot, N. C., Giese, B., Jenal, U., and Schirmer, T. (2004) Structural basis of activity and allosteric control of diguanylate cyclase, *Proc Natl Acad Sci U S A 101*, 17084-17089.
[16] Paul, R., Abel, S., Wassmann, P., Beck, A., Heerklotz, H., and Jenal, U. (2007) Activation of the diguanylate cyclase PleD by phosphorylation-mediated dimerization, *The Journal of biological chemistry 282*, 29170-29177.

# Chapter 4

## An Unusual PLP-Dependent Enzyme in Enduracididine Biosynthesis

### 4.1 Introduction

The emergence of antibiotic-resistant pathogens is a serious and growing threat to global health. There is an urgent need for new antibiotics to combat this threat. Unfortunately, the pace of antibiotic development has slowed almost to a standstill (Figure 4-1).

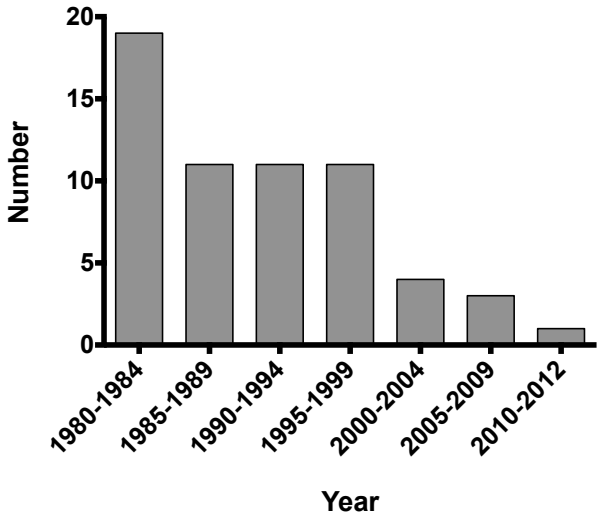


**Figure 4-1:** The numbers of new antibiotic compounds approved have been declining steadily since 1980. Data from the FDA Center for Drug Evaluation and Research.

In response to the dismal rate of antibiotic development, among other problems, Congress passed the Food and Drug Administration Safety and Innovation Act (FDASIA).

Title VIII of this law, Generating Antibiotic Incentives Now (GAIN), created a fast track for new antibiotic approvals that seems to be paying off. While there have been no new classes of antibiotics, a number of new drugs based on old scaffolds have been introduced since the passage of the FDASIA; in 2014-15 six new antibiotics were approved by the FDA. Happily, it seems that interest in antibiotic development is on the rise. Consequently, any information regarding the biosynthesis or activity of antibiotics or key building blocks of these compounds, is potentially useful in these renewed efforts to discover new antibiotics.

In this context, the non-proteinogenic amino acid L-enduracididine (L-End, **1**, Scheme 4-1) is particularly interesting. This conformationally restricted form of arginine is present in a number of antibiotics, including some with potent activity against antibiotic-resistant strains like methicillin-resistant *Staphylococcus aureus* (MRSA) and vancomycin-resistant enterococci (VRE). Some prominent examples are the cyclic depsipeptide antibiotics enduracidin [3], mannopeptimycin [4] and the recently discovered teixobactin [5].

Enduracidin was first isolated from *Streptomyces fungicidicus* No. B 5477[3]. It is a seventeen amino acid lipodepsipeptide containing one residue of L-End and one of D-End (Scheme 4-2). In spite of having different amino acids and acyl chain, the overall structure enduracidin is similar to the cyclodepsipeptide antibiotic ramoplanin [6]. Both enduracidin and ramoplanin are active against resistant Gram-positive bacteria by binding to the external membrane surface of the lipid II intermediate, inhibiting the transglycosylation reaction of cell wall biosynthesis [7]. Ramoplanin has entered phase III clinical trials for VRE suppression in gastrointestinal tract infections and prevention of bloodstream infections, but enduracidin is hampered by its low aqueous solubility [8].

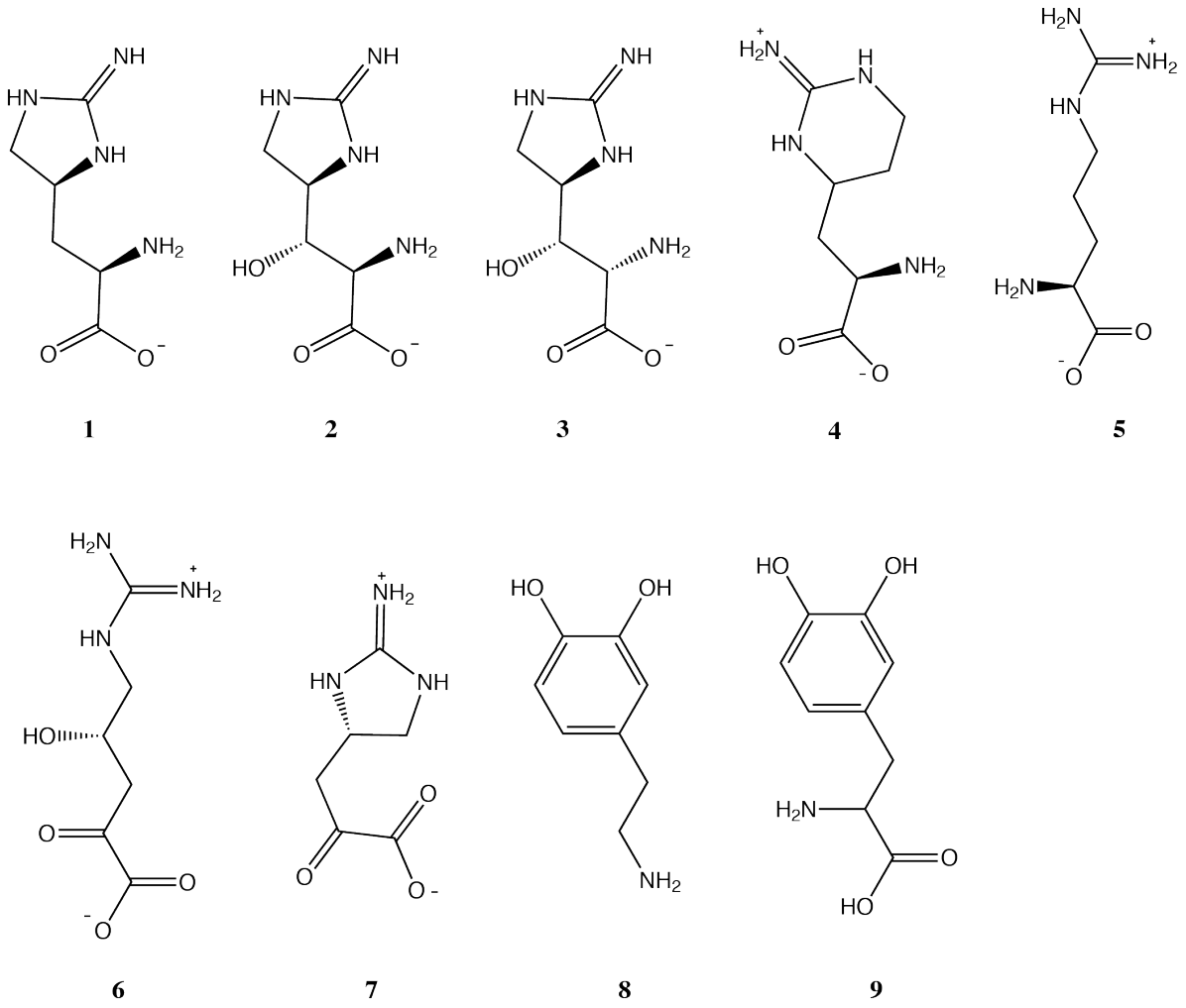

**Scheme 4-1:** Compounds mentioned in this chapter. **1**, L-enduracididine; **2**, L-β-hydroxyenduracididine; **3**, D-β-hydroxyenduracididine; **4**, capreomycidine; **5**, L-arginine; **6**, 2-oxo-4-hydroxy-5-guanidinovaleric acid (*i.e.* 4-hydroxy-ketoarginine, 4HKA); **7**, 2-ketoenduracididine (2KE); **8**, L-3,4-dihydroxyphenylalanine (L-DOPA); **9**, dopamine.

Another cyclic End-containing nonribosomal antibiotic, mannopeptimycin, is a glycosylated hexapeptide that also has activity against resistant Gram-positive bacteria, including MRSA and VRE[4, 9]. Mannopeptimycin also inhibits peptidoglycan synthesis by binding to lipid II[9]. Studies of the mechanism of action suggested that mannopeptimycin

may first bind to the lipoteichoic acids of the Gram-positive cell wall, and then accumulates to interact with lipid II[9]. The structure of mannopeptimycins α, β, γ, δ, and ε from *Streptomyces hygroscopicus* LL-AC98 were characterized in 2002[4]. They contain the non-proteinogenic amino acids L-β-hydroxyenduracididine (**2**, L-βhEnd) and D-β-hydroxyenduracididine (**3**, D-βhEnd). Methods for the total synthesis of mannopeptimycins α and β were published recently[10], but these two mannopeptimycins have relatively poor anti-bacterial activities. Much work (a Sci-Finder search returns more than 2000 analogs) has gone into making derivatives in the hope of finding one that has better therapeautic properties than the mannopeptimycins[11-17]. However, almost all of these involve changes to the attached glycans; very few of them alter the peptide core itself.

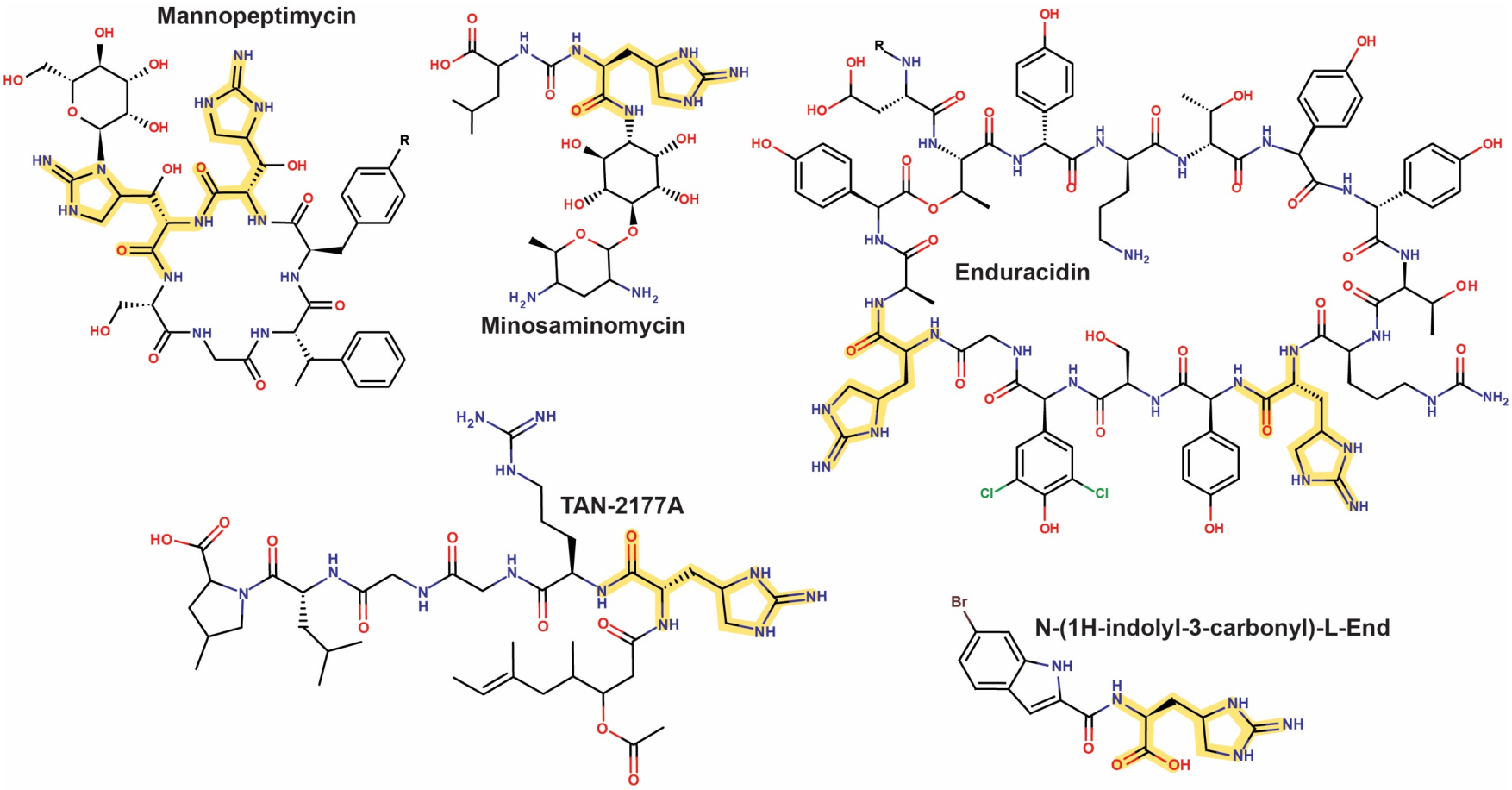


**Scheme 4-2**: Enduracididine-containing natural products. Enduracididine residues are highlighted in yellow

Mannopeptimycin and enduracidin are both antibiotics with potent activity against antibiotic-resistant strains. To improve the physico-chemical properties and/or biological activities for therapeutic applications, they probably require further chemical modifications. However, the total syntheses of enduracidin and mannopeptimycin are limited by the complexity of the structures and lmited commercial availability of some non-proteinogenic amino acid building blocks like enduracididine and its derivatives. Hence, a supply of L-End in quantities suitable to support drug development would greatly facilitate efforts to make derivatives of L-End-containing natural products.

Several synthetic routes to L-End or its β-hydroxy analogs have been published. Shiba et al. began with the methyl ester of L-histidine, which underwent cleavage of the imidazole ring to give a protected amide that was subsequently deprotected, guanidinylated, and treated with HF to give L-End as a diasteriomeric mixture [18]. The whole procedure involves only 4 steps, but it requires HF, which is hazardous, and the yield of the proper diasteriomer is low (22%). Dodd et al. used an aziridine-based method to synthesize 9-phenylfluorenyl-protected L-End with 4 steps, but the yield is still low (33%) [19]. No improvement in the yield was obtained after many attempts. The azide derivatives of β-hydroxy-End were first synthesized by Oberthür et al.[20]. It takes 21 steps to synthesize **2** with ~16% overall yield, and 24 steps to synthesize compound **3** with ~10% yield. After optimization, shorter routes were developed (*e.g.* 8 steps from Garner's aldehyde), but with no improvement in the yields (16% for **2** and 8% for **3**)[21]. Recently, the most efficient route to N-mannosyl-D-β-hydroxy-End was published by Cheng et al., which gave 43% yield[22]. Given the difficulties of synthesizing the nitrogen-rich iminoimidazolidine ring of the L-

End, and the presence of two chiral centers, an enzymatic or chemo-enzymatic route to L-End may prove to be the most efficient means of producing large quantities of L-End.

### 4.2 Biosynthesis of enduracididine

The enduracididine biosynthetic genes were first identified by comparing the enduracidin biosynthetic cluster in *S. fungicidicus* to that of the mannopeptimycins from *S. hygroscopicus* [23, 24]. The enduracidin and mannopeptimycin scaffolds are very different. In fact, aside from the presence of L-End in both products, and the fact that both are non-ribosomally produced depsipeptides, there are no similarities between them. Thus, the presence of 3 pairs of genes in the two biosynthetic clusters with high pairwise sequence identity suggested that these genes are likely responsible for L-End biosynthesis. The products encoded by these gene pairs are MppP/EndP (85%), MppQ/EndQ (66%), and MppR/EndR (73%) (Mpp = mannopeptimycin; End = enduracidin; Figure 4-2). Primary sequence analysis suggested that products P and Q were pyridoxal-5'-phosphate (PLP)-dependent aminotransferases, and that R was likely an acetoacetate decarboxylase.

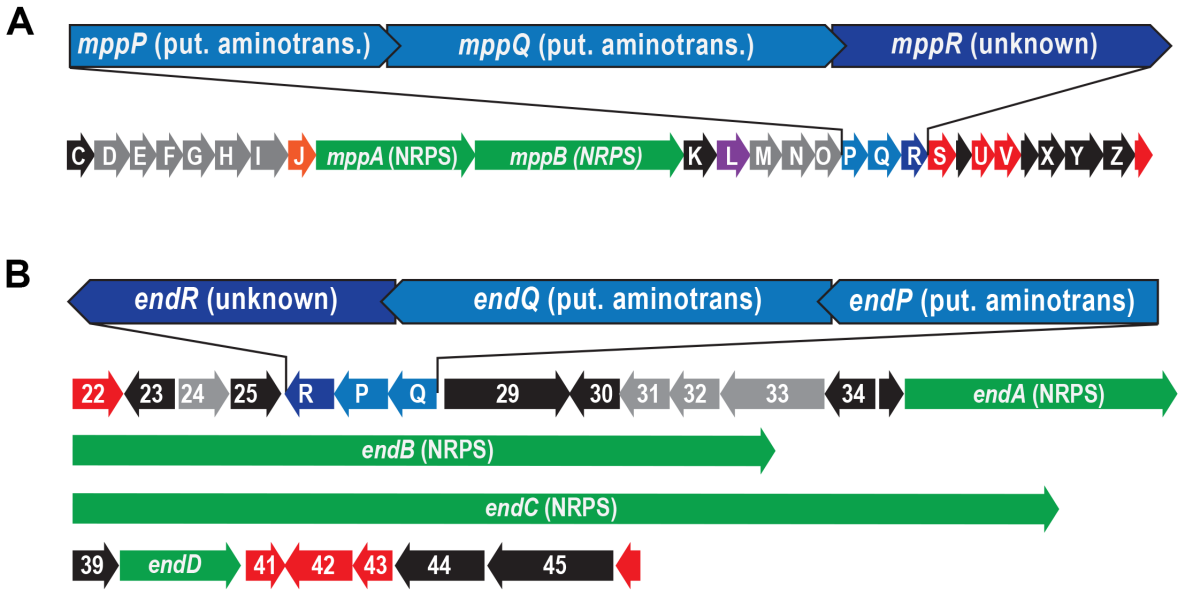


C

| Proteins | Sequence similarity | Predicted function |
|---|---|---|
| MppP | 85% with EndP | PLP-dependent aminotransferase |
| MppQ | 66% with EndQ | PLP-dependent aminotransferase |
| MppR | 73% with EndR | Acetoacetate decarboxylase |

**Figure 4-2:** Comparison of the mannopeptimycin biosynthetic cluster (A) with that of enduracidin (B) suggested that the three genes *mppP/endP*, *mppQ/endQ* and *mppR/endR* are involved in enduracididine biosynthesis. These genes are enlarged and colored in blue. Comparing the sequences of MppP with EndP, MppQ with EndQ, and MppR with EndR (C) shows a high degree of pairwise sequence identity. On the basis of their sequences, Mpp/EndP and Mpp/EndQ are predicted to be PLP-dependent aminotransferases and Mpp/EndR is predicted to be an acetoacetate decarboxylase.

Experiments by K. Hatano et al.[25] used radio-labeled amino acids to investigate the biosynthetic origin of L-End and found that the most radioactivity was incorporated into

the L-End fraction of the enduracidin that was produced when cultures were fed with labeled L-Arg. Thus, it was concluded that the biosynthesis of L-End, now presumed to be carried out by Mpp/EndP, Mpp/EndQ, and Mpp/EndR, likely begins from L-Arg[25]. This, in turn, suggests that the iminoimidazolidine ring of End is probably formed by cyclization between the γ-carbon and one of the guanidine N atoms of arginine [25]. There is precedent for this sort of transformation in the biosynthesis of another arginine-derived non-proteinogenic amino acid, L-capreomycidine (L-Cap, **4**; Scheme 4-3). Capreomycidine is found in the antibiotic viomycin, and its biosynthesis was initially thought to provide a possible chemical logic for L-End biosynthesis. In the viomycin biosynthetic cluster from *S. vinaceus*, L-Cap (compound **4**) is produced from L-Arg (compound **5**) by two enzymes: VioC and VioD. VioC is an Fe(II)/α-ketoglutarate-dependent oxygenase that hydroxylates L-Arg at the β-carbon to give 3S-hydroxy-L-Arg [26]. This product is then cyclized by VioD, a PLP-dependent aminotransferase that catalyzes an intra-molecular transamination to give the 6-membered capreomycidine ring[27, 28].

According to their amino acid sequences, MppP and MppQ were both predicted to be class I/II aminotransferases, while MppR was predicted to be an acetoacetate decarboxylase. Assuming that L-End biosynthesis likely occurs in a similar way to L-Cap biosynthesis, that is by activation of L-Arg by hydroxylation followed by transamination, it was not clear exactly how two aminotransferases and a decarboxylase would accomplish this transformation. Clearly, there had to be a difference in the biosynthetic schemes of L-Cap and L-End.

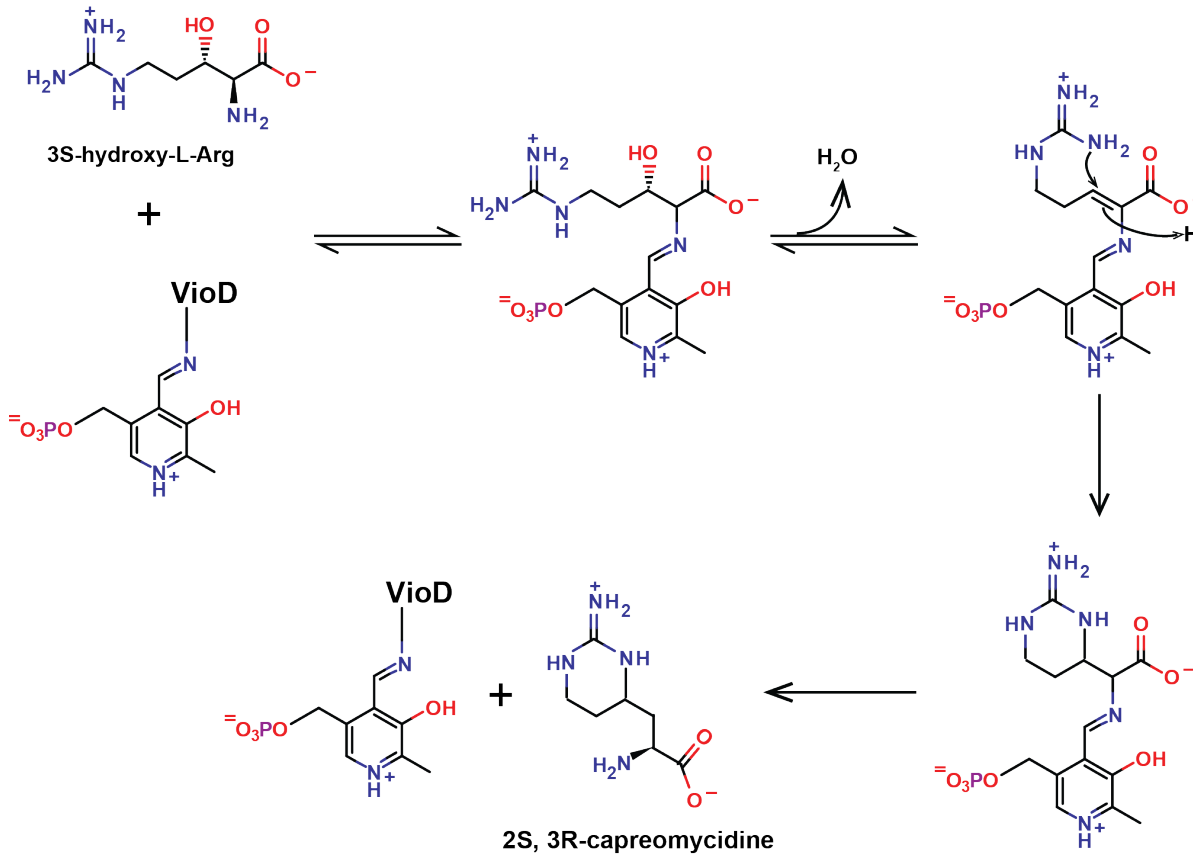


**Scheme 4-3:** L-capreomycidine biosynthesis mechanism by VioD.

The first clues came from studies of MppR [29]. In spite of its low (~20%) sequence identity with acetoacetate decarboxylase, MppR was shown to have a nearly identical tertiary structure. Differences in the active site of MppR, such as the loss of key residues for the decarboxylation reaction, suggested that MppR was not a decarboxylase. This was subsequently confirmed experimentally. The real breakthrough came when it was demonstrated that MppR is able to cyclize the ketone derived from γ-hydroxy-L-arginine, to give the ketone form of enduracididine (i.e. 2-keto-End, compound **7**, Scheme 4-1). This product is actually observed bound to the catalytic lysine residue of MppR in crystals

soaked with 2-oxo-4-hydroxy-5-guanidinovaleric acid (4HKA, compound **6**). In addition, experiments with MppQ showed that it was a true aminotransferase, capable of transaminating L-Arg and pyruvate or glyolxylate, or the reverse, 2-ketoarginine and alanine or glycine (unpublished results). These observations suggest that MppR generates **7** from the highly oxidized arginine derivative **6**, which is then transaminated by MppQ to give the amino acid, L-End. The L-β-hydroxy-End found in mannopeptimycin is produced from L-End by the Fe(II)-dependent oxygenase MppO, which hydroxylates the β-carbon of L-End to give L-βhEnd (compound **2**) [30]. D-βhEnd is presumably generated from L-βhEnd by epimerization [31]. All of this was plausible based on the data available at the time, but raised the question of where the highly oxidized arginine derivative **6** comes from.

Extensive work by predecessors on the enduracididine project failed to produce any of the *S. hygroscopicus* MppP in soluble form. Multiple strategies beyond the typical optimization of expression conditions were employed, including for example, truncation of the N- and C-termini, codon optimization, and site-directed mutagenesis. Switching to the *S. fungicidicus* homolog EndP from the enduracidin pathway gave no better results. A final BLAST search preparatory to throwing the MppP project away altogether returned a homolog from *Streptomyces wadayamensis* that was significantly longer than either MppP or EndP. Both of these are listed in GenBank at 293 amino acids, which is considerably shorter than the ~415 residues typical of aminotransferases. The *S. wadayamensis* homolog is 376 amino acids, so it would seem that a non-standard initiation codon fooled the annotation software into thinking the MppP and EndP coding sequences began about 100 codons into the gene. This at least made it clear why the protein would not express—all of

the expression constructs tried to date contained at most ~3/4 of the gene! The *S. wadayamensis* enzyme expressed well in *E. coli.*

With soluble protein in hand, we were finally able to begin the work of identifying the catalytic activity of MppP. *S. wadayamensis* is an endophytic strain isolated from mandarin organge trees (*Citrus reticulata*), which produces, among other natural products, mannopeptimycin [32]. Since it was expected from the work with MppR and MppQ that MppP must catalyze the first step of the pathway, the *S. wadayamensis* MppP (SwMppP) was incubated with L-Arg and monitored by UV-Vis spectroscopy. The results of these first crude experiments, which will be discussed in detail in Chapter 5, indicated that MppP reacted with L-Arg, finally accumulating a colored (pale pink) intermediate when the cuvette had been exhausted of dioxygen. Before delving into the experimental results we ultimately obtained, however, it will be instructive to investigate the chemistry of PLP and some properties of well-characterized PLP-dependent enzymes.

### 4.3 Pyridoxial 5'-phosphate is a versatile cofactor

PLP is a versatile cofactor catalyzing manifold reactions, including transamination, racemization, C-C bond formation or cleavage, β- and γ-elimination/substitution, and oxidative decarboxylation [33]. Some general reaction mechanisms are shown in Scheme 4-4. Due to its electron sink properties, PLP is inherently reactive and readily catalyzes reactions with amino acids, for example, without the aid of any enzyme. In fact, it has been said that, in general, PLP-dependent enzymes do not so much accelerate the PLP-catalyzed

reaction, but rather direct the catalytic power of PLP in a single direction [34]. In other words, PLP-dependent enzymes provide modest rate accelerations and strictly control the reaciton specificity. Toney [35] reviewed and summarized the three major factors that determine the reaction specificity in PLP-dependent enzymes: stereoelectronic control, the electrophilic strength of the Schiff base-pyridine ring π-electron system, and the placement of the substrate's side chain. Certain factors are common to most PLP-dependent enzymes, such as the covalent complex between a catalytic lysine residue on the enzyme and the PLP cofactor; this is the internal aldimine. When substrates bind, they react, normally by attack on the C4' of PLP to displace the enzyme lysine side chain and form the external aldimine.

As shown in Scheme 4-4, the external aldimine is the branch-point for many of the reaction types, such as decaboxylation or Cα-H abstraction. Which bond is going to be broken depends on the orientation relative to the pyridine ring. Thus, the bond aligned parallel to the π-orbitals (perpendicular to the PLP plane) promotes π–σ-orbital overlap, is weakened and is more easily cleaved [35]. Hence, decarboxylases bind their substrates so that the bond to the carboxyl group is located perpendicular to the PLP plane. Conversely, enzymes that begin with Cα-H proton abstraction, such as transaminases and racemases, orient the Cα-H bond perpendicular to the PLP ring.

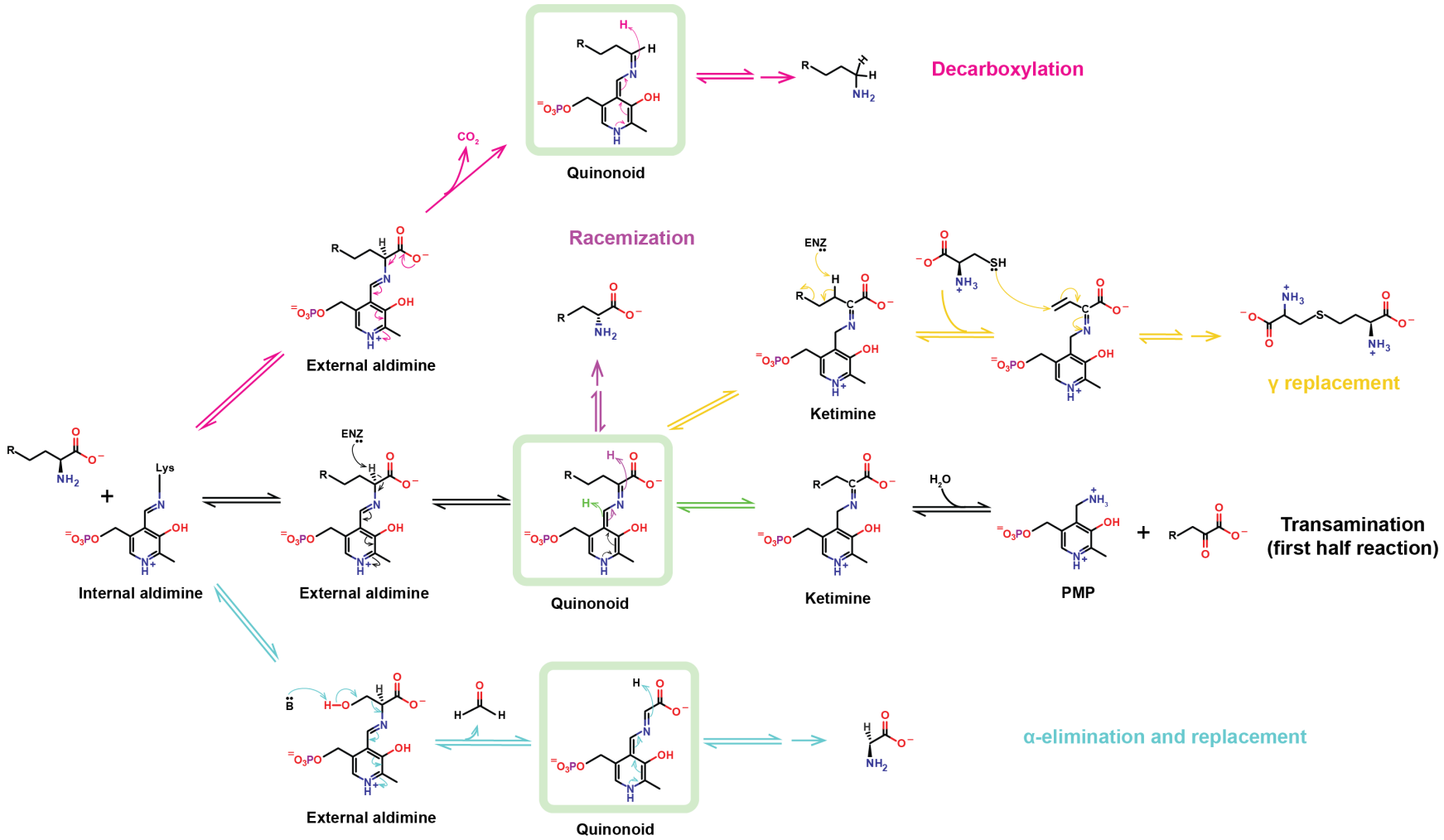


**Scheme 4-4:** Some examples of reactions involving PLP. Quinonoid intermediates are highlighted by green squares.

The protonation state of the pyridine nitrogen atom is another key factor influencing the reaction specificity. In aspartate aminotransferase, for example, this nitrogen is kept in the protonated, pyridinium form by the juxtaposition of the negatively charged carboxyl group of a conserved aspartic acid residue [36]. In enzymes like alanine racemase, where the carbanion at Cα must be stabilized, the pyridine nitrogen is kept deprotonated via interaction with the guanidinium group of a conserved arginine [37].

Percudani and Peracchi have created a B6 database utilizing hidden Markov models to compare the sequences of PLP-dependent enzymes. Their analysis distributes PLP-dependent enzymes into seven separate clusters based on their functions[38]. The representatives of these seven clusters are shown in Figure 4-3. Five of these clusters are essentially identical to the traditional classification system for PLP-dependent enzymes, which is based on 5 distinct topologies or "Fold Types"[39]. The Type I PLP-dependent enzymes are also called the aspartate aminotransferase (ATase) superfamily. Enzymes in this superfamily are typically dimeric (sometimes higher order oligomers) and have three discontinuous domains: the N-terminal extension, the large domain, and the small domain. The active site is located at the interface between the large and small domains, and is composed of residues from two protomers of the oligomer. Fold Type I is the largest and most diverse in terms of function and structure of N terminal domain, including class I, II, III, and V aminotransferases as well as enzymes catalyzing other PLP-dependent reactions like cystathionine γ-lyase, serine hydroxymethyltransferase[39, 40]. Class I ATase mainly contains aspartate aminotransferase, tyrosine ATase, aromatic ATase, alanine ATase and l-aminocyclopropane-1-carboxylate synthase. Class II ATase mainly comprises glycine acetyltransferase, 5-aminolevulinic acid synthase, histidinol-phosphate aminotransferase.

Class III mainly contains ornithine ATase, 4-aminobutyrate ATase, ω-amino acid-pyruvate ATase. Class V ATase mainly contains phosphoserine ATase, serine-pyruvate ATase.

The Type II PLP-depedent enzymes are evolutionarily distinct from the Type I enzymes, despite having similar tertiary structures[33, 41]. Fold type II includes the tryptophan synthase family of enzymes that mainly catalyze replacement and elimination reactions at Cβ, while most aspartate ATase family proteins promote reactions on the Cα atom of the substrate[41]. Fold Type II also contains acetyltransferases, ammonia lyases, and some racemases. In contrast to the Type I enzymes, the active sites of Type II enzymes are consist entirely of residues from a single protomer (such as tryptophan synthase[42]). Another distinguishing characteristic of these two enzyme families is the existence of a regulatory domain in the Type II enzymes[43, 44], whereas this is lacking in the Type I proteins.

The other fold types have fewer members than either of those discussed above. Fold Type III, also called the alanine racemase family, contains primarily amino acid racemases and decarboxylases. The structures of these proteins consist of an N-terminal β/α barrel and a C-terminal mostly β sheets domain [39]. Fold Type IV contains the class IV aminotransferases, which take mainly branched-chain amino acids and D-amino acids as substrates. The structures of the Type IV enzymes are very similar to the Type I ATases, but the PLP is bound in the opposite orientation compared to the Type I ATases. Fold Type V contains just one enzyme: glycogen phosphorylase (EC 2.4.1.1), which uses the phosphate group of PLP for catalysis[54]. The two new classifications obtained from the hidden markov model analysis by Percudani and Peracchi are designated Type VI and Type VII. Type VI includes the L- and D-lysine 5,6-aminomutases (EC 5.4.3.3 and 5.4.3.4; e.g. PDB ID: 1XRS[55])

and D-ornithine 4,5-aminomutase (EC 5.4.3.5). Type VII contains the lysine 2,3-aminomutase family enzymes (*e.g.* PDB ID: 2A5H [56]).

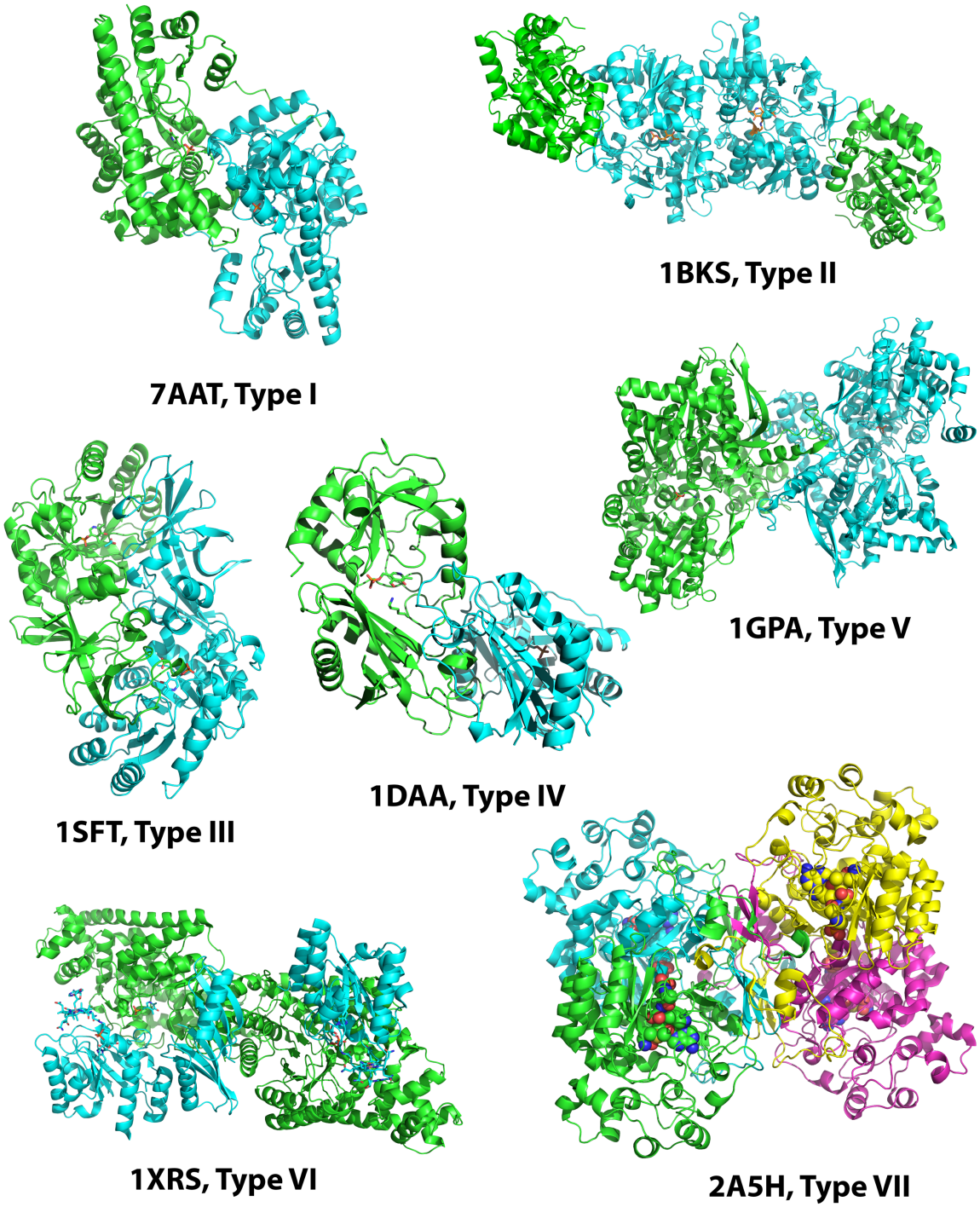

**Figure 4-3:** Ribbon diagrams of representative structures of the seven Fold Types of PLP-dependent enzymes. Each depicts the functional oligomeric state. The PLP and catalytic lysine, as well as substrates when available, are shown as sticks. PDB ID 7AAT[45] is the structure of mitochondrial aspartate aminotransferase from *Gallus gallus*, which is the representative of fold type I and functions as a dimer (chain A colored in green, chain B colored in cyan). PDB ID 1BKS[46] is the structure of tryptophan synthase from *Salmonella typhimurium*, which functions as an $\alpha_2\beta_2$ complex (α subunit colored in green, β subunit colored in cyan). The α and β subunits catalyze different reactions and indole is the channeled intermediate connecting the two reactions (α and β)[47-49]. The β subunit belongs to PLP Fold Type II. PDB ID 1SFT[37] is the structure of alanine racemase from *Bacillus stearothermophilus*, which is the representative of fold type III and functions as dimer (chain A colored in green, chain B colored in cyan). Each monomer contains two domains: and N-terminal eight-stranded α/β barrel and a C-terminal mostly β-strand domain. PDB ID 1DAA[50] is the structure of D-amino acid aminotransferase from *Baccilus* sp. YM-1, which is the representative of fold type IV and functions as a dimer (chain A colored in green, chain B colored in cyan). Each monomer contains two domains that are very different from the structures of the L-amino acid aminotransferases. PDB ID 1GPA[51] is the structure of glycogen phosphorylase from *Oryctolagus cuniculus*, which belongs to Fold Type V and functions as dimer (chain A colored in green, chain B colored in cyan). PDB ID 1XRS[52] is the structure of lysine 5,6-aminomutase from *Clostridium sticklandii*, which is the representative of fold type VI and functions as an $\alpha_2\beta_2$ tetramer (α subunits colored in green, β subunits colored in cyan). The larger α subunit consists of a PLP binding α/β barrel surrounded with additional α helices and β strands. The smaller β subunit contains two domains: the dimerization domain and the adenosylcobalamin ($B_{12}$)-binding Rossmann domain. PDB ID 2A5H[53] is the structure of lysine-2,3-aminomutase from *Clostridium subterminale*, which belongs to Fold Type VII and functions as a tetramer (chain A colored in green, chain B colored in cyan, chain C colored in magenta, and chain D colored in yellow). This enzyme is S-adenosylmethionine-, $[4Fe\text{-}4S]^{2+}$-, and PLP-dependent. S-adenosylmethionine and PLP are shown as sticks; $[4Fe\text{-}4S]^{2+}$ is shown in sphere.

### 4.4 Aminotransferases (ATase)

The PLP-dependent aminotransferases catalyze transamination reactions in which the α amino group of an amino acid is transferred onto the α-carbon of a 2-oxo acid, forming the 2-oxo acid form of the amino acid and the amino acid form of the 2-oxo-acid. The example of the thoroughly studied asparate aminotransferase-catalyzed reaction is shown in Figure 4-4A. Aspartate aminotransferase (AATase) has a large domain, a small domain and an N-terminal extension (Figure 4-4B). It functions as a dimer with the active site residues contributed by both domains and by both chains of the dimer, as discussed above. In L-amino acid aminotransferases, the catalytic lysine residue is located on the *si* face of C4' of the cofactor and the *re* face is accessible by solvent or substrate.

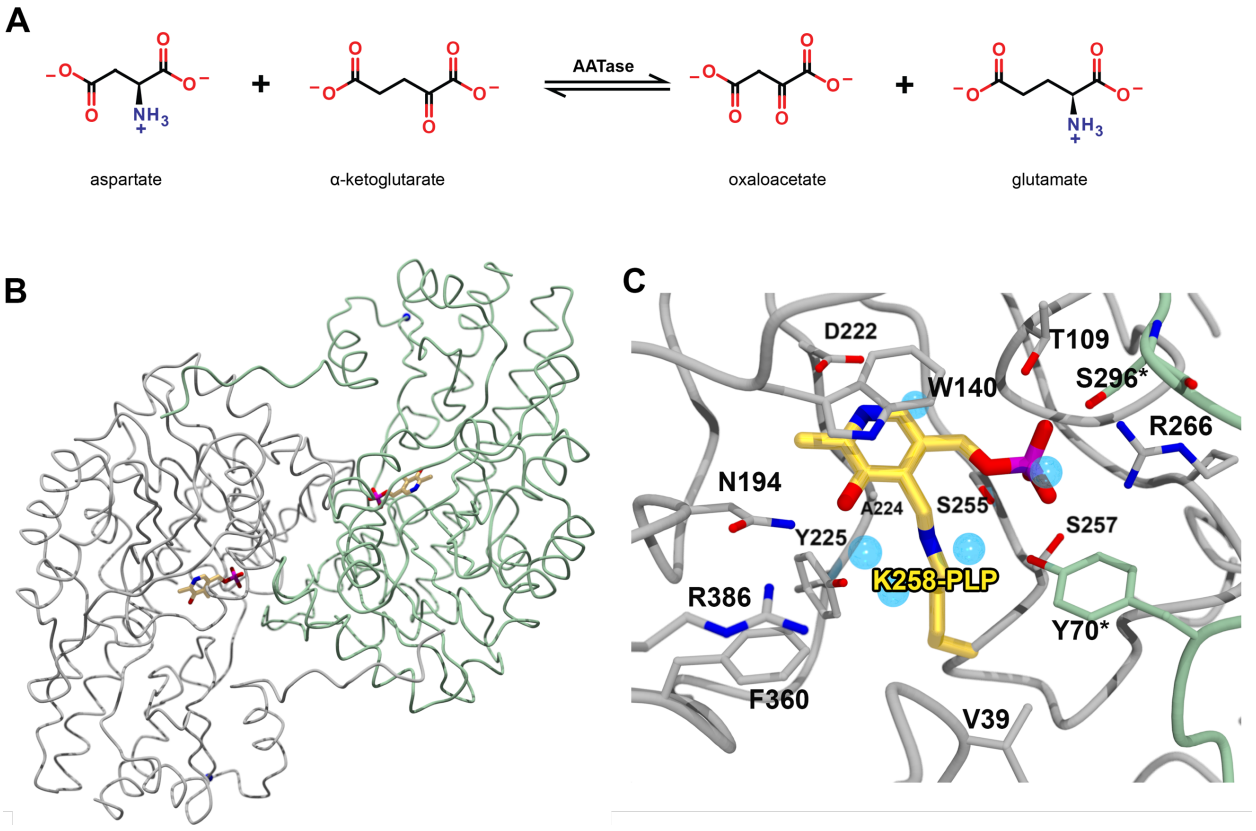

**Figure 4-4:** The reaction catalyzed by aspartate aminotransferase (A). Ribbon representation of the aspartate aminotransferase dimer (PDB ID: 1ARS[57]). Chain A is colored grey, chain B is colored light green. The active site of AATase shows the binding mode of PLP in this and similar enzymes (C). The catalytic K258 and PLP are shown as sticks with yellow carbon atoms. The asterisk on atom labels denotes that the residue is contributed by the other chain of the dimer.

### 4.4.1 The AATase active site

As shown in Figure 4-4C, the catalytic K258 of the *E. coli* AATase is covalently bound to the PLP as the internal aldimine. The negatively charged D222 stabilizes the pyridine N atom of PLP as the pyridinium, which allows the ring to accept electrons from the substrate stabilizing the carbanion that forms during catalysis. The C3' hydroxyl group of PLP makes a hydrogen bonding interaction with N194 and Y225, both highly conserved among the Type I AATases. The phosphate group of the cofactor interacts with R266, T109, S257, Y70* (from the other protomer of the dimer); S296* interacts with the phosphate group through an intervening water molecule. The pyridine ring of PLP is clamped between W140 above and A224 below. W140 is important for retaining PLP in the active site. Mutating W140 to His in the *E. coli* AATase resulted in a 50-fold increase in the dissociation rate constant for PLP[58]. Also, the angled, unstacked imidazole ring of this W140H variant facilitated water access to the *re* face of the substrate Cα, resulting in a faster rate of racemization and decreased aminotransferase activity[58].

### 4.4.2 Conformational changes associated with catalysis

Because the substrates of AATase are aspartate and α-ketoglutarate, the elimination and replacement reactions cannot happen. In the structure of the *E. coli* AATase with the inhibitor 2-methyl-L-aspartate (PDB ID: 1ART[59]), R386 coordinates the α-carboxylate group of the inhibitor and holds in in the plane of the PLP ring, which discourages decarboxylation. After the deprotonation of Cα, the resulting quinonoid intermediate is capable of undergoing either transamination or racemization. Kochhar and Christen found that human mitochondrial AATase that had been truncated by limited proteolysis with trypsin (residues 27/32-410) had the same racemization activity as the intact protein, but much lower transamination activity[60]. In addition, increasing organic solvent (methanol) proportion in the reaction resulted in decreased racemization but the same transamination activity of AATase[60]. Thus, it appears that AATases have evolved a strategy to discourage the racemization reaction by limiting the access of water to the catalytic center. This strategy involves closing the active site with N-terminal extension. This excludes water from the active site, preventing water molecules from pronating the *re* side of the quinonoid intermediate.

The small domains of many Type I aminotransferases also shift towards the large domains upon substrate binding, forming a "closed" conformation[57, 61, 62]. In *E. coli* AATase, this movement of the small domain creates a repulsive interaction between G38 and Y225, which may reduce the $pK_a$ of the aldimine and, thus, enhance catalysis[61]. The lower imine $pK_a$ of the internal aldimine is mainly due to the 90 ° torsion angle of the C4-C4' bond (C3-

C4-C4'-Nζ) and the repulsive interaction between G38 and Y225 that destabilizes the unprotonated aldimine in the Michaelis complex [61, 63].

### 4.4.3 Dual substrate recognition

As mentioned above, the aminotransferase reaction involves two different substrates being transformed, in succession, into two products. In many cases, these two substrates have very different side chains, such as different charges (*e.g.* alanine vs α-ketoglutarate), inverse absosolute configuration (*e.g.* D-p-hydroxyphenylglycine and L-glutamate), and/or different size side chains (*e.g.* aspartate and α-ketoglutarate). Aminotransferases have evolved several ways to solve the problem of having such different substrates binding in the same active site in the same orientation relative to the same PLP cofactor. These include the "glutamate switch," the "arginine switch," and remodeling of hydrogen bonding networks[33, 64].

The "glutamine switch" works as shown in Figure 4-5. When the substrate, lysine, forms the external aldimine with PLP (PDB ID: 2CJD[65]) in the lysine ε-aminotransferase from *Mycobacterium tuberculosis*, the carboxylate group of E243 neutralizes the guanidinium group of R422. This prevents repulsion due to the juxtaposition of like charges. However, in the structure of the lysine ε-aminotransferase with α-ketoglutarate bound (PDB ID: 2CJH[65]), E243 rotates out of the active site, which allows the interaction between R422 and the α-carboxylate group of α-ketoglutarate. The "arginine switch" works in a similar way, as it is also based on the flexibility of active site residues as demonstrated in the active site

of GABA aminotransferase. Comparing the structures of GABA aminotransferase in complexes with either an inactivator CPP-115 with one carboxylate group (similar to GABA) (PDB ID: 4ZSY [66]) or the metabolite of CPP-115 with two carboxylate groups that is similar to glutamate (PDB ID: 4ZSW [66]), R445 that interacts with the one carboxylate group of the CCP-115 metabolite, switches out and interacts with E270 in the CPP-115 bound structure [66, 67].

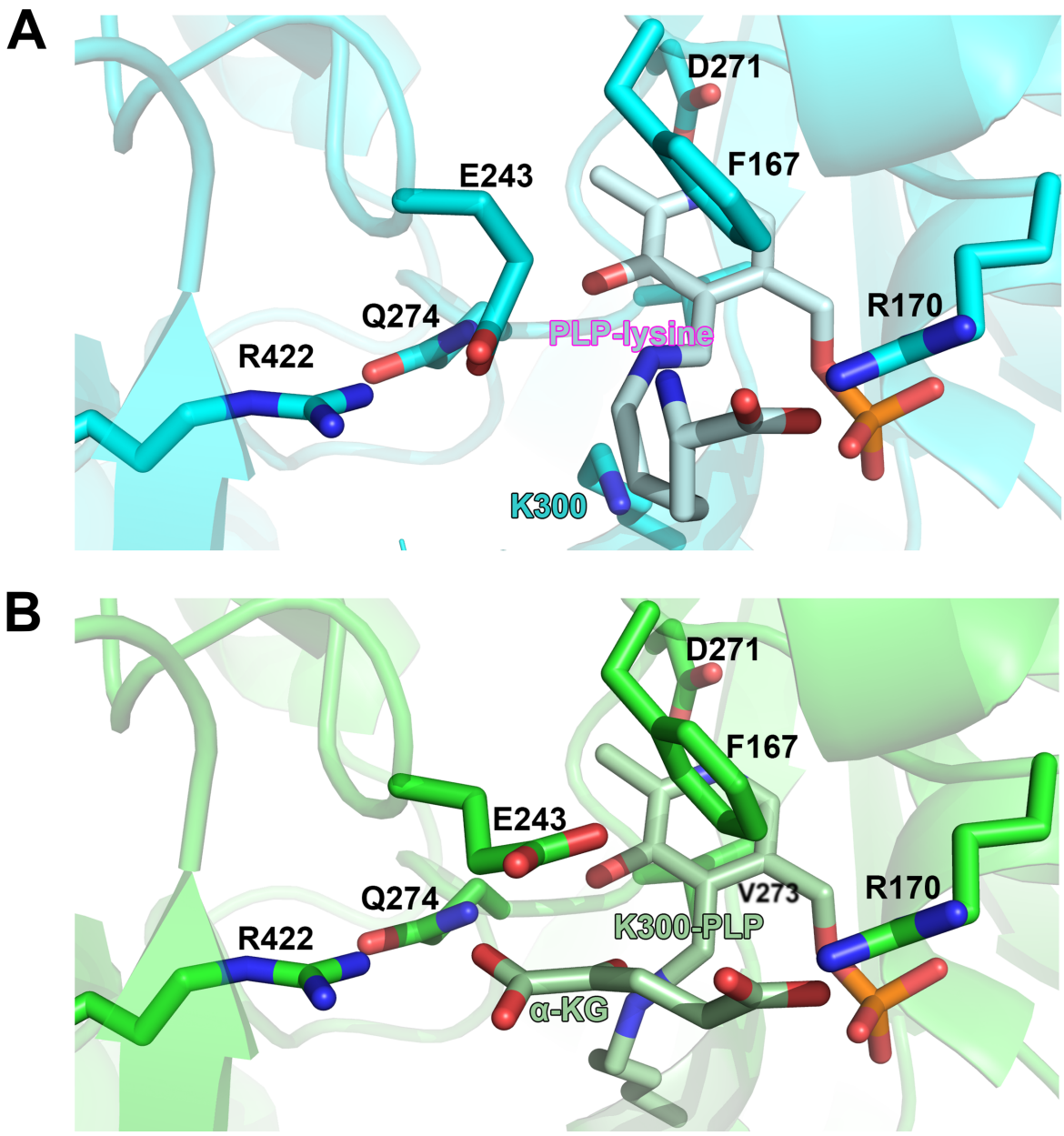


**Figure 4-5:** Dual substrate recognition in lysine ε-aminotransferase from *Mycobacterium tuberculosis*. When lysine is bound in the active site of lysine ε-aminotransferase as the external aldimine (A), E243 forms a salt bridge with R422. When α-ketoglutarate is bound in the active site (B), E243 rotates away from R422, which allows R422 to interact with the α-carboxylate group of α-ketoglutarate.

## 4.5 L-3,4-dihydroxyphenylalanine (L-DOPA) decarboxylase

### 4.5.1 Mechanisms of decarboxylation and oxidative deamination

Some PLP dependent enzymes were found to react with $O_2$, such as 3,4-dihydroxyphenylalanine (DOPA) decarboxylase/L-aromatic amino acid decarboxylase [68], and so-called "paracatalytic" reactions [69] with $O_2$ have been described. DOPA decarboxylase catalyzes the conversion of L-DOPA (compound **8**) and L-5-hydroxy tryptophan into two important neurotransmitters, dopamine (compound **9**) and serotonin. The mechanism is shown in Scheme 4-5A. Upon substrate binding, the internal aldimine is converted into external aldimine. Due to the orientation of the substrate carboxyl group perpendicular to the PLP ring, decarboxylation happens. The subsequent quinonoid intermediate is protonated at Cα position, giving the corresponding amine product (**9**). Mutagenesis studies of Y332 demonstrated that this residue is probably the proton donor in the step of quinonoid protonation[70]. Notably, the mutant Y332F has a decarboxylation-dependent oxidative deaminase activity, rather than decarboxylase[70]. In other words, Y332F reacts with L-amino acids and dioxygen to generate the corresponding aromatic aldehydes, $CO_2$ and ammonia.

DOPA decarboxylase also catalyzes the oxidative deamination of serotonin and dopamine[71, 72]. The proposed oxidative mechanism of **9** is shown in Scheme 4-5B. The internal aldimine is converted into the external aldimine with dopamine, and after deprotonating on Cα, the quinonoid intermediate forms. Based on its close proximity to the substrate Cα and mutagenesis studies, T246 is thought to function as a nucleophile to abstract the α-proton [73]. In the presence of $O_2$, the quinonoid intermediate reacts with $O_2$

and forms a superoxide anion and semiquinone, followed by a hydroperoxy-PLP intermediate. After several steps, the final aldehyde product, $H_2O_2$, and ammonia form. In the absence of $O_2$, the quinonoid intermediate would equilibrate with a ketimine[73].

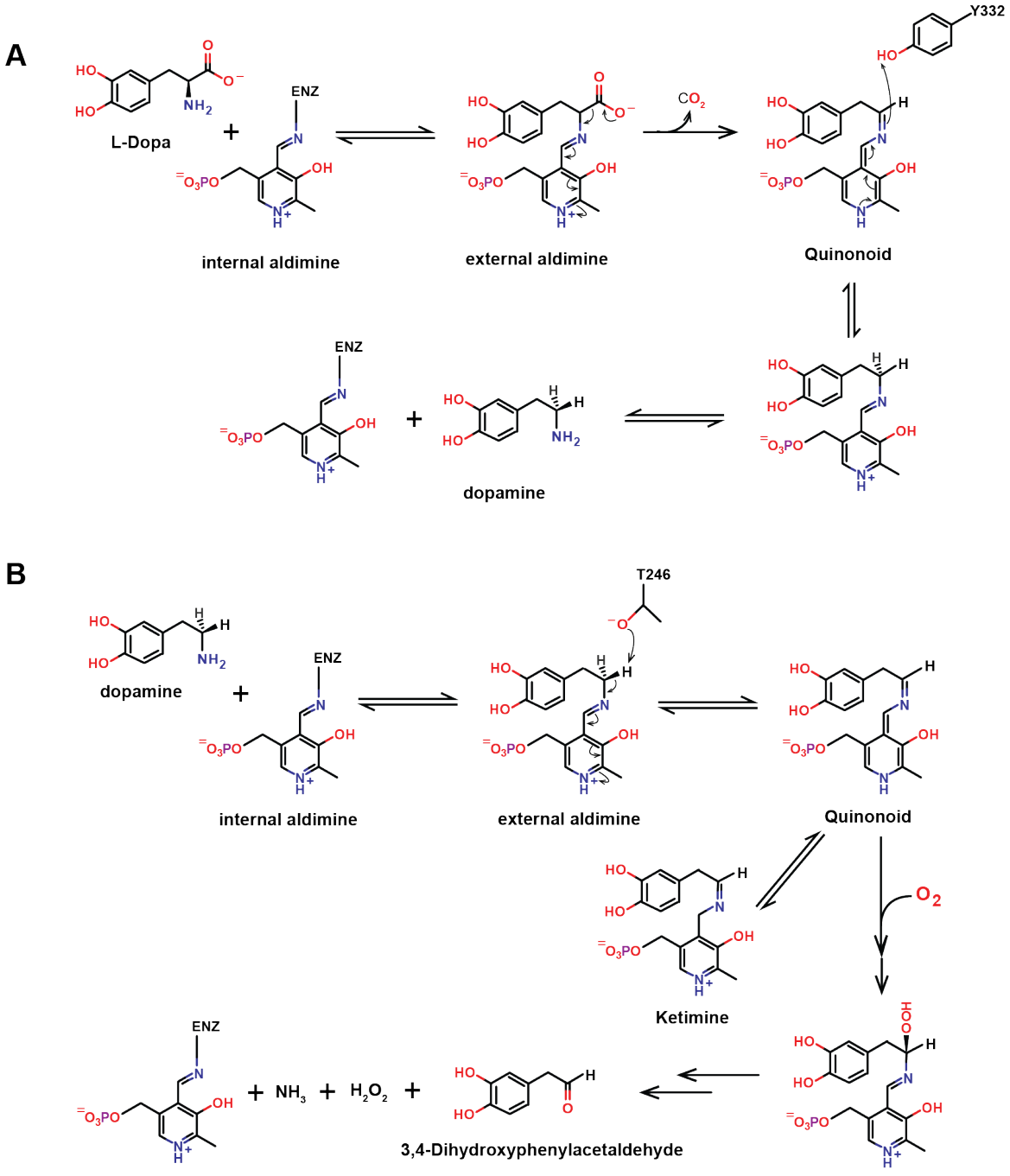


**Scheme 4-5:** Decarboxylation (A) and oxidation deamination (B) by DOPA decarboxylase.

### 4.5.2 Structure of human DOPA decarboxylase

DOPA decarboxylase belongs to group II of Fold Type I, which contains the L-amino acid decarboxylases. The group II of L-amino acid decarboxylases include aromatic amino acid decarboxylase, histidine decarboxylase, and glutamate decarboxylase [74]. They share a similar active site conformation and many conserved features. Binding of PLP into the apoenzyme is thought to be the essential regulator of activity [75]. Upon PLP binding, DOPA decarboxylase undergoes a large conformational change into a more compact and less solvent accessible conformation [1].

As shown in Figure 4-7, human DOPA decarboxylase is a homodimer with three domains: a N-terminal domain composed of three α-helices that contact with the other protomer, a large domain with a central seven-stranded β-sheet surrounded by α helices, and a C-terminal domain with a 4-stranded β-sheet covered by α helices on one side. The apoenzyme adopts an open conformation (PDB ID: 3RBL [1]); while after PLP binds in the two active sites, it forms a closed conformation (PDB ID: 1JS6[2]). In the apoenzyme structure, Y274 interacts with H302. After PLP binding, this movement (from open to closed conformation) makes the aromatic stacking interactions among W304, F80 and Y274 (Figure 4-7B). In the active site, the catalytic K303 covalently binds to PLP as the internal aldimine. H192 and A273 are stacked above and below the PLP ring. H192 is also involved in the catalysis of oxidative deamination. In the substrate analog-bound structure (PDB ID: 1JS3[2]), the iminic nitrogen of H192 is 4.8 Å away from the OH group of T246, which facilitates the deprotonation of T246 [76]. As mentioned above, the deprotonated T246

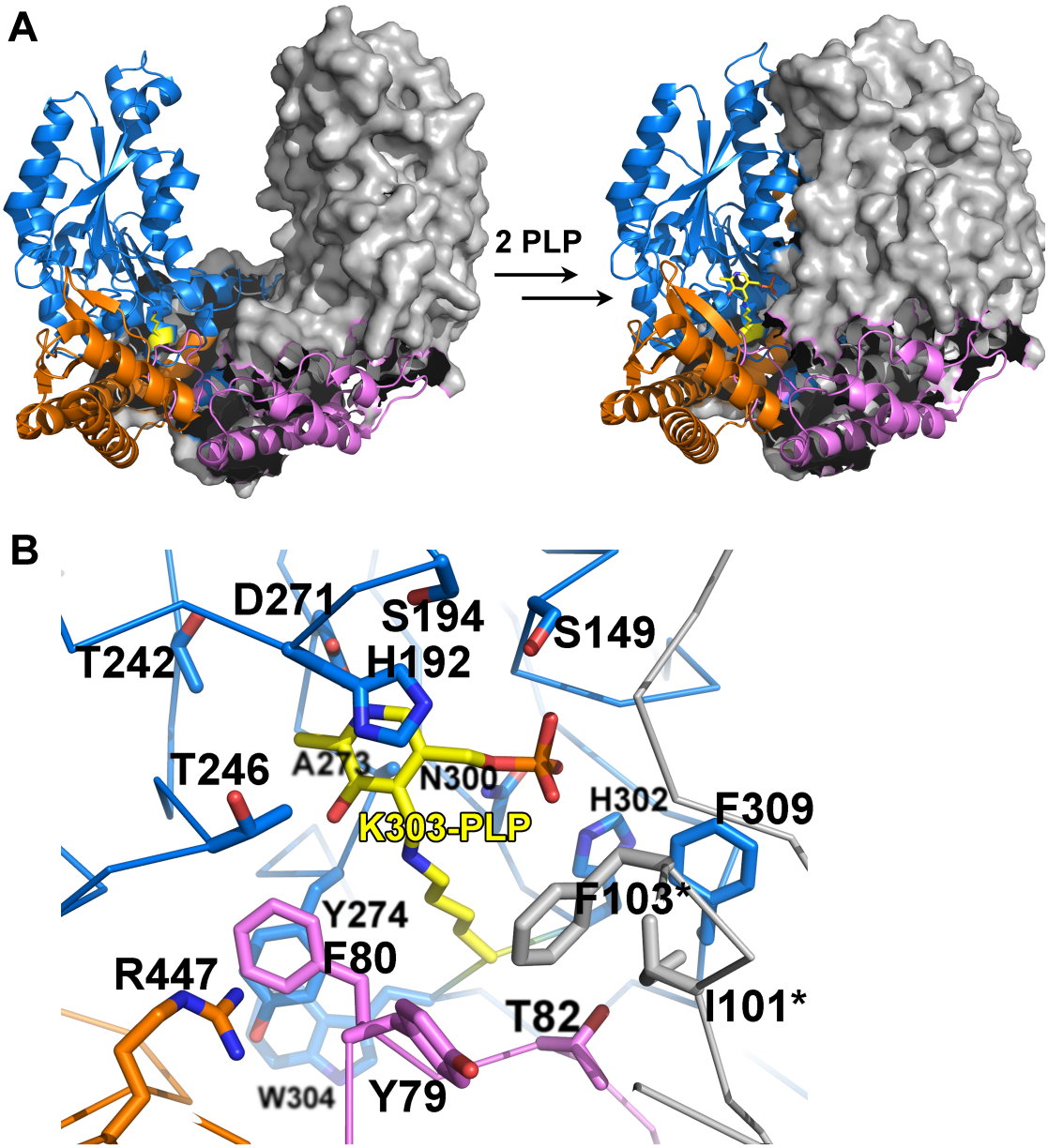


Figure 4-7: (A) The structure of DOPA decarboxylase in an open (PDB ID: 3RBL [1]) and closed (PDB ID: 1JS6[2]) conformation. The domain organization of chain A is highlighted with different colors (N-terminal domain colored in purple, large domain colored in blue, and C-terminal domain colored in orange). Chain B colored in grey. (B) Conserved residues in human DOPA decarboxylase are shown in stick.

would abstract the Cα hydrogen and trigger the formation of the quinonoid intermediate (Scheme 4-5B). D271 makes a salt bridge interaction with the protonated pyridine nitrogen of PLP. Several residues, including S194, S149, H302, F309, are involved in interacting with phosphate group of PLP. I101* and F103* (from the other chain), Y79, F80, T82 are involved in substrate binding.

The sequence of SwMppP suggests that it belongs to the class I/II ATase group of the Fold Type I PLP-dependent enzymes. The sequence identity between SwMppP and a Fold Type I ATase (PDB ID 1ARS[57]) or DOPA decarboxylase (PDB ID 3RBL[1]) is quite low (20% and 17%, respectively). In addition, many of the key active site residues of both the ATases and DOPA decarboxylase are different in SwMppP, suggesting that SwMppP probably has a different function. Two other genes in the L-End biosynthesis gene cluster, MppR and MppQ, are involved in the cyclization of **6** into **7** and the transamination of **7** into L-End (**1**), respectively (Figure 4-2). Hence, we speculate that SwMppP can only be a novel PLP-dependent hydroxylase/deaminase to catalyze the oxidation of L-Arg (**5**) into its γ-hydroxy, 2-oxo derivative **6**. To find out the relationship between the function and structure, we used biophysical methods, as well as enzyme kinetics, to characterize SwMppP. Our findings are detailed in Chapter 5.

## 4.6 References


[1] Giardina, G., Montioli, R., Gianni, S., Cellini, B., Paiardini, A., Voltattorni, C. B., and Cutruzzola, F. (2011) Open conformation of human DOPA decarboxylase reveals the mechanism of PLP addition to Group II decarboxylases, *Proc Natl Acad Sci U S A 108*, 20514-20519.

[2] Burkhard, P., Dominici, P., Borri-Voltattorni, C., Jansonius, J. N., and Malashkevich, V. N. (2001) Structural insight into Parkinson's disease treatment from drug-inhibited DOPA decarboxylase, *Nature structural biology 8*, 963-967.

[3] Higashide, E., Hatano, K., Shibata, M., and Nakazawa, K. (1968) Enduracidin, a new antibiotic. I. Streptomyces fungicidicus No. B5477, an enduracidin producing organism, *The Journal of antibiotics 21*, 126-137.

[4] Singh, M. P., Petersen, P. J., Weiss, W. J., Janso, J. E., Luckman, S. W., Lenoy, E. B., Bradford, P. A., Testa, R. T., and Greenstein, M. (2003) Mannopeptimycins, new cyclic glycopeptide antibiotics produced by Streptomyces hygroscopicus LL-AC98: antibacterial and mechanistic activities, *Antimicrobial agents and chemotherapy 47*, 62-69.

[5] Ling, L. L., Schneider, T., Peoples, A. J., Spoering, A. L., Engels, I., Conlon, B. P., Mueller, A., Schäberle, T. F., Hughes, D. E., Epstein, S., Jones, M., Lazarides, L., Steadman, V. A., Cohen, D. R., Felix, C. R., Fetterman, K. A., Millett, W. P., Nitti, A. G., Zullo, A. M., Chen, C., and Lewis, K. (2015) A new antibiotic kills pathogens without detectable resistance, *Nature 517*, 455.

[6] Castiglione, F., Marazzi, A., Meli, M., and Colombo, G. (2005) Structure elucidation and 3D solution conformation of the antibiotic enduracidin determined by NMR spectroscopy and molecular dynamics, *Magnetic Resonance in Chemistry 43*, 603-610.

[7] Fang, X., Tiyanont, K., Zhang, Y., Wanner, J., Boger, D., and Walker, S. (2006) The mechanism of action of ramoplanin and enduracidin, *Molecular bioSystems 2*, 69-76.

[8] Cudic, P., Behenna, D. C., Kranz, J. K., Kruger, R. G., Wand, A. J., Veklich, Y. I., Weisel, J. W., and McCafferty, D. G. Functional Analysis of the Lipoglycodepsipeptide Antibiotic Ramoplanin, *Chemistry & biology 9*, 897-906.

[9] Ruzin, A., Singh, G., Severin, A., Yang, Y., Dushin, R. G., Sutherland, A. G., Minnick, A., Greenstein, M., May, M. K., Shlaes, D. M., and Bradford, P. A. (2004) Mechanism of action of the mannopeptimycins, a novel class of glycopeptide antibiotics active against vancomycin-resistant gram-positive bacteria, *Antimicrob. Agents Chemother. 48*, 728-738.

[10] Wang, B., Liu, Y., Jiao, R., Feng, Y., Li, Q., Chen, C., Liu, L., He, G., and Chen, G. (2016) Total Synthesis of Mannopeptimycins alpha and beta, *Journal of the American Chemical Society 138*, 3926-3932.

[11] Sum, P.-E., How, D., Torres, N., Petersen, P. J., Lenoy, E. B., Weiss, W. J., and Mansour, T. S. (2003) Novel ether derivatives of mannopeptimycin glycopeptide antibiotic, *Bioorganic & Medicinal Chemistry Letters 13*, 1151-1155.

[12] Sum, P.-E., How, D., Torres, N., Petersen, P. J., Ashcroft, J., Graziani, E. I., Koehn, F. E., and Mansour, T. S. (2003) Synthesis and evaluation of ether and halogenated derivatives

of mannopeptimycin glycopeptide antibiotics, *Bioorganic & Medicinal Chemistry Letters 13*, 2805-2808.
[13] He, H., Wang, T.-Z., Dushin, R. G., Feng, X., Shen, B., Ashcroft, J. S., Koehn, F. E., and Carter, G. T. (2004) Structural determination of mannopeptimycin cyclic acetals, *Tetrahedron Letters 45*, 5889-5893.
[14] Dushin, R. G., Wang, T.-Z., Sum, P.-E., He, H., Sutherland, A. G., Ashcroft, J. S., Graziani, E. I., Koehn, F. E., Bradford, P. A., Petersen, P. J., Wheless, K. L., How, D., Torres, N., Lenoy, E. B., Weiss, W. J., Lang, S. A., Projan, S. J., Shlaes, D. M., and Mansour, T. S. (2004) Hydrophobic Acetal and Ketal Derivatives of Mannopeptimycin-α and Desmethylhexahydromannopeptimycin-α: Semisynthetic Glycopeptides with Potent Activity Against Gram-Positive Bacteria, *Journal of Medicinal Chemistry 47*, 3487-3490.
[15] Petersen, P. J., Wang, T. Z., Dushin, R. G., and Bradford, P. A. (2004) Comparative in vitro activities of AC98-6446, a novel semisynthetic glycopeptide derivative of the natural product mannopeptimycin alpha, and other antimicrobial agents against gram-positive clinical isolates, *Antimicrobial agents and chemotherapy 48*, 739-746.
[16] Sum, P.-E., How, D., Torres, N., Newman, H., Petersen, P. J., and Mansour, T. S. (2003) Synthesis and activity of novel benzoxazole derivatives of mannopeptimycin glycopeptide antibiotics, *Bioorganic & Medicinal Chemistry Letters 13*, 2607-2610.
[17] He, H., Shen, B., Petersen, P. J., Weiss, W. J., Yang, H. Y., Wang, T.-Z., Dushin, R. G., Koehn, F. E., and Carter, G. T. (2004) Mannopeptimycin esters and carbonates, potent antibiotic agents against drug-resistant bacteria, *Bioorganic & Medicinal Chemistry Letters 14*, 279-282.
[18] Tsuji, S., Kusumoto, S., and Shiba, T. (1975) SYNTHESIS OF ENDURACIDIDINE, A COMPONENT AMINO ACID OF ANTIBIOTIC ENDURACIDIN, *Chemistry Letters 4*, 1281-1284.
[19] Sanière, L., Leman, L. c., Bourguignon, J.-J., Dauban, P., and Dodd, R. H. (2004) Iminoiodane mediated aziridination of α-allylglycine: access to a novel rigid arginine derivative and to the natural amino acid enduracididine, *Tetrahedron 60*, 5889-5897.
[20] Schwörer, C. J., and Oberthür, M. (2009) Synthesis of Highly Functionalized Amino Acids: An Expedient Access to L- and D-β-Hydroxyenduracididine Derivatives, *European Journal of Organic Chemistry 2009*, 6129-6139.
[21] Fischer, S. N., Schwörer, C. J., and Oberthür, M. (2014) A Short Synthesis of Partially Protected l- and d-β-Hydroxyenduracididines and a Structurally Simplified Dipeptide Analogue, *Synthesis 46*, 2234-2240.
[22] Lin, C.-K., Yun, W.-Y., Lin, L.-T., and Cheng, W.-C. (2016) A concise approach to the synthesis of the unique N-mannosyl d-[small beta]-hydroxyenduracididine moiety in the mannopeptimycin series of natural products, *Organic & Biomolecular Chemistry 14*, 4054-4060.
[23] Magarvey, N. A., Haltli, B., He, M., Greenstein, M., and Hucul, J. A. (2006) Biosynthetic pathway for mannopeptimycins, lipoglycopeptide antibiotics active against drug-resistant gram-positive pathogens, *Antimicrobial agents and chemotherapy 50*, 2167-2177.
[24] Yin, X., and Zabriskie, T. M. (2006) The enduracidin biosynthetic gene cluster from Streptomyces fungicidicus, *Microbiology (Reading, England) 152*, 2969-2983.

[25] Hatano, K., Nogami, I., Higashide, E., and Kishi, T. (1984) Biosynthesis of Enduracidin: Origin of Enduracididine and Other Amino Acids, *Agricultural and Biological Chemistry 48*, 1503-1508.
[26] Yin, X., and Zabriskie, T. M. (2004) VioC is a non-heme iron, alpha-ketoglutarate-dependent oxygenase that catalyzes the formation of 3S-hydroxy-L-arginine during viomycin biosynthesis, *Chembiochem : a European journal of chemical biology 5*, 1274-1277.
[27] Ju, J., Ozanick, S. G., Shen, B., and Thomas, M. G. (2004) Conversion of (2S)-Arginine to (2S,3R)-Capreomycidine by VioC and VioD from the Viomycin Biosynthetic Pathway of Streptomyces sp. Strain ATCC11861, *Chembiochem : a European journal of chemical biology 5*, 1281-1285.
[28] Yin, X., McPhail, K. L., Kim, K.-j., and Zabriskie, T. M. (2004) Formation of the Nonproteinogenic Amino Acid 2S,3R-Capreomycidine by VioD from the Viomycin Biosynthesis Pathway, *Chembiochem : a European journal of chemical biology 5*, 1278-1281.
[29] Burroughs, A. M., Hoppe, R. W., Goebel, N. C., Sayyed, B. H., Voegtline, T. J., Schwabacher, A. W., Zabriskie, T. M., and Silvaggi, N. R. (2013) Structural and functional characterization of MppR, an enduracididine biosynthetic enzyme from streptomyces hygroscopicus: functional diversity in the acetoacetate decarboxylase-like superfamily, *Biochemistry 52*, 4492-4506.
[30] Haltli, B., Tan, Y., Magarvey, N. A., Wagenaar, M., Yin, X., Greenstein, M., Hucul, J. A., and Zabriskie, T. M. (2005) Investigating beta-hydroxyenduracididine formation in the biosynthesis of the mannopeptimycins, *Chemistry & biology 12*, 1163-1168.
[31] Bodanszky, M., and Perlman, D. (1968) Origin of D-Amino-acids in Microbial Peptides: Rule of [alpha]-Epimerization, *Nature 218*, 291-292.
[32] Araujo, W. L., Marcon, J., Maccheroni, W., Jr., Van Elsas, J. D., Van Vuurde, J. W., and Azevedo, J. L. (2002) Diversity of endophytic bacterial populations and their interaction with Xylella fastidiosa in citrus plants, *Applied and environmental microbiology 68*, 4906-4914.
[33] Eliot, A. C., and Kirsch, J. F. (2004) Pyridoxal phosphate enzymes: mechanistic, structural, and evolutionary considerations, *Annu. Rev. Biochem 73*, 383-415.
[34] Toney, M. D. (2005) Reaction specificity in pyridoxal phosphate enzymes, *Archives of Biochemistry and Biophysics 433*, 279-287.
[35] Toney, M. D. (2011) Controlling reaction specificity in pyridoxal phosphate enzymes, *Biochimica et Biophysica Acta (BBA) - Proteins and Proteomics 1814*, 1407-1418.
[36] McPhalen, C. A., Vincent, M. G., and Jansonius, J. N. (1992) X-ray structure refinement and comparison of three forms of mitochondrial aspartate aminotransferase, *Journal of molecular biology 225*, 495-517.
[37] Shaw, J. P., Petsko Ga Fau - Ringe, D., and Ringe, D. Determination of the structure of alanine racemase from Bacillus stearothermophilus at 1.9-A resolution.
[38] Percudani, R., and Peracchi, A. (2009) The B6 database: a tool for the description and classification of vitamin B6-dependent enzymatic activities and of the corresponding protein families, *BMC Bioinformatics 10*, 273.
[39] Grishin, N. V., Phillips, M. A., and Goldsmith, E. J. (1995) Modeling of the spatial structure of eukaryotic ornithine decarboxylases, *Protein Science 4*, 1291-1304.

[40] Schneider, G., Kack, H., and Lindqvist, Y. (2000) The manifold of vitamin B6 dependent enzymes, *Structure (London, England : 1993) 8*, R1-6.
[41] Mehta, P. K., and Christen, P. (2000) The molecular evolution of pyridoxal-5'-phosphate-dependent enzymes, *Advances in enzymology and related areas of molecular biology 74*, 129-184.
[42] Hyde, C. C., Ahmed, S. A., Padlan, E. A., Miles, E. W., and Davies, D. R. (1988) Three-dimensional structure of the tryptophan synthase alpha 2 beta 2 multienzyme complex from Salmonella typhimurium, *The Journal of biological chemistry 263*, 17857-17871.
[43] Madison, J. T., and Thompson, J. F. (1976) Threonine synthetase from higher plants: stimulation by S-adenosylmethionine and inhibition by cysteine, *Biochemical and biophysical research communications 71*, 684-691.
[44] Wessel, P. M., Graciet, E., Douce, R., and Dumas, R. (2000) Evidence for two distinct effector-binding sites in threonine deaminase by site-directed mutagenesis, kinetic, and binding experiments, *Biochemistry 39*, 15136-15143.
[45] McPhalen, C. A., Vincent Mg Fau - Jansonius, J. N., and Jansonius, J. N. X-ray structure refinement and comparison of three forms of mitochondrial aspartate aminotransferase.
[46] Rhee, S., Parris Kd Fau - Ahmed, S. A., Ahmed Sa Fau - Miles, E. W., Miles Ew Fau - Davies, D. R., and Davies, D. R. Exchange of K+ or Cs+ for Na+ induces local and long-range changes in the three-dimensional structure of the tryptophan synthase alpha2beta2 complex.
[47] Dunn, M. F., Aguilar, V., Brzovic, P., Drewe, W. F., Houben, K. F., Leja, C. A., and Roy, M. (1990) The tryptophan synthase bienzyme complex transfers indole between the .alpha.- and .beta.-sites via a 25-30 .ANG. long tunnel, *Biochemistry 29*, 8598-8607.
[48] Hyde, C. C., and Miles, E. W. (1990) The Tryptophan Synthase Multienzyme Complex: Exploring Structure-Function Relationships with X-Ray Crystallography and Mutagenesis, *Nat Biotech 8*, 27-32.
[49] Dunn, M. F. (2012) Allosteric Regulation of Substrate Channeling and Catalysis in the Tryptophan Synthase Bienzyme Complex, *Archives of biochemistry and biophysics 519*, 154-166.
[50] Sugio, S., Petsko Ga Fau - Manning, J. M., Manning Jm Fau - Soda, K., Soda K Fau - Ringe, D., and Ringe, D. Crystal structure of a D-amino acid aminotransferase: how the protein controls stereoselectivity.
[51] Barford, D., Hu Sh Fau - Johnson, L. N., and Johnson, L. N. Structural mechanism for glycogen phosphorylase control by phosphorylation and AMP.
[52] Berkovitch, F., Behshad E Fau - Tang, K.-H., Tang Kh Fau - Enns, E. A., Enns Ea Fau - Frey, P. A., Frey Pa Fau - Drennan, C. L., and Drennan, C. L. A locking mechanism preventing radical damage in the absence of substrate, as revealed by the x-ray structure of lysine 5,6-aminomutase.
[53] Lepore, B. W., Ruzicka Fj Fau - Frey, P. A., Frey Pa Fau - Ringe, D., and Ringe, D. The x-ray crystal structure of lysine-2,3-aminomutase from Clostridium subterminale.
[54] Fletterick, R. J., and Sprang, S. R. (1982) Glycogen phosphorylase structures and function, *Accounts of Chemical Research 15*, 361-369.
[55] Berkovitch, F., Behshad, E., Tang, K. H., Enns, E. A., Frey, P. A., and Drennan, C. L. (2004) A locking mechanism preventing radical damage in the absence of substrate, as

revealed by the x-ray structure of lysine 5,6-aminomutase, *Proc Natl Acad Sci U S A 101*, 15870-15875.
[56] Lepore, B. W., Ruzicka, F. J., Frey, P. A., and Ringe, D. (2005) The x-ray crystal structure of lysine-2,3-aminomutase from Clostridium subterminale, *Proc Natl Acad Sci U S A 102*, 13819-13824.
[57] Okamoto, A., Higuchi, T., Hirotsu, K., Kuramitsu, S., and Kagamiyama, H. (1994) X-ray crystallographic study of pyridoxal 5'-phosphate-type aspartate aminotransferases from Escherichia coli in open and closed form, *Journal of biochemistry 116*, 95-107.
[58] Vacca, R. A., Christen, P., Malashkevich, V. N., Jansonius, J. N., and Sandmeier, E. (1995) Substitution of Apolar Residues in the Active Site of Aspartate Aminotransferase by Histidine, *European Journal of Biochemistry 227*, 481-487.
[59] Okamoto, A., Higuchi T Fau - Hirotsu, K., Hirotsu K Fau - Kuramitsu, S., Kuramitsu S Fau - Kagamiyama, H., and Kagamiyama, H. X-ray crystallographic study of pyridoxal 5'-phosphate-type aspartate aminotransferases from Escherichia coli in open and closed form.
[60] Kochhar, S., and Christen, P. (1992) Mechanism of racemization of amino acids by aspartate aminotransferase, *European Journal of Biochemistry 203*, 563-569.
[61] Hayashi, H., Mizuguchi, H., Miyahara, I., Nakajima, Y., Hirotsu, K., and Kagamiyama, H. (2003) Conformational change in aspartate aminotransferase on substrate binding induces strain in the catalytic group and enhances catalysis, *The Journal of biological chemistry 278*, 9481-9488.
[62] McPhalen, C. A., Vincent, M. G., Picot, D., Jansonius, J. N., Lesk, A. M., and Chothia, C. (1992) Domain closure in mitochondrial aspartate aminotransferase, *Journal of molecular biology 227*, 197-213.
[63] Islam, M. M., Hayashi, H., Mizuguchi, H., and Kagamiyama, H. (2000) The substrate activation process in the catalytic reaction of Escherichia coli aromatic amino acid aminotransferase, *Biochemistry 39*, 15418-15428.
[64] Steffen-Munsberg, F., Vickers, C., Kohls, H., Land, H., Mallin, H., Nobili, A., Skalden, L., van den Bergh, T., Joosten, H. J., Berglund, P., Hohne, M., and Bornscheuer, U. T. Bioinformatic analysis of a PLP-dependent enzyme superfamily suitable for biocatalytic applications.
[65] Mani Tripathi, S., and Ramachandran, R. Direct evidence for a glutamate switch necessary for substrate recognition: crystal structures of lysine epsilon-aminotransferase (Rv3290c) from Mycobacterium tuberculosis H37Rv.
[66] Lee, H., Le, H. V., Wu, R., Doud, E., Sanishvili, R., Kellie, J. F., Compton, P. D., Pachaiyappan, B., Liu, D., Kelleher, N. L., and Silverman, R. B. (2015) Mechanism of Inactivation of GABA Aminotransferase by (E)- and (Z)-(1S,3S)-3-Amino-4-fluoromethylenyl-1-cyclopentanoic Acid, *ACS Chemical Biology 10*, 2087-2098.
[67] Lee, H., Doud, E. H., Wu, R., Sanishvili, R., Juncosa, J. I., Liu, D., Kelleher, N. L., and Silverman, R. B. (2015) Mechanism of Inactivation of γ-Aminobutyric Acid Aminotransferase by (1S,3S)-3-Amino-4-difluoromethylene-1-cyclopentanoic Acid (CPP-115), *Journal of the American Chemical Society 137*, 2628-2640.
[68] Bertoldi, M., and Borri Voltattorni, C. (2003) Reaction and substrate specificity of recombinant pig kidney Dopa decarboxylase under aerobic and anaerobic conditions, *Biochimica et Biophysica Acta (BBA) - Proteins and Proteomics 1647*, 42-47.

[69] Bunik, V. I., Schloss, J. V., Pinto, J. T., Dudareva, N., and Cooper, A. J. L. (2011) A SURVEY OF OXIDATIVE PARACATALYTIC REACTIONS CATALYZED BY ENZYMES THAT GENERATE CARBANIONIC INTERMEDIATES: IMPLICATIONS FOR ROS PRODUCTION, CANCER ETIOLOGY, AND NEURODEGENERATIVE DISEASES, *Advances in enzymology and related areas of molecular biology 77*, 307-360.
[70] Bertoldi, M., Gonsalvi, M., Contestabile, R., and Voltattorni, C. B. (2002) Mutation of tyrosine 332 to phenylalanine converts dopa decarboxylase into a decarboxylation-dependent oxidative deaminase, *The Journal of biological chemistry 277*, 36357-36362.
[71] Bertoldi, M., Moore, P. S., Maras, B., Dominici, P., and Voltattorni, C. B. (1996) Mechanism-based inactivation of dopa decarboxylase by serotonin, *The Journal of biological chemistry 271*, 23954-23959.
[72] Bertoldi, M., Dominici, P., Moore, P. S., Maras, B., and Voltattorni, C. B. (1998) Reaction of Dopa Decarboxylase with α-Methyldopa Leads to an Oxidative Deamination Producing 3,4-Dihydroxyphenylacetone, an Active Site Directed Affinity Label, *Biochemistry 37*, 6552-6561.
[73] Bertoldi, M., Cellini, B., Montioli, R., and Borri Voltattorni, C. (2008) Insights into the mechanism of oxidative deamination catalyzed by DOPA decarboxylase, *Biochem 47*, 7187-7195.
[74] Hayashi, H. (1995) Pyridoxal Enzymes: Mechanistic Diversity and Uniformity, *The Journal of Biochemistry 118*, 463-473.
[75] Rahman, M. K., Nagatsu, T., Sakurai, T., Hori, S., Abe, M., and Matsuda, M. (1982) Effect of pyridoxal phosphate deficiency on aromatic L-amino acid decarboxylase activity with L-DOPA and L-5-hydroxytryptophan as substrates in rats, *Japanese journal of pharmacology 32*, 803-811.
[76] Bertoldi, M., Castellani, S., and Bori Voltattorni, C. (2001) Mutation of residues in the coenzyme binding pocket of Dopa decarboxylase. Effects on catalytic properties, *European journal of biochemistry / FEBS 268*, 2975-2981.

# Chapter 5

## *Streptomyces wadayamensis* MppP is a PLP–Dependent L-Arginine Oxidase in the L-Enduracididine Biosynthetic Pathway

### 5.1 Background

A UV-visible spectrum of SwMppP with L-Arg (Figure 5-1A) has the peak at 415-420 nm associated with the internal aldimine form of Fold Type I PLP-dependent aminotransferases. In buffers with pH < 7.0, like MES pH 6.7, the spectrum of SwMppP was unchanged over a full hour at room temperature. Thus, 10 mM MES pH 6.7 was chosen as the storage buffer for the enzyme. In high pH buffers, like $NaPO_4$ pH 8.4 or BIS-TRIS propane pH 9.0, the enzyme exhibits much higher activity, even though the enzyme loses both its color and the peak at 415 nm ($t_{1/2} \approx 30$ min). So we use high pH buffers for later kinetics study.

Since enduracididine biosynthesis is thought to begin from L-Arg, and the other two enzymes in the pathway, MppR and MppQ, are thought, based on our own results, to be involved in later steps, we tested SwMppP for activity with L-Arg. Upon addition of 1 mM L-Arg to a solution of 30.0 μM SwMppP in 50 mM Bis-TRIS propane, pH 9.0, the peak at 415-420 nm shifted ~10 nm to the right (425-430 nm), indicative of formation of the external aldimine [1, 2] (Figure 5-1A). After approximately 70 seconds, two new species absorbing at 510 and 560 nm began to accumulate. The former reached a maximum and plateaued, while the latter only accumulated for a short time and then quickly decayed (Figure 5-1A,

inset). Agitating the cuvette resulted in the disappearance of the 510 nm peak. After a short time, the 510 nm peak would accumulate again. This observation suggested that SwMppP reacts with molecular oxygen as well as L-Arg. To confirm this putative reaction with $O_2$, we performed the same experiments in a Clark electrode to monitor the consumption of dioxygen directly. As is evident in Figure 5-1B, dioxygen is consumed upon addition of the enzyme, and the rate of $O_2$ consumption increases with the concentration of L-Arg.

**Figure 5-1:** SwMppP reacts with L-Arg. Absorbance spectra recorded on a Hewlett-Packard 8453 diode array spectrophotometer for the reaction of 30 μM SwMppP with 2 mM L-Arg and ambient (~250 μM) $O_2$ (A). Spectra were recorded every 0.5 s, but only the traces every 10 s are shown here for clarity. The purple line represents the enzyme alone in 50 mM BIS-TRIS propane pH 9.0. The blue gradient traces represent the absorbance changes over 300 s (10 s interval data from lighter to darker blue as time goes). The inset shows the absorbance changes at 510 (green), and 560 nm (orange). The consumption of dioxygen was confirmed by monitoring the reaction in a Hansatech Oxygraph Clark electrode (B). Reactions were initiated by adding SwMppP into solutions containing different concentrations of L-Arg (black arrow).

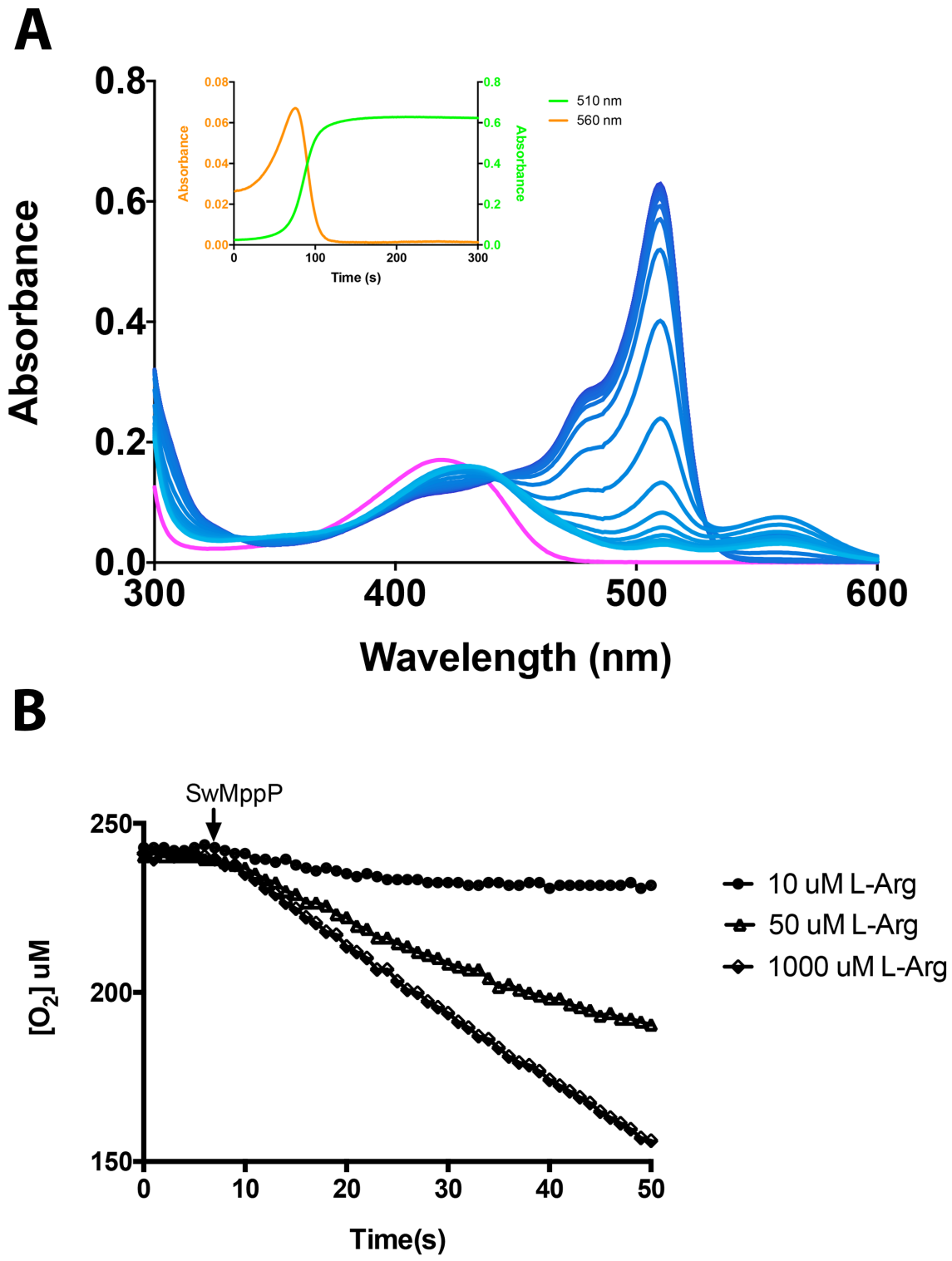
A
Absorbance
0.0
0.2
0.4
0.6
0.8
300
400
500
600
Wavelength (nm)
Absorbance
Time (s)
510 nm
560 nm
B
SwMppP
[O2] uM
250
200
150
0
10
20
30
40
50
Time(s)
10 uM L-Arg
50 uM L-Arg
1000 uM L-Arg

Having established that SwMppP reacts specifically with L-Arg and molecular oxygen, we set about identifying the product(s) of the reaction. Proton NMR analysis of SwMppP reaction mixtures and an L-Arg standard (Figure 5-2), showed that SwMppP converted L-Arg into at least one new product. Preliminary data from $^{1}H$ COSY, $^{1}H$-$^{13}C$ HSQC, and $^{1}H$-$^{13}C$ HMBC spectra (Appendix 5-1) showed that the SwMppP-catalyzed reaction between L-Arg and molecular oxygen yields two products: 2-oxo-4(R)-hydroxy-5-guanidinovaleric acid (*i.e.* 4-hydroxy-2-ketoarginine, compound **2** in Figure 5-3) and 2-oxo-5-guanidinovaleric acid (*i.e.* 2-ketoarginine, compound **3** in Figure 5-3).

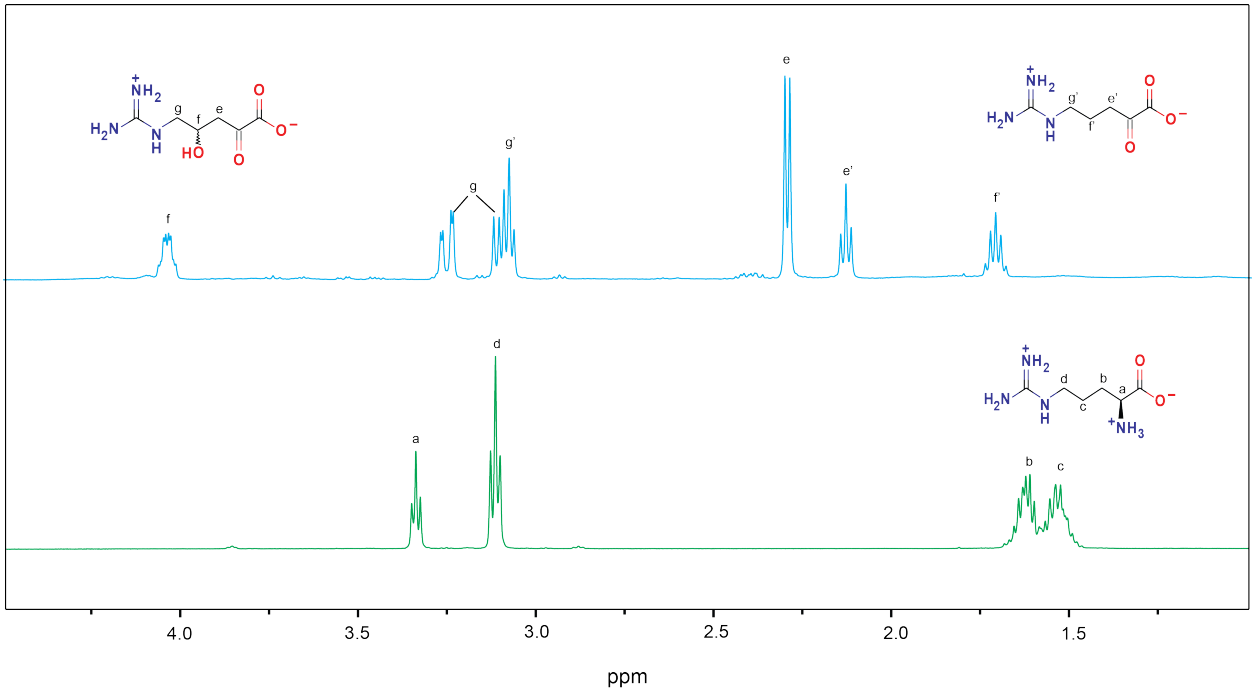


**Figure 5-2:** Proton NMR results of L-Arg (2.0 mM, bottom) and the reaction of 10 µM SwMppP with 2.0 mM L-Arg (top), both in 20 mM sodium phosphate pH 8.4 buffer.

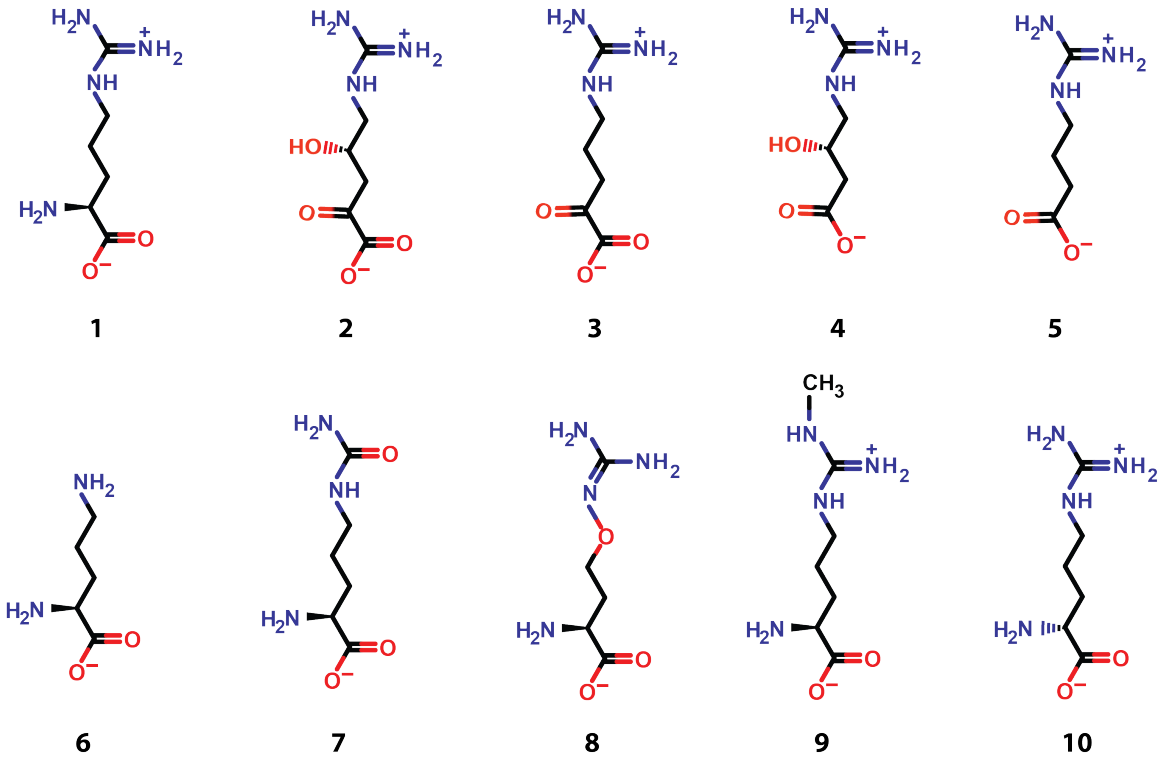


**Figure 5-3:** Compounds encountered in our studies of SwMppP. **1** is L-arginine. **2** and **3** are the two products of the reaction of SwMppP with L-Arg, 2-oxo-4(R)-hydroxy-5-guanidinovaleric acid (**2**) and 2-oxo-5-guanidinovaleric acid (**3**), respectively. **4** and **5** are the $H_2O_2$-catalyzed decarboxylation products of **2** and **3** that were observed by mass spectrometry in the absence of catalase, 4-guanidino-(S)-3-hydroxybutyric acid and 4-guanidinobutyric acid, respectively. Compounds **6 -10** are analogs of L-Arg used to explore the substrate specificity of SwMppP: **6** is L-ornithine; **7** is L-citrulline; **8** is L-canavanine; **9** is $N^G$-methyl-L-arginine; **10** is D-arginine.

## 5.2 Methods

### 5.2.1 Cloning, expression, and purification of *S. wadayamensis* and *Streptomyces globisporus* MppP

The coding sequences of SwMppP (GenBank accession code KDR62041) and *Streptomyces globisporus* MppP (SgMppP; GenBank accession code IH67_RS0105915) were optimized for expression in *E. coli* and synthesized by GenScript Inc. (Piscataway, NJ). The synthetic genes were subcloned into the pE-SUMO$_{kan}$ expression vector (LifeSensors Inc., Malvern, PA) using primers containing BsaI and XbaI restriction sites (Table 5-1). The integrity of the SwMppP coding sequence was confirmed by Sanger sequencing (GeneWiz, Inc). The H29S and F191Y mutants of SwMppP were constructed by the QuickChange mutagenesis method with primers pSUMO-SwPH29A_F/R or pSUMO-SwPF191Y_F/R, respectively, and the pSUMO-SwMppP plasmid as the template. The H29A, F115Y, S190A, D218S, E15A and E15Q mutants of SwMppP were generated with the Q5 site-directed mutagenesis kit (New England Biolabs).

**Table 5-1:** Primers used for mutagenesis

| **Names** | **Primers sequences** |
|---|---|
| pSUMO-SwMppP_F | 5′ -GGTCTCAAGGTATGACGACGCAACCGC-3 |
| pSUMO-SwMppP_R | 5′ -GCTCTAGATCATTAGCGGGTTTCCAGGAC-3′ |
| pSUMO-SgMppP_F | 5′ -GCGGTCTCAAGGTATGAACCGCATTCTGCCGAAAGTC-3′ |
| pSUMO-SgMppP_R | 5′ -GCTCTAGATTAGCCTTGACGTTCAGCGGTATC-3′ |
| pSUMO-SwP$_{H29A}$_F | 5’-CGCAGACGGCGCCGCCCGTCAGG-3’ |
| pSUMO-SwP$_{H29A}$_R | 5’-ATGTTCAGTTCGGAGTTCAGTGC-3’ |
| pSUMO-SwP$_{H29A}$_F | 5’-GAACATCGCAGACGGCAGCGCCCGTCAGGCAC-3’ |
| pSUMO-SwP$_{H29A}$_R | 5’-GTGCCTGACGGGCGCTGCCGTCTGCGATGTTC-3’ |
| pSUMO-SwP$_{F115Y}$_F | 5’-TCATCCGACGTATGATAACATCGCTG-3’ |
| pSUMO-SwP$_{F115Y}$_R | 5’-ACCAGTGCCACGCGATCG-3’ |
| pSUMO-SwP$_{F191Y}$_F | 5’-CACTGGATACGAGTTATCGTGGTTTCGATG-3’ |
| pSUMO-SwP$_{F191Y}$_R | 5’-CATCGAAACCACGATAACTCGTATCCAGTG-3’ |
| pSUMO-SwP$_{S190A}$_F | 5’-ACTGGATACGGCTTTTCGTGGTTTCGATGCG-3’ |
| pSUMO-SwP$_{S190A}$_R | 5’-GCCAGAACGGTGCCATGT-3’ |
| pSUMO-SwP$_{D218S}$_F | 5’-GGTTATTGAATCTACCGGTAAACTGTGGCCGACGC-3’ |
| pSUMO-SwP$_{D218S}$_R | 5’-ACCCAGCGACAGCCAGCT-3’ |
| pSUMO-SwP$_{T12A}$_F | 5’-CTGAAAGAAAACCTGGCGCAATGGG-3’ |
| pSUMO-SwP$_{T12A}$_R | 5’-CCCATTGCGCCAGGTTTTCTTTCAG-3’ |
| pSUMO-SwP$_{E15A}$_F | 5’-GACGCAATGGGCATACCTGGCAC-3’ |
| pSUMO-SwP$_{E15A}$_R | 5’-AGGTTTTCTTTCAGTTGCGGTTG-3’ |
| pSUMO-SwP$_{E15Q}$_F | 5’-GACGCAATGGCAATACCTGGCAC-3’ |
| pSUMO-SwP$_{\Delta 1\text{-}22}$_F | 5’- TAGGTCTCTAGGTCTGAACATCGCAGACGGC-3’ |

The $His_6$-SUMO-SwMppP fusion proteins were expressed from *E. coli* BL21 Star (DE3) cells (Invitrogen Inc., Carlsbad, CA) carrying the pE-SUMO-SwMppP plasmid. Cultures were grown in Luria-Bertani medium with 50 μg/mL kanamycin at 37 °C. When the cultures reached an $OD_{600nm}$ of ~1.0, protein expression was induced with 0.4 mM isopropyl β-D-1-thiogalactopyranoside (IPTG). The temperature was reduced to 25°C, and the cultures were grown overnight while being shaken at 250 rpm. Cells were harvested by centrifugation, resuspended in 5 mL/g of buffer A (25 mM TRIS pH 8.0, 300 mM NaCl, 10 mM imidazole, and 100 μM PLP) supplemented with 0.1 mg/mL DNase I (Worthington Biochemical Corp., Lakewood, NJ). The cells were lysed using a Branson Sonifier S-450 cell disruptor (Branson Ultrasonics Corp., Danbury, CT) for a total of 10 min at 60% amplitude with 30 s pulses separated by 50 s rest periods. The temperature was maintained at or below 4 °C by suspending the steel beaker in an ice bath directly over a spinning stir bar. The lysate was clarified by centrifugation at 39000 x g for 45 min and then applied to a 5 mL HisTrap column (GE Lifesciences, Piscataway, NJ) at a flow rate of 5 mL/min to isolate the $His_6$-SUMO-SwMppP fusion protein. The protein was eluted by a four-step gradient of buffer B (25 mM TRIS (pH 8.0), 300 mM NaCl, and 250 mM imidazole; 5, 15, 50, and 100%). The $His_6$-SUMO-SwMppP fusion protein eluted in the third and fourth steps and was ~90% pure, as judged by Coomassie-stained sodium dodecyl sulfate–polyacrylamide gel electrophoresis (SDS-PAGE). Peak fractions were pooled and dialyzed overnight against 4 L of 25 mM TRIS pH 8.0, 150 mM NaCl, 100 μM PLP, and ~3 μM SUMO protease (LifeSensors Inc.). The dialysate was passed through the HisTrap column a second time to remove the cleaved $His_6$-SUMO tag as well as the protease. The resulting SwMppP preparation was >95% pure. The protein was desalted using a HiTrap desalting column (GE Lifesciences)

into 10.0 mM MES pH 6.7 and 20 μM PLP and stored at −80°C. All SwMppP mutants were purified by the same protocol as the wild type enzyme. Selenomethionine-labeled SgMppP was expressed from T7 Express Crystal cells (New England Biolabs, Ipswich, MA) carrying the pE-SUMO-SgMppP plasmid. Cells were grown in Selenomethionine Medium Complete (Molecular Dimensions, Newmarket, Suffolk, U.K.) with 50 μg/mL kanamycin. SgMppP was expressed and purified using the same protocols described for SwMppP, except that SgMppP was desalted into three different buffers based on the results of differential scanning fluorimetry experiments with the Slice pH screen (10 mM ADA pH 7.0, 20 μM PLP; 10 mM DL-Malic acid pH 6.0, 20 μM PLP; 10 mM Succinic acid pH 6.0, 20 μM PLP).

### 5.2.2 UV/Vis spectroscopy of SwMppP and its mutants reacting with L-Arginine and dioxygen

Hewlett-Packard 8453 diode array spectrophotometer was used for scanning the 700 μL reaction of ~30 μM enzyme (SwMppP or its mutants) with 2 mM L-Arg and ambient (~250 μM) $O_2$ in 50 mM BisTris propane pH 9.0 buffer. The scan was taken every 0.5 s from 200 nm and 700 nm.

### 5.2.3 Characterization of MppP reaction products by NMR

Reactions (4.8 mL) were conducted in 50 mL conical tubes with gentle agitation to prevent depletion of dioxygen. All enzymes were stored in 10 mM MES pH 6.7, 20 μM PLP

buffer. To avoid side reactions due to free PLP, the concentration of free PLP was limited by concentrating the proteins to ~600 μM, thus limiting the volume of enzyme (with free PLP) required for the reaction. For wild type SwMppP, ~10 μM SwMppP was added to a solution of 2 mM L-Arg in 20mM sodium phosphate pH 8.4. Due to the reduced catalytic efficiency of the mutants, more enzyme (~65 μM) was used in these reactions. The $SwMppP_{F115Y}$ variant was desalted into 20 mM sodium phosphate pH 8.4, 10 μM PLP buffer, since it was not stable in the absence of free PLP. Control reactions contained 2 mM L-Arg in 20 mM sodium phosphate pH 8.4, with the same volume of enzyme storage buffer (*i.e.* no enzyme). All reactions were shaken at 25°C, 200 rpm for 2.5 h and protected from light. At the end of the reaction time, samples were evaporated to dryness using a Centrifan PE Rotary Evaporator (KD Scientific, Holliston, MA) at 40°C for 6 h. The resulting residue was taken up in 600 μL $D_2O$ and centrifuged at 13,000 x g for 10 min to remove any remaining particulates. The supernatants (500 μL) were loaded into NMR tubes for $^1H$ NMR, $^{13}C$ NMR, and 2D NMR ($^1H$-$^1H$ COSY, HSQC, and HMBC) to determine the structures of the reaction products.

### 5.2.4 Characterization of MppP reaction products by mass spectrometry

Reactions (1.0 mL) contained 2 mM L-Arg in MilliQ $H_2O$, 10 μM SwMppP in MilliQ $H_2O$, with or without 53 U of catalase from bovine liver (Sigma-Aldrich, St. Louis, MO). The two negative controls were 2 mM L-Arg in MilliQ $H_2O$ and 2mM L-Arg in water with 53 U catalase. Reactions were run in the dark at 25 °C for 2.5 h with shaking at 200 rpm. All samples were boiled for 10 min and centrifuged at 30,000 x g for 10 min. The supernatants were diluted 10-fold with MilliQ $H_2O$ and then directly injected into a Shimadzu LCMS-

2020.

### 5.2.5 Ammonium detection by NADH based GDH assay[3]

To detect ammonium formation in the reaction of SwMppP with L-Arg and $O_2$, I referred to the well-known method summarized in Scheme 5-1. L-glutamate dehydrogenase (GDH) is an NAD(P)H-dependent enzyme that catalyzes the conversion of α-ketoglutarate, $NH_4^+$ and NADH into glutamate, $NAD^+$, and $H_2O$. NADH absorbs UV light at 340 nm, but NAD+ does not. So upon addition of GDH, the absorbance at 340 nm decreases in the presence of $NH_4^+$.

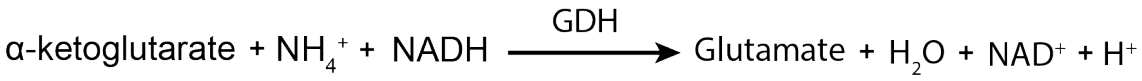


**Scheme 5-1:** Ammonia assay reaction. The assay detects the absorbance decrease at 340 nm, due to the NADH oxidation.

The 1000 µl reactions were conducted in 50 mM HEPES pH 7.5 buffer and included 20 µM SwMppP, 20 µM or 50 µM L-Arg, 140 µM NADH and 3.5 mM α-ketoglutarate. The reaction components were mixed and incubated for 10 min at room temperature. This was used to blank the spectrophotometer and the absorbance at 340 nm was monitored to ensure a flat baseline. The reaction was initiated by the addition of $10^{-2}$ units of GDH (Sigma) and the absorbance at 340 nm was recorded for ~15 min, until the absorbance reached a plateau.

### 5.2.6 Defining the relationship between $O_2$ usage and $H_2O_2$ formation

To determine how many $O_2$ were used to generate $H_2O_2$, the regeneration of $O_2$ by catalase was measured in a Hansatech dioxygen electrode. The reaction mixtures contained 25 μM, 50 μM, or 100 μM L-Arg in 50 mM BIS-TRIS propane pH 9.0. When the $O_2$ concentration was stable, 10 μM SwMppP was added into the solution and $O_2$ consumption was monitored. When the reaction reached equilibrium (plateau in the dioxygen concentration), 10 μl of 0.5 mg/mL catalase was added to the 1 mL reaction to disproportionate two equivalents of $H_2O_2$ into one equivalent of $O_2$ and two equivalents of water.

### 5.2.7 Reactions with $^{18}O_2$, $H_2{}^{18}O$

Reactions in the presence of $^{18}O_2$ were conducted in a tonometer, a closed, airtight reaction vessel. The body of the tonometer contained 10 μM SwMppP in 100 mM ammonium bicarbonate pH 9.0 with 50 ng/mL catalase. One short arm of the tonometer contained 20 μL of 500 mM L-Arg, and the other was connected to a 500 mL bottle of $^{18}O_2$ with an air-tight valve. The tonometer was connected to a Schlenk line, which was used to purge the tonometer of oxygen by 45 cycles of vacuum (~5 s) and flushing with argon (45 s). Prior to removing the tonometer from the Schlenk line, the atmosphere was removed with the vacuum pump to enable the labelled dioxygen to fill the tonometer. The tonometer was closed and removed from the Schlenk line. The reaction was started by mixing the enzyme solution in the tonometer body with the L-Arg in the side arm. Without $O_2$, the

quinonoid I intermediate accumulated, which has a pale pink to orange color. Then the $^{18}O_2$ was allowed to fill the tonometer. The reaction was carried out at room temperature for 2 h. After the reaction, the tonometer was opened and samples were analyzed by ESI-MS.

The 200 µl reaction of SwMppP and L-Arg in $H_2{}^{18}O$ was conducted in 1.7 mL eppendorf tubes at room temperature overnight. The reaction contained 10 µM SwMppP, 2 mM L-Arg and ~95.4% $H_2{}^{18}O$. The products of the reaction were identified by ESI-MS.

### 5.2.8 Crystallization of wild-type and mutant forms of SwMppP, as well as SgMppP

Initial crystallization conditions were identified by screening 15 mg/mL SwMppP and its mutants against the Index HT screen (Hampton Research). After optimization, diffraction-quality SwMppP crystals were obtained by the hanging drop vapor diffusion method from 30% polyethylene glycol monomethyl ether 550 (PEG MME 550), 50 mM $MgCl_2$, and 0.1 M HEPES pH 8.0. Drops contained 2 µL of protein solution at 15 mg/mL and 1 µL of crystallization solution. Crystals formed as plates or rods after 3–4 days and grew to maximum dimensions of ~200 µm × ~50 µm × ~5 µm. Initial crystallization conditions for the homologous enzyme SgMppP (*S. globisporus*) were identified in the same way by screening 15 mg/mL SgMppP against the Index HT screen. Crystals of SeMet-substituted SgMppP in 10 mM ADA pH 7.0, 20 µM PLP were grown from 10% PEG MME 5000, 5% Tacsimate pH 7.0, and 0.1 M HEPES pH 7.5. SgMppP crystallized as small rods (~100 µm × ~10 µm × ~10 µm). Both types of crystals were cryo-protected by sequential soaks in

holding solutions containing 5, 10, or 20% glycerol and flash cooled by plunging into liquid nitrogen.

The structure of SwMppP with D-Arg bound was obtained by transferring crystals into 30 µL drops of the crystallization solution supplemented with 35 mM D-Arg. After being soaked for 5 min at RT, crystals were treated with paratone N and flash-cooled. The structure of SwMppP with L-Arg bound was obtained by transferring crystals into 30 µL drops of the crystallization solution supplemented with 10 mM L-Arg and 20% glycerol. After being soaked for 5 h at RT, crystals were plunged into liquid N2. The structure of SwMppP with **2** bound was obtained by transferring crystals into 30 µL drops of the crystallization solution supplemented with 10 mM 2-keto-Arg (contaminated with ~10% L-Arg) with 20% glycerol. After being soaked for 2 h at RT, crystals were plunged into liquid $N_2$.

$SwMppP_{H29A}$ and $SwMppP_{H29A}$ crystalized under the same conditions as the wild-type protein. $SwMppP_{H29A}$ and $SwMppP_{H29A}$ at 12 mg/ml in 10 mM MES pH 6.7, 20 µM PLP were mixed 2:1 with 30% (w/v) PEG MME 550, 0.1 M HEPES pH 7.5, 0.1 M $MgCl_2$. The volume of the resulting drops was 3 µl. Crystals of $SwMppP_{F115Y}$ were grown by mixing 1 µl of enzyme at 12 mg/ml in 10 mM MES pH 6.7, 20 µM PLP with 1 µl of 17.5% PEG 3350, 0.04 M citric acid, 0.06 M BIS-TRIS propane, pH 6.4. Crystals of $SwMppP_{D218S}$ were grown by mixing 2 µl of enzyme at 12 mg/ml in 10 mM MES pH 6.7, 20 µM PLP with 1 µl of 20% (w/v) PEG 3350, 0.1 M magnesium formate. The well solution contained microseeds derived from poor crystals grown during screening. The structures of Ala and Ser mutants of H29 (SwMppP(H29A/S)) with L-Arg bound were obtained by transferring crystals into 30 µL

drops of the crystallization solution supplemented with 10 mM L-Arg and 20% glycerol. After being soaked for 5 h at RT, crystals were plunged into liquid $N_2$.

X-ray diffraction data for SeMet SgMppP and native SwMppP were collected at beamline 21-ID-D of the Life Science Collaborative Access Team (LS-CAT) at the Advanced Photon Source (APS). The SwMppP·D-Arg data set was collected at LS-CAT beamline 21-ID-G. All data were processed with HKL2000[4].

The structure of SgMppP was determined by the single wavelength anomalous diffraction (SAD) method using 3.5 Å resolution data collected from a crystal of SeMet-substituted SgMppP at 0.97889 Å, 61.0 eV below the tabulated K-edge wavelength for Se (0.97950 Å). AutoSHARP[5] was used to determine the Se substructure, which contained 14 of the 16 Se atoms in the asymmetric unit, and calculate density-modified electron density maps. An initial model comprising ~90% of the asymmetric unit content was built using BUCCANEER[6].

Chain A of this partially refined model (with B factors set to 20.0 $Å^2$) was used as the search model for molecular replacement in PHASER[7] to phase the unliganded SwMppP data set. The molecular replacement solution was subjected to iterative cycles of manual model building in COOT[8] and maximum likelihood-based refinement using the PHENIX package (phenix.refine[9]). Ordered solvent molecules were added automatically in phenix.refine and culled manually in COOT. Hydrogen atoms were added to the model using phenix.reduce[10] and were included in the later stages of refinement to improve the stereochemistry of the model. Positions of H atoms were refined using the riding model with a global B factor. Regions of the model for translation-libration-screw (TLS)

refinement were identified using phenix.find_tls_groups (P. V. Afonine, unpublished work), and the TLS parameters were refined in phenix.refine. Once the refinement converged (R = 0.136, and $R_{free}$ = 0.162), the model was validated using the tools implemented in COOT and PHENIX[9, 11]. Sections of the backbone with missing or uninterpretable electron density were not included in the final model. Side chains with poor or missing electron density were modeled in favored rotameric conformations, and the B factors were allowed to refine without additional restraints. This was done to alert end users, who are more likely to display a model colored by B factors than to pay attention to atom occupancy values or download electron density maps, that these residues are not well defined in the electron density.

The final, refined model of SwMppP, stripped of water molecules and H atoms, and with all B factors set to 20.0 $Å^2$, was used to determine the structure of the enzyme with L–Arg bound, **2**, **3** and D-Arg bound by difference Fourier. The model was also used to determine the mutants' structures. Restraints for the L-Arg-PLP, **2**, **3** and D-Arg-PLP external aldimine were generated with phenix.elbow[12]. Data collection and model refinement statistics are listed in Appendix C. Coordinates and structure factors for both SwMppP and SwMppP·D-Arg models have been deposited in the Protein Data Bank (www.rcsb.org) with accession codes 5DJ1 and 5DJ3.

### 5.2.9 Preparation of 2-keto-arginine (3)

The 2-oxo acids used in this study were prepared by a modification of the procedure first described by Meister[13]. For example, compound **3** was prepared by dissolving 2 g of L-Arg in 50 mL of water and the pH was adjusted to 7.2 with concentrated HCl. Next, 100 mg of *Crotalus atrox* L -amino acid oxidase (LAAO) and 1.5 mg of catalase were dissolved in 10 mL of water and added to the amino acid solution. The volume was adjusted to 100 mL with water, and the reaction mixture was incubated in the dark at room temperature while being vigorously stirred. After 18 h, the 100 mL reaction mixture was concentrated to 7 mL at 50 °C under vacuum. The 2-oxo acid crystallized from the concentrated reaction mixture at 4 °C after approximately 1 week. The crystalline material was harvested, dried, and stored at − 20 °C. The compound was characterized by nuclear magnetic resonance (NMR) and ESI-MS and found to be predominantly the desired product.

### 5.2.10 Steady State Enzyme Kinetics

All 1.0 mL kinetic assays were conducted in triplicate at 25 °C in 50 mM BIS-TRIS propane, pH 9.0. The initial velocity of SwMppP-catalyzed hydroxylation of L-Arg was measured directly by monitoring the decrease in the dioxygen concentration using a dioxygen electrode (Hansatech Instruments, Norfolk, U.K.). The concentration of L-Arg was varied from 10 to 10,000 μM. The $k_{cat}$ and $K_M$ values were determined from the initial velocity data using the equation $v_0 = V_m[A]/(K_M + [A])$, where [A] is the concentration of L-Arg, $v_0$ is the initial velocity, $V_m$ is the maximal velocity, and $K_M$ is the Michaelis constant.

### 5.2.11 The stoichiometry of L-Arg and $O_2$ in the reaction

The stoichiometry of the reaction was determined by measuring the quantity of $O_2$ consumed in reactions with a constant enzyme concentration (10 μM SwMppP or its mutants) and different L-Arg concentrations. Reactions were monitored using the Hansatech dioxygen electrode. The concentration of dioxygen remaining when the reaction reached equilibrium was subtracted from the starting concentration to obtain the concentration of dioxygen consumed. The stoichiometry was computed using the following formula:

$$Eq.\ of\ O_2\, consumed\ per\ eq.of\ Arg\ added = \frac{[O_2]initial - [O_2]remaining}{[L - Arg]}$$

### 5.2.12 SwMppP substrate specificity

Reactions containing 686 μl of 30 μM SwMppP in 50 mM BIS-TRIS propane pH 9.0 were initiated by adding different L-Arg analogs (compounds **6**, **7**, **8**, **9** and **10**) to a final concentration of 2 mM. The reactions were monitored by recording spectra from 200-700 nm (0.5 s between scans) for 300 s in a Hewlett-Packard 8453 diode array spectrophotometer. The products of these reactions were identified by NMR and ESI-MS as discussed previously.

The inhibition constant of D-Arg was determined using the $O_2$ consumption assay

described above for the steady state kinetics. D-Arg concentrations ranging of 0, 250, 500, 1,000, 2,500, 5,000, and 10,000 μM were added to different L-Arg solutions (5, 10, 25, 50, 100, 250, 500, 1000, 2500 and 5000 μM) in 50 mM BIS-TRIS propane pH 9.0. Reactions were initiated by the addition of SwMppP to a final concentration of 10 μM and initial velocities were recorded. The inhibition constant was determined using the following equation:

$$vo = \frac{\Delta[O_2]}{t} \qquad \text{Equation 1}$$

Each data set of rate vs L-Arg concentrations was fitted with Michaelis-Menten equation (Equation 2).

$$v = (v_{max} * [\text{L-Arg}])/(K_M + [\text{L-Arg}]) \qquad \text{Equation 2}$$

Reciprocal plot of resulting $v_{max}$ and L-Arg concentration gives a series of linear plot at different D-Arg concentrations. The slope is $K_M/v_{max}(1+[\text{D-Arg}]/K_i)$, and the intercept is $1/V_{max}$. Reploting the slope vs [D-Arg], and the data were fitted linearly, which gives $K_i$ (-x intercept).

Fluorescence titration experiments were conducted to measure the binding constant of D-Arg. SwMppP (10 μM after mixing) was mixed with different concentrations of D-Arg (40 μM, 80 μM, 160 μM, 320 μM, 640 μM and 1280 μM) and the total fluorescence was measured with excitation at 415 nm. The results are shown in Figure 5-25. By fitting the fluorescence data into the following single exponential equation:

$$y = A1\text{^}\exp(-k_{obs} * x) + C \qquad \text{Equation 3}$$

In this equation, A1 is the amplitudes associates with the phase rate constants $k_{obs}$. The C is the constant of fluorescence intensity at the end of the reaction. The dependence of the observed rate constants $k_{obs}$ was fitted into the following hyperbola equation to give the $K_{d,app}$:

$$k_{obs} = k_{max} * [\text{D-Arg}] / (K_{d,app} + [\text{D-Arg}]) \qquad \text{Equation 4}$$

### 5.2.13 Testing for communication between the two binding sites of SwMppP$_{D188A}$

#### 5.2.13.1 Isothermal Titration Calorimetry (ITC)

The D188A mutant was used for the determination of binding constants, since this mutant is catalytically dead. About 3 mL of ~300 μM SwMppP$_{D188A}$ was prepared for ITC analysis by dialysis against 2 L of 15 mM MES pH 6.7 overnight at 4 $^{o}$C. The dialysis buffer was used to dilute the protein to 90 μM, and was also used to prepare a solution of 80 mM L-Arg. All solutions were degassed at 4$^{o}$C for 30 min before loading into the Nano ITC instrument (TA Instruments, New Castle, DE). The protein solution was placed in the reaction chamber, and the 80 mM L-Arg solution in the syringe. Injections of 2.5 μl were made every 300 s for a total of 20 injections. The titration experiments were done in triplicate at 4, 10, 12, 18 and 20 °C in order to find the optimal temperature (maximal signal-to-noise and best baseline).

#### 5.2.13.2 Determination of binding constants by fluorescence titration

Binding constants for the D188A mutant of SwMppP were also determined by fluorescence titration. Reactions were prepared by mixing 1.5 mL of 14 μM $SwMppP_{D188A}$ in 100 mM BIS-TRIS propane pH 9.0 with 1.5 mL of solutions with concentrations of L-Arg ranging from 5 to 2560 μM in the same buffer. The reactions were mixed by pipetting and incubated at room temperature for 8 min. Fluorescence data were collected on a RF-6000 spectrofluorophotometer (Shimadzu, Japan). Samples were excited at 415 nm (5 nm bandwidth) and the emission was measured from 436-700 nm (15 nm bandwidth).

The delta fluorescence data at 480 nm on each L-Arg concentration was obtained by subtract the fluorescence intensity with 0 μM L-Arg in 100 mM BIS-TRIS propane pH 9.0 buffer. Then the fraction of sites occupied and the concentration of D188A•L-Arg complex were calculated. The plot of calculated [D188A•L-Arg] complex versus [L-Arg] at 480 nm was fitted to hyperbolic equation:

$$[EL]_{480} = ([EL]_{480,\,max} * [L\text{-}Arg])/(K_{d,app} + [L\text{-}Arg]) \qquad \text{Equation 5}$$

### 5.2.14 Pre-steady state enzyme kinetics

Pre-steady state kinetics data were collected on a model SF-61 DX2 double-mixing stopped flow spectrophotometer. Since the reaction of SwMppP with L-Arg consumes oxygen, the substrate binding and related changes at the PLP center could be monitored by watching the total fluorescence signal when exciting the internal aldimine at 415 nm in samples of anaerobic enzyme and L-Arg. Likewise, the rate of formation of the first quinonoid intermediate (Q1) could be measured by monitoring the absorbance at 510 nm

under anaerobic conditions. The instrument was prepared for anaerobic work by overnight incubation with a solution of 1 mM dextrose, 10 U/mL glucose oxidase, which had been flushed through the entire system. Solutions for anaerobic stopped flow experiments were prepared in a tonometer. Briefly, 7 ml of 20 μM SwMppP in 10 mM MES pH 6.7, 20 μM PLP and 100 μM glucose (with or without 5 ng/mL catalase) were placed in the main body of the tonometer and 25 μl (1 U/μl) glucose oxidase were placed in the side arm. The tonometer was attached to a Schlenk line and dioxygen was removed from the solution using 45 cycles of vacuum (~5 s) and flushing with argon (~30 s). Because the SwMppP protein is light-sensitive and somewhat unstable at room temperature, this procedure was conducted on ice and the tonometer was covered with foil to protect it from light. Different concentrations of L-Arg in 100 mM BIS-TRIS propane pH 9.0 with 200 μM glucose were placed in glass syringes and sparged with argon gas for 5 min to remove dioxygen. Before removing the argon nozzle and mounting the syringe on the stopped flow instrument, 10 μl of glucose oxidase were injected through the luer tip. Single mixing experiments were conducted at 25 °C with 10 μM SwMppP and 10 to 1280 μM L-Arg (all concentrations are after mixing 1:1)

To measure the rates of the $O_2$-dependent steps, double mixing experiments were performed where anaerobic enzyme was mixed 1:1 with a saturating amount of anaerobic L-Arg. This was then mixed 1:1 with buffer containing various concentrations of dioxygen. As above, the instrument was made anaerobic overnight with the glucose/glucose oxidase treatment described above. The first tonometer contained 40 μM enzyme, 10 ng/mL catalase in 10 mM MES pH 6.7, 20 μM PLP under anaerobic conditions. The second tonometer, made anaerobic as described above, contained 2,560 μM L-Arg in 100 mM BIS-

TRIS propane pH 9.0. The third tonometer contained 100 mM BIS-TRIS propane pH 9.0 with different concentrations of dioxygen (20, 40, 78, 158, 296, 465 μM). Defined dioxygen concentrations were obtained using a Maxtec Maxblend gas blender to mix high purity $O_2$ gas with gaseous $N_2$. The concentrations of dioxygen produced at different settings of the mixing valve were determined using the Clark-type electrode. Samples of oxygenated buffer were prepared by sparging the 100 mM BIS-TRIS propane pH 9.0 buffer with set concentrations of dioxygen for 5 min. After the first mixing step, the reactions were aged for 20 s prior to the second mixing step in order to convert all of the enzyme to the Q1 intermediate. The second step mixed the anaerobic reaction mixture with buffer containing different concentrations of dissolved $O_2$. The reactions were monitored at 510 nm and 560 nm for 100 s for each data set.

## 5.3 Results

### 5.3.1 The products of SwMppP with L-Arg and $O_2$

The products of SwMppP with L-Arg was also confirmed by mass spectrometry with electrospray ionization (ESI-MS), which detected peaks in the positive mode spectrum at m/z=146 and m/z=162. These masses correspond to the five-carbon products derived from **2** and **3**, 4-guanidino-3(S)-hydroxybutyric acid (**4**) and 4-guanidinobutyric acid (**5**). The result was also verified by $^{13}$C-NMR (Figure 5-4). These products are the result of oxidative decarboxylation of **2** and **3**, like catalyzed by $H_2O_2$ as has been observed for other α-keto acids [14, 15]. This observation was the first suggestion that $H_2O_2$ might be a product of

SwMppP-catalyzed oxidation of L-Arg. Therefore, the experiment was repeated, this time with catalase in the reaction mixture. The masses for both products are 174 and 190, corresponding to **3** and **2**. The fully oxidized product **2** is produced at a ratio of ~1.7:1 compared to the partially oxidized product **3**. Thus, once in every two to three turnover cycles, the enzyme loses its substrate to hydrolysis before it can be fully oxidized. This observation likely has important implications for the mechanism of this novel enzyme. Note that **2** is the same compound that MppR was able to cyclize to give the iminoimidazolidine ring of L-End observed in a crystal structure of MppR in the presence of **2**. MppP is therefore the first enzyme in L-End biosynthesis, reacting directly with L-Arg to create the substrate for MppR.

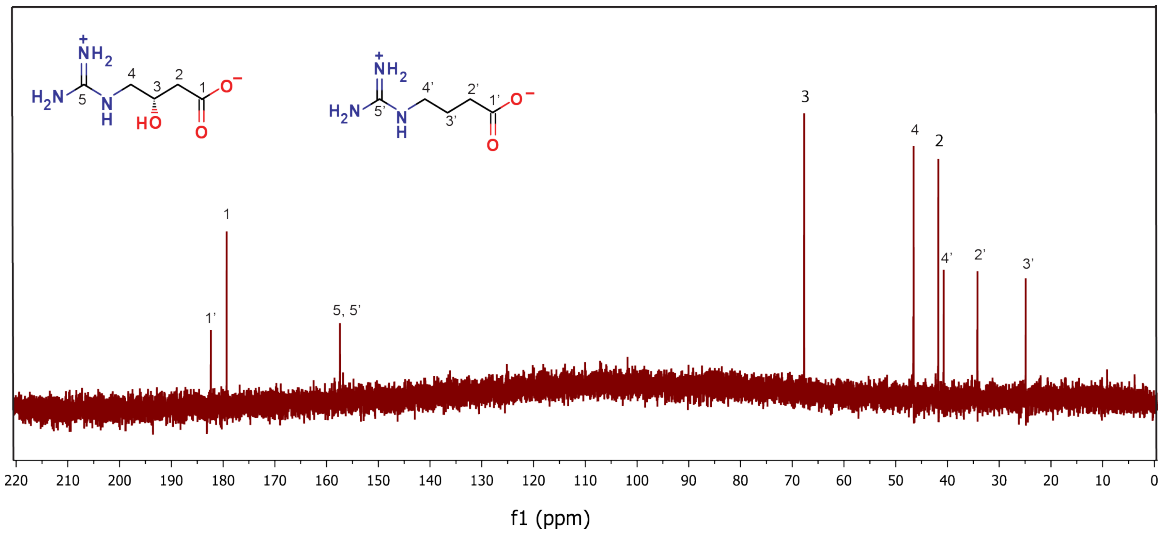


**Figure 5-4:** $^{13}$C-NMR spectrum of the reaction of 10 μM SwMppP with 2.0 mM L-Arg in 20 mM sodium phosphate pH 8.4 buffer.

### 5.3.2 Ammonia is also a product of SwMppP with L-Arg and $O_2$

The 4-electron oxidation of L-Arg suggested by the results detailed above would require ammonia to also be a product of the reaction, since the PLP cofactor needs to be converted from the pyridoxamine form to the aldehyde (PLP) at the end of the reaction cycle. A glutamate dehydrogenase (GDH)-coupled assay was employed to determine whether or not the reaction of SwMppP with L-Arg produces ammonia. The assay takes advantage of the fact that GDH can be run in reverse, where α-ketoglutarate is reduced by ammonia and NADH to give glutamate, water, $NAD^+$, and a proton. By constructing a standard curve of the rate of loss of absorbance from NADH at 340 nm vs the concentration of ammonia, it is possible to estimate the concentration of ammonia in, for example, SwMppP reaction mixtures. The results of these experiments are shown in Figure 5-5. The correlation coefficient ($R^2$) of the standard curve is 0.9992, so the response of the GDH initial velocity to the ammonia concentration is linear. In the reaction of 20 μM SwMppP and different concentrations of L-Arg, after the GDH addition, the absorbance at 340 nm decreased and the rate of this decrease is proportional to the centration of L-Arg. In 15 min, approximately 80% of the L-Arg was consumed and an equal amount of ammonia was released.

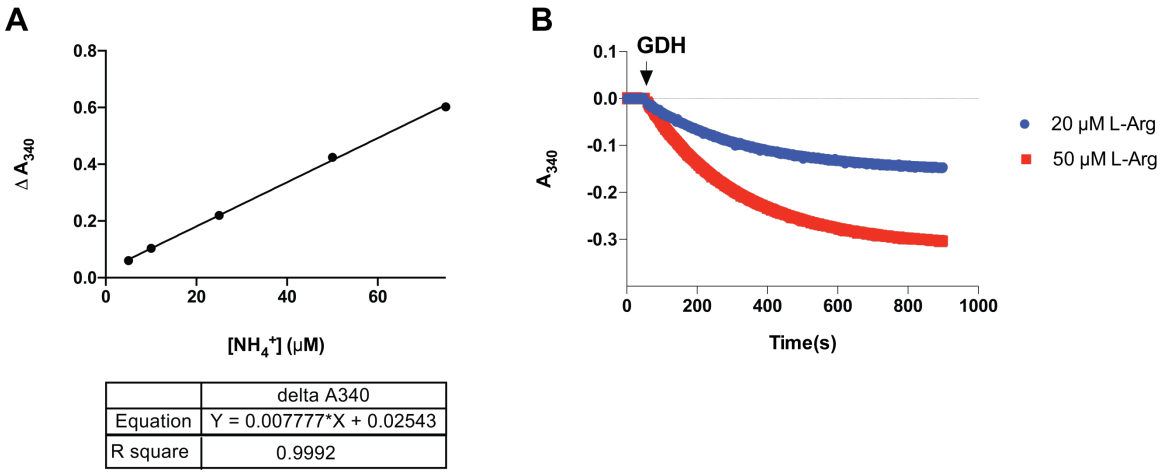


| | delta A340 |
|---|---|
| Equation | Y = 0.007777*X + 0.02543 |
| R square | 0.9992 |

**Figure 5-5:** (A) The standard curve of NADH based GDH assay. (B) The ammonium formation is proportional to the L-Arg concentration according to the GDH assay.

### 5.3.3 SwMppP is an oxidase and not an oxygenase

Reactions of SwMppP with 3 concentrations of L-Arg were monitored using an oxygen electrode (Figure 5-6). When the reactions reached equilibrium, catalase was added. The addition of catalase resulted in the regeneration of dioxygen amounting to half of that originally consumed by SwMppP in each reaction. This result indicates that $H_2O_2$ is another formal product of the SwMppP reaction, and that each molecule of $O_2$ consumed by SwMppP is reduced to $H_2O_2$ during the catalytic cycle.

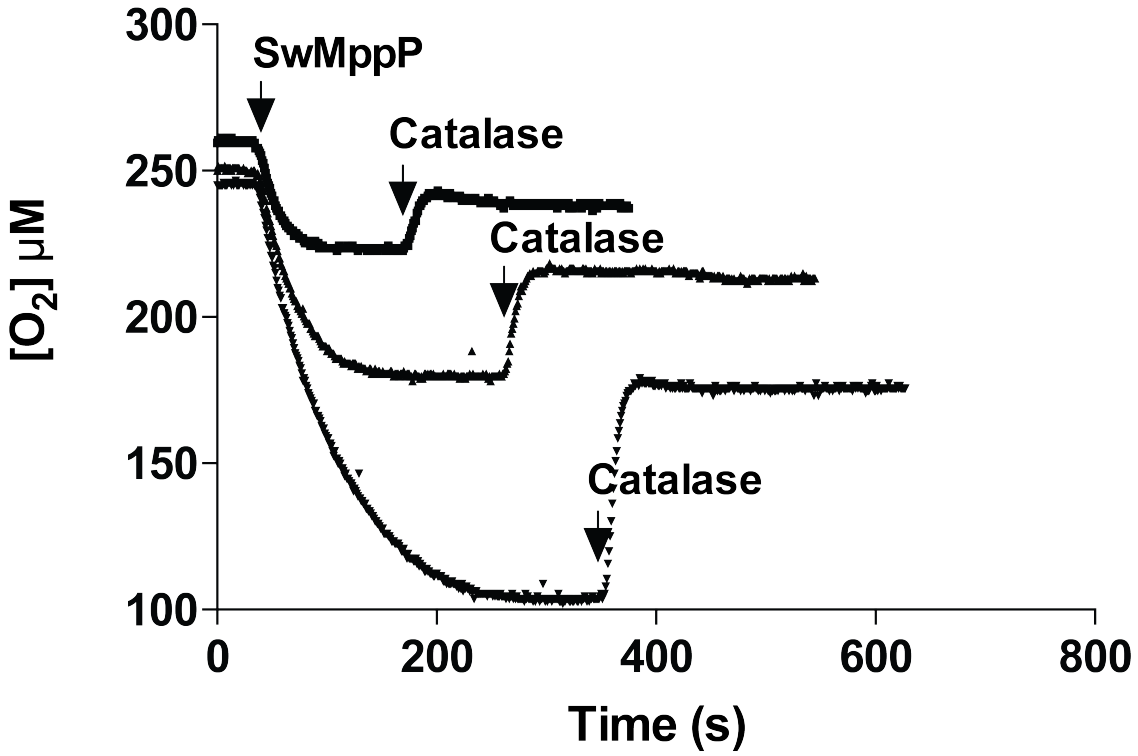


| L-Arg (µM) | [$O_2$ consumed] after SwMppP addition (µM) | [$O_2$ generated] after catalase addition (µM) |
|---|---|---|
| 25 | 38.07 ± 1.60 | 19.00 ± 1.00 |
| 50 | 69.33 ± 1.16 | 35.67 ± 0.58 |
| 100 | 140.33 ± 2.31 | 71.67 ± 2.08 |

**Figure 5-6:** $O_2$ regeneration after adding catalase into equilibrated SwMppP with varied [L-Arg] solutions. The concentration of dioxygen was monitored in a Hansatech dioxygen electrode. The reactions were initiated by add 10 µM SwMppP into solutions containing 25 µM (■, top), 50 µM (▲, middle), and 100 µM (▼, bottom) L-Arg in 50 mM BisTris Propane pH 9.0 buffer. When the reaction was equilibrated, 50 ng/mL catalase were added into the solution. As the table shown, the regenerated $O_2$ is around half of the $O_2$ consumed by SwMppP, which suggests that all $O_2$ was consumed to form $H_2O_2$.

The observation that each molecule of dioxygen consumed is reduced to hydrogen peroxide logically dictates that none of the oxygen atoms incorporated into the products (**2** or **3**) can come from dioxygen. SwMppP is therefore an oxidase, and not an oxygenase. To confirm that the oxygen atoms incorporated into the products do indeed derive from water and not dioxygen, reactions of SwMppP with L-Arg were conducted with either $^{18}O_2$ or $H_2{}^{18}O$. Catalase was included in the reactions to prevent the $H_2O_2$-mediated decarboxylation of the products that would complicate the interpretation of the results. The products of these reactions were analyzed by ESI-MS. This analysis showed that in the presence of $^{18}O_2$, the products were detected at m/z=174 and m/z=190, indicating that neither product contained $^{18}O$. When the reactions were run in $H_2{}^{18}O$, the products were detected at m/z=176 and m/z=194. This is consistent with the incorporation of two atoms of $^{18}O$ into the fully oxidized **2**, and a single atom of $^{18}O$ into **3** (Figure 5-7).

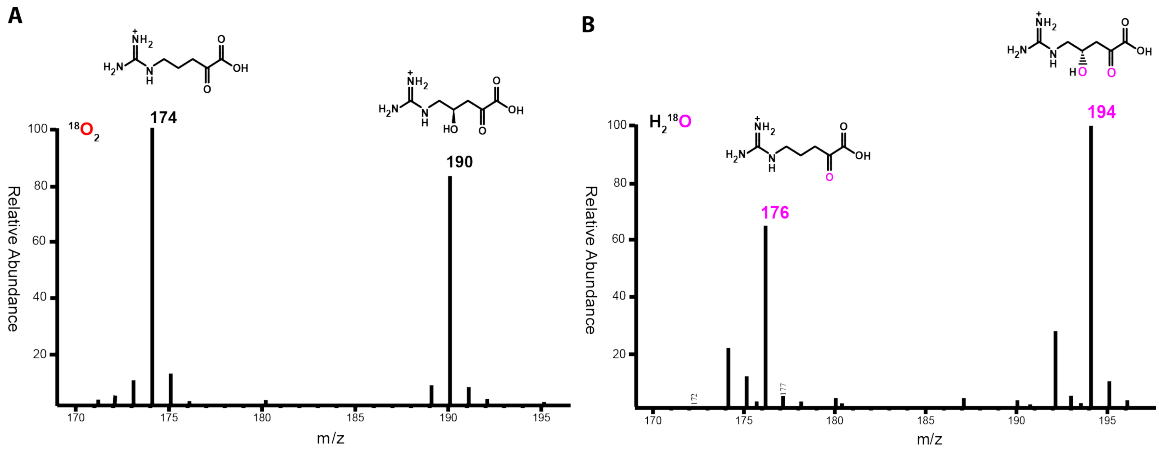


**Figure 5-7:** Mass spectrometric analysis results. A) Spectrum of SwMppP with L-Arg in the presence of $^{18}O_2$. The mass of both products did not change. B) Spectrum of SwMppP with L-Arg in $H_2{}^{18}O$. The hydroxy oxygen atom of **2** product originated from $H_2{}^{18}O$. And the keto oxygen atom of both products also came from the $H_2{}^{18}O$ by hydrolysis.

While other PLP-dependent enzymes are known to react with molecular oxygen, such as DOPA decarboxylase/aromatic L-amino acid decarboxylase [16, 17], and so-called "paracatalytic" reactions with $O_2$ have been described [18], SwMppP is the first PLP-dependent enzyme to produce a hydroxylated product. Given the sequence similarity between SwMppP and more typical PLP-dependent aminotransferases, it would be particularly interesting to know how the structure of SwMppP differs, and why these differences result in the enzyme acting as an L-Arg γ-hydroxylase rather than a decarboxylase or aminotransferase.

### 5.3.4 The structures of SwMppP

The experiments described thus far show that SwMppP is an L-Arg oxidase. However, analysis of the primary sequence suggests that SwMppP likely has a very similar structure to the Fold Type I aminotransferases. So what structural features of SwMppP allow it to catalyze a very difficult reaction (oxidation of an unactivated carbon center) using a scaffold normally associated with simple aminotransfer chemistry? To explore the relationship between the structure and function of SwMppP, we set out to determine its structure by X-ray diffraction. SwMppP crystallized by the hanging drop vapor diffusion method from 2 μL of protein solution at 15 mg/mL in 10 mM MES pH 6.7, 20 μM PLP and 1 μL of crystallization solution (30% polyethylene glycol monomethyl ether 550 (PEG MME 550), 50 mM $MgCl_2$, and 0.1 M HEPES (pH 8.0)). These crystals diffracted to 2.1 Å resolution. A number of aminotransferases, including the human kynurenine aminotransferase II (PDB ID 5EUN [19]) had ~30% sequence identity to SwMppP, so we first

sought to obtain initial phases for the structure by molecular replacement. Numerous search models were tested, including those based on different aminotransferase structures, with separated domains (in case the domains had a different orientation in MppP), and ensemble structures built from superpositions of several models. None of these resulted in suitable phase estimates. We then attempted SAD phasing, but were stymied by the unusually low number of methionine residues (3 methionines of 376 AA) in the *S. wadayamensis* enzyme. Rather than attempt to soak in compounds with anomalously scattering atoms, we decided to target a highly similar homolog of MppP that had more methionine residues.

The MppP from *S. globisporus* (SgMppP) was identified through BLAST searches of the SwMppP sequence and is XX% identical to SwMppP. This enzyme crystallized from XXX, but the crystals were not well ordered and only diffracted to ~3.5 Å resolution. However, this was sufficient to build a nearly complete model of the protein that was then used as the search model for successful molecular replacement phasing of the SwMppP data set.

SwMppP crystallized in space group $P2_12_12_1$ with the following unit cell dimensions: a = 85.7 Å, b = 108.3 Å, and c = 195.4 Å. The asymmetric unit contained four molecules that formed two independent homodimers (Figure 5-8). The overall structure of SwMppP, as expected from the sequence analysis, is very similar to typical Type I aminotransferases like aspartate aminotransferase. As in AATase, there are also two domains in SwMppP: a large domain (A33-G272), a small domain (L23 – Q32 and G273 – R376) and an N-terminal extension (M1-E22). The large domain contains a seven-stranded mixed β–sheet flanked by ten α–helices (α-β-α sandwich), while small domain has a mixed α-β topology.

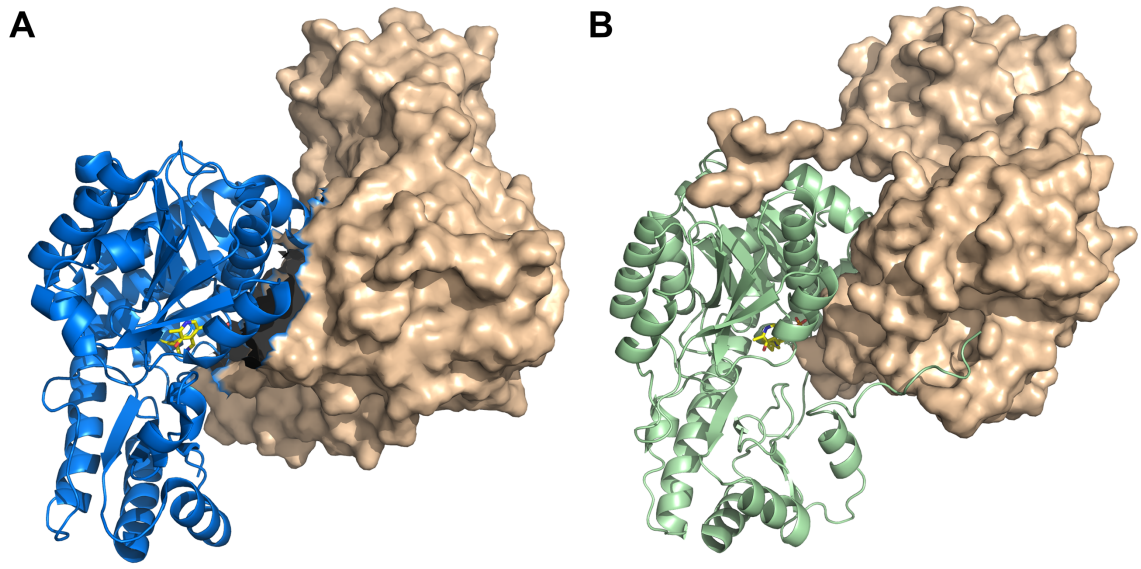


**Figure 5-8:** (A) SwMppP dimer with one chain shown as a blue ribbon representation and the other shown as a wheat surface representation. The K221-PLP internal aldimine in the active sites is shown in yellow stick. The N terminus (1-22 aa) is disordered in the crystal. (B) *E. coli* aspartate aminotransferase (PDB ID: 1ARS[20]) with one chain shown as a light green ribbon representation and the other shown as a wheat surface representation. The K258-PLP internal aldimine in the active sites is shown in yellow stick. The N terminus (1-30 aa) ordered and interacts with the large domain of the other chain.

Three of the four chains in the asymmetric unit are missing 22 residues from the N-terminus, while the fourth (chain D) is missing only 10 residues. The extra 12 residues in chain D form a loop and α helix that points outward, away from the enzyme and interacts with a symmetry-related molecule (25 Å from the active site). There is nothing in these interactions to suggest that they are physiologically relevant. All four chains are missing one to three residues from the C-terminus.

As alluded to above, and as shown in Figure 5-8, the tertiary structure of SwMppP is

similar to the type I aminotransferases (ATases)[21]. The *E. coli* aspartate ATase (PDB entry 1ARS[20]) superimposes well onto the structure of the SwMppP dimer. The root-mean-square deviation (rmsd) value obtained using secondary structure matching (SSM)[22] of 3.4 Å for 567 of the 704 Cα atoms in SwMppP underscores the similarity of these two enzymes. For reference, different structures of *the same* protein can have rmsd values of more than 0.5 Å. The most obvious difference between the tertiary structures of SwMppP and AATase is that the N-terminal extension is disordered or points outward in SwMppP, which leaves the active sites open to the solvent, whereas this part of the AATase structure closes over the active site, covering the cofactor almost completely.

As in the ATases, the active site is located at the interface between the large and small domains of each protomer. Unlike the ATases, however, there is minimal contribution from the other chain in the dimer. The position of the cofactor is also similar to that seen in all known Fold Type I aminotransferases, in a cleft formed by the central β-sheet and the N-termini of helices α4 and α5 (Figure 5-8). In the absence of bound ligands, PLP is covalently attached to K221 by an aldimine linkage. The C5' phosphate of PLP is held by fewer direct interactions than in other PLP-dependent enzymes. In SwMppP, the only direct interactions between the enzyme and the C5' phosphate are an electrostatic interaction with K229 and a hydrogen-bonding interaction with S91. There may also be a weak hydrogen bond to H29. The remaining interactions constituting the C5' phosphate-binding site are water-mediated hydrogen bonding interactions with D218 as well as Y88* and the main chain amide of L252* from the other protomer of the dimer (Figure 5-9). As in all fold type I aminotransferases, there is a negatively-charged residue, D188, placed near the pyridine N atom of the cofactor to stabilize the positive charge that forms during the catalytic cycle [23-

[25]. The C3' hydroxyl of PLP is involved in a hydrogen-bonding interaction with N160, which also makes a hydrogen-bonding interaction with R352, an absolutely conserved residue in the Type I aminotransferases. In the *E. coli* aspartate aminotransferase (EcAAT), for example, the equivalent Arg residue (R386) interacts with the α-carboxylate group of the substrate. Finally, the pyridine ring of PLP is clamped between F115 above and S190 below. Aminotransferases typically have an aromatic side chain packed against the "top" surface of the PLP ring, though the residue below the ring is more typically an Ala.

While there are a number of similarities between the active sites of SwMppP and EcAAT, there are a number of interesting differences that likely play a role in the divergent activity of SwMppP. As mentioned above, the phosphate-binding site is anchored by Lys instead of Arg, and whereas most ATases have 2-3 Ser/Thr residues binding the phosphate group, and SwMppP has only one. One of the positions typically occupied by a Ser/Thr is taken by D218 in SwMppP. The carboxylate group of D218 is within hydrogen bonding distance of S190; this interaction is not observed in most other PLP-dependent enyzmes, most of which have Ala in the position occupied by S190. In many ATases, such as EcAAT, there is a Tyr residue that makes a hydrogen bond to the C3' hydroxyl of PLP and affects the electron distribution in the cofactor [26]. This residue is a Phe in SwMppP. The last unusual feature of the SwMppP active site is H29. This position is not conserved in other PLP-dependent enzymes, but is absolutely conserved among MppP homologs[27]. H29 is adjacent to the catalytic K221 and makes hydrogen bonding interactions with D27 and, perhaps, with the phosphate moiety of the cofactor. In two of the four molecules in the asymmetric unit, H29 takes on at least two conformations.

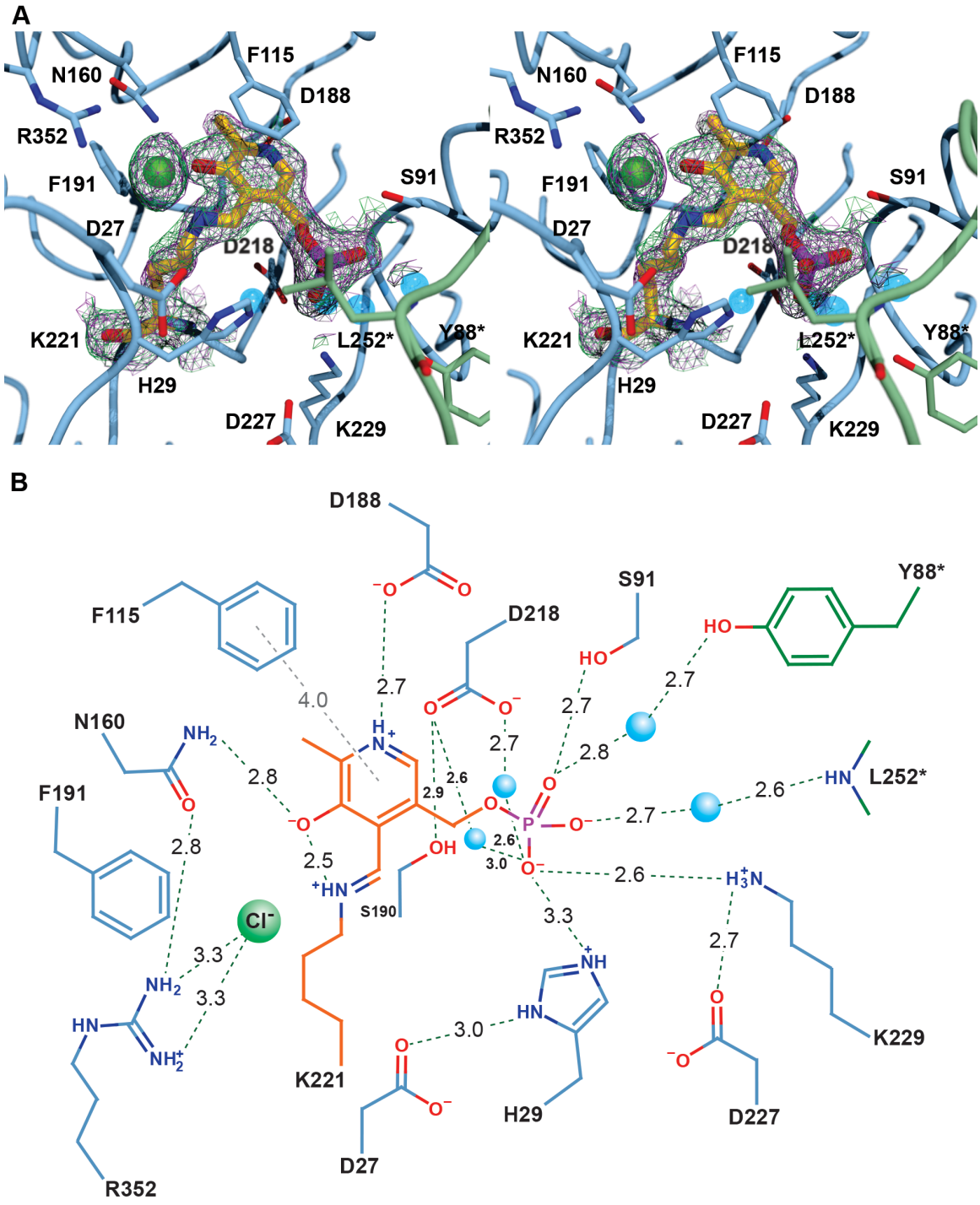


**Figure 5-9:** The active site of SwMppP. The stereoview of the SwMppP active site (A) shows the PLP covalently bound to enzyme, forming internal aldimine. The $2|F_o| - |F_c|$ electron density map contoured at 1.0σ, is shown as magenta mesh, and the $2|F_o| - |F_c|$ composite omit map also contoured at 1.0σ, is shown as green mesh. The schematic view of the active site (B) shows potential hydrogen bonding interactions as

green, dashed lines. Water molecules are shown as blue spheres. The chloride ion is shown as a green sphere. Panel A was generated using POVSCRIPT and POV-Ray. Panel B was created using a combination of MarvinSketch (https://www.chemaxon.com) and Adobe Illustrator CS6.

### 5.3.5 The structure of the SwMppP•L-Arg complex

The structure of SwMppP•L-Arg was obtained by soaking SwMppP crystals in a solution containing 10 mM L-Arg. Unlike the unliganded structure, where the N-terminus is disordered and leaves the active site exposed to the solvent, in the structure with L-Arg bound, the N-terminal extension orders and covers the active site (Figure 5-10). Superimposition of the unliganded SwMppP and SwMppP•L-Arg structures gives a root-mean-square deviation of 0.356 for Cα atoms in the SwMppP dimer, indicating that, except for the N-termini, there are no significant structural alterations as a result of ligand binding. So unlike many ATases, there is no closing movement of the small domain.

Once the substrate binds in the active site, the α-amino group attacks C4' of internal aldimine to form the external aldimine, displacing K221. Compared with the unliganded SwMppP, there are no significant changes in the active site, only a few subtle side chain movements, as shown in Figure 5-11. The $Cl^-$ ion bound to R352 is replaced by the α-carboxylate of L-Arg. T12 and E15 in the N-terminal helix form hydrogen bonds with guanidine group and carboxyl group of L-Arg, respectively. The guanidine group also forms hydrogen bonds with N117, S91, and the carbonyl groups of S248 and D249 from the other protomer. The side chains of H29, D27 and R31 are shifted towards the external aldimine. The ring of F115 rotates away from the PLP ring and is closer to L-Arg.

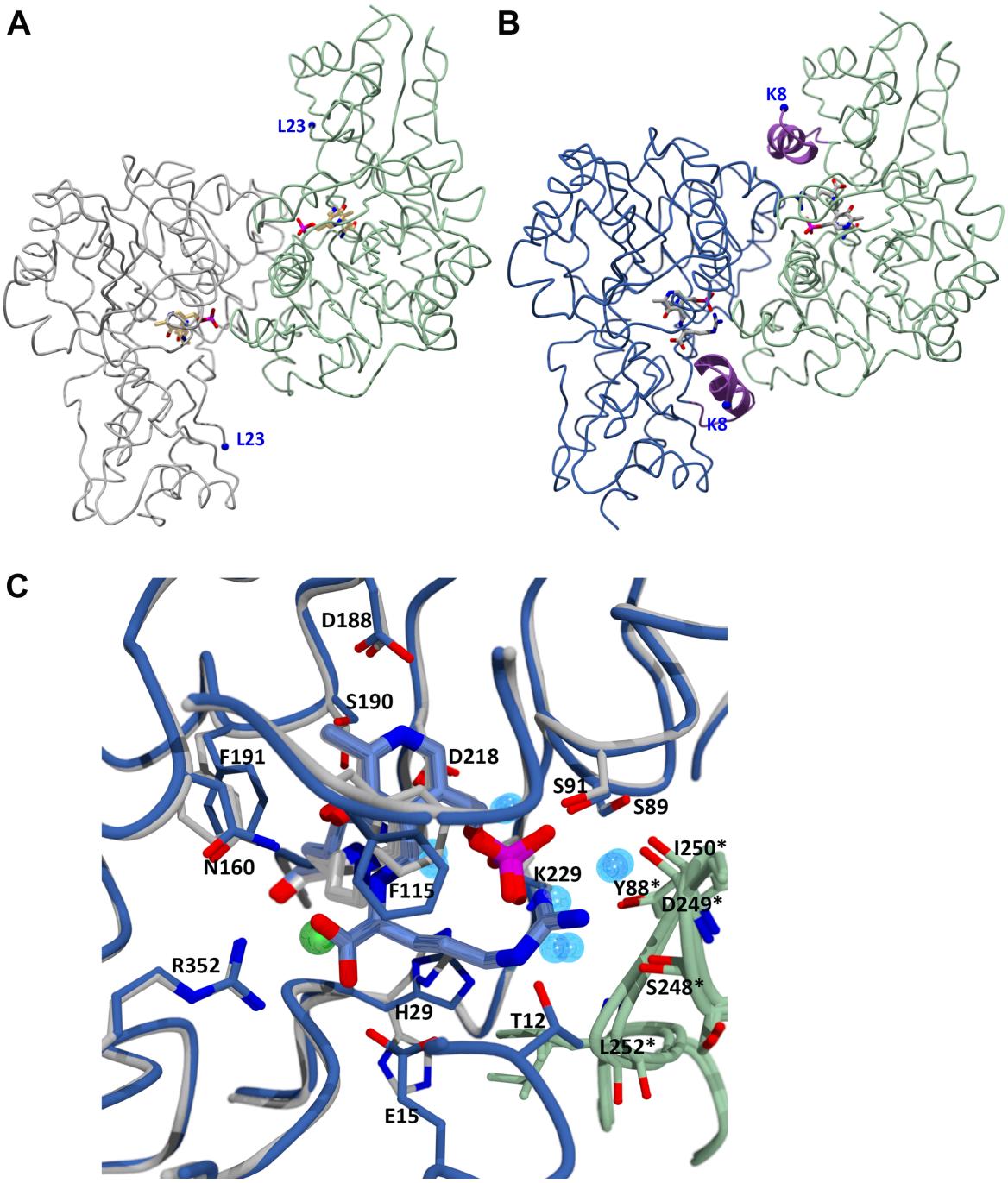


**Figure 5-10:** Ribbon representation of SwMppP (A) and SwMppP•L-Arg (B) dimers. (A) Chain A is colored in grey, chain B is colored in light green. The N termini of both chains are disordered. The L23 Cα atoms in both chains are shown as blue spheres. (B) Chain A colored dark blue, chain B colored light green and the N-terminal helices colored purple. The PLP cofactors in the active sites are shown in stick. The N-terminal helix

ordered and covers the active site. The K8 Cα atoms in two chains are shown as blue dots. (C) Overlaying the active site of SwMppP and SwMppP•L-Arg. The major change is the E15 and T12 interactions with L-Arg. Also, the rings of F115 and F191Y shift.

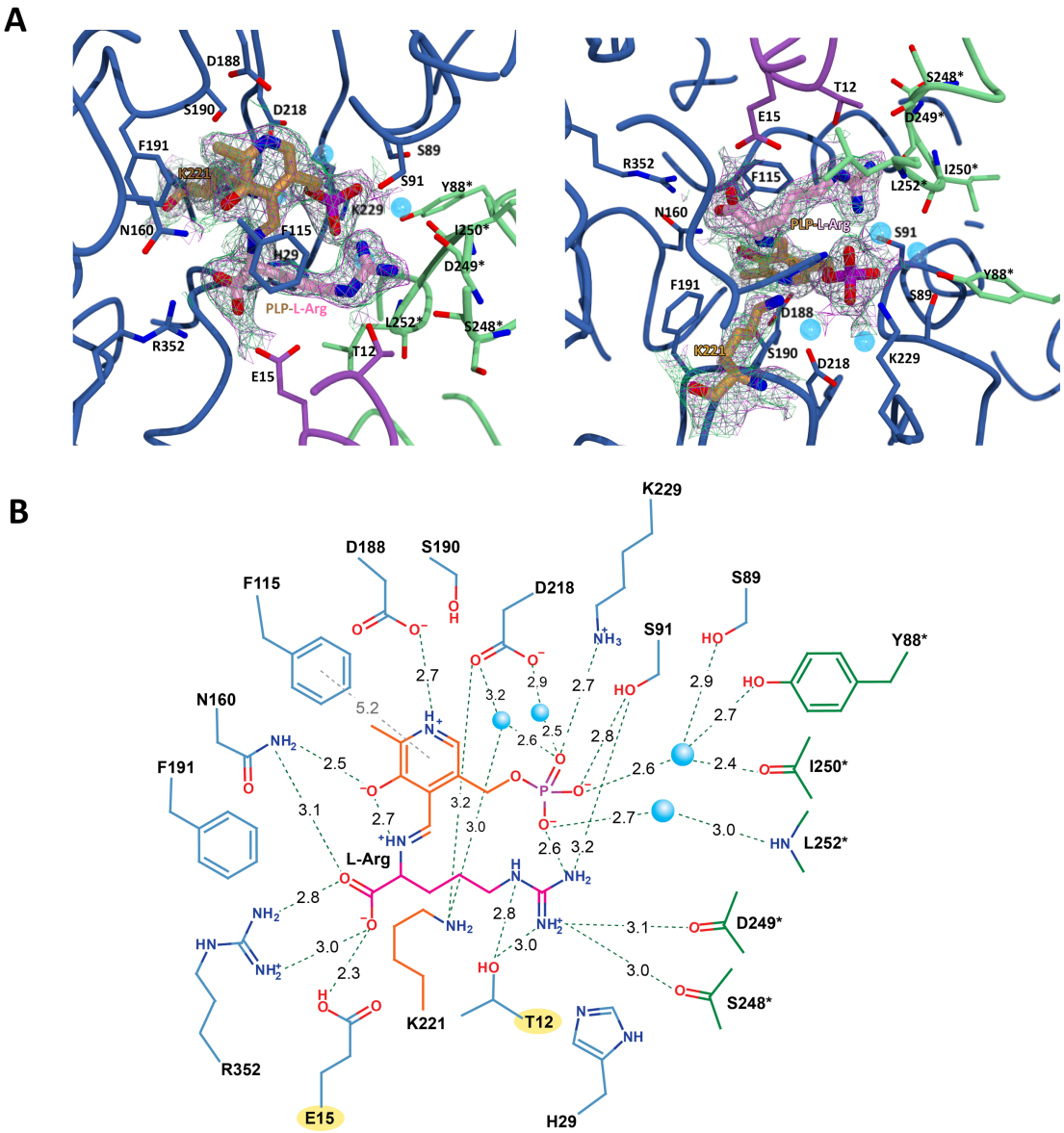


**Figure 5-11:** The external aldimine structure in active site of SwMppP•L-Arg. (A) SwMppP•L-Arg active site showing the L-Arg covalently bound to the PLP as the external aldimine. The $2|F_o| - |F_c|$ electron density map contoured at 1.0σ, shown as magenta mesh, and the $2|F_o| - |F_c|$ composite omit map also contoured at 1.0σ, is shown as green mesh. (B), Schematic view of the active site showing potential hydrogen bonding interactions

as green, dashed lines. Water molecules are shown as blue spheres. Panel A was generated using POVSCRIPT and POV-Ray. Panel B was created using a combination of MarvinSketch (https://www.chemaxon.com) and Adobe Illustrator CS6.

### 5.3.6 Structures of SwMppP•product complexes

The structures of the SwMppP•**2** complex (Figure 5-12) and the SwMppP•**3** complex (Figure 5-13) have no big difference on the guanidine is bound from SwMppP•L-Arg structure, but the fact that the products are not external aldimine is a big difference. Also there are several residues side chain movements (overlay results are shown in Appendix F and Appendix G). S190 side chain shifted to hydrogen bond with D218. In the structure of SwMppP•**2**, 4HKA hydroxyl group made hydrogen-bonding interactions with the phosphate group and H29.

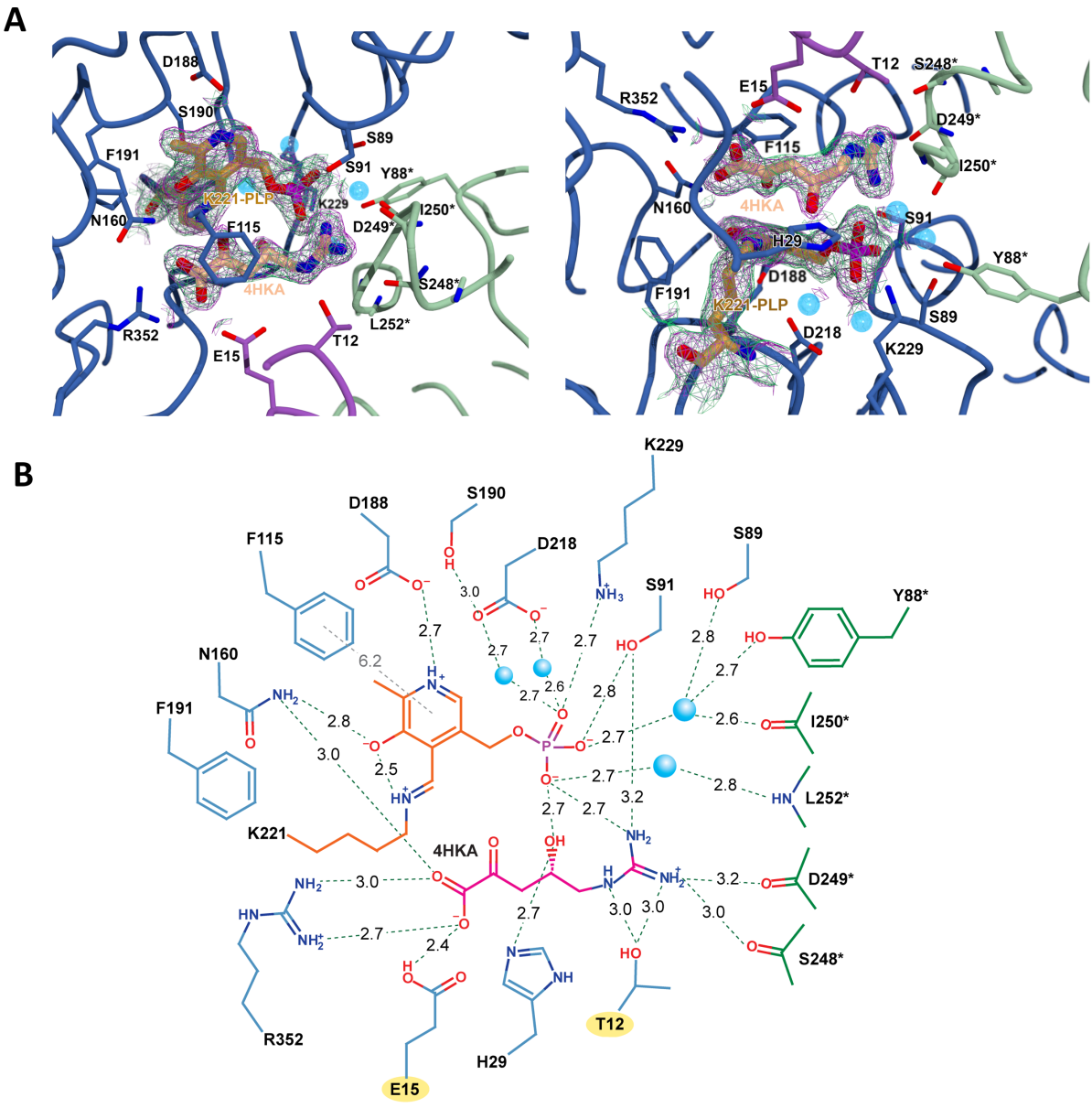


**Figure 5-12:** The active site of SwMppP•**2**. (A) SwMppP•**2** active site showing the PLP covalently bound to the enzyme as the internal aldimine. E15 and T12 interact with **2** carboxylate group and guanidine group, respectively. His29 bonds to hydroxyl group of **2**. The $2|F_o|-|F_c|$ electron density map contoured at 1.0σ, shown as magenta mesh, and the $2|F_o|-|F_c|$ composite omit map also contoured at 1.0σ, is shown as green mesh. (B) Schematic view of the active site showing potential hydrogen bonding interactions as green, dashed lines. Water molecules are shown as blue spheres. Panel A was generated using POVSCRIPT and POV-Ray. Panel B was created using a combination of MarvinSketch (https://www.chemaxon.com) and Adobe

Illustrator CS6.

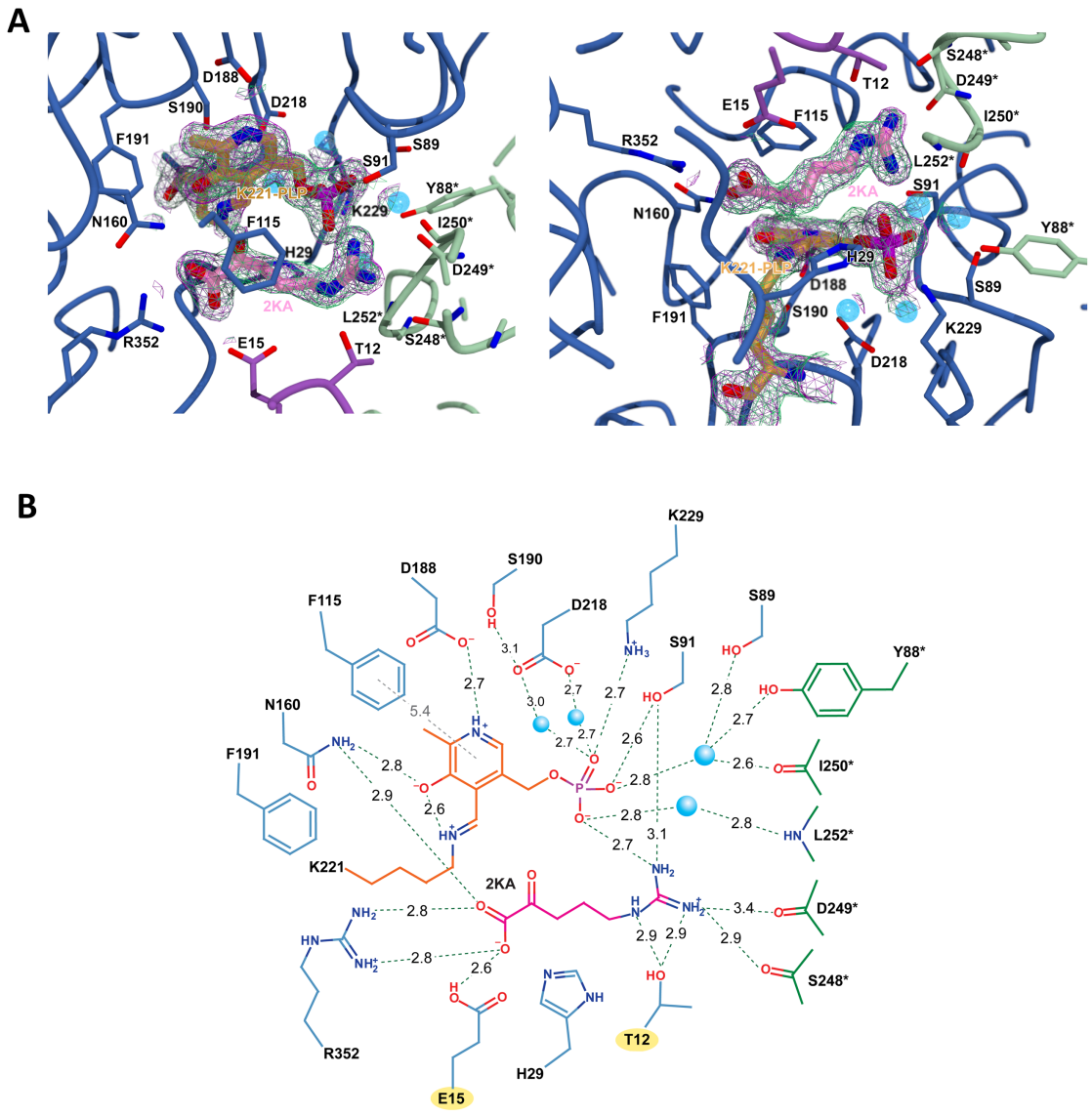


**Figure 5-13:** The active site of SwMppP•**3**. (A) SwMppP•**3** active site showing the PLP covalently bound to the enzyme as the internal aldimine. E15 and T12 interact with **3** carboxylate group and guanidine group, respectively. The $2|F_o|-|F_c|$ electron density map contoured at 1.0σ, shown as magenta mesh, and the $2|F_o|-|F_c|$ composite omit map also contoured at 1.0σ, is shown as green mesh. (B) Schematic view of the active site showing potential hydrogen bonding interactions as green, dashed lines. Water molecules are shown as blue spheres. Panel A was generated using POVSCRIPT and POV-Ray. Panel B was created using a combination of MarvinSketch (https://www.chemaxon.com) and Adobe Illustrator CS6.

### 5.3.7 Characterization of N-terminus and active site residues

The tertiary structure of SwMppP is very similar with type I aminotransferase, there are several residues differences in the active site, which probably results in the hydroxylase-deaminase activity rather than aminotransferase. Bioinformatic analysis[27] showed that H29, F115, F191, and D218 are conserved in all of the MppP homologs but not in the Type I aminotransferases. To explore the specific roles of these different residues, site-directed mutagenesis was used to make point mutants that were characterized both structurally and kinetically.

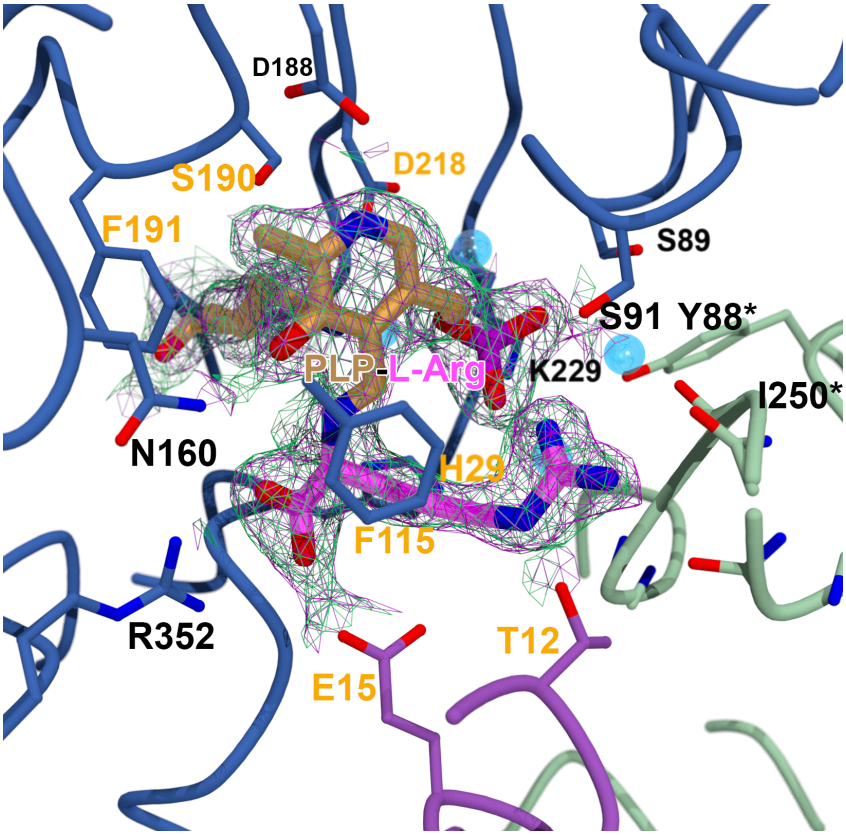


**Figure 5-14:** Different residues (colored in orange) in the active site of SwMppP•L-Arg. The $2|F_o| - |F_c|$ electron density map contoured at 1.0σ, shown as magenta mesh, and the $2|F_o| - |F_c|$ composite omit map also contoured at 1.0σ, is shown as green mesh.

### 5.3.8 Characterization of SwMppP and mutants

#### 5.3.8.1 Stability of SwMppP and mutants by differential scanning fluorimetry

The $T_m$ value for each mutant is listed in Table 5-2. Except $SwMppP_{F191Y}$, other mutants' stability are same with that of wild-type SwMppP. The $T_m$ value of $SwMppP_{F191Y}$ is so low that only flat curve was got.

**Table 5-2:** $T_m$ values of SwMppP and mutants

| Proteins | $T_m$ ($^oC$) |
|---|---|
| SwMppP | 53.3 ± 0.1 |
| $SwMppP_{E15A}$ | 55.75 ± 0.1 |
| $SwMppP_{E15Q}$ | 53.3 ± 0.1 |
| $SwMppP_{H29A}$ | 47.5 ± 0.1 |
| $SwMppP_{H29A}$ | 46.6 ± 0.1 |
| $SwMppP_{F115Y}$ | 51.4 ± 0.2 |
| $SwMppP_{F191Y}$ | Not applicable |
| $SwMppP_{D218S}$ | 50.0 ± 0.1 |
| $SwMppP_{\Delta 1\text{-}22}$ | 50.2 ± 0.1 |

#### 5.3.8.2 Determination of the reaction products of the mutants

To determine what reaction these mutants catalyzed, the 4.8 mL reaction contains ~65 μM mutants protein and 2 mM L-Arg in 20 mM sodium phosphate pH 8.4 buffer were shaked at 25°C, 200 rpm overnight. Then the solutions were concentrated for 8 fold and analyzed by proton NMR. The results are summarized in Table 5-3.

**Table 5-3:** The products of SwMppP and its mutants with L-Arg and $O_2$

| | Products | [**2**]/[**3**] |
|---|---|---|
| SwMppP | **2** and **3** | 1.7:1 |
| $SwMppP_{T12A}$ | **3** | 0:1 |
| $SwMppP_{E15A}$ | **3** | 0:1 |
| $SwMppP_{E15Q}$ | **2** and **3** | 1:2.4 |
| $SwMppP_{T12A/E15A}$ | **3** | 0:1 |
| $SwMppP_{H29A}$ | **3** | 0:1 |
| $SwMppP_{H29A}$ | **3** | 0:1 |
| $SwMppP_{F115Y}$ | **3** | 0:1 |
| $SwMppP_{F191Y}$ | **2** and **3** | 1.6:1 |
| $SwMppP_{D218S}$ | Trace **3** | - |
| $SwMppP_{\Delta 1-22}$ | Trace **3** | - |

SwMppP catalyzes the oxidation of L-Arg and $O_2$ into **2** and **3** in the ratio of 1.7 : 1. Except $SwMppP_{F191Y}$ and $SwMppP_{E15Q}$, all mutants lost the hydroxylase activity. They only

produce the side product **3**. The products ratio of variant F191Y is 1.6 :1, which is same with that of wild-type SwMppP. However, because the $T_m$ of F191Y is low, the amounts of substrate F191Y catalyzed are much less. Another mutant E15Q still have the hydroxylase activity, although it does make less hydroxylated products (with the [**2**] : [**3**] at the ratio of 1 : 2.4). The substitution of same residue E15 into alanine lost the hydroxylase activity. To figure out why the E15A variant lost the hydroxylase activity, I crystallized the E15A proteins and soaked the crystals with 10 mM L-Arg to get the E15A•L-Arg structure (shown in Figure 5-15). In the structure of E15A•L-Arg structure, L-Arg covalently bonds to PLP, forming external aldimine. The N terminus still covers the active site when substrate binds. And T12 residue interacts with the guanidine group of L-Arg. The main chain of A15 is same with that of E15 in wild type protein. But the shorter side chain of A15 probably creates a void where water can be retained, and which could hydrolyze the quinonoid intermediate prematurely.

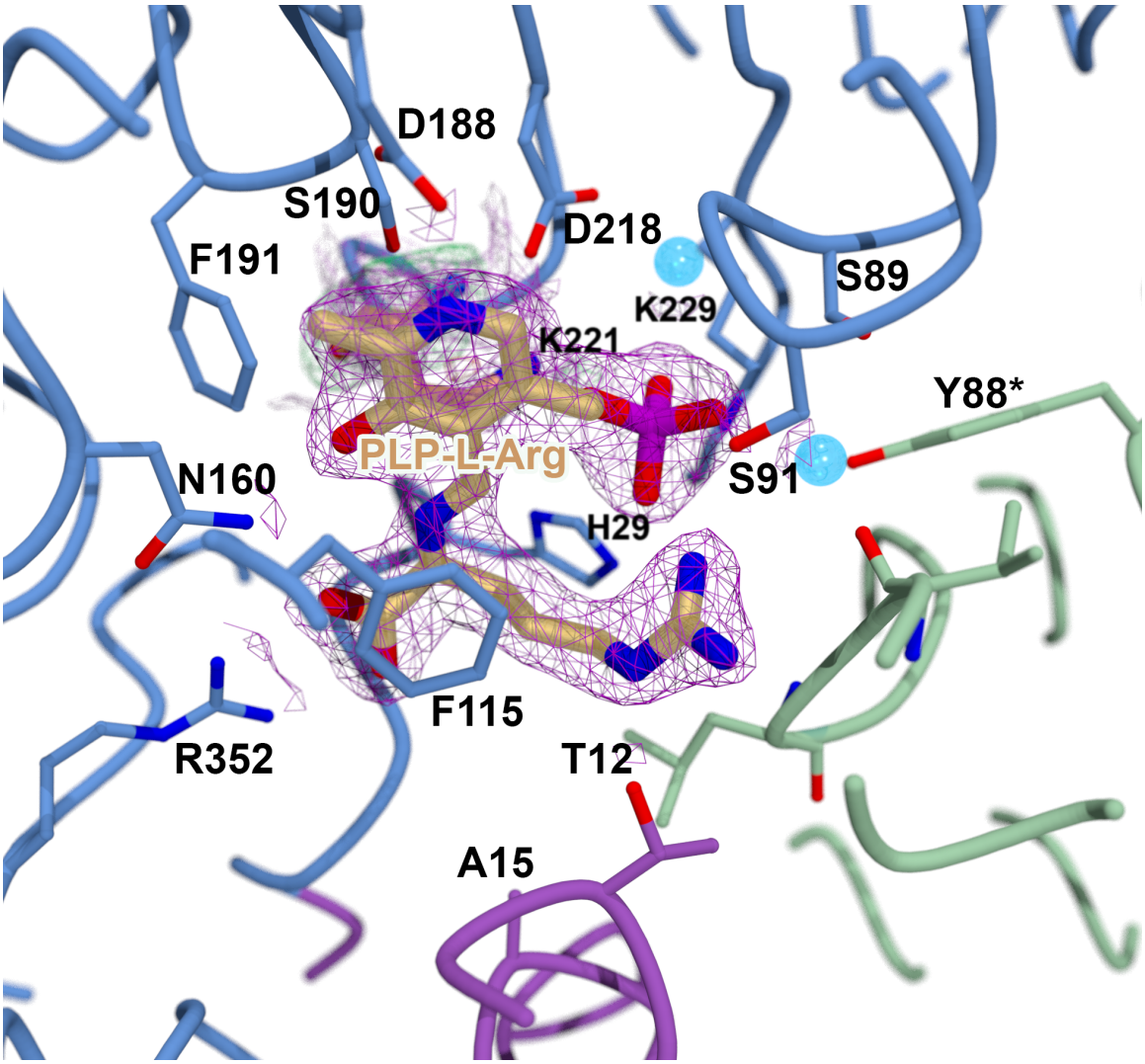


**Figure 5-15:** The active site of E15A•L-Arg. The N terminus colored in purple. Chain A colored in blue, chain B colored in light green. PLP-L-Arg is shown in golden stick. The $2|F_o| - |F_c|$ electron density map contoured at 1.0σ, shown as magenta mesh, and the $2|F_o| - |F_c|$ composite omit map also contoured at 1.0σ, is shown as green mesh.

### 5.3.8.3 The steady state parameters monitored by $O_2$ consumption

SwMppP reacts with L-Arg and $O_2$ forming **2** and **3**. The catalytic parameters ($K_M$, $k_{cat}$) of $O_2$ usage were determined and are listed in Table 5-4.

**Table 5-4:** Steady state parameters monitored by $O_2$ consumption

| Proteins | $K_{M,L\text{-}Arg}$ (μM) | $k_{cat}$ ($s^{-1}$) | $k_{cat}/K_M$ ($M^{-1}$ $s^{-1}$) |
|---|---|---|---|
| SwMppP | 26.5 ± 4.2 | 0.20 ± 0.006 | 7641.5 ± 1232.8 |
| T12A | 105.8 ± 12.1 | 0.05 ± 0.0016 | 483.2 ± 57.4 |
| E15A | 28.0 ± 4.0 | 0.24 ± 0.006 | 8424.4 ± 1212.7 |
| E15Q | 19.0 ± 3.5 | 0.24 ± 0.007 | 12538.3 ± 2340.2 |
| T12A/E15A | 74.5 ± 7.7 | 0.035 ± 0.002 | 465.2 ± 54.3 |
| Δ1-22 | 234.8 ± 33.4 | 0.072 ± 0.002 | 306.0 ± 44.6 |
| H29A | 25.4 ± 5.6 | 0.11 ± 0.004 | 4472.9 ± 1003.2 |
| H29S | 16.9 ± 3.6 | 0.07 ± 0.003 | 4327.6 ± 931.3 |
| F115Y | 66.5 ± 4.8 | 0.20 ± 0.003 | 2940.3 ± 217.7 |
| F191Y* | 8.9 ± 2.4 | 0.05 ± 0.003 | 4983.2 ± 1349.4 |
| D218S | 353.2 ± 53.5 | 0.07 ± 0.003 | 183.5 ± 28.7 |

* means inaccurate data due to the instability of protein F191Y.

The $K_M$ of the T12A and T12A/E15A mutants were 3- to 5-fold higher than that of wild type. The turnover numbers ($k_{cat}$) of the two mutants were also lower than the wild type, which makes the catalytic efficiency ($k_{cat}/K_M$) ~15-fold less than the wild type. In Figure 5-

16, the spectra of both the T12A and T12A/E15A variants exhibit a shift from the external aldimine peak (435nm) back to the internal aldimine peak (415 nm) as the reaction goes. The truncation mutant, however, showed an approximately 10-fold increase in $K_M$ and a 3-fold decrease in $k_{cat}$, which reduced the pseudo-second order rate constant by almost 25-fold. The truncation mutant also produced only 2-ketoarginine. According to the spectrum of SwMppP$_{\Delta 1\text{-}22}$ with L-Arg and $O_2$ (Figure 5-16), the external aldimine also shifts into internal aldimine as the reaction goes. The mutants E15A and E15Q have no effect on $K_M$, $k_{cat}$ or catalytic efficiency. Interestingly, although the steady state kinetics (as measured by dioxygen consumption) is indistinguishable for the E15A and E15Q variants, the E15A variant does not produce **2**, only the abortive product **3** based on the NMR results (Table 5-4).

Alteration of the N-terminus altered the ratios of products produced, but had no, or only a modest effect on the steady state kinetics as monitored by dioxygen consumption. However, as the spectra shown in Figure 5-16 demonstrate, the external aldimine peak (435 nm) gradually shifted to internal aldimine peak (415 nm) as reaction went, demonstrating that the N-terminal helix, especially T12, plays a key role in stabilizing the external aldimine and Quinonoid intermediate.

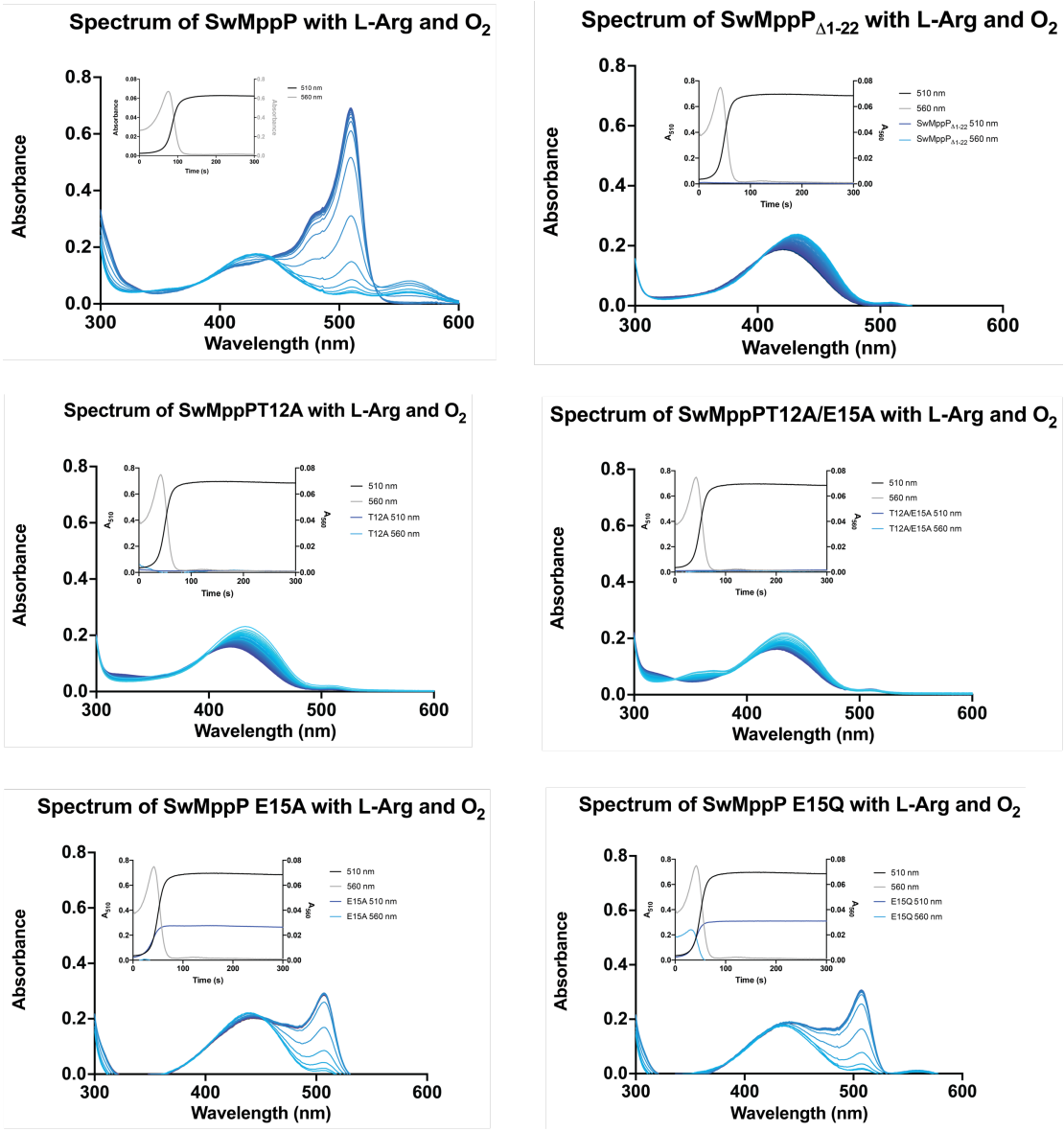


**Figure 5-16:** The spectrum (300 nm-600 nm) of SwMppP and its N terminus mutants with L-Arg. The insets are the changes at 510 nm and 560 nm for each mutant. There are 3 major peaks (430 nm, 510 nm, 560 nm) for wt SwMppP with L-Arg. The blue lines from lighter to darker represents the data collect from 1.4 s to 300 s. The insets also describe the trends of these mutants reactions in a timer order in comparison with wt SwMppP. For the truncated N-terminal helix mutant $SwMppP_{\Delta 1\text{-}22}$, the only peak (430 nm) shifted to 420 nm as the reactions goes. For $SwMppP_{E15A}$, there are only 2 peaks (430 nm, 510 nm). But for the mutant $SwMppP_{E15Q}$, there are three peaks (430 nm, 510 nm and small 560 nm).

In unliganded protein structure, H29 is close to the catalytic K221 and make hydrogen bonding with D27. In the product **2** bound structure, H29 hydrogen bonds to the hydroxyl group. To study the role of this special histidine residue, it was substituted into aliphatic alanine and polar serine. The steady state parameters on $O_2$ consumption are very similar to wild type SwMppP (Table 5-4). The structures of H29A and H29S are both obtained. The structures and spectra of both mutants are identical, so only the spectrum of H29A is shown in Figure 5-17. Only the external aldimine and quinonoid I peak formed. No absorbance at 560 nm was observed. In the first 20 s, the Quinonoid I intermediate accumulated are more than wild type SwMppP (the inset in Figure 5-17A). However, the Quinonoid I intermediate accumulation rate and final amounts of H29A/S are less than those of wild type SwMppP. Overlaying the H29A structure with wild type SwMppP, (Figure 5-17B), there is no difference on the active site residues. However, in the H29A mutant active site, there are more water molecules around the PLP, which suggests that H29, together with F115 and F191, may be involved in the water exclusion in the active site. Given that H29 coordinates the hydroxyl group of **2** and the H29A/S mutants lose the hydroxylase activity, H29 may also be involved in positioning a water molecule for hydroxylation.

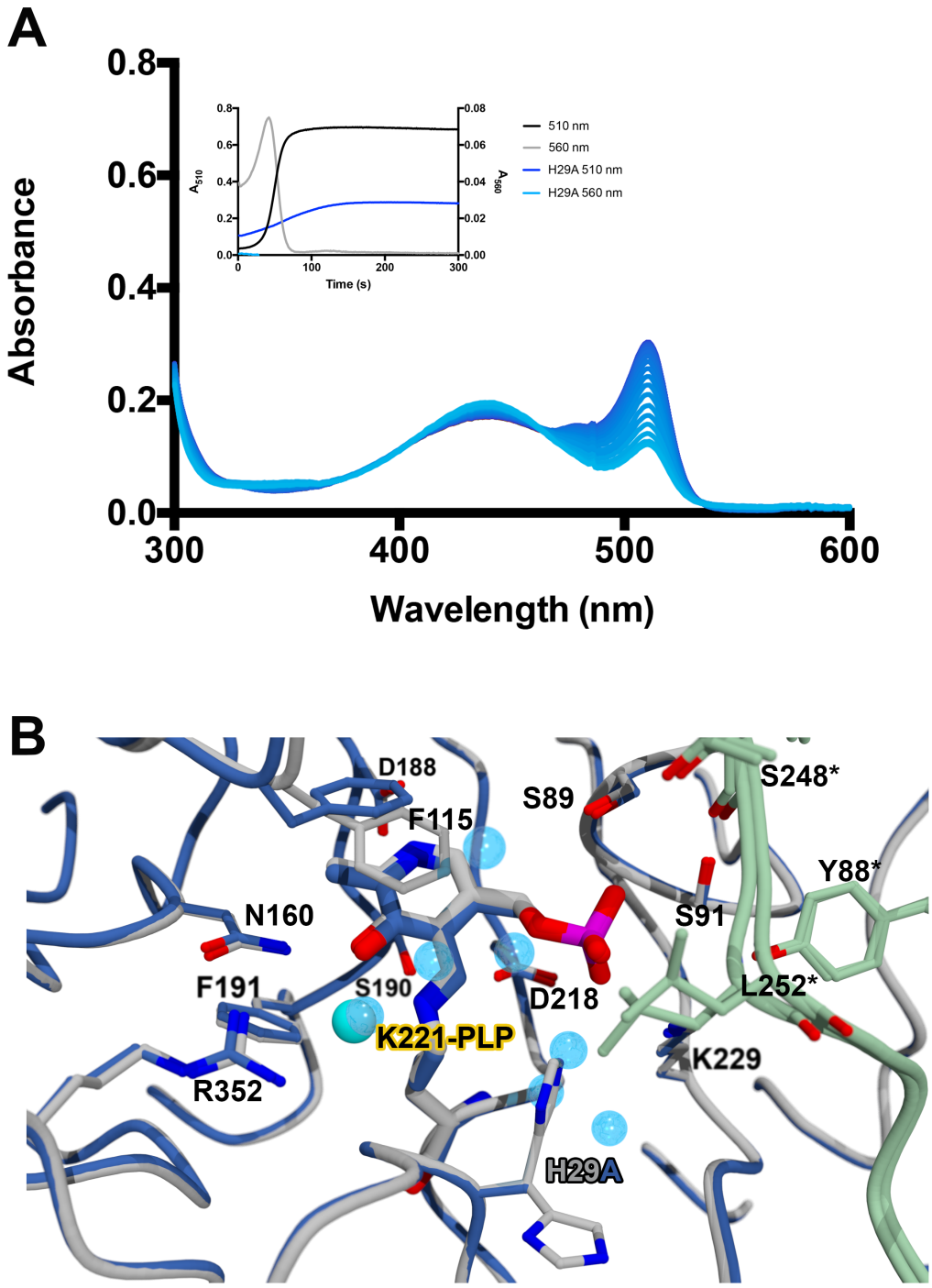


**Figure 5-17:** (A) The spectrum of H29A with L-Arg. The 700µl solution containing 30 µM H29A proteins with 1.4 mM L-Arg were scanned on diode array spectrophotometer every second over 300 s. The blue color gets darker as time goes. The inset is the 510nm 560 nm change comparison between SwMppP and H29A. (B)

Superposition of the active sites of SwMppP (colored in grey) with H29A (dark blue). Water molecules all from H29A are shown in blue sphere. $Cl^-$ ion in SwMppP is shown as cyan sphere. In the active site, the H29A has more water molecules.

The structure of H29A with L-Arg was obtained by soaking 5 mM L-Arg. The asymmetric unit contained four molecules that form two independent homodimers. Three of the four chains have L-Arg bound forming external aldimine with PLP, while there is nothing bound in the active site of chain D and PLP covalently bound to catalytic K221 that forms internal aldimine. As mentioned above, there are more water molecules in the active site of H29A mutant. When the substrate L-Arg bound into the active site, L-Arg covalently bonds to PLP and excludes the water molecules. The water molecules in Figure 5-18A are from H29A internal aldimine structure. The ring of F151 moves close to L-Arg and packed with the Cα of L-Arg. The ring of F191 rotates about 90 degree and packed to the oxygen atom of carboxylate group. Except these two residues, other residues in the active site are same with apo enzyme SwMppP. Overlaying theH29A•L-Arg structure with SwMppP•L-Arg, the active site residues are exactly same (Figure 5-18B). However, the short side chain of A29 cannot exclude the water molecules from the active site, so there are two water molecules close to A29 that are not found in the structure of wild-type SwMppP with L-Arg bound.

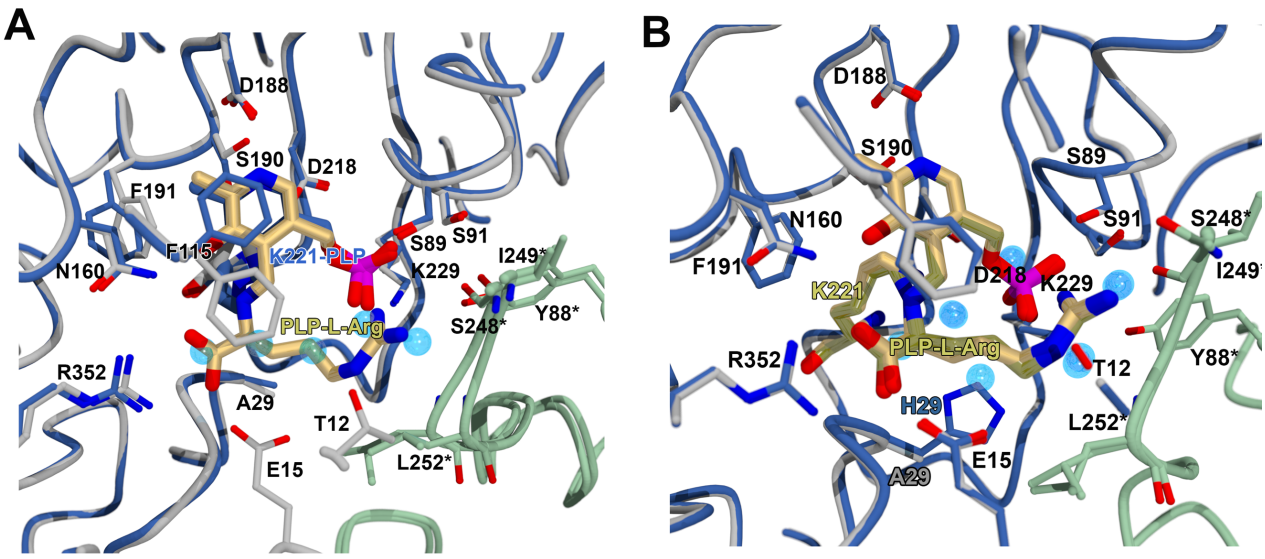


**Figure 5-18:** (A) Overlaying the active site of H29A (chain A colored in blue) and H29A•L-Arg (chain A colored in grey). Both chain B colored in light green. Upon the substrate bound, N terminus cover the active site. E15 and T12 interact with the carboxylate group and guanidinium group of L-Arg, respectively. The ring of F115 and F191 moves closer to the L-Arg. (B) Overlaying the active site of SwMppP•L-Arg (chain A colored in blue) and H29A•L-Arg (chain A colored in grey) demonstrates that there is no difference between them except two more molecules in the active site due to the short side chain of A29. Both chain B colored in light green.

F115 is another conserved residue in MppP homologs. To study the specific role of F115 play in the mechanism, it was mutated into tyrosine. The $K_M$ of F115Y mutant were 3 folds higher than that of wild type SwMppP. The turnover numbers ($k_{cat}$) of F115Y is same with that of swMppP, which makes the catalytic specificity ($k_{cat}/K_M$) were ~3 fold less than the wild type SwMppP protein. As time goes, the external aldimine peak shifted back to internal aldimine peak (Figure 5-19A). The quinonoid I intermediate peak firstly accumulated, then decayed gradually. These features suggest that mutated Y115 probably

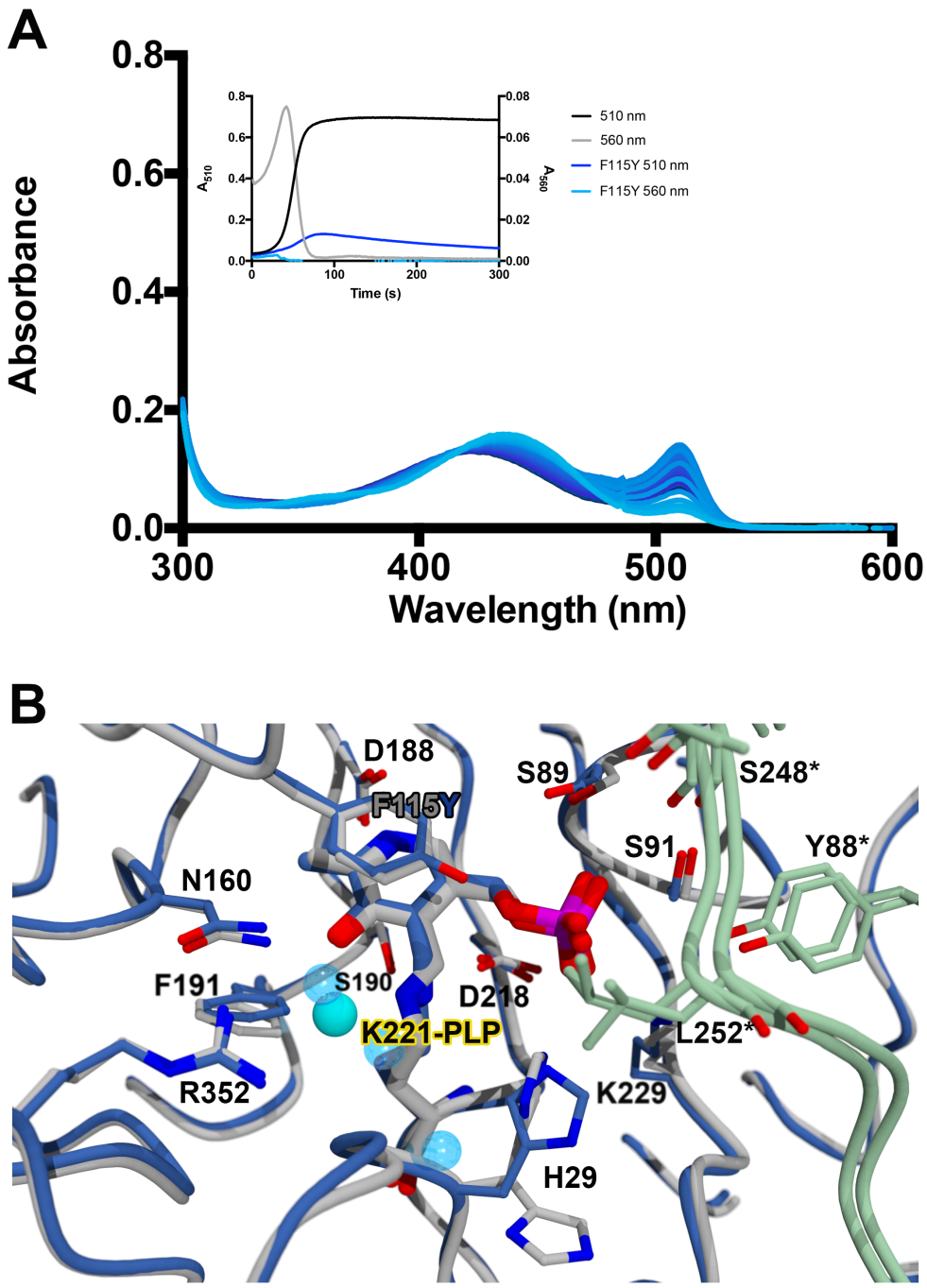


**Figure 5-19:** (A) The spectrum of F115Y with L-Arg. The 700µl solution containing 30 µM F115Y proteins with 1.4 mM L-Arg were scanned on diode array spectrophotometer every second over 300 s. The blue color gets darker as time goes. The inset is the 510nm 560 nm change comparison between SwMppP and F115Y. (B) Superposition of the active sites of SwMppP (colored in grey) with F115Y (dark blue). Water molecules all

from F115Y are shown in blue sphere. $Cl^-$ ion in SwMppP is shown as cyan sphere. In the active site, the F115Y has more water molecules.

disrupts the stability of Quinonoid I and external aldimine, thus the equilibrium shifted into internal aldimine. The quinonoid II intermediate did not accumulate. Overlaying the F115Y structure with wild type SwMppP (Figure 5-19B), there are no differences in the active site residues with the exception of H29. In the structure of $SwMppP_{F115Y}$, H29 only adopts one conformation. Water molecules align differently between the active site of chain A and chain B. In chain B, one water molecule mediates the interaction between OH of mutated Y115 side chain and NE2 of H29.

S190 and F191 are two adjacent conserved residues in MppP homologs. To study the specific role of S190 and F191, they were mutated into alanine and tyrosine, respectively. The purification of S190A failed because this mutant does not fold correctly and forms inclusion bodies. The mutant F191Y is also not stable due to the low $T_m$ value mentioned above. The turnover numbers ($k_{cat}$) of F115Y is much slower than that of SwMppP. The $K_M$ of F191Y mutant were 3 folds lower than that of wild type SwMppP. which makes the catalytic specificity ($k_{cat}/K_M$) were ~2 fold less than the wild type SwMppP protein. These parameters are based on the enzyme concentration, but the accurate concentration of active F191Y enzyme in the solution is unknown due to the instability property. The F191Y mutant is not stable, so I did not get the protein crystallized. As shown in Figure 5-20, there are four small peaks (358 nm, 430 nm, 510 nm, 560 nm) formed in the reaction of F191Y with L-Arg. The Quinonoid I intermediates accumulate much less than that in SwMppP,

while the Quinonoid II intermediates accumulates much more than that in SwMppP (Figure 5-20 inset). The peak with maximum absorbance at ~358 nm probably corresponds to ketimine intermediate that forms in aminotransferase (Figure 4-5). This peak first accumulated and then decreased as time goes. The position of F191 is usually tyrosine in aminotransferase (Figure 4-7C). These facts suggest that F191 is probably involved in exclusion of water close to C5. Substitution of F191 into tyrosine, the water may exist close to C5 and results in the ketimine intermediates formation.

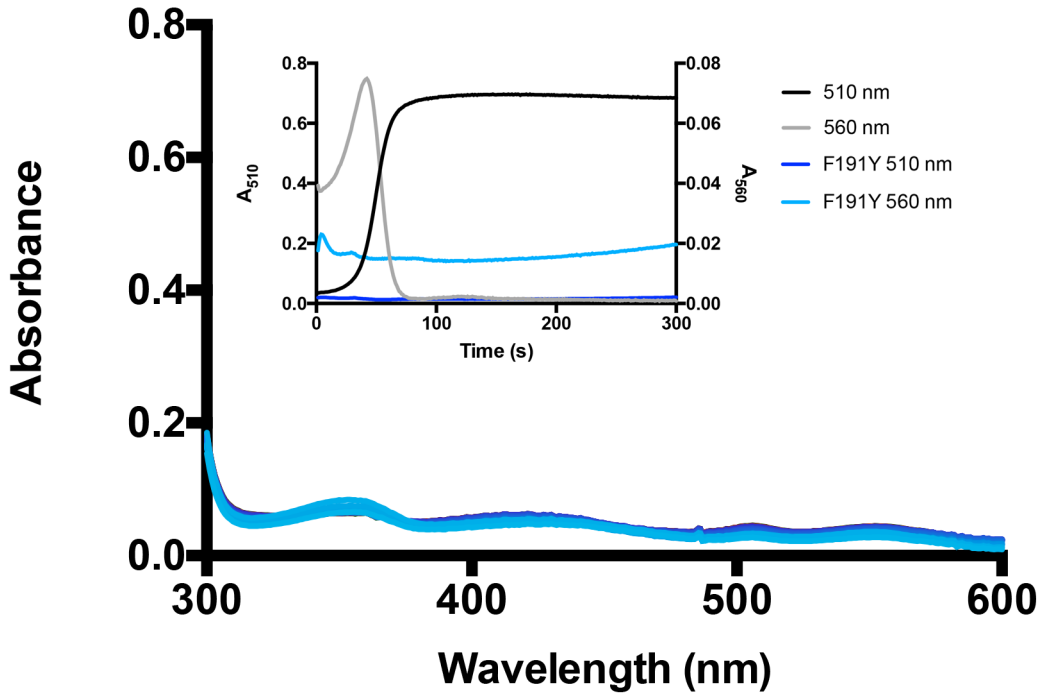


**Figure 5-20:** The spectrum of F191Y with L-Arg. F191Y enzyme (30 μM) was mixed with 1.4 mM L-Arg and recorded every second in 300s. There are 4 small peaks (358 nm, 430 nm, 510 nm, 560 nm) formed. Based on the thermo-Fluor assay results, F191Y mutant is not stable, which probably resulted in the small peaks.

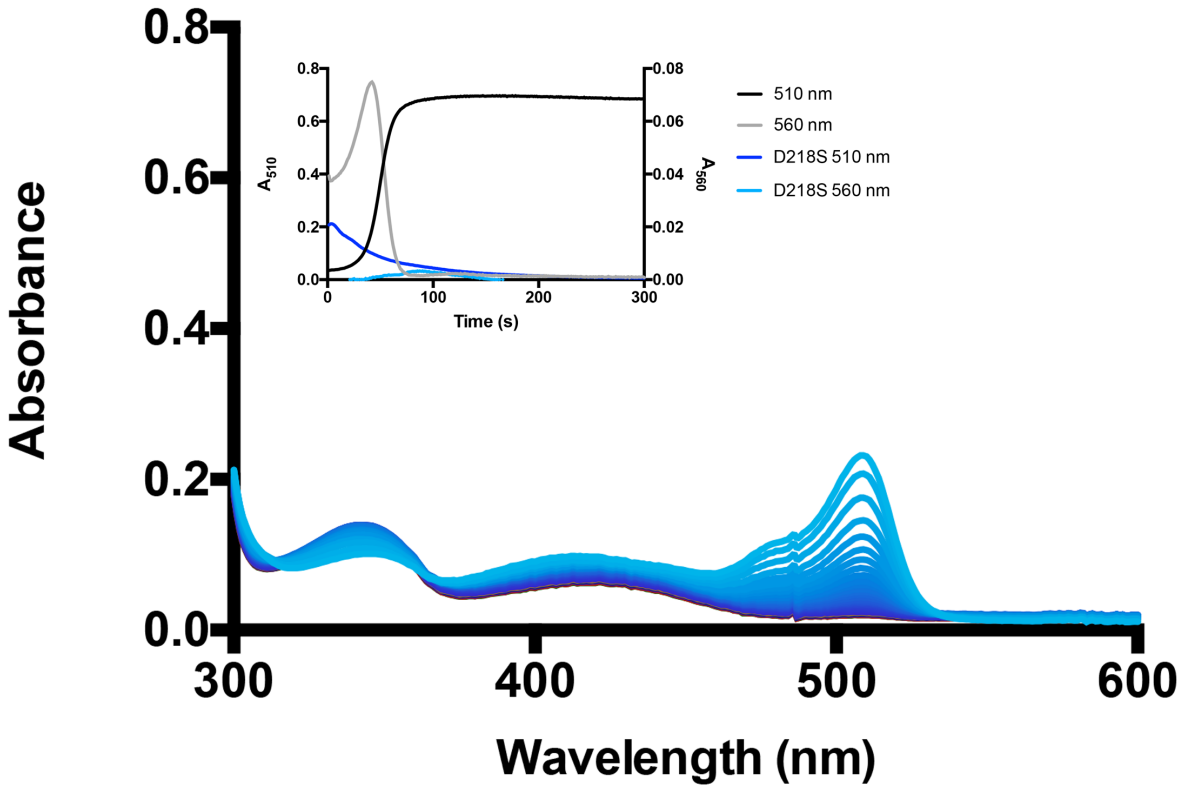


**Figure 5-21:** The spectrum of D218S with L-Arg. D218S enzyme (30 μM) was mixed with 1.4 mM L-Arg and recorded every second in 300s. There are 3 peaks (344 nm, 430 nm, 510 nm). The inset is the 510 nm and 560 nm comparison with wild type SwMppP.

In the PLP bound internal aldimine structure of SwMppP, D218 hydrogen bonding to the OH of S190, C5 of PLP and the main chain amine of T219 and G220. In the substrate bound external aldimine structure, D218 also interacts with the free K221. The SwMppP protein is yellow with PLP bound. However, the color of mutant D218S is less yellow even they are stored in the same buffer. The structure of D218S with poor electron density map showed that there is no PLP in the active site. The crystallization condition needs to be optimized for better diffraction. The spectrum of D218S demonstrates that there are three peaks (maximum absorbance at 340 nm, 430 nm and 510 nm) formed. As shown in the

inset in Figure 5-21, the external aldimine and Quinonoid I peaks decrease as time goes, while the peak with maximum absorbance at 340 nm keeps increase. This peak range from 310 nm to 370 nm may be pyridoxamine phosphate (PMP) or ketimine. Given that no PLP bound in the D218S active site and little products formed by NMR, the peak probably represents PMP (or both by hydrolyzing ketamine into PMP). If PMP cannot be hydrolyzed into PLP and form internal aldimine with K221, the PMP may dissociate out of the active site. So the D218 probably participates in PMP hydrolysis or internal aldimine formation.

### 5.3.9 Full oxidation of L-Arg requires two equivalents of $O_2$

The stoichiometry of $O_2$ consumed and L-Arg added was explored by $O_2$ electrode (Table 5-5). For wild type SwMppP producing **2** and **3** in the ratio of 1.7:1, the ratio of [$O_2$] consumed to [L-Arg added] is 1.4:1. The variant E15A, which only produces one product **3**, only needs 1 equivalent of $O_2$. But for E15D that producing both products, the ratio of [$O_2$] consumed to [L-Arg added] is >1, suggesting that the **2** branch requires more than one (probably two) equivalent of $O_2$ and the **3** branch only needs one. The ratios for mutants T12A, T12A/E15A and SwMppP$_{\Delta 1\text{-}22}$ were lower than 1:1, which was probably due to the lower catalytic efficiency as shown in Table 5-4.

For wt SwMppP, E15Q and F191Y, producing both products, the ratio is > 1:1. And for those mutants only forming keto-Arg as the product, the ratio is ≤ 1:1. Because both **3** and **2** are the products of SwMppP with L-Arg and $O_2$, we assumed that **3** pathway only consumed one equivalent of $O_2$ and **2** pathway consumed two equivalents of $O_2$.

**Table 5-5:** The ratio of [$O_2$ consumption]/[L-Arg added] of SwMppP and its mutants reactions

| [L-Arg]/μM | SwMppP | T12A | E15A | E15Q | T12A/E15A | H29A | H29S | F115Y | F191Y | D218S | SwMppP$_{\Delta 1\text{-}22}$ |
|---|---|---|---|---|---|---|---|---|---|---|---|
| 25 | 1.40:1 | 0.64:1 | 1.05:1 | 1.44:1 | 0.76:1 | 0.70:1 | 0.84:1 | 0.85:1 | 1.54:1 | | 0.61:1 |
| 50 | 1.43:1 | 0.54:1 | 0.95:1 | 1.28:1 | 0.65:1 | 0.77:1 | 0.82:1 | 0.77:1 | 1.38:1 | little activity | 0.45:1 |
| 100 | 1.38:1 | 0.59:1 | 0.95:1 | 1.29:1 | 0.72:1 | 0.81:1 | 0.80:1 | 0.80:1 | 1.37:1 | | 0.47:1 |

### 5.3.10 Substrate specificity

Reacting with L-Arg and $O_2$ showed the Cγ-hydroxylation activity of SwMppP[27]. To check if the L-Arginine precursors L-ornithine and L-citrulline are the possible substrates, the hydroxylation reaction was determined by spectrometric scan of the intermediates and MS analysis of the products. No intermediate peak formed by spectroscopy (Figure 5-22), even the external aldimine peak. As shown in Figure 6A, when SwMppP reacted with L-ornithine, the broad internal aldimine peak became smaller and a new peak at ~320 nm showed up. When SwMppP reacts with L-citrulline, the broad internal aldimine peak got smaller and red shifted (~425 nm to ~410 nm) as shown in Figure 5-22B. To detect the substrate specificity in more detail, the reactions of SwMppP with L-Arg derivatives L-canavanine, methyl-L-arginine and D-arginine were also determined (Figure 5-22). Upon D-Arg addition, the external aldimine formed and gradually shifted back holoenzyme (internal aldimine). There is no intermediate and product formed by NMR and MS (data not shown). The inhibitory constant ($K_i$) of D-arginine is 325 μM by monitoring the fluorescence signal at 415 nm on stop-flow. But for the L-canavanine reaction, the intermediate quinonoid I, which has maximum absorbance at 510 nm, accumulated when $O_2$ was used up in the cuvette. And there is one species formed at ~370 nm and decayed when another species formed which have broad absorbance around 330 nm. After several hours, the quinonoid I intermediate peak disappeared and two broad peaks at ~330 nm and ~425 nm still exist. For the reaction of SwMppP with methyl-L-arginine, quinonoid I peak quickly accumulated and gradually decreased. The NMR results showed that only keto-methyl-L-arginine formed. SwMppP did not catalyze the hydroxylation of methyl-L-arginine. Apparently, SwMppP exhibits very strong substrate specificity for hydroxylation.

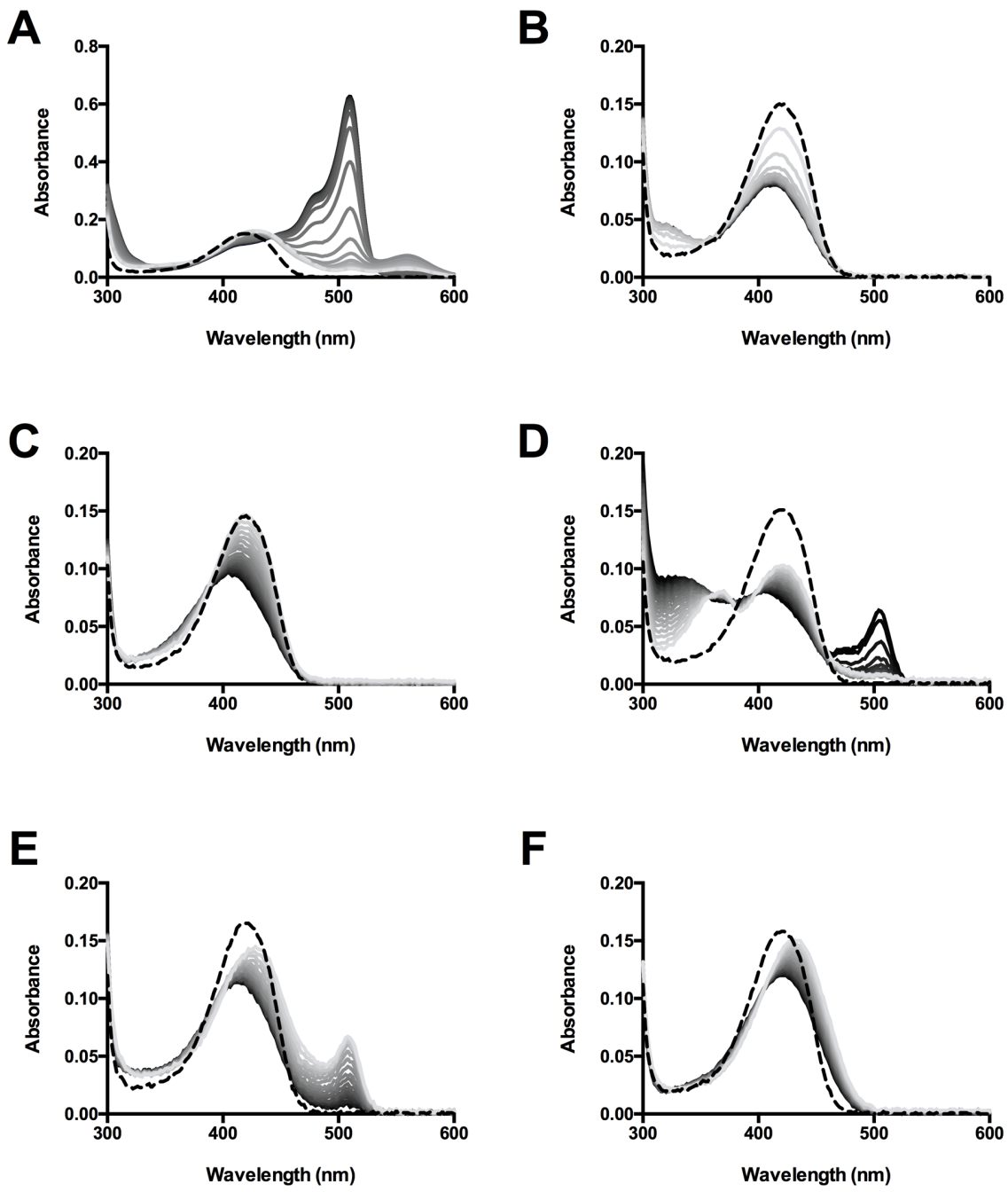


**Figure 5-22:** The spectrum of SwMppP with L-arginine (A), L-ornithine (B), L-citrulline (C), L-canavanine (D), methyl-L-arginine (E) and D-arginine (F). The spectrum of enzyme only was shown as dash line. After compounds addtion, the spectrum was recorded (from light grey to black).

### 5.3.11 The structure of SwMppP with D-Arg

As shown in Figure 5-22F, D-Arg is not the substrate of SwMppP, but it can bind to PLP forming external aldimine (peak shiftment from internal aldimine to external aldimine). Based on this, SwMppP crystals were soaked in 35 mM D-Arg to obtain the SwMppP•D-Arg external aldimine structure (Figure 5-23). The active site explains why D-Arg is not a substrate: the α-proton points toward the bulk solvent and away from any suitable general base catalyst (probably K221). Except the aldimine covalent bond, the carboxyl group of D-Arg forms salt bridges with R352 (Figure 5-23B). The guanidine group interacts with D27 and D227 and located in the position of N-terminal helix lid, which disrupts the N terminus covering the active site. Hence, unlike the L-Arg binding, N terminus disorders in the structure of SwMppP•D-Arg. Comparison of the SwMppP•L-Arg (Figure 5-11) and SwMppP•D-Arg (Figure 5-23), there are less interactions from the other chain in SwMppP•D-Arg. Because the side chain of L-Arg well aligned in the active site, the S248* and D249* from the other chain interacts with the guanidinium group of L-Arg. And the S91 also interacts with the guanidinium group. However, the side chain of D-Arg points away from the active site, so it loses these interactions.

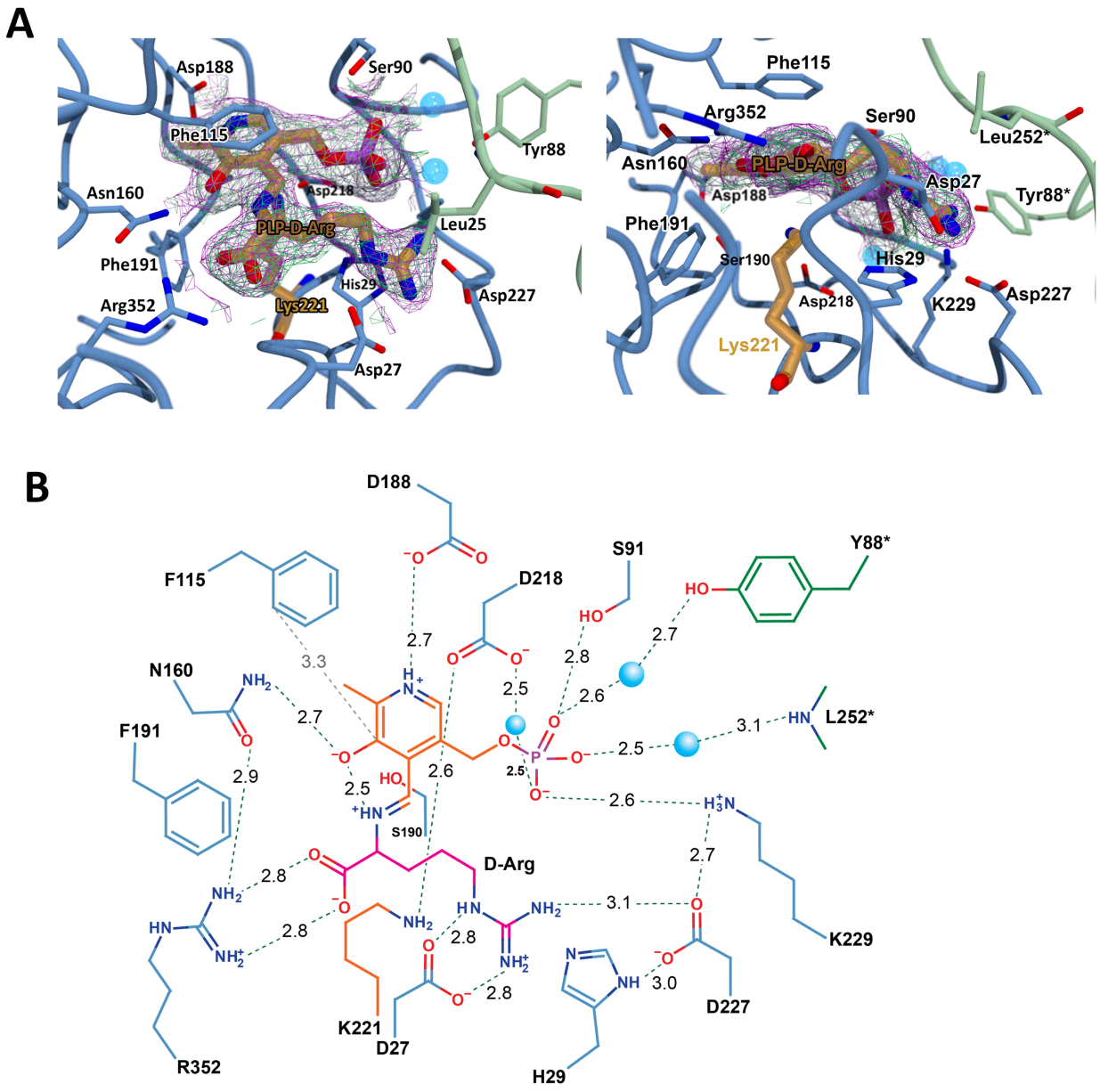


**Figure 5-23:** The active site of SwMppP•D-Arg. (A) SwMppP•D-Arg active site showing the PLP covalently bound to the enzyme as the internal aldimine. The $2|F_o| - |F_c|$ electron density map contoured at 1.0σ, shown as magenta mesh, and the $2|F_o| - |F_c|$ composite omit map also contoured at 1.0σ, is shown as green mesh. (B) Schematic view of the active site showing potential hydrogen bonding interactions as green, dashed lines. Water molecules are shown as blue spheres. Panel A was generated using POVSCRIPT and POV-Ray. Panel B was created using a combination of MarvinSketch (https://www.chemaxon.com) and Adobe Illustrator CS6.

D-Arg, as a competitive inhibitor, forms external aldimine with PLP in SwMppP active site. The dissociation constant of D-Arg (Ki) is determined by both $O_2$ probe assay and fluorescence change at 415 nm on stop flow. For $O_2$ probe assay, 10 μM SwMppP firstly incubated with 0 μM, 250 μM, 500 μM, 1 mM, 2.5 mM, 5 mM and 10 mM D-Arg in 50 mM BisTris propane pH 9.0 buffer for 5 min. For each data set (e.g 10 μM SwMppP with 250 μM D-Arg), a series of L-Arg were added and the $O_2$ consumption rate was determined. The result is shown in Figure 5-24. Each data set of rate vs L-Arg concentrations was fitted into Equation 2. Reciprocal plot of resulting $v_{max}$ and L-Arg concentration gives a series of linear plot at different D-Arg concentrations. The slope is $K_M/v_{max}(1+[D\text{-}Arg]/K_i)$, and the intercept is $1/v_{max}$. Linearly fitting the slope vs [D-Arg] data gives $K_i$ of 253.4 μM.

.

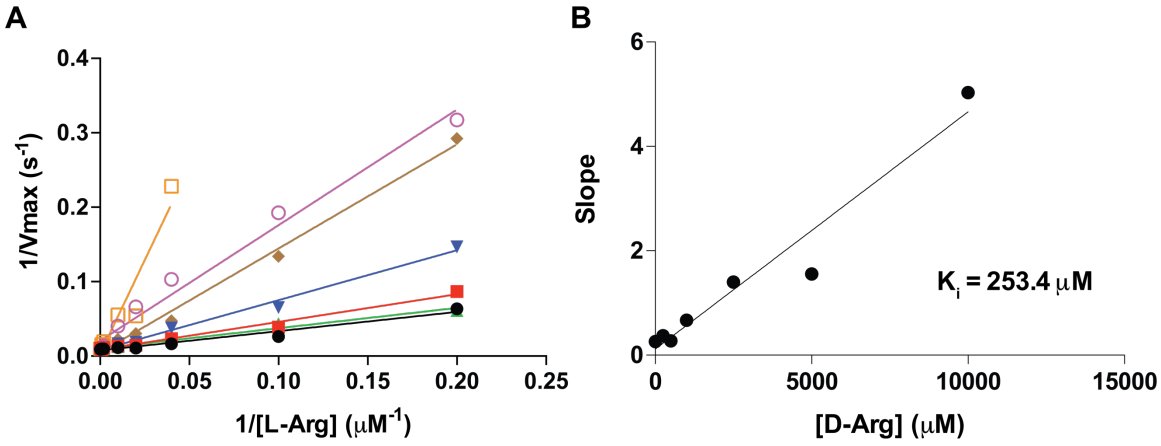


**Figure 5-24:** The D-Arg dissociation constant (Ki) determination. (A) The reciprocal plot of Vmax and L-Arg concentration gives a series of linear plot at different D-Arg concentrations. ●represents 0 μM D-Arg. ■ represents 250 μM D-Arg. ▲represents 500 μM D-Arg. ▼represents 1000 μM D-Arg. ◆represents 2500 μM D-Arg. ○ represents 5000 μM D-Arg, □ represents 10000 μM D-Arg. (B) The slope from (A) was plotted versus D-Arg concentration and the data is fitted linearly. The absolute x-intercept is the Ki (253.4 μM).

Fluorescence titration experiments were conducted to measure the kinetics of external aldimine formation step with D-Arg. SwMppP (10 μM after mixing) was mixed with different concentrations of D-Arg (40 μM, 80 μM, 160 μM, 320 μM, 640 μM and 1280 μM) and the total fluorescence was measured with excitation at 415 nm. The results are shown in Figure 5-25. The fluorescence data of SwMppP with different concentrations of D-Arg only have one phase and were fitted into Equation 3. The dependence of kobs were fitted into Equation 4 and gave $K_{d,app}$ of 329.3 μM.

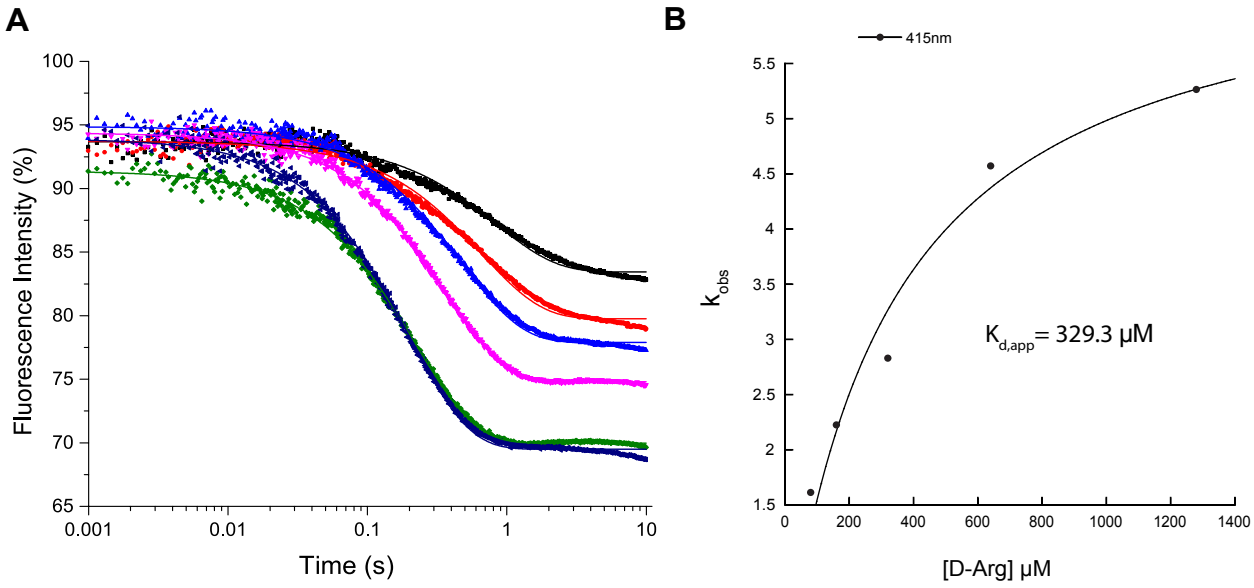


**Figure 5-25:** Dissociation constant ($K_i$) determination of D-Arg into SwMppP by fluorescence determination excited at 415 nm. (A) Fluorescence signal fitting by first exponential. . ■represents 40 μM D-Arg. ●represents 80 μM D-Arg. ▲represents 160 μM D-Arg. ▼represents 320 μM D-Arg. ◆represents 640 μM D-Arg. ◀ represents 1280 μM D-Arg. (B) The plot of $k_{obs}$ from data (A) versus D-Arg concentration gives the $K_{d,app}$ value of 329.3 μM.

### 5.3.12 Proposed mechanism of SwMppP

Based on all structural and kinetics studies shown above, we proposed the mechanism of SwMppP with L-Arg and $O_2$ (Scheme 5-2). Upon L-Arg binding, it attacks the internal aldimine, forming external aldimine. The free Lys221 on the enzyme would abstract the α proton, resulting in the formation of the Q1 intermediate, which has maximum absorption at 510 nm. Residues that differentiate the MppP active site from those of aminotransferases, like D218 and H29, likely play roles in stabilizing the electron-rich intermediate Q1. In the presence of $O_2$, one of the β protons is attacked by superoxide anion. After rearrangement, quinonoid 2 likely forms and it is at this point that Q2 can break down to release $H_2O_2$ and **3**, or Q2 could react with dioxygen to give **2** and a second molecule of hydrogen peroxide. The PLP is regenerated by hydrolysis of PMP with the release of ammonia. It is also a possibility that the product is released as the imine, recycling PLP directly. Subsequent non-enzymatic hydrolysis of the imine would yield **2** and ammonia.

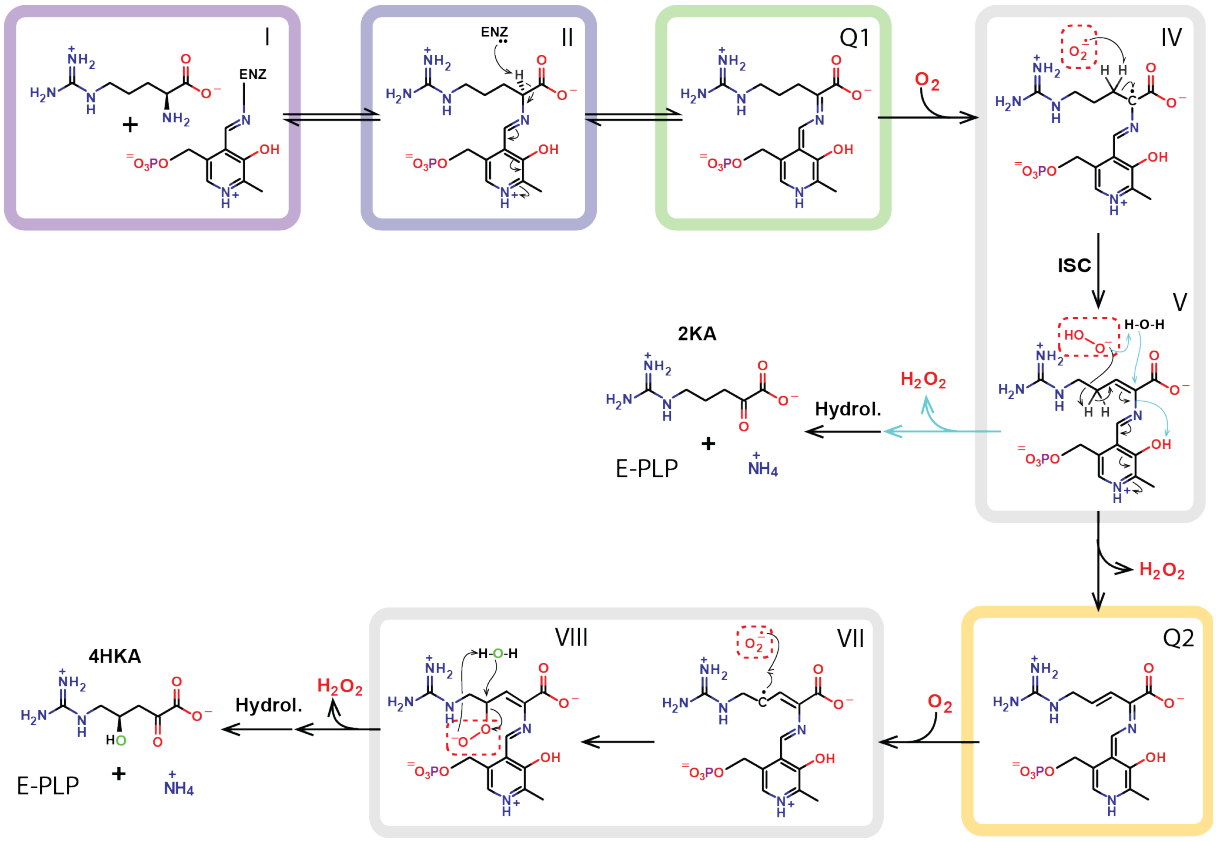


**Scheme 5-2:** Proposed mechanism of SwMppP.

### 5.3.13 Presteady state kinetics of SwMppP

Changes at the PLP center upon binding of L-Arg were monitored using stopped flow spectroscopy under anaerobic conditions, and exciting the internal aldimine at 415 nm. When the enzyme (10 μM after mixing) is mixed with various concentrations of L-Arg in the absence of dioxygen, there is a biphasic decay of fluorescence (Figure 5-26A), indicating that there are at least two steps occuring. The external aldimine absorbs UV light at 425-430 nm, rather than 415 nm, so the first phase likely corresponds to rapid binding of L-Arg

and conversion to the external aldimine. Since there is no dioxygen in the reaction, the second phase, must be due to the conversion of the external aldimine to the fist quinonoid intermediate (Q1). Put another way, the internal aldimine, which has its absorbance maximum at 415 nm, fluoresces strongly, as would the non-covalent enzyme-arginine complex. The first phase in the observed loss of fluorescence is due to the conversion of the internal aldimine to the external aldimine, which has a slightly longer wavelength absorbance and therefore gives rise to a lower fluorescence signal when excited at 415 nm. The second phase is due to conversion from the external aldimine to a quinonoid intermediate, which absorbs at 510 nm and would therefore not fluoresce when excited at 415 nm.

This identification of the second phase in the fluorescence data is confirmed by monitoring the increase in absorbance at 510 nm (Figure 5-26B). In this experiment, the increase in absorbance is due to the accumulation of the first quinonoid intermediate (Q1) in the absence of dioxygen. This proves two things: first that the electron-rich quinonoid species is the form of the enzyme that reacts with dioxygen. Second, that the enzyme stabilizes the quinonoid intermediate to an unusual degree. Quinonoids are not unusual in PLP-dependent enzymes, but one that persists for the length of time observed with SwMppP is unprecedented. Comparing the timing of the second decay phase in the fluorescence data (Figure 5-26A) with the appearance of Q1 at 510 nm (Figure 5-26B), it is clear that these two signals represent the same event, that is, the appearance of the first quinonoid intermediate. The lag phase in the beginning of the experiment in Figure 5-26B corresponds to the substrate binging step and conversion to the external aldimine.

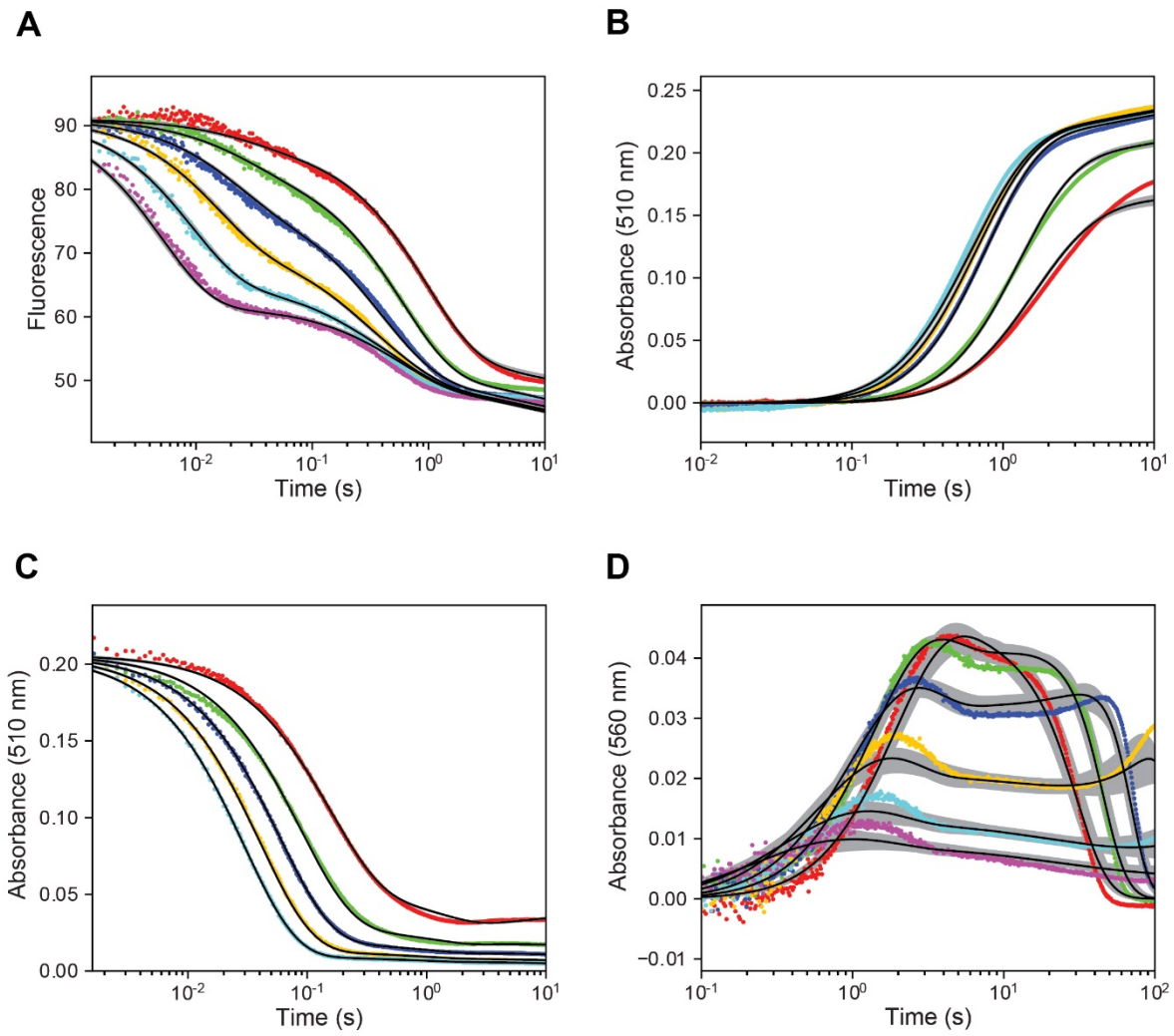


**Figure 5-26:** Global fitting of pre-steady state kinetics data in KinTek Explorer. (A) The change in fluorescence upon mixing 20 μM anaerobic SwMppP with various concentrations of anaerobic L-Arg (20 [red], 40 [green], 80 [blue], 160 [yellow], 320 [cyan], and 640 μM [purple]). (B) The same reaction conditions as in A, but monitoring absorbance at 510 nm. (C) Double mixing experiments where anaerobic SwMppP (40 μM) was mixed with 1280 μM anaerobic L-Arg and aged for 10 s before mixing with buffer containing various concentrations of dioxygen (81 [red], 160 [green], 250 [blue], 375 [yellow], and 519 μM [cyan]). The loss of absorbance at 510 nm due to the first quinonoid intermediate was monitored. (D) Double mixing experiments where anaerobic SwMppP (40 μM) was mixed with 1280 μM anaerobic L-Arg and aged for 10 s before mixing with buffer containing various concentrations of dioxygen (20 [red], 42.5 [green], 78 [blue], 158 [yellow], 296 [cyan] and 465 μM [purple]). The absorbance at 560 nm was monitored. In all panels, the black lines show the results of the fitting by simulation based in the model in Figure 5-27. The grey shading beneath the fits show the fit through the entire ranges of all parameters derived from the fitting.

In order to examine the later, oxygen-dependent steps in the reaction, we employed double mixing stopped flow experiments where anaerobic SwMppP was mixed with anaerobic L-Arg and aged for 10 s to allow the first quinonoid intermediate to accumulate. The second mixing step introduced buffer with varying concentrations of oxygen to the pre-formed Q1 intermediate. The data in Figure 5-26C show that there is a monophasic decrease in the absorbance at 510 nm as Q1 reacts with dioxygen. The rate of the reaction with dioxygen does not appear to saturate, but increases with the concentration of dioxygen. The lack of saturation indicates that there is no defined binding site for dioxygen and the rate is governed by the frequency with which dioxygen encounters the quinonoid intermediate.

A peak was observed at 560 nm in earlier UV-vis spectroscopy experiments. This peak is likely due to a second quinonoid intermediate, Q2, having more extended conjugation (*i.e.* an additional double bond compared with Q1). The rates of formation and decay of this intermediate were probed using the same double mixing experiment described above (with slightly different dioxygen concentrations) and monitored at 560 nm (Figure 5-26D). That this second quinonoid evolves from Q1 is established by the fact that Q2 only accumulates after Q1 decays, as can be seen by comparing the times in Figures 5-26C and D. The dependence on the accumulation of Q2 on the concentration of dioxygen is counterintuitive; it accumulates most in the reactions with the least dioxygen. This behavior is most likely due to the "2-ketoarginine branch." Including this uncoupled product in the model for global fitting by simulation was the only way to reproduce this pattern in the simulated data.

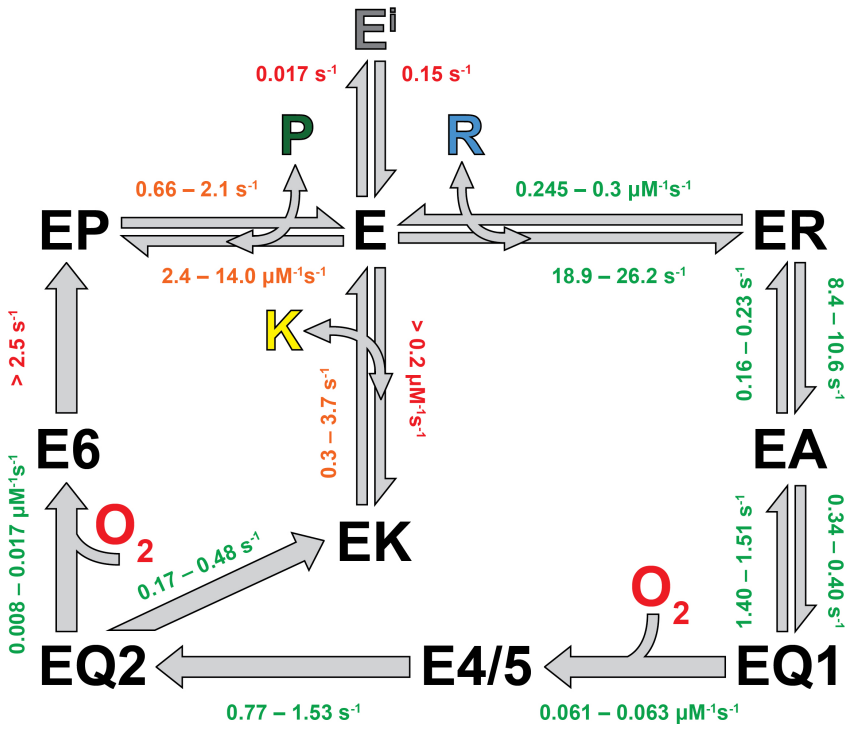


**Figure 5-27:** The model used for global fitting by simulation in KinTek Explorer. The rate constants for each step are given as the boundaries identified by the FitSpace routine in KinTek Explorer. The green rate constant estimates are well constrained by the data. Those in orange range somewhat widely, and those in red have only an upper or lower limitdefined and were fixed at those limits. Steps with unidirectional arrows had the corresponding reverse rates fixed at zero in the simulation.

Owing largely to the pseudo-first order conditions used in these experiments, much of these data, particularly those monitoring Q2 (Figure 5-26D) were difficult, if not impossible, to fit well by traditional non-linear least squares fitting. The multiple up and down phases in Figure 5-26D make it impossible to know the amplitudes of each phase with certainty. On top of this, the complicated mechanism (*e.g.* Figure 5-27), makes it difficult to assign the various $k_{max}$ or $K_{eq}$ terms that would be obtained from secondary plots of $k_{obs}$ vs concentration to specific steps in the mechanism. For these reasons, all of the data were fit simultaneously in KinTek Explorer[35-37]. In this program, one defines a model for

the reaction, and the software derives all of the differential equations required to calculate the concentrations of all reactants, products, and intermediates over the timecourses of the experiments. The FitSpace routine within KinTek explorer is used to validate the resulting models by calculating "confidence contours" for each parameter estimated from the fitting. This analysis defines the range of values for each parameter that would result in essentially the same fit. Thus, the tighter the FitSpace boundaries, the better determined the parameter. KinTek Explorer was used to build a model of the SwMppP reaction (Figure 5-27). The experiments described above adequately defined rate constants for most of the steps in this very complicated model. Key points of the mechanism that were only clarified by the global fitting analysis include the suggestion that the "2-ketoarginine branch" occurs at the second quinonoid intermediate and that the intersystem crossing step presumed in the proposed mechanism (Scheme 5-2) is fast enough that it appears to be a single step in the modelling. Changing either point in the model—placing the branch at E4/5 or breaking E4/5 into two separate steps (e.g. E4 = E5) resulted in a significant degradation of the fitting results. The other interesting conclusion that resulted from the fitting is the possibility of a slow isomerization step (*e.g.* $E^i$ = E). Inclusion of this pre-equilibration was the only parameterization of the model that reproduced the slow up-phase in the accumulation of Q1 (Figure 5-26B). This is a plausible addition to the model, since the enzyme is essentially inactive in the storage buffer (10 mM MES pH 6.7) and active, but minimally stable in the reaction buffer (100 mM BIS-TRIS pH 9.0). It is conceivable that the activation may not be instantaneous upon the shift to pH 9.0.

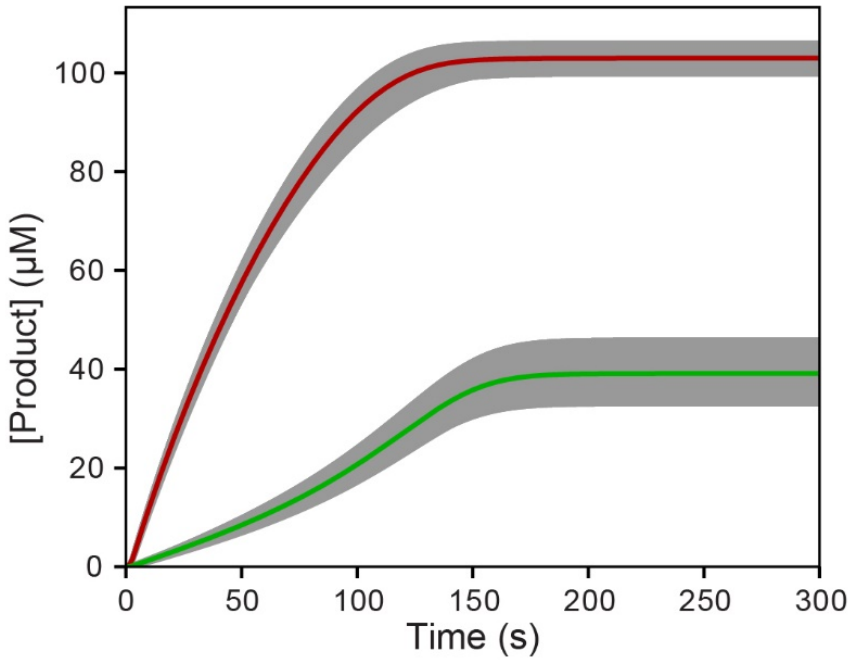


**Figure 5-28**: Accumulation of the fully oxidized 4-hydroxy-2-ketoarginine (red) and the uncoupled 2-ketoarginine (green) products based on the global fitting by simulation. The grey swathes represent the range of values consistent with the model. The ~2:1 ratio predicted by the proposed mechanism and associated model is not far from the ~1.7:1 ratio observed experimentally. Note that in the simulation, the dioxygen concentration was not replenished, as it was by stirring in the actual experiments.

### 5.3.14 Preliminary pre-steady state kinetics analysis of SwMppP$_{H29A}$

As shown in Figure 5-29, the kinetics of the H29A mutant of SwMppP are significantly altered from the wild-type enzyme (compare Figure 5-29A (wild-type) and B (H29A)). Qualitatively speaking, the first phase observed in the fluorescence experiments (exciting the internal aldimine) do not appear to be changed much from the wild-type. This suggests that H29 does not have a central role in substrate binding and/or attack on the internal

aldimine to form the external aldimine. Both the second phase of the fluorescence change and the increase in absorbance at 510 nm due to formation of the first quinonoid intermediate have much lower amplitudes than observed in the wild-type. This indicates a likely role for H29 in promoting the conversion of the external aldimine to Q1.

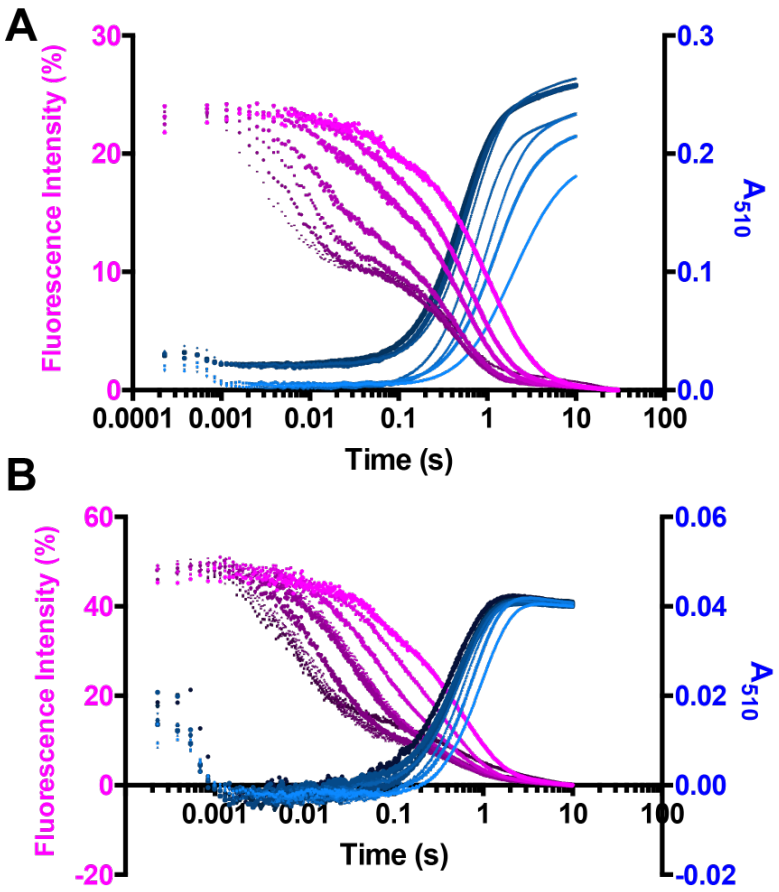


**Figure 5-29:** Comparison of fluorescence ($\lambda_{ex}$=415 nm) and absorbance (510 nm) of wild-type SwMppP (A) and the H29A mutant (B) reacting with L-Arg (10, 25, 50, 125, 250, 500, 1000 μM for WT or 25, 50, 100, 150, 200, 400, 600, 800, 1200 μM for H29A). The fluorescence traces in both panels are shown in a gradient from pink (low [Arg] to purple [high [Arg]. Likewise, the absorbance data are shown as a gradient from light blue (low [Arg]) to dark blue (high [Arg]).

### 5.3.15 Preliminary pre-steady state kinetics analysis of SwMppP$_{\Delta 1\text{-}22}$

The changes in total fluorescence ($\lambda_{ex}$ = 415 nm) upon mixing SwMppP$_{\Delta 1\text{-}22}$ (10 μM after mixing) with concentrations of L-Arg ranging from 25 to 1200 μM are shown in Figure 5-30. The amplitudes of the transients observed are smaller than those seen with either the wild-type or H29A mutant. These data did not fit well to simple exponential equations, and were instead fit globally in KinTek Explorer using the first 3 steps of the new model mentioned above as the model. However, the data was still fitted well. So we need to do more studies to optimize the experiments in the future.

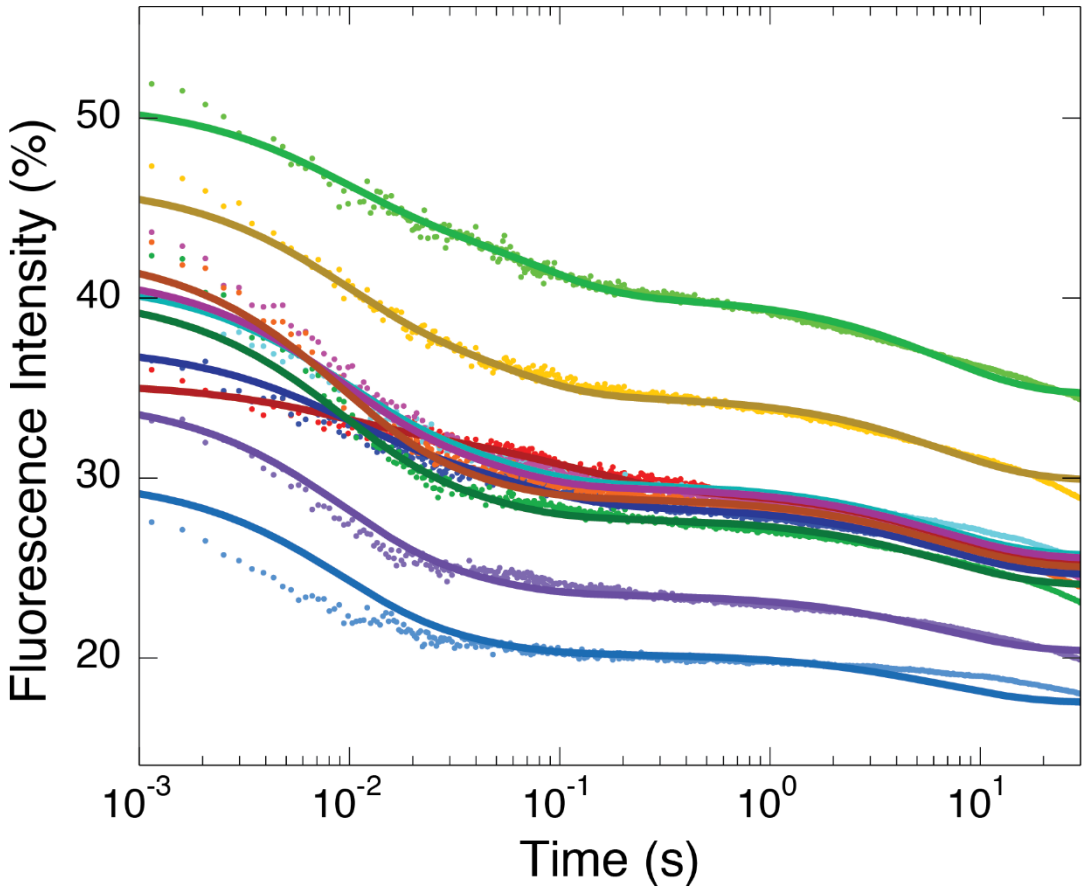


**Figure 5-30:** Fluorescence excited at 415 nm of SwMppP$_{\Delta 1\text{-}22}$ with L-Arg substrate under anaerobic condition.

The fluorescence data (dots) of SwMppP$_{\Delta 1\text{-}22}$ (10 μM) versus different L-Arg concentrations (●25, ●50, ●75, ● 100, ●150, ●200, ●400, ●600, ●800 and ●1200 μM) was fitted globally (lines with different colors) to the same model mentioned above.

### 5.3.16 Independent binding between two binding sites of SwMppP

The structures of SwMppP or mutant H29A/S with L-Arg shows two different states in the two binding sites within one dimer. For example, in the two active sites of SwMppP•L-Arg, chain A has the L-Arg bound to PLP while chain B has the product **2** bound. Some structures have **3** bound and internal aldimine state in chain A and chain B, respectively. In the structure of H29A•L-Arg, chain A has L-Arg bound but chain B has PLP covalently bound to catalytic lysine. So to check if the two binding sites within one dimer are independent or not, ITC and fluorescence experiment that monitoring the internal aldimine decay was determined. SwMppP would form Quinonoid I eventually under anaerobic condition, which make the data harder to analyze. D188 hydrogen bonds to the NH of PLP ring, which is important for Quinonoid I formation. After mutated D188 into alanine, the variant D188A reacts with L-Arg to form external aldimine. So this mutant was used to study the dependence binding of two binding sites.

ITC is a physical technique that works by determining the heat released or absorbed during a binding event. Before the experiment, the system is chemically calibrated. The sample cell containing 300 μl of 90 μM dialyzed, degassed SwMppP$_{D188A}$ protein in 15 mM MES pH 6.7 buffer was incremental titrated with 2.5 μl of 800 μM L-Arg in the same buffer each titration. After load both sample cell and the burret with L-Arg, the system would keep

equilibrate the system with stirrer on, which usually takes 1.5 h to get acceptable heat change deviation. And the later titration experiment takes about 1 hour. The titration heat rate curve has a shifted baseline due to the instability of D188A protein. After continuous agitating for 2.5 h, the protein D188A precipitated and the baseline shifted upwards. I tried to decrease the temperature to 4 $^{o}$C, the baseline is almost flat but periodic noise peak show up at this low temperature. Then I tried 10 $^{o}$C, 12 $^{o}$C and 18 $^{o}$C, they all have shifted baseline. After many attempts, the ITC results are not satisfactory. So fluorescence experiments with short time and gentle treatment was used to monitor the internal aldimine decay and determine the binding relationship. The reaction containing 1.5 mL of SwMppP$_{D188A}$ (14 μM) and equal volume of different concentrations of L-Arg (0 - 2560 μM) in 100 mM BisTris propane buffer was incubated for 8 min before excitation at 415 nm. As shown in Figure 5-31A, there are two species changing during the experiment. As substrate concentration increases, the peak with maximum absorbance at 480 nm decreased, while the peak with maximum absorbance at 542 nm increased. Hence, the species that emissions maximally at 480 nm corresponds to internal aldimine, and the species that emissions maximally at 542 nm corresponds to external aldimine. According to the data, SwMppP$_{D188A}$ is almost saturated with 1280 μM L-Arg. Both 480 nm and 542 nm delta fluorescence data are not fitted into Hill equation, which suggested independence binding between two binding sites. The plot of calculated [D188A•L-Arg] complex versus [L-Arg] at 480 nm was fitted to Equation 4 and the $K_d$ for internal aldimine decay is 92.8 μM (Figure 5-31B).

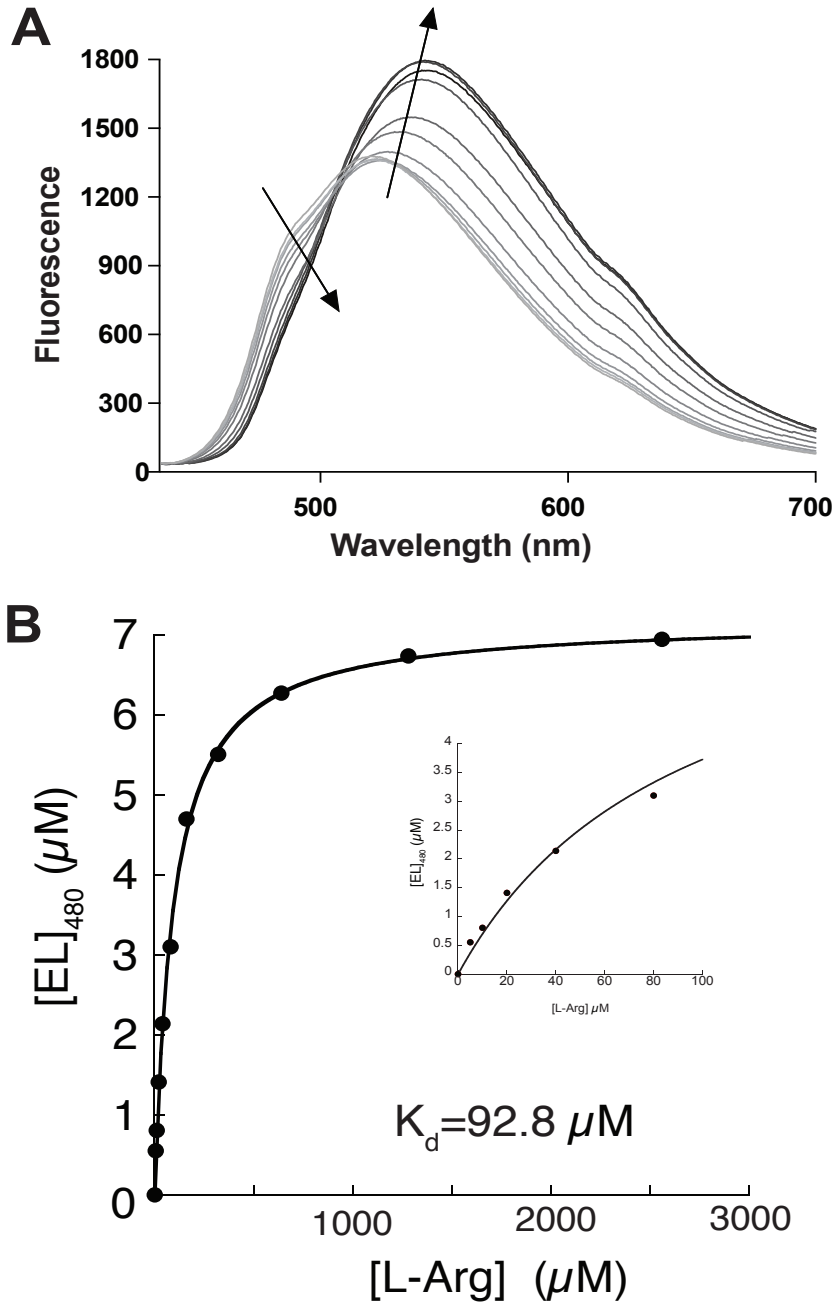


**Figure 5-31:** (A) Fluorescence change of SwMppP$_{D188A}$ with different concetrations of L-Arg (0, 5, 10, 20, 40, 80, 160, 320, 640, 1280 and 2560 μM). There are two major peaks changing as the substrate concentration increases. The peak with maximum absorbance at ~480 nm decreased as [L-Arg] increases, which suggests this species is internal aldimine. The other peak with maximum absorbance at ~542 nm corresponds to external aldimine increases as substrate increases. (B) The fitting data of enzyme and L-Arg complex versus

[L-Arg] at 480 nm was fitted hyperbolically, rather than Hill plot. The inset is the zoomed initial data points and fitting. The data fits hyperbola pretty well, rather than a sigmoid curve.

## 5.4 Discussion

The nonproteinogenic amino acid L-enduracididine is a critical component of the mannopeptimycins, a family of cyclic glycopeptide antibiotics with potent activities against drug-resistant pathogens like MRSA. Creating derivatives of mannopeptimycin and other L-End-containing natural products is hampered by the limited availability of L-End. We are investigating the L-End biosynthetic pathway in order to develop an efficient enzymatic or chemo-enzymatic route to produce this unusual amino acid. Recently, we found that MppP is a PLP-dependent L-Arg oxidase in L-End biosynthesis in *S. wadayamensis*, and not an aminotranferase as the sequence suggested. The quaternary structure of SwMppP is very similar to the Fold Type I aminotransferases. The major difference is the N-terminus. For type I aminotransferases, the N-terminal helix interacts with the small domain of the other chain, and the small domain shifts towards the large domain forming a "closed" conformation when the substrate binds[20, 28, 29]. However, SwMppP mainly exists as homodimer with the active site exposed to the solvent in the unliganded state; the N-terminus is disordered. The fluorescence data of SwMppP $_{D188A}$ with L-Arg demonstrated that the two active sites within the SwMppP dimer are independent; there is no evidence of half-sites reactivity or cooperativity. Upon substrate binding, the N-terminus orders to form an α-helix that covers the active site and interacts with L-Arg. In addition, there is no movement of the small domain, as is often, though no always, observed in

aminotransferases. The PLP-dependent cystathionase MalY from *E. coli* (PDB entry: 1D2F[30]) and a number of aminotransferases (*e.g.* PDB entry 4DQ6 and 3DZZ) have a high degree of structural similarity with SwMppP. Overlaying the SwMppP structure with these demonstrates that the small domain of SwMppP is closer to the large domain, and that the small domain and large domain arrangement of unliganded SwMppP is more like the "closed" conformation of the aminotransferases.

In *E. coli* aspartate aminotransferase, the inward movements of the small domain create steric clashes between G38 and Y225, which results in a lower pKa of the aldimine and enhanced catalysis[28]. The lower imine pKa of the internal aldimine is mainly due to the 90° torsion angle of the C3-C4-C4'-Nζ bond and the repulsive interactions between G38 and Y225[28, 31]. However, the corresponding torsion angle of SwMppP is ~9°. And SwMppP has a higher catalysic activity at higher pH[27], which suggests a pronated internal aldimine form in SwMppP.

SwMppP reacts with L-Arg and dioxygen to yield two products, **2** and **3** in a ratio of ~1.7:1. Compound **2** is the products that can be cyclized by MppR (Figure 4-4B). Compound **3** is the result of uncoupled turnover. L-Arg is an important amino acid, which is involved in many pathways and serves as a carbon and nitrogen source[32]. MppQ has been shown to catalyze the transamination of **3** back to L-Arg (unpublished data), which brings the deadend product **3** back into the metabolite pool of the cell.

Two N-terminal residues, T12 and E15, interact with L-Arg in the active site. To understand what roles these two residues and the N terminus play, we made mutations of these two residues as well as truncation on the N terminus (Δ1-22 aa). The N-terminal

variants T12A, E15A, T12A/E15A and SwMppP$_{\Delta 1\text{-}22}$ only produce **3**, which indicates that the N-terminal helix is essential for hydroxylation. In addition, T12A, T12A/E15A and SwMppP$_{\Delta 1\text{-}22}$ have lower catalytic efficiency. As the spectra shown in Figure 5-16 indicate, the external aldimine peak (435 nm) gradually shifts back to the internal aldimine peak (415 nm) during the reaction, suggesting that the N-terminal helix, especially T12, plays a key role in stabilizing external aldimine. The mutant E15A has similar $K_M$ and $k_{cat}$ values with wild type SwMppP but is deficient in the hydroxylase activity. In the structure of E15A•L-Arg, the N terminus also orders and covers the active site. T12 in N terminus still interacts with the guanidine group of L-Arg. But the short side chain of Ala15 creates a void that is filled by water, which probably disrupts the hydroxylation pathway. E15Q variant still produced the mixture of **2** and **3**, although it does make less of the hydroxylated product. Hence, the N terminus interaction is crucial for the stability of external aldimine and later hydroxylation activity.

The reaction of SwMppP with L-Arg and $O_2$ forms two quinonoid intermediates (Q1 at 510 nm and Q2 at 560 nm). Under anaerobic conditions, the accumulated Quinonoid I is very stable, which suggests this carbanion is stabilized by SwMppP to some extent. When the $O_2$ is present, Quinonoid I quickly reacts with $O_2$, which is similar to the PLP-dependent DOPA/aromatic L-amino acid decarboxylases[33]. When the substrate covalently bonds to PLP, the free catalytic K221 forms a hydrogen bonding interaction or salt bridge with D218, which is similar in DOPA/aromatic L-amino acid decarboxylases (PDB ID 1JS3[34]). To study the role of this residue, D218 was substituted with Ser. There is a peak at ~430 nm in the reaction of the D218S mutant withL-Arg that is most likely due to either PMP or a ketamine intermediate that results from deprotonation of the quinonoid by K221. In addition, there

is no PLP in the structure of the D218S mutant. These results suggest that D218 either participates in the PMP hydrolysis or helps to stabilize the quinonoid intermediate by preventing K221 from readily deprotonating the Q1 intermediate. In the structures of H29A, F115Y and H29A•L-Arg, there are more water molecules in the active sitethat are not seen in the wild-type structure. In the reaction of F191Y with L-Arg, there is a ketimine intermediate formed. The ketimine formation needs a water or K221 to provide H to the imine. In conclusion, the water molecule is an important factor to regulate the product pathway. In addition, E15, H29, F115 and F191 are all involved in water exclusion. In SwMppP with L-Arg spectrum, Q2 first accumulates and then quickly decays. But according to the spectrum of F191Y with L-Arg, Q2 persists, which suggests that F191 is also involved in the reaction of Q2 with $O_2$.

According to the spectra of all proteins mentioned above, Q2 only accumulates in the enzymes producing both products. For those mutants producing **3** only, no Q2 intermediate peak was observed. These facts suggest that Q2 formation belongs to the hydroxylation pathway. Pre-steady state data of Quinonoid I decay and Quinonoid 2 formation shows that Quinonoid 2 only forms after Quinonoid I decay.

The portion of $O_2$ consumed to form $H_2O_2$ was determined by adding catalase after the reaction attained equilibration. Catalase catalyzes 2 moles of $H_2O_2$ into 1 mole of $O_2$, and the ratio of $O_2$ consumed over $O_2$ regenerated is 2:1, which indicated that each equivalent of $O_2$ consumed is converted to 1 equivalent of $H_2O_2$. In addition, the products mass of SwMppP with L-Arg and $O_2$ conducted in $H_2{}^{18}O$ demonstrates that the hydroxyl O atom of **2** comes from water. So SwMppP is an oxidase.

The mutant E15A, producing **3** only, has similar catalytic efficiency with wild type. The ratio of [$O_2$ consumed] over [L-Arg added] for variant SwMppP $_{E15A}$ that produces **3** only is 1:1, which suggested that **3** formation only requires one equivalent of $O_2$. For the other mutants (T12A, T12A/E15A, SwMppP$_{\Delta 1\text{-}22}$, H29A/S and F115Y) that producing **3** only, the ratios of [$O_2$ consumed] over [L-Arg added] are smaller than 1. The ratio is based on the amounts of L-Arg added, not L-Arg consumed, so the mutants with lower catalytic efficiency would give a smaller ratio. The ratios of [$O_2$ consumed] over [L-Arg added] of wild type SwMppP, E15Q and F191Y, producing both **3** and **2**, is 1.4:1, which suggested that **2** formation requires 2 equivalents of $O_2$.

The structural and kinetic characterization of the wild-type and several variants of SwMppP allowed us to propose a model where the oxygen atom incorporated in the **2** product is derived from water rather than from dioxygen. And **2** formation requires 2 equivalents of $O_2$, while the abortive product, **3**, requires only 1 equivalent.

As described above, SwMppP catalyzes the Cγ-hydroxylation of a non-activated methylene moiety on L-Arg with very high stereospecificity. The stereochemistry of the Cα atom is crucial for the reaction. The α proton of D-arginine is located opposite to the general base catalyst for the Q1 intermediate formation[27], and the external aldimine conformation is not stabilized by the interactions in the active site. Hence, the external aldimine gradually shifted into internal aldimine by the K221 attack. In addition, the position of the guanidinium group is essential for the hydroxylation activity. The guanidinium group of L-Arg is hydrogen bonding with the PLP phosphate group, T12, S91 and the carbonyl groups of S248 and D249 from the other chain. The L-Arg homologs, L-

citrulline, L-canavanine and methyl-L-arginine, disrupt the coordinations and resulted in the loss of hydroxylation. The side chain of D-Arg pointed away from the PLP cofactor and disrupted the N-terminus interaction, which also leads to the inactivity. The length of the substrate is also important for SwMppP activities. Shorter L-Arg analog, L-Orn cannot be deaminated or hydroxylated.

## 5.5 Reference


[1] Goldberg, J. M., and Kirsch, J. F. (1996) The Reaction Catalyzed by Escherichia coli Aspartate Aminotransferase Has Multiple Partially Rate-Determining Steps, While That Catalyzed by the Y225F Mutant Is Dominated by Ketimine Hydrolysis, *Biochemistry 35*, 5280-5291.

[2] Lu, Z., Nagata, S., McPhie, P., and Miles, E. W. (1993) Lysine 87 in the beta subunit of tryptophan synthase that forms an internal aldimine with pyridoxal phosphate serves critical roles in transimination, catalysis, and product release, *The Journal of biological chemistry 268*, 8727-8734.

[3] Han, L., Schwabacher, A. W., Moran, G. R., and Silvaggi, N. R. (2015) Streptomyces wadayamensis MppP Is a Pyridoxal 5'-Phosphate-Dependent L-Arginine alpha-Deaminase, gamma-Hydroxylase in the Enduracididine Biosynthetic Pathway, *Biochemistry 54*, 7029-7040.

[4] Pacheco, A. A., McGarry, J., Kostera, J., and Corona, A. (2011) Techniques for investigating hydroxylamine disproportionation by hydroxylamine oxidoreductases, *Methods in enzymology 486*, 447-463.

[5] Otwinowski, Z., and Minor, W. (1997) Processing of X-ray diffraction data collected in oscillation mode, *Methods in enzymology 276*, 307-326.

[6] Vonrhein, C., Blanc, E., Roversi, P., and Bricogne, G. (2007) Automated structure solution with autoSHARP, *Methods in molecular biology (Clifton, N.J.) 364*, 215-230.

[7] Cowtan, K. (2006) The Buccaneer software for automated model building. 1. Tracing protein chains, *Acta crystallographica. Section D, Biological crystallography 62*, 1002-1011.

[8] McCoy, A. J., Grosse-Kunstleve, R. W., Adams, P. D., Winn, M. D., Storoni, L. C., and Read, R. J. (2007) Phaser crystallographic software, *Journal of applied crystallography 40*, 658-674.

[9] Emsley, P., Lohkamp, B., Scott, W. G., and Cowtan, K. (2010) Features and development of Coot, *Acta crystallographica. Section D, Biological crystallography 66*, 486-501.

[10] Adams, P. D., Afonine, P. V., Bunkóczi, G., Chen, V. B., Davis, I. W., Echols, N., Headd, J. J., Hung, L.-W., Kapral, G. J., Grosse-Kunstleve, R. W., McCoy, A. J., Moriarty, N. W.,

Oeffner, R., Read, R. J., Richardson, D. C., Richardson, J. S., Terwilliger, T. C., and Zwart, P. H. (2010) PHENIX: a comprehensive Python-based system for macromolecular structure solution, *Acta Crystallographica Section D: Biological Crystallography 66*, 213-221.
[11] Word, J. M., Lovell, S. C., Richardson, J. S., and Richardson, D. C. (1999) Asparagine and glutamine: using hydrogen atom contacts in the choice of side-chain amide orientation11Edited by J. Thornton, *Journal of molecular biology 285*, 1735-1747.
[12] Urzhumtseva, L., Afonine Pv Fau - Adams, P. D., Adams Pd Fau - Urzhumtsev, A., and Urzhumtsev, A. Crystallographic model quality at a glance.
[13] Terwilliger, T. C., Adams, P. D., Read, R. J., McCoy, A. J., Moriarty, N. W., Grosse-Kunstleve, R. W., Afonine, P. V., Zwart, P. H., and Hung, L.-W. (2009) Decision-making in structure solution using Bayesian estimates of map quality: the PHENIX AutoSol wizard, *Acta Crystallographica Section D 65*, 582-601.
[14] Meister, A. (1952) Enzymatic preparation of alpha-keto acids, *The Journal of biological chemistry 197*, 309-317.
[15] Vlessis, A. A., Bartos, D., and Trunkey, D. (1990) Importance of spontaneous alpha-ketoacid decarboxylation in experiments involving peroxide, *Biochemical and biophysical research communications 170*, 1281-1287.
[16] Li, C., and Lu, C.-D. (2009) Arginine racemization by coupled catabolic and anabolic dehydrogenases, *Proceedings of the National Academy of Sciences 106*, 906-911.
[17] Bertoldi, M., and Borri Voltattorni, C. (2000) Reaction of dopa decarboxylase with L-aromatic amino acids under aerobic and anaerobic conditions, *The Biochemical journal 352 Pt 2*, 533-538.
[18] Bertoldi, M., and Borri Voltattorni, C. (2003) Reaction and substrate specificity of recombinant pig kidney Dopa decarboxylase under aerobic and anaerobic conditions, *Biochim Biophys Acta 1647*, 42-47.
[19] Bunik, V. I., Schloss, J. V., Pinto, J. T., Dudareva, N., and Cooper, A. J. (2011) A survey of oxidative paracatalytic reactions catalyzed by enzymes that generate carbanionic intermediates: implications for ROS production, cancer etiology, and neurodegenerative diseases, *Advances in enzymology and related areas of molecular biology 77*, 307-360.
[20] Nematollahi, A., Sun, G., Harrop, S. J., Hanrahan, J. R., and Church, W. B. (2016) Structure of the PLP-Form of the Human Kynurenine Aminotransferase II in a Novel Spacegroup at 1.83 A Resolution, *International journal of molecular sciences 17*, 446.
[21] Okamoto, A., Higuchi, T., Hirotsu, K., Kuramitsu, S., and Kagamiyama, H. (1994) X-ray crystallographic study of pyridoxal 5'-phosphate-type aspartate aminotransferases from Escherichia coli in open and closed form, *Journal of biochemistry 116*, 95-107.
[22] Eliot, A. C., and Kirsch, J. F. (2004) Pyridoxal phosphate enzymes: mechanistic, structural, and evolutionary considerations, *Annual review of biochemistry 73*, 383-415.
[23] Krissinel, E., and Henrick, K. (2004) Secondary-structure matching (SSM), a new tool for fast protein structure alignment in three dimensions, *Acta crystallographica. Section D, Biological crystallography 60*, 2256-2268.
[24] Kirsch, J. F., Eichele, G., Ford, G. C., Vincent, M. G., Jansonius, J. N., Gehring, H., and Christen, P. (1984) Mechanism of action of aspartate aminotransferase proposed on the basis of its spatial structure, *Journal of molecular biology 174*, 497-525.

[25] Mehta, P. K., Hale, T. I., and Christen, P. (1993) Aminotransferases: demonstration of homology and division into evolutionary subgroups, *European Journal of Biochemistry 214*, 549-561.
[26] Yano, T., Kuramitsu, S., Tanase, S., Morino, Y., and Kagamiyama, H. (1992) Role of Asp222 in the catalytic mechanism of Escherichia coli aspartate aminotransferase: the amino acid residue which enhances the function of the enzyme-bound coenzyme pyridoxal 5'-phosphate, *Biochemistry 31*, 5878-5887.
[27] Yano, T., Mizuno, T., and Kagamiyama, H. (1993) A hydrogen-bonding network modulating enzyme function: asparagine-194 and tyrosine-225 of Escherichia coli aspartate aminotransferase, *Biochemistry 32*, 1810-1815.
[28] Hayashi, H., Mizuguchi, H., Miyahara, I., Nakajima, Y., Hirotsu, K., and Kagamiyama, H. (2003) Conformational change in aspartate aminotransferase on substrate binding induces strain in the catalytic group and enhances catalysis, *The Journal of biological chemistry 278*, 9481-9488.
[29] McPhalen, C. A., Vincent, M. G., Picot, D., Jansonius, J. N., Lesk, A. M., and Chothia, C. (1992) Domain closure in mitochondrial aspartate aminotransferase, *Journal of molecular biology 227*, 197-213.
[30] Clausen, T., Schlegel, A., Peist, R., Schneider, E., Steegborn, C., Chang, Y. S., Haase, A., Bourenkov, G. P., Bartunik, H. D., and Boos, W. (2000) X-ray structure of MalY from Escherichia coli: a pyridoxal 5'-phosphate-dependent enzyme acting as a modulator in mal gene expression, *The EMBO journal 19*, 831-842.
[31] Islam, M. M., Hayashi, H., Mizuguchi, H., and Kagamiyama, H. (2000) The substrate activation process in the catalytic reaction of Escherichia coli aromatic amino acid aminotransferase, *Biochemistry 39*, 15418-15428.
[32] Cunin, R., Glansdorff, N., Piérard, A., and Stalon, V. (1986) Biosynthesis and metabolism of arginine in bacteria, *Microbiological Reviews 50*, 314-352.
[33] Bertoldi, M., Cellini, B., Montioli, R., and Borri Voltattorni, C. (2008) Insights into the mechanism of oxidative deamination catalyzed by DOPA decarboxylase, *Biochemistry 47*, 7187-7195.
[34] Burkhard, P., Dominici, P., Borri-Voltattorni, C., Jansonius, J. N., and Malashkevich, V. N. (2001) Structural insight into Parkinson's disease treatment from drug-inhibited DOPA decarboxylase, *Nature structural biology 8*, 963-967.
[35] Johnson, K. A. (2009) Chapter 23 Fitting Enzyme Kinetic Data with KinTek Global Kinetic Explorer, In *Methods in enzymology*, pp 601-626, Academic Press.
[36] Johnson, K. A., Simpson, Z. B., and Blom, T. (2009) FitSpace Explorer: An algorithm to evaluate multidimensional parameter space in fitting kinetic data, *Analytical Biochemistry 387*, 30-41.
[37] Johnson, K. A., Simpson, Z. B., and Blom, T. (2009) Global Kinetic Explorer: A new computer program for dynamic simulation and fitting of kinetic data, *Analytical Biochemistry 387*, 20-29.

## Appendices

### Appendix A: Crystallographic data collection and refinement statistics.

| | **RitR(C128S) (5U8K)** | **$RitR_{ox}$ (5U8M)** | **RitR(C128D) (5VFA)** | **rdlv** | **rd2lv** |
|---|---|---|---|---|---|
| Space group | C121 | P212121 | C121 | C121 | P21212 |
| Cell dimensions | | | | | |
| a, b, c (Å) | 141.1, 60.1, 53.3 | 74.3, 74.8, 102.8 | 142.8, 59.7, 52.5 | 93.9, 50.0, 63.0 | 40.2, 115.3, 125.4 |
| α, β, γ (°) | 90.0, 96.0, 90.0 | 90.0, 90.0, 90.0 | 90.0, 96.3, 90.0 | 90.0, 121.4, 90.0 | 90.0, 90.0, 90.0 |
| Resolution (Å) (last shell)[a] | 40.33-1.69 (1.75-1.69) | 50.00-2.10 (2.14-2.10) | 50.00-1.45 (1.48-1.45) | 50.00-1.83 (1.86-1.83) | 50.00-2.60 (2.64-2.60) |
| Wavelength (Å) | 0.97872 | 0.97872 | 0.97857 | 0.97857 | 0.97872 |
| No. of reflections | | | | | |
| Observed | 276131(24543) | 206898(8842) | 396912(14482) | 81689(3266) | 263987(10059) |
| Unique | 49527(4856) | 33913(1667) | 76689(3384) | 21809(1033) | 18645(919) |
| Completeness (%)[a] | 99.6 (97.9) | 99.9 (99.6) | 99.0 (89.1) | 99.1(97.0) | 100.0 (100.0) |
| $R_{merge}$ (%)[a,b] | 0.090 (0.340) | 0.071 (0.586) | 0.046 (0.498) | 0.082 (0.436) | 0.147 (0.890) |
| Multiplicity | 5.6 (5.1) | 6.1 (5.3) | 5.2 (4.3) | 3.7 (3.2) | 14.2 (10.9) |
| $\langle I/\sigma(I)\rangle$[a] | 16.6 (8.1) | 25.2 (2.5) | 28.6 (2.9) | 13.3 (2.6) | 16.9 (3.3) |
| **Model Refinement Statistics** | | | | | |
| Reflections in work set | 91682 | 64031 | 76664 | 23890 | 17730 |

| | | | | | |
|---|---|---|---|---|---|
| Reflections in test set | 3718 | 3805 | 2000 | 1204 | 1770 |
| $R_{cryst}$ ($R_{free}$) | 0.1435 (0.1685) | 0.1881 (0.2309) | 0.1641 (0.1854) | 0.2357 (0.2767) | 0.1976 (0.2886) |
| No. of residues | 459 | 458 | 443 | 234 | 499 |
| No. of solvent atoms | 733 | 185 | 610 | 242 | 49 |
| Number of TLS groups | 18 | 17 | 16 | 1 | 1 |
| Average *B*-factor ($Å^2$) [c] | | | | | |
| Protein atoms | 12.9 | 46.3 | 25.9 | 24.1 | 43.3 |
| Solvent | 27.4 | 40.7 | 36.4 | 30.5 | 38.0 |
| RMS deviations | | | | | |
| Bond lengths (Å) | 0.010 | 0.011 | 0.008 | 0.012 | 0.015 |
| Bond angles (°) | 1.021 | 1.053 | 0.976 | 1.311 | 1.474 |
| Coordinate error (Å) | 0.11 | 0.26 | 0.14 | 0.22 | 0.40 |
| Ramachandran statistics (favored/allowed/ outliers) | 98.5/1.5/0.0 | 98.0/2.0/0.0 | 97.0/3.0/0.0 | 95.7/3.0/1.3 | 91.3/4.7/4.0 |

**Appendix B: Crystallographic data collection and refinement statistics.**

| | **Q15Z91** | **Q15Z91·GTP** |
|---|---|---|
| Space group | P212121 | P212121 |
| Cell dimensions | | |
| a, b, c (Å) | 82.1, 116.0, 167.6 | 82.9, 116.5, 167.3 |
| α, β, γ (°) | 90.0, 90.0, 90.0 | 90.0, 90.0, 90.0 |
| Resolution (Å) | 50.00-1.85 | 50.00-1.95 |
| (last shell)[a] | (1.88-1.85) | (1.98-1.95) |
| Wavelength (Å) | 0.97872 | 0.97857 |
| No. of reflections | | |
| Observed | 797511(33484) | 720622(28138) |
| Unique | 135739 (6671) | 117445(5618) |
| Completeness (%)[a] | 100.0 (99.8) | 98.8(95.6) |
| $R_{merge}$ (%)[a,b] | 0.090 (0.613) | 0.103 (0.540) |
| Multiplicity | 5.9 (5.0) | 6.1 (5.0) |
| $\langle I/\sigma(I)\rangle$[a] | 17.9 (2.7) | 13.5 (2.7) |
| **Model Refinement Statistics** | | |
| Reflections in work set | 135607 | 117218 |
| Reflections in test set | 2000 | 1996 |
| $R_{cryst}$ ($R_{free}$) | 0.1662 (0.1833) | 0.2616 (0.3161) |
| No. of residues | 1192 | 1073 |
| No. of solvent atoms | 931 | 427 |
| Number of TLS groups | 8 | 9 |
| Average *B*-factor (Å$^2$) [c] | | |
| Protein atoms | 38.2 | 56.8 |
| Ligand[d] | 25.4 | 41.5 |
| Solvent | 41.8 | 45.1 |
| RMS deviations | | |
| Bond lengths (Å) | 0.011 | 0.013 |
| Bond angles (°) | 1.259 | 1.667 |
| Coordinate error (Å) | 0.17 | 0.27 |
| Ramachandran statistics (favored/allowed/outliers) | 96.8/2.5/0.7 | 90.1/6.2/3.8 |

[a] Values in parentheses apply to the high-resolution shell indicated in the resolution row.

[b] $R = \Sigma(||F_{obs}|\text{-scale}*|F_{calc}||) / \Sigma |F_{obs}|$.

[c] Isotropic equivalent B factors, including contribution from TLS refinement.

[d] In the structure of Q15Z91, "ligands" refers to c-di-GMP and citrate. In the structure of Q15Z91·GTP, "ligands" refers to c-di-GMP and GTP.

## Appendix C: Crystallographic data collection and refinement statistics.

| | SwMppP | SwMppP·D-Arg | SwMppP·L-Arg | SwMppP·2KA | SwMppP·4HKA |
|---|---|---|---|---|---|
| Space group | P212121 | P212121 | P212121 | P212121 | P212121 |
| Cell dimensions | | | | | |
| a, b, c (Å) | 85.7, 108.3, 195.4 | 86.8, 109.1, 194.8 | 85.8, 108.4, 196.2 | 85.9, 108.8, 195.5 | 86.0, 108.4, 196.5 |
| α, β, γ (°) | 90.0, 90.0, 90.0 | 90.0, 90.0, 90.0 | 90.0, 90.0, 90.0 | 90.0, 90.0, 90.0 | 90.0, 90.0, 90.0 |
| Resolution (Å) (last shell)[a] | 41.45-2.10 (2.14-2.10) | 44.53-2.25 (2.29-2.25) | 50.00-2.20 (2.24-2.20) | 44.59-1.83 (1.87-1.83) | 50.00-1.93 (1.96-1.93) |
| Wavelength (Å) | 0.97852 (D) | 0.97856 (G) | 0.97872 | 0.97849 | 0.97856 |
| No. of reflections | | | | | |
| Observed | 1532933(60186) | 256371 (12494) | 408941 (15090) | 1055413 (53434) | 650654 (25173) |
| Unique | 106188 (5236) | 79816 (3984) | 85820 (3839) | 160466 (7902) | 135654 (6682) |
| Completeness (%)[a] | 100.0 (100.0) | 90.2 (91.2) | 91.6 (84.1) | 99.9 (100.0) | 98.4 (98.3) |
| $R_{merge}$ (%)[a,b] | 0.106 (0.734) | 0.106 (0.726) | 0.057 (0.193) | 0.074 (0.567) | 0.066 (0.488) |
| Multiplicity | 14.4 (11.5) | 3.2 (3.1) | 4.8 (3.9) | 6.6 (6.8) | 4.8 (3.8) |
| $\langle I/\sigma(I)\rangle$[a] | 30.7 (5.2) | 10.0 (1.9) | 24.7 (6.1) | 14.4 (3.3) | 21.8 (2.3) |
| **Model Refinement Statistics** | | | | | |
| Reflections in work set | 100876 | 76747 | 85724 | 160326 | 135549 |
| Reflections in test set | 5256 | 3015 | 1999 | 2000 | 2000 |
| $R_{cryst}$ ($R_{free}$) | 0.148 (0.177) | 0.162 (0.197) | 0.145 (0.195) | 0.151 (0.175) | 0.156 (0.178) |
| No. of residues | 1417 | 1404 | 1458 | 1434 | 1454 |
| No. of solvent atoms | 903 | 693 | 745 | 1032 | 930 |
| Number of TLS groups | 29 | 33 | 30 | 31 | 20 |
| Average *B*-factor (Å$^2$)[c] | | | | | |
| Protein atoms | 32.0 | 34.1 | 28.8 | 31.2 | 32.4 |
| Ligands | 30.9 | 43.9 | 31.6[d] | 37.6[d] | 41.9[d] |
| Solvent | 35.6 | 36.6 | 33.0 | 37.3 | 36.9 |

| | | | | | |
|---|---|---|---|---|---|
| RMS deviations | | | | | |
| Bond lengths (Å) | 0.013 | 0.015 | 0.010 | 0.010 | 0.011 |
| Bond angles (°) | 1.395 | 1.565 | 1.141 | 1.140 | 1.155 |
| Coordinate error (Å) | 0.17 | 0.22 | 0.17 | 0.19 | 0.19 |
| Ramachandran statistics (favored/allowed/outliers) | 98.3 / 1.7 /0.0 | 98.4 / 1.6 / 0.0 | 97.2 / 2.5 / 0.3 | 97.6/ 2.0 / 0.4 | 98.2/ 1.8 / 0 |

[a] Values in parentheses apply to the high-resolution shell indicated in the resolution row.

[b] $R = \Sigma(||F_{obs}|\text{-scale}*|F_{calc}||) / \Sigma |F_{obs}|$.

[c] Isotropic equivalent B factors, including contribution from TLS refinement.

[d] In L-Arg complex structure, “ligands” refers to the L-Arg-PLP unit; in the 2KA complex structure, it refers to the 2KA and L-Arg-PLP molecules; and in the 4HKA complex structure, it refers to the 4HKA molecules. In the protein only, “ligands” refer to $Cl^-$ ion.

| | E15A·L-Arg | H29A | H29S | H29A·L-Arg | H29S·L-Arg | F115Y |
|---|---|---|---|---|---|---|
| Space group | P1 21 1 | P212121 | P212121 | P212121 | P212121 | I121 |
| Cell dimensions | | | | | | |
| a, b, c (Å) | 64.4, 200.5, 139.9 | 85.9, 108.3, 195.7 | 85.8, 108.0, 195.6 | 85.8, 108.0, 195.7 | 85.5, 107.7, 195.5 | 111.62, 63.25, 243.10 |
| α, β, γ (°) | 90.0, 103.3, 90.0 | 90.0, 90.0, 90.0 | 90.0, 90.0, 90.0 | 90.0, 90.0, 90.0 | 90.0, 90.0, 90.0 | 90.0, 90.29, 90.0 |
| Resolution (Å) (last shell)[a] | 50.00-2.20 (2.28-2.24) | 50.00-1.90 (1.93-1.90) | 50.00-1.95 (1.98-1.95) | 50.00-2.30 (2.34-2.30) | 50.00-2.10 (2.14-2.10) | 60.77-1.92 (1.96-1.92) |
| Wavelength (Å) | | | | | | 0.97872 |
| No. of reflections | | | | | | |
| Observed | 977686(170041) | 837303(143854) | 252515(12536) | 494009(79839) | 726298 (27943) | 433940 (18551) |
| Unique | 36991(8030) | 35984 (7049) | 131339(6470) | 17981(3685) | 104882 (5113) | 128901 (6294) |
| Completeness (%)[a] | 97.0 (92.2) | 99.4 (99.1) | 99.8 (99.3) | 97.8 (92.3) | 99.8(98.9) | 99.7 (98.7) |
| $R_{merge}$ (%)[a,b] | 0.110 (0.588) | 0.076 (0.555) | 0.083 (0.551) | 0.078 (0.369) | 0.088 (0.460) | 1.162 (3.647) |
| Multiplicity | 5.7 (4.6) | 5.8 (5.1) | 7.1 (6.8) | 6.2 (4.9) | 6.9 (5.5) | 3.4 (2.9) |
| $\langle I/\sigma(I)\rangle$[a] | 14.9 (2.1) | 21.7 (2.8) | 22.9 (3.1) | 20.5 (3.7) | 22.6 (3.4) | 1.9 (0.3) |
| **Model Refinement Statistics** | | | | | | |
| Reflections in work set | 156239 | 143740 | 131221 | 79748 | 104781 | 120037 |
| Reflections in test set | 2001 | 2000 | 1999 | 1999 | 2000 | 1827 |
| $R_{cryst}$ ($R_{free}$) | 0.2054(0.2656) | 0.1503(0.1818) | 0.1508(0.1838) | 0.1607(0.2183) | 0.1562(0.1989) | 0.2620(0.3453) |
| No. of residues | 2839 | 1421 | 1421 | 1456 | 1455 | 1441 |
| No. of solvent atoms | 1432 | 1072 | 943 | 472 | 688 | 468 |
| Number of TLS groups | 72 | 30 | 25 | 26 | 30 | 18 |
| Average *B*-factor (Å$^2$)[c] | | | | | | |
| Protein atoms | 46.5 | 29.1 | 30.4 | 41.4 | 37.8 | 23.1 |
| Ligands | 38.0[d] | 25.1[d] | 28.1[d] | 38.8[d] | 35.4[d] | - |
| Solvent | 39.0 | 37.5 | 36.9 | 39.2 | 40.1 | 23.1 |
| RMS deviations | | | | | | |
| Bond lengths (Å) | 0.012 | 0.009 | 0.010 | 0.011 | 0.011 | 0.014 |

| | | | | | | |
|---|---|---|---|---|---|---|
| Bond angles (°) | 1.255 | 1.055 | 1.108 | 1.181 | 1.173 | 1.411 |
| Coordinate error (Å) | 0.29 | 0.17 | 0.15 | 0.22 | 0.17 | 0.38 |
| Ramachandran statistics (favored/allowed/outliers) | 97.2 / 2.5 / 0.3 | 98.1 / 1.6 / 0.4 | 98.2 / 1.5 / 0.4 | 97.1/ 2.6 / 0.3 | 97.2/ 2.4 / 0.4 | 90.6 / 7.4 / 2.0 |

## Appendix D: Proton NMR spectra for the products of SwMppP and its N-terminal mutants with L-Arg.

(A) Pure L-Arg (2.0 mM, ▬); (B) a reaction mixture containing 10.0 µM SwMppP and 2.0 mM L-Arg (▬),; (C) a reaction mixture containing 50.0 µM SwMppP$_{\Delta 1\text{-}22}$ and 2.0 mM L-Arg (▬); (D) a reaction mixture containing 50.0 µM SwMppPT12A and 2.0 mM L-Arg (▬); (E) a reaction mixture containing 50.0 µM SwMppPE15A and 2.0 mM L-Arg (▬); (F) a reaction mixture containing 50.0 µM SwMppPE15Q and 2.0 mM L-Arg (▬); (G) a reaction mixture containing 50.0 µM SwMppPT12A/E15A and 2.0 mM L-Arg (▬). All in 20 mM sodium phosphate buffer (pH 8.4).

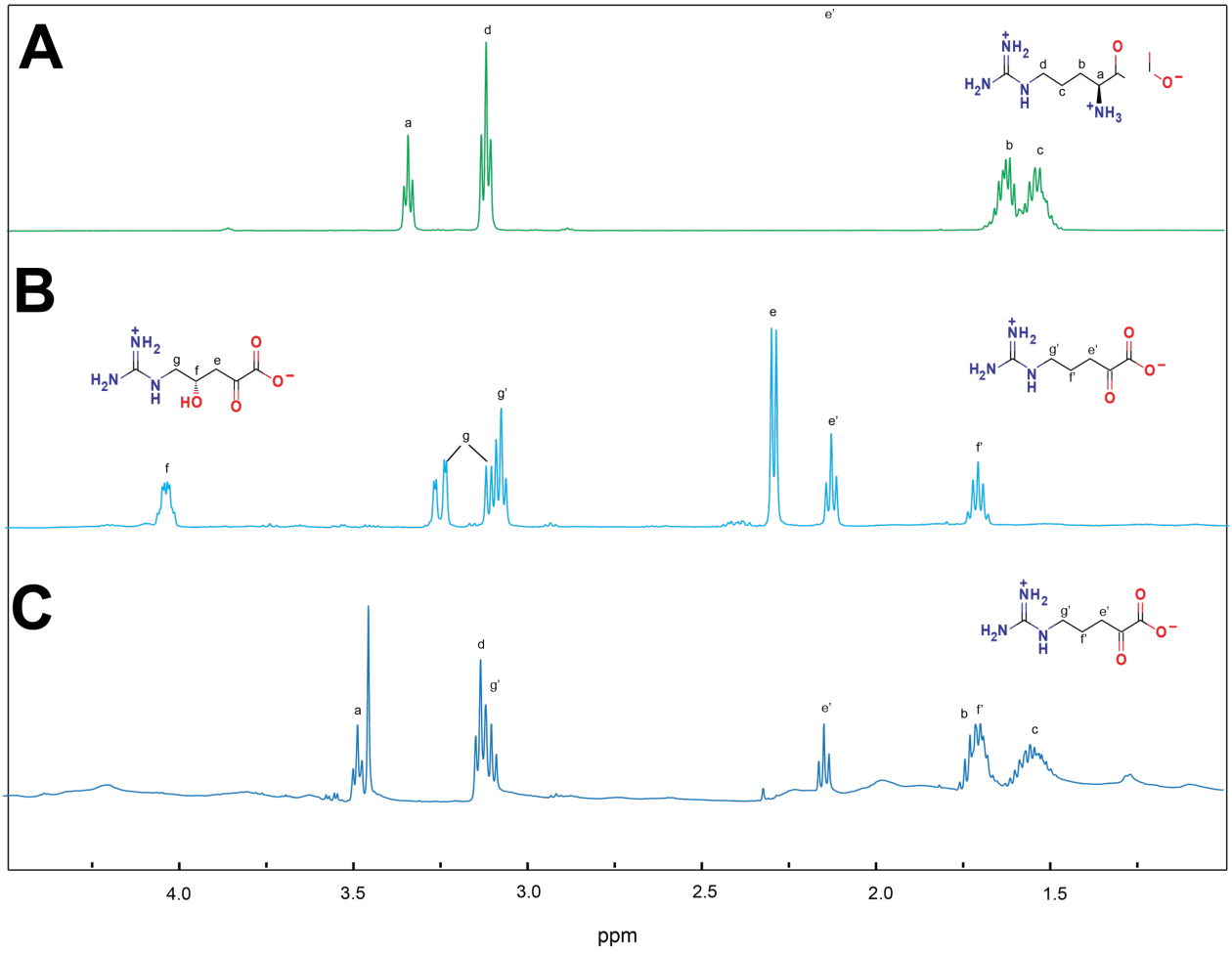

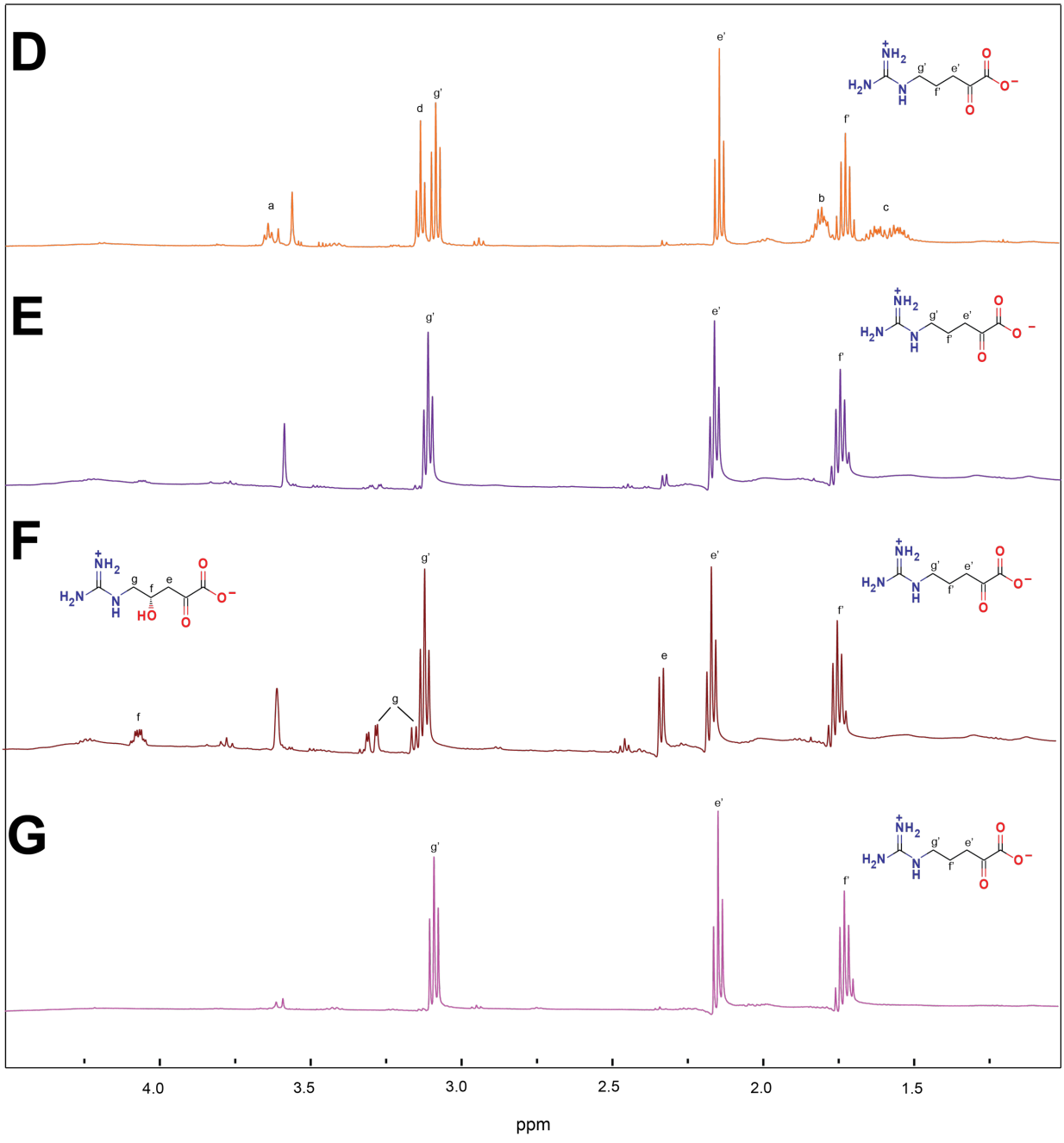
D
E
F
G
a
b
c
d
e
f
g
e'
f'
g'
4.0
3.5
3.0
2.5
2.0
1.5
ppm

## Appendix E: Proton NMR spectra for SwMppP active site mutants with L-Arg.

(A) L-Arg (2.0 mM) with MES (2.0 mM); (B) a reaction mixture containing 10.0 μM $SwMppP_{H29A}$ in MES pH 6.7 (2 mM, final concentration) buffer and 2.0 mM L-Arg; (C) a reaction mixture containing 10.0 μM $SwMppP_{H29A}$ in MES pH 6.7 (2 mM, final concentration) buffer and 2.0 mM L-Arg; (D) a reaction mixture containing 10.0 μM $SwMppP_{F115Y}$ in MES pH 6.7 (2 mM, final concentration) buffer and 2.0 mM L-Arg; (E) a reaction mixture containing 10.0 μM $SwMppP_{F191Y}$ in MES pH 6.7 (2 mM, final concentration) buffer and 2.0 mM L-Arg; (F) a reaction mixture containing 10.0 μM $SwMppP_{D218S}$ in MES pH 6.7 (2 mM, final concentration) buffer and 2.0 mM L-Arg.

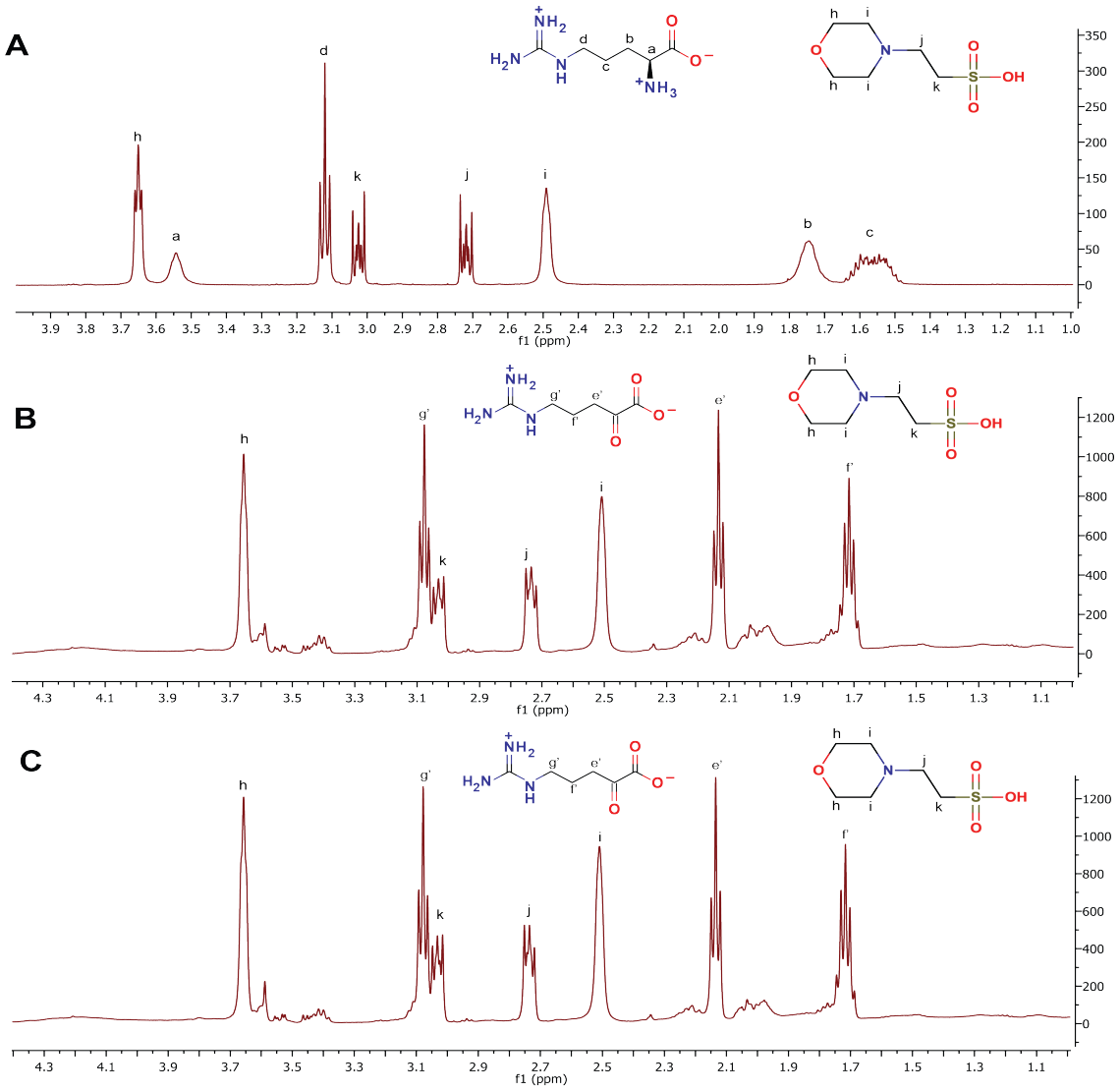

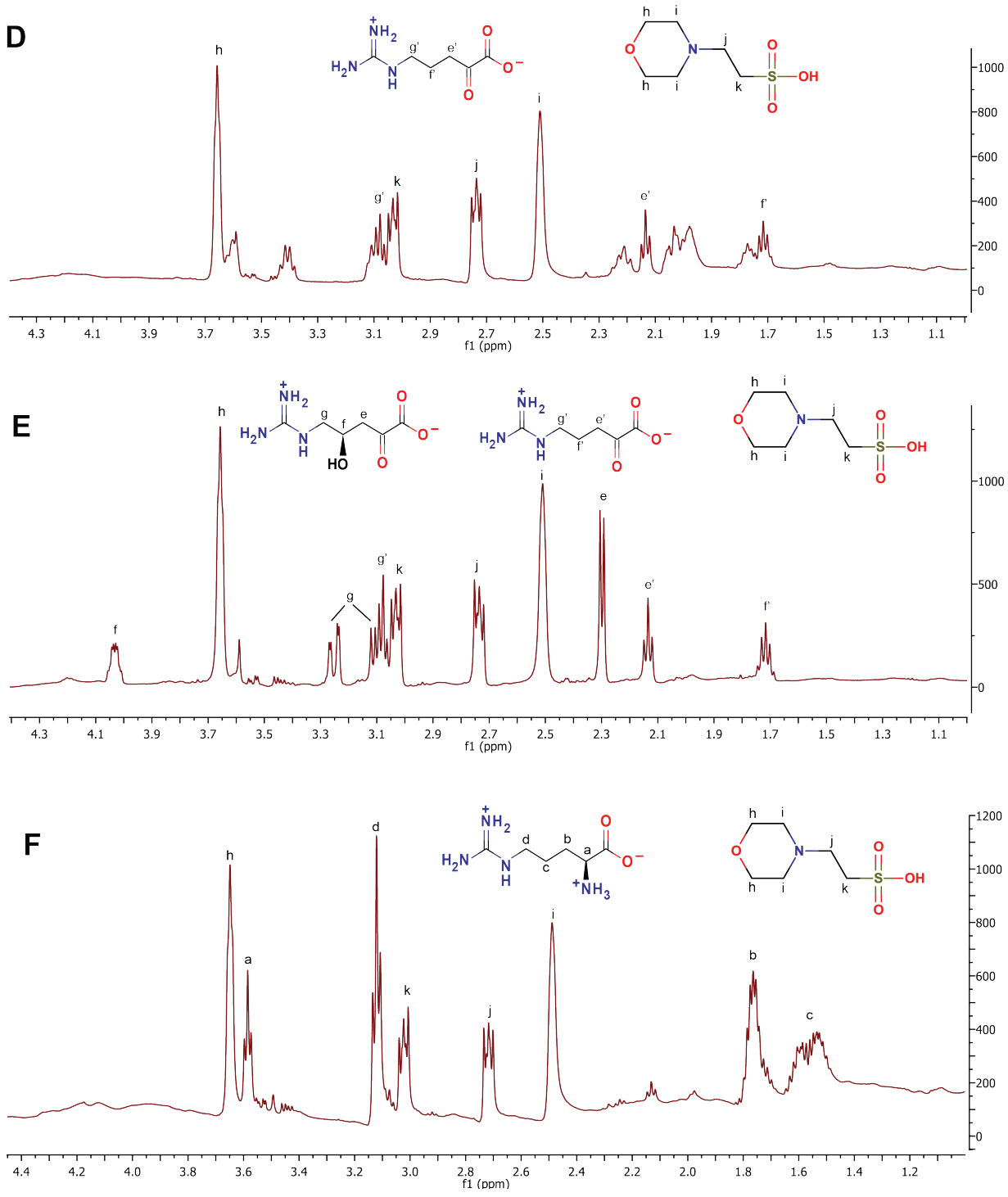
D
E
F
f1 (ppm)

**Appendix F: Overlay the structure (A) and active site (B) of SwMppP•L-Arg with SwMppP•2**

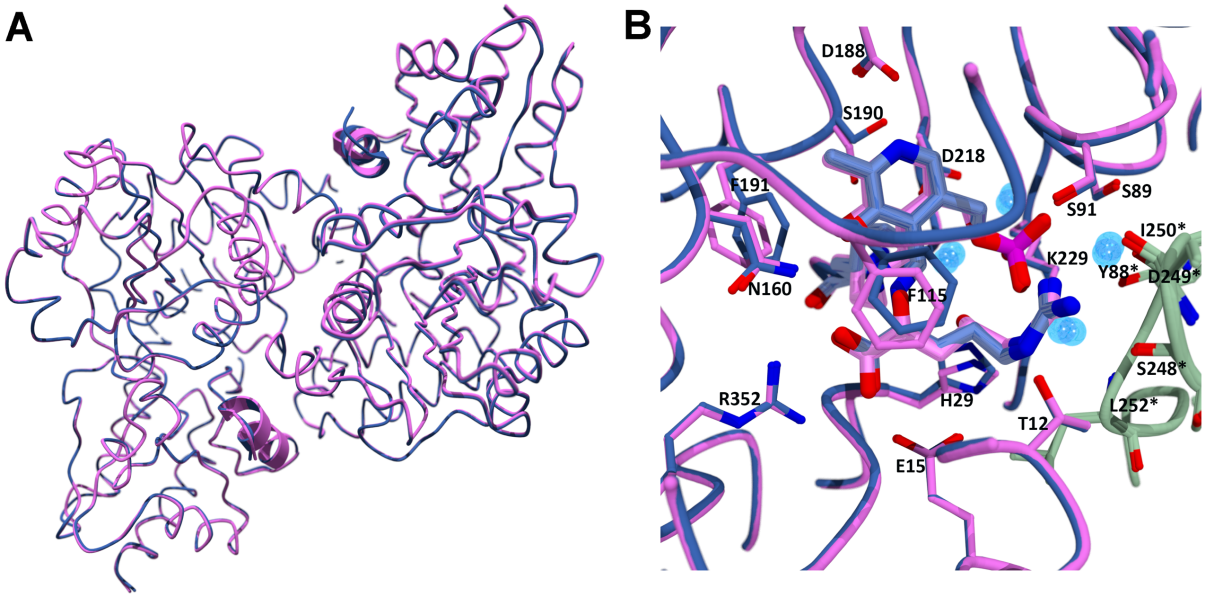


**Appendix G: Overlay the structure (A) and active site (B) of SwMppP•L-Arg with SwMppP•3**

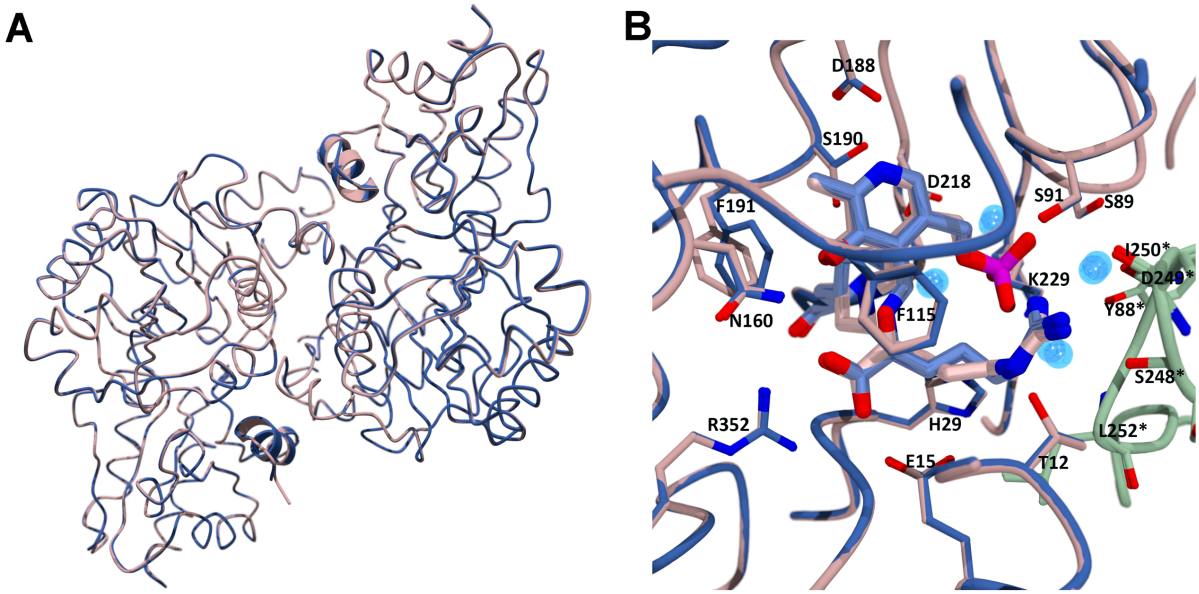

# CURRICULUM VITAE

Lanlan Han

Place of birth: Yancheng, Jiangsu Province, China

## Education

Ph.D., University of Wisconsin-Milwaukee, December 2017
Major: Biochemistry
Title of Thesis: Structure-Function Relationships in Bacterial Regulatory Proteins and an Enzyme Involved in Antibiotic Biosynthesis

M.E., Shandong University, June 2012
Major: Bioengineering
Title of Thesis: Screening and Preliminary Separation of Pectinase; Construction of Novel Surface Display Systems of Lactic Acid Bacteria for Oral Vaccines

B. S. in Soochow University, June 2009
Major: Bioscience
Title of Thesis: Screening Bacteria with an Ability of Coaggregation from Town Sewage

## Honors and Awards

May 2017 Sosnovksy Award for Excellence in Graduate Research

2016-2017 UWM Graduate Student Excellence Fellowship (GSEF) Award

Sep 2015 The Chair's Prize for my poster titled "A Novel PLP-Dependent L-Arginine Hydroxylase in L-Enduracididine Biosynthesis" on the 35th Midwest Enzyme Chemistry Conference

May 2013 The Student Accessibility Center (SAC) Excellence Award

2008-2009 People's comprehensive scholarship at Soochow University

2007-2008 People's comprehensive scholarship at Soochow University

2006-2007 People's comprehensive scholarship at Soochow University

## Publications

1. Zhu Y, Han L, Hefferon KL, Sivaggi NR, Wilson DB, McBride MJ. Periplasmic Cytophaga hutchinsonii endoglucanases are required for use of crystalline cellulose as sole carbon and energy source. *Applied and Environmental Microbiology*. 2016, 82 (15): 4835-4845

2. Han L, Schwabacher AW, Moran GR, Silvaggi NR. Streptomyces wadayamensis MppP is a PLP-Dependent L-Arginine α-deaminase, γ-Hydroxylase in the Enduracididine Biosynthetic Pathway. *Biochemistry*. 2015, 54: 7029−7040

3. Maule AF, Wright DP, Weiner JJ, Han L, Peterson FC, Volkman BF, Silvaggi NS, Ulijasz AT. The aspartate-less receiver (ALR) domains: distribution, structure and function. *PLOS Pathogens*. 2015, 11(4): e1004795

4. Guthrie ML, Sidhu PS, Hill EK, Horan TC, Nandhikonda P, Teske KA, Yuan NY, Sidorko M, Rodali R, Cook JM, Han L, Silvaggi NR, Bikle DD, Moore RG, Singh RK, Arnold LA. Antitumor Activity of 3-Indolylmethanamines 31B and PS121912. *Anticancer Research*. 2015, 35(11): 6001-6007

5. Teske K, Nandhikonda P, Bogart JW, Feleke B, Sidhu P, Yuan N, Preston J, Goy R, Han L, Silvaggi NR, Singh RK, Bikle DD, Cook JM, Arnold LA. Identification of VDR antagonists among nuclear receptor ligands using virtual screening. *Nuclear Receptor Research*. 2014, 1. pii: 101076

6. Sidhu PS, Teske K, Feleke B, Yuan NY, Guthrie ML, Fernstrum GB, Vyas ND, Han L, Preston J, Bogart JW, Silvaggi NR, Cook JM, Singh RK, Bikle DD, Arnold LA. Anticancer activity of VDR-coregulator inhibitor PS121912. *Cancer Chemotherapy Pharmacology*. 2014, 74(4): 787-798

7. Zhang X, Hu S, Du X, Li T, Han L, Kong J. Heterologous expression of carcinoembryonic antigen in Lactococcus lactis via LcsB-mediated surface displaying system for oral vaccine development. *Journal of Microbiology, Immunology, and Infection*. 2016, 49(6): 851-858

8. Hu S, Kong J, Sun Z, Han L, Kong W, Yang P. Heterologous Protein Display on the Cell Surface of Lactic Acid Bacteria Mediated by the S-Layer Protein. *Microbial Cell Factories* 2011, DOI: 10.1186/1475-2859-10-86

## Manuscripts in Preparation

1. Han L, Silvaggi NR. Structure and Mechanism of the Novel PLP-dependent L-Arginine Oxidase MppP in Streptomyces wadayamensis. 2017, In preparation for *Structure*.

2. Glanville DG, Han L, Maule AF, Weiner J, Perea-Pallares J, Cheverton A, Lourim D, Morrissey JA, Woodacre A; Clarke TB, Silvaggi NR and Ulijasz AT. A novel family of redox sensors in the streptococci evolved from two-component response regulators. 2017, In preparation for *Molecular Cell*.

3. Han L, Silvaggi NR. The diguanylate cyclase Q15Z91 possesses a non-canonical aspartate-less receiver domain. 2017, In preparation for *Journal of Biological Chemistry*.

## Oral Presentations and Posters

Lanlan Han, Nicholas R. Silvaggi. "A Novel PLP-Dependent L-Arginine Hydroxylase in L-Enduracididine Biosynthesis" Poster at the American Society for Biochemistry and Molecular Biology Annual Meeting, Chicago, IL. April 26, 2017

Lanlan Han, Nicholas R. Silvaggi. “RitR, A Response Regulator with an Aspartate-Less Receiver Domain” Presentation to the American Crystallographic Association Annual Meeting, Philadelphia, PA. July 26, 2015

Lanlan Han, Nicholas R. Silvaggi. "A Novel PLP-Dependent L-Arginine Hydroxylase in L-Enduracididine Biosynthesis" Poster at the 35th Midwest Enzyme Chemistry Conference. Illinois Institute of Technology, Chicago, IL, September 12, 2015

Lanlan Han, Nicholas R. Silvaggi. “Structure and Function of the Atypical Response Regulator RitR” Poster at the departmental research symposia (Awards Day), 2015

Lanlan Han, Nicholas R. Silvaggi. “Structure and Function of the Atypical Response Regulator RitR” Poster at the 34th Midwest Enzyme Chemistry Conference. Northwestern University, Evanston IL, September 27, 2014

Lanlan Han, Nicholas R. Silvaggi. “Structure and Function of the Atypical Response Regulator RitR” Poster at the departmental research symposia (Awards Day), 2014

Lanlan Han, Nicholas R. Silvaggi. “Structure and Function of the Atypical Response Regulator RitR” Poster at the departmental research symposia (Awards Day), 2013

Lanlan Han, Nicholas R. Silvaggi. “Structure and Function of the Atypical Response

Regulator RitR" Poster at the departmental research symposia (Awards Day), 2012

## Teaching and Research Experience

09/2012-05/2013 Teaching Assistant on CHEM 104: General Chemistry and Qualitative Analysis

06/2013- Now Research Assistant in Dr. Silvaggi Lab